UNIVERSITY OF LIVERPOOL

School of Engineering

Electrochemical Properties of Porous Metals Manufactured by Lost Carbonate Sintering

Thesis submitted in accordance with the requirements of the University of Liverpool for the degree of Doctor of Philosophy

By

KAIKAN DIAO

June 2016

Abstract

Porous metals have recently attracted much attention in both academia and industry. They have many potential applications ranging from light weight structure, thermal management and sound absorption, because of their unique structural, mechanical, thermal and acoustic properties. Open-cell porous metal can be an ideal material for electrochemical applications due to its high surface area, permeability and electric conductivity.

The electro-active surface area of porous electrodes is the most important factor in electrochemical applications, such as fuel cells, because it largely determines the current density in the electrode. However, most research to date on the surface area of porous metals has been focused on the geometric and real surface areas. Very little research has been conducted to study the electro-active surface area.

The mass transfer coefficient of a solid electrode is a very important factor in flow cell applications, such as flow battery and wastewater treatment, because high mass transfer coefficient means high reaction performance. However, very little research has been carried out on the mass transfer coefficient of open-cell porous metal manufactured by the space-holder method.

The main objective of this study is to investigate the electrochemically relevant structural properties of porous Cu and Ni fabricated by the Lost Carbonate Sintering (LCS) process, which is a cost-effective process for manufacturing open-cell porous metals with controlled porosity, pore size and pore shape. In this project, the geometric, electro-active and real surface areas of porous Cu and Ni have been measured by quantitative stereology, cyclic voltammetry (peak current) and cyclic voltammetry (double layer capacitance) methods, respectively. The mass transfer coefficient of porous Ni has been measured by linear sweep

voltammetry, using a purpose-built flow cell. The tortuosity of porous Cu has been measured by a diffusion method, using a purpose-built diaphragm cell.

The geometric, electro-active and real surface areas of porous metal are due to the contributions from the primary porosity, the primary and secondary porosities, and the surfaces of metal particles, respectively. The geometric, electro-active and real surface areas of porous Cu and Ni samples with pore sizes 75-1500 μm and porosities 0.53-0.81 were in the ranges of 18-110 cm^{-1}, 24-369 cm^{-1} and 700-1200 cm^{-1}, respectively. Both the geometric and electro-active surface area increased with porosity and decreased with pore size. The real surface area decreased with porosity but the effect of pore size was not pronounced. The values of electro-active surface area of LCS porous metal can be similar to and often greater than those of the existing porous metals, e.g. incofoam Ni.

The mass transfer coefficient of porous Ni with pore sizes 250-1500 μm and porosities 0.63-0.81 at different flow rates from 0.24 ml/s to 2.8 ml/s was in the range of 0.0035-0.0727 cm/s. Both the limiting current and mass transfer coefficient increased with flow rate and had the maximum values at a porosity of around 0.65-0.70. The maximum limiting current decreased and the maximum mass transfer coefficient increased with pore size. Compared with a smooth Ni plate at the same flow velocity, the mass transfer coefficient of the LCS porous Ni was increased by up to 9 times. The enhancement is due to the Ni particles providing a rough surface for the cell walls and the tortuous pore structure resulting in a high level of fluid turbulence.

The tortuosity of the porous Cu samples, with pore sizes 250-1500 μm and porosities 0.56-0.84, was in the range of 1.33-1.78. It increased with pore size and decreased with porosity, agreeing with an empirical formula for porous media.

This research has successfully applied cyclic voltammetry to the measurement of electro-active surface area of porous metals for the first time. It is the first systematic study of the structural properties of relevance to electrochemical applications of porous metals manufactured by LCS process.

Declaration

I hereby certify that the content of this project work entitled “Electrochemcial Properties of Porous Metals Manufactured by Lost Carbonate Sintering”, submitted for the degree of Doctor in Philosophy in the Faculty of Science and Engineering at the University of Liverpool, is a record of an original work done by me under the supervision of Prof. Yuyuan Zhao of the School of Engineering, University of Liverpool, and this project work has not been used as the basis for the award of any other degree/diploma.

Kaikan Diao

June 2016

Acknowledgments

Primarily, I must express my deepest gratitude to my supervisor, Prof. Y. Zhao, for his supervision and guidance in my PhD programme and the help in the experimental and theoretical modelling work.

I would also like to thank Dr. L. Zhang for help with the manufacturing of samples. Her help, knowledge, and insight are invaluable.

In addition, I wish to extend my thanks to Mr. D. Atkinson for help with cleaning, grinding and polishing of samples. I also would like to thank Mr. J. Mathew for training of machine operations.

I would also like to thank Dr. Z. Xiao for his help in the measurement of geometric surface area.

Finally, I would like to thank my family and friends. Their help and support are invaluable in my PhD programme.

List of Publications

Diao, K., Xiao, Z., & Zhao, Y., 2015, “Specific surface area of porous Cu manufactured by Lost Carbonate Sintering: Measurements by quantitative stereology and cyclic voltammetry”, *Materials Chemistry and Physics*, vol. 162, pp. 571-579

List of Symbols

A	Surface area	cm^2
A_C	Area of phere crown on the K_2CO_3	cm^2
A_{disc}	Cross-sectional area of the circular disc sample	cm^2
A_E	Electro-active surface area	cm^2
A_G	Geometric surface area	cm^2
A_p	Surface area of a K_2CO_3 particle	cm^2
A_R	Real surface area	cm^2
a	Fitted constant depends on both electrode geometry and flow conditions	
a'	Fitted constant depends on both electrode geometry and flow conditions	
b	Fitted constant depends on flow conditions	
b'	Fitted constant depends on flow conditions	
C	Double layer capacitance	mF
c	Concentration	mol/L
c'	Schmidt exponent	
$c_{b,t}$	Concentration in bottom compartment at time t	mol/L
$c_{b,i}$	Concentration in bottom compartment at initial	mol/L
$c_{t,t}$	Concentration in top compartment at time t	mol/L
$c_{t,i}$	Concentration in top compartment at initial	mol/L
D	Diffusion coefficient	cm^2/s
D_0	Standard diffusion coefficient	cm^2/s
D_e	Effective diffusion coefficient	cm^2/s

D[2,3]	Surface weighted mean diameter	μm
D[3,4]	Volume weighted mean diameter	μm
d'	Fitted constant depends on both electrode geometry and flow conditions	
d_p	Pore size (K_2CO_3 particle size)	μm
d_M	Metal particle size	μm
E_{pa}	Peak potential of anodic process	V
E_{pc}	Peak potential of cathodic process	V
e_0	Elementary charge	Q
F	Faraday constant	C/mol
f	Frequency	Hz
Gr	Grashof number	
g	Acceleration of gravity	m/s^2
k	Mass transfer coefficient	cm/s
k_B	Boltzmann constant	J/K
I	Charge current	mA
i	Current	mA
I_L	Limiting current	mA/cm^3
I_p	Peak current	mA
I_{pa}	Peak current of anodic process	mA
I_{pc}	Peak current of cathodic process	mA
Δj	Current difference	mA
ja	Current in the charge	mA
jb	Current in the discharge	mA
L	Thickness of the sample	cm

L'	End to end length of the pore channel	cm
L_0	Length of a pore channel	cm
L_T	Length of test line	cm
$\overline{L_e}$	Average length of pathways	cm
l	Characteristic length	cm
ln	Natural logarithm of $(c_{b,i}-c_{t,i})/(c_{b,t}-c_{t,t})$	
M	Mass	g
$M_{K_2CO_3}$	Mass of K_2CO_3 powder	g
M_{Metal}	Mass of metal powder	g
n	Number of electronic transfer	
P	Number of intersections on test line	
P_L	Number of intersections with surfaces per unit length of test line	
P_P	Point fraction	
P_{pore}	Number of points in the pores	
P_{total}	Total grid points in the test area	
p	Fitted constant depends on pore size	
Q	Flow rate	ml/s
R	Gas constant	J/kmol
R^2	Coefficient of determination	
r	Electrolyte resistance	Ω
Re	Reynolds number	
S_{ME}	Gravimetric specific electro-active surface area	cm^2/g
S_{MG}	Gravimetric specific geometric surface area	cm^2/g
S_{MR}	Gravimetric specific real surface area	cm^2/g

S_V	Specific surface area	cm^{-1}
S_{VE}	Volumetric specific electro-active surface area	cm^{-1}
S_{VG}	Volumetric specific geometric surface area	cm^{-1}
S_{VR}	Volumetric specific real surface area	cm^{-1}
Sc	Schmidt number	
Sh	Sherwood number	
St	Stanton number	
T	Temperature	K
t	Time	s
U	Flow velocity	cm/s
u	Potential	V
V	Volume	cm^3
V_b	Volume of bottom compartment	cm^3
V_p	Volume of a K_2CO_3 particle	cm^3
V_t	Volume of top compartment	cm^3
v	Scan rate	V/s
Y	Correlation coefficient	
z	Ion charge	Q

Greek symbols

α	Product of the constants *D*, *A*, $1/V_t$, $1/V_b$ and *1/L*	
β	Diaphragm cell constant	
δ	Diffusion layer thickness	μm
δ_{peak}	Diffusion layer thickness at the time that the peak current is reached	μm

ε	Porosity	
ε_P	Primary porosity	
ε_S	Secondary porosity	
ε'	Relative dielectric permittivity of the solvent	F/m
ε_0'	Permittivity of the vacuum	F/m
η	Viscosity of the air	cm^2/s
θ	Ratio of electro-active and geometric surface areas	
θ_M	Ratio between the maximum electro-active surface area and the geometric surface area	
κ^{-1}	Debye-Huckel length	m
μ	Average number of K_2CO_3/K_2CO_3 contacts on a single K_2CO_3 particle	
μ_0	Dynamic viscosity	cm^2/s
ν	Kinematic viscosity	cm^2/s
ρ	Density	g/cm^3
$\rho_{K_2CO_3}$	Density of K_2CO_3	g/cm^3
ρ_{Metal}	Density of metal	g/cm^3
τ	Tortuosity	
$\emptyset$	K_2CO_3-to-metal particle size ratio	
ω	Uncertainty	
ω'	Angular frequency	Hz
ω_R	Rotation rate	rpm

Contents

Abstract.....i
Declaration.....iv
Acknowledgments.....v
List of Publications.....vi
List of Symbols.....vii
Chapter 1 Introduction.....1
1.1 Background and Motivation of Research.....1
1.2 Objectives of Research.....4
1.3 Structure of Thesis.....5
Chapter 2 Literature Review.....7
2.1 Introduction to Porous Metals.....7
2.1.1 Structures.....7
2.1.2 Applications: an Overview.....8
2.1.3 Applications: Electrochemistry.....9
2.2 Production Methods and Techniques for Porous Metals.....11
2.2.1 Melt Gas Injection.....13
2.2.2 Gas-Releasing Particle Decomposition in the Melt.....14
2.2.3 Casting Using a Polymer/Wax Template.....15
2.2.4 Metal Deposition on Cellular Preforms.....16
2.2.5 Entrapped Gas Expansion.....19
2.2.6 Hollow Sphere Structures.....21
2.2.7 Casting of Two Materials.....22
2.2.8 Gas-Metal Eutectic Solidification.....23
2.2.9 Space-Holder Methods.....25
2.2.9.1 Sintering Dissolution Process (SDP).....25
2.2.9.2 Lost Carbonate Sintering (LCS).....26
2.3 Fundamentals of Electrochemistry and Electrochemical Characterisation Techniques 29
2.3.1 Electrical Double Layer.....29
2.3.2 Diffusion Layer.....31
2.3.3 Cyclic Voltammetry (CV).....32
2.3.3.1 Experimental Setup and Voltammogram.....32
2.3.3.2 Effect of Diffusion Layer.....34

2.3.3.3 Cyclic Voltammetry of Non-Noble Metals....37
2.3.4 Double Layer Capacitance....40
2.3.5 Linear Sweep Voltammetry (LSV)....42
2.4 Techniques for Surface Area Measurements....43
2.4.1 Introduction....43
2.4.2 Quantitative Stereology....44
2.4.3 Brunauer-Emmett-Teller Method....45
2.4.4 Electrochemical Method....46
2.5 Measurement of Mass Transfer Coefficient....48
2.5.1 Introduction....48
2.5.2 Measurement Technique....49
2.5.3 Dimensionless Numbers for Mass Transport....53
2.5.4 Effect of Porosity....54
2.6 Techniques for Tortuosity Measurements....55
2.6.1 Introduction to Tortuosity....55
2.6.2 X-ray Computed Tomography....56
2.6.3 Acoustic Method....58
2.6.4 Diffusion Method....59
2.7 Summary....61
Chapter 3 Experimental....63
3.1 Preparation of Test Samples by LCS....63
3.1.1 Raw Materials....64
3.1.2 Mixing and Compaction....64
3.1.3 Sintering....66
3.2 Structural Characterisation....68
3.3 Measurement of Geometric Surface Area and Primary Porosity by Quantitative Stereology....69
3.4 Measurement of Tortuosity by the Diffusion Method....72
3.4.1 Experimental Apparatus....73
3.4.2 Sample Preparation and Test Procedure....74
3.5 Measurement of Surface Area by Cyclic Voltammetry....76
3.5.1 Experimental Apparatus....76
3.5.2 Preparation of Samples....77
3.5.2.1 Cu and Ni Plates....77

3.5.2.2 Porous Cu and Ni Samples 78
3.5.3 Test Procedure 79
3.5.3.1 Electro-Active Surface Area of Porous Cu 79
3.5.3.2 Electro-Active Surface Area of Porous Ni 80
3.5.3.3 Actual Surface Area of Porous Cu 82
3.6 Measurement of Mass Transfer Coefficient by Linear Sweep Voltammetry 84
3.6.1 Experimental Apparatus 84
3.6.2 Test Procedure 86
Chapter 4 Structural Characteristics of Porous Metals 88
4.1 Particle Sizes of Metal and K_2CO_3 Powders 88
4.2 Pore Structure 92
4.3 Porosity 95
4.4 Purity of Metal Matrix 96
4.5 Primary Porosity 100
4.6 Primary and Secondary Porosities 102
Chapter 5 Tortuosity of Porous Cu 105
5.1 Standard Diffusion Coefficient of NaCl 105
5.2 Tortuosity of Porous Cu Samples 106
5.3 Uncertainty Analysis 107
5.4 Effects of Pore Size and Porosity 110
Chapter 6 Geometric Surface Area 113
6.1 Quantitative Stereology 113
6.2 Stochastic Modelling 114
6.3 Comparison of Calculated and Experimental Values 116
Chapter 7 Electro-active Surface Area of Porous Cu 121
7.1 Calibration of Electro-active Surface Area by Cu Plates 121
7.2 IR Compensation in CV Experiment 122
7.3 Cyclic Voltammograms and Electro-Active Surface Area of Porous Cu 126
7.4 Effects of Porosity and Pore Size 129
7.5 Discussion 131
Chapter 8 Electro-Active Surface Area of Porous Ni 135
8.1 Calibration of Electro-Active Surface Area by Ni Plates 135
8.2 IR Compensation 137

8.3 CV voltammograms and Electro-Active Surface Area for Porous Ni 141
8.4 Effect of Scan Rate 153
8.5 Effects of Porosity and Pore Size 158
8.6 Discussion 161
Chapter 9 Real Surface Area of Porous Cu 165
9.1 Voltammograms, Capacitance and Real Surface Area 165
9.2 Effects of Porosity and Pore Size 176
9.3 Discussion 178
Chapter 10 Mass Transfer Coefficient 180
10.1 Effect of Flow Rate on Limiting Current 180
10.2 Effects of Porosity and Pore Size on Limiting Current 193
10.3 Mass Transfer Coefficient 196
10.4 Effects of Porosity and Pore Size on Mass Transfer Coefficient 197
10.5 Reynolds Number vs. Sherwood Number 200
10.6 Empirical Correlation 202
Chapter 11 Conclusions and Future Work 205
11.1 Conclusions 205
11.1.1 Pore Structure 205
11.1.2 Tortuosity 206
11.1.3 Geometric Surface Area 206
11.1.4 Electro-Active Surface Area 207
11.1.5 Real Surface Area 208
11.1.7 Mass Transfer Coefficient 208
11.2 Future Work 209
11.2.1 Measurement of Tortuosity 209
11.2.2 Measurement of Electro-Active Surface Area 209
11.2.3 Measurement of Mass Transfer Coefficient 210
11.2.4 Investigation of Electrochemical Applications 210
References 211
Appendixes 221

Chapter 1 Introduction

1.1 Background and Motivation of Research

Porous metals have attracted considerable attention in both academia and industry in the last few decades, due to their unique mechanical, thermal, acoustic, electrical and chemical properties (Gibson & Ashby 1999, Ashby 2000, Banhart 2001, Ma et al. 2005). Open-cell porous metals, in particular, have many potential applications such as heat exchange (Zhang et al. 2009, Xiao et al. 2013), sound absorption (Han et al. 2003), catalyst support (Ashby 2000) and porous electrode (Ashby 2000) because of their high internal surface area and good permeability for fluid flows.

Very little research has been conducted to date to understand the characteristics of electrochemical properties such as electro-active surface area and mass transfer coefficient of porous metals manufactured by the space holder methods, which are an important family of methods developed recently for manufacturing open cell porous metals. In powder metallurgy based space-holder methods (Banhart 2001, Zhao 2013), a metal powder is first mixed with a sacrificial powder (space holder), such as NaCl (Zhao et al. 2001), K_2CO_3 (Zhao et al. 2005) or urea (Laptev et al. 2004), and then compacted into a preform, followed by sintering. The space holder material is removed before, during or after sintering by either dissolution or decomposition to create pores. The metal particles are bonded during sintering to form a metal network.

The Lost Carbonate Sintering (LCS) process (Zhao et al. 2005) is one of the leading technologies capable of manufacturing open-cell micro-porous metals and is a representative powder metallurgy based space holder method. Porous metals manufactured by the LCS process have open cells and are potential materials for electrodes in

electrochemical applications. The previous research showed that open-cell metal foams can replace metal meshes in electrode applications (Bidault et al. 2009). Compared with traditional mesh electrodes, the advantages of metal foams include low manufacturing cost and high electrochemical activity.

Therefore, it is important to study the electrochemical properties of metal foams for such electrodes application as fuel cells and flow batteries, including electro-active surface area and mass transfer coefficient.

Surface area of porous metals is generally characterised either by geometric area or by true area, which can be different by more than two orders in magnitude. The active or effective surface area for a particular application depends on the length scale at which the surface plays a role. It is often greater than the geometric area but lower than the true area. For different applications, different surface areas are used. For an example, real surface area is the key parameter for applications such as super capacitors (Li et al. 2012, Lewandowski et al. 2012); in applications involving electrochemical reactions, however, the electro active surface area, which depends on how well the electrolyte accesses the pores, is the key parameter, and the magnitude of the diffusion or Nernst layer in the electrolyte and the surface roughness of the electrode are also important (Davies et al. 2005, Ward et al. 2013).

In the design of an electrochemical reactor, a number of factors should be considered which include geometry of electrode, fluid flow and reaction in electrolyte, mass and heat transport, cost and reliability (Recio et al. 2013). In all of these factors, the mass transfer is the most important because it limits the rate of electrochemical processes (Brown et al. 1993). In order to increase the rate of mass transport, a usual method is to increase the velocity of the electrolyte flowing through the electrode surface. However, it leads to higher energy consumption for pumping (Brown et al. 1993). As an alternative method, an inert

turbulence promoter (e.g., polymer meshes) in the path of the electrolyte can increase the rate of mass transport by introducing a high level turbulence (Leitz et al. 1977, Letord-Quemere 1988, Focke 1983). The open-cell pore structures in LCS porous metal are formed by the random arrangement of the potassium carbonate particles and lead to tortuous and bifurcated flow paths, which are expected to lead to high level turbulence when the fluid flows through the porous metal electrode. However, the mass transfer performance of LCS porous metals has not been investigated so far.

This project measures the electrochemical and related properties, at different length scales, of porous Cu and Ni samples manufactured by the LCS process. Specifically, this project measures the geometric surface area by the quantitative stereology (QS) method, the tortuosity by the diffusion method, the electro active and the real surface areas by two Cyclic Voltammetry (CV) methods and the mass transfer coefficient by the Linear Sweep Voltammetry (LSV) method. The effects of pore size and porosity on the surface areas, mass transfer coefficient and tortuosity are analysed. This project is devoted to providing a basis for quantitative understanding of the electrochemical and related properties of porous metals produced by solid route space holder methods. It also introduces the electrochemical techniques (CV, LSV) to the measurements of effective surface areas and mass transfer coefficient of porous metals.

1.2 Objectives of Research

In this project, the main purpose is to study the effects of pore structures (pore size and porosity) of the LCS porous Cu and Ni to the electrochemical properties. This project is to fabricate LCS porous metals with tailored structures (pore size and porosity) and to study their electrochemical (electro-active and real surface areas and mass transfer coefficient) and related properties (geometric surface area and tortuosity).

The main objectives are:

- To determine the relationship between pore structures (pore size and porosity) and geometric, electro-active and real surface areas.
- To determine the relationship between geometric and electro-active surface area.
- To determine the relationship between pore structures (pore size and porosity) and mass transfer coefficient.
- To determine the relationship between real surface area and the total surface area of the metal particles.
- To determine the relationships between pore structures (pore size and porosity) and tortuosity.

The main tasks are:

- To fabricate porous metals (Cu and Ni) with tailored structures (different pore sizes and porosities) by LCS process.
- To measure the geometric surface area of porous metals by the Quantitative Stereology (QS) method and to calculate the primary geometric surface area by stochastic modelling.

- To measure the electro-active surface area of porous metals by Cyclic Voltammetry (CV).
- To measure the real surface area of porous metals by the measurement of double layer capacitance.
- To measure the mass transfer coefficient of the porous metals by the Linear Sweep Voltammetry (LSV).
- To measure the tortuosity of the porous metals by the diffusion method.

1.3 Structure of Thesis

Chapter 2 reviews the literature on the experimental and theoretical work on the manufacture and characterisation of LCS porous metals and on the measurements of electrochemical and related properties. The literature on the other open-cell porous metals and the basic principles of electrochemical characterisation is also reviewed.

In Chapter 3, the details of the manufacturing method of the test samples and the experimental procedures used in characterising these samples are described, including the fabrication procedures for LCS porous Cu and Ni samples for the measurements of electrochemical and other related properties, the measurement methods, experimental equipment and test procedures for the measurements of geometric, electro-active and real surface areas, mass transfer coefficient and tortuosity.

Chapter 4 presents the results obtained from the experiments. The porous metals (Cu and Ni) with different pore sizes and porosities were tested to analyse the effects of pore parameters (pore size and porosity) on electrochemical and related properties, such as geometric, electro-active and real surface areas, mass transfer coefficient and tortuosity.

Chapter 5 discusses and analyses the experimental results presented in Chapter 4. Stochastic modelling will be used to calculate the primary geometric surface area in LCS porous metals. The relationship between electrochemical properties (electro-active and real surface areas and mass transfer coefficient) and related properties (geometric surface area and tortuosity) will be analysed.

Chapter 6 summarizes the conclusions obtained from this project.

Chapter 2 Literature Review

2.1 Introduction to Porous Metals

Porous metals (or metal foams) are a relatively new class of materials with low densities and novel physical, mechanical, thermal, electrical and acoustic properties (Ashby 2000). They are widely used in everyday life, e.g. cushioning, insulating, damping, construction, filtering and many other applications (Eifert & Banhart 1998). Porous metals are also known to have a high stiffness combined with low weight and low manufacturing cost (Ashby 2000). Therefore, porous metals have attracted considerable attention in both academia and industry in the last few decades (Ma et al. 2005).

2.1.1 Structures

A porous metal can be characterized structurally by its cell topology (open cells, closed cells), relative density, cell size and cell shape. The relative density is defined by the ratio of the density of porous metal to the density of the solid metal of the cell wall (Ashby 2000). Density can be measured by weighing a sample of known volume which can be obtained by direct measurement or Archimedes method. The other structural properties require microscopy. Figs. 2.1 (a) and (b) show the pore structures (cell size and cell shape) of an open-cell INCO nickel foam and a closed-cell Alulight foam obtained by a scanning electron microscopy (SEM) and X-ray tomography, respectively (Ashby 2000). Open-cell porous metals have open pores distributed in the metal matrix and interconnected through windows on cell walls. Conversely, closed-cell porous metals have intact cell walls and non-interconnected pores. In general, SEM is most informative for open-cell porous metals but reliable data for size and shape are not easily extracted from SEM for closed-cell porous metal (Ashby 2000).

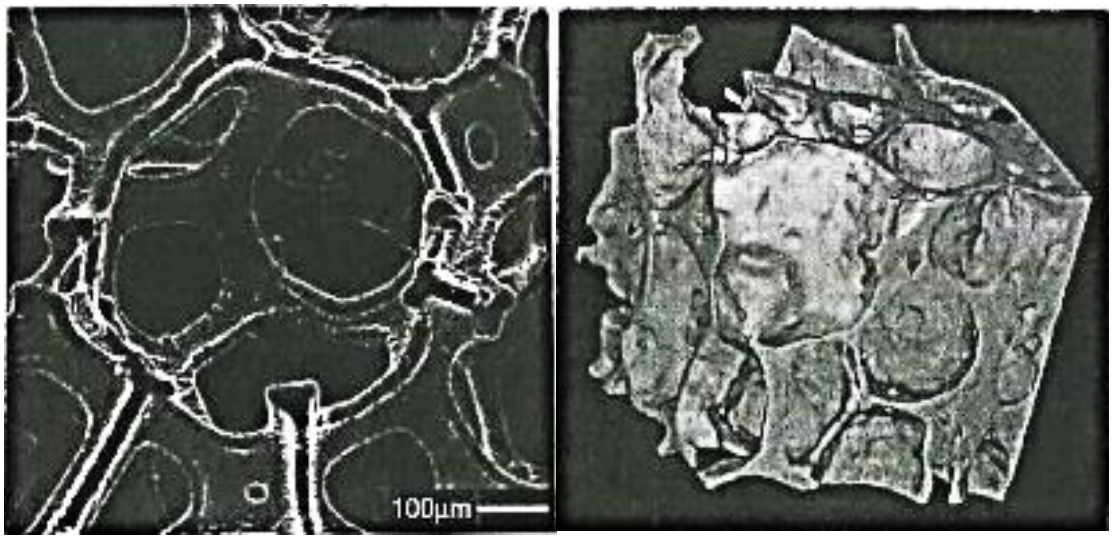

(a) (b)

Fig. 2.1, *(a) A SEM micrograph of an INCO nickel foam. (Ashby 2000) (b) An X-ray tomography of an Alulight foam. (Bart-Smith et al. 1998)*

2.1.2 Applications: an Overview

Porous metals offer significant performance gains in light, stiff structures, for the efficient absorption of energy, for thermal management and perhaps for acoustic control and other, more specialized, applications (Ashby 2000).

Since most methods for cheap production of bulk material tend to generate closed-cell porous metals, attention has been concentrated on these porous metals for many structural applications. The applications include various components designed to absorb energy progressively under relatively low applied loads. If the cell size can be kept fine and uniform, compared with solid metals, porous metals with the reduced constraint on cell walls can sustain large plastic strains in deformation, with substantial absorption of energy. In some cases, the cell walls in the porous metals contain severely embrittling constituents, such as large ceramic particles and thick oxide films. They are often deliberately introduced during processing in order to raise the melt viscosity and thus inhibit cell coarsening and drainage (Gergely et al. 2000). Recent work has confirmed that these constituents can have

highly deleterious effects on the mechanical characteristics of the porous metals (Markaki & Clyne 2001). Closed-cell porous metals are also of interest for other types of applications such as thermal barriers (Degischer & Kriszt 2002).

Suggested and actual applications of open-cell porous metals include filters, catalyst supports, heat exchangers, fluid flow damping conduits, biomedical prostheses, internally-cooled shape memory actuators, air batteries, and protective permeable membranes and sheathes. The scale of the cell structure is very important for the functional characteristics and affects a basic specification for filters and fluid flow limiting devices. A fine cell size would often be preferred for heat exchangers while bone in-growth into prosthetic implants might require relatively coarse pores (Degischer & Kriszt 2002).

2.1.3 Applications: Electrochemistry

Open-cell porous materials have been used in the electrode applications, such as fuel cells (Bidault et al. 2009), flow batteries (Li et al. 2012), super capacitors (Li et al. 2012, Brevnov et al. 2006) and wastewater treatment (Nava et al. 2008) due to their unique pore structure and electrochemical performance.

Currently, open-cell porous Ni is being researched and considered for use as electrodes in fuel cells (Bidault et al. 2009). A fuel cell is a device that converts chemical energy into electricity through a chemical reaction such as oxidation-reduction reaction. As a type of energy generation with low carbon dioxide emissions and environmental impacts, fuel cells are attracting attention in both academia and industry. Fuel cells have been successfully used in space applications for decades (Vielstich et al. 2003). At present, the electrodes of fuel cells use nickel meshes (Bidault et al. 2009). The disadvantages of nickel mesh electrodes are high relative cost and limited electrochemically active surface area. Recently,

scientists have pointed out that porous metal electrodes are more effective than the traditional metal mesh electrodes (Bidault et al. 2009).

Porous metals are low cost and high performance materials in electrode applications. With a lower weight-surface ratio, porous metal electrodes can have higher electrochemically active surface area than metal mesh electrodes and can improve the performance of electrodes in fuel cells. Bidault et al. (2009) pointed out that if silver is also plated on the surface of porous metal electrodes, better electrochemical properties will be obtained. Silver plated porous nickel showed a decrease in Ohmic and charge transfer resistance, and also an increase of the double layer capacitance compared to the uncoated nickel foam (Bidault et al. 2009).

Another electrochemical application of porous metal is found in flow batteries. Compared with normal fuel cells, the advantages of flow batteries are high energy efficiency, short response time and long cycle life (Li et al. 2011). As with normal fuel cells, the electrodes determine the performance of flow batteries. Porous metal, with a high electrochemically active surface area and good permeability (Montillet et al. 1992, Thewsey & Zhao 2008), would be a good material for electrode applications in flow batteries. The open-cell porous materials which are used in flow cell applications include porous Ni (Montillet et al. 1992, Montillet et al. 1994), vitreous carbon (De Radiguès et al. 2012) and graphite felts (Chen et al. 2015, Nikiforidis & Daoud 2015, Suárez et al. 2014). In addition to the high effective surface area, porous materials also offer a high level of turbulence in the fluid, improving the performance of the electrochemical reactions (Montillet et al. 1994).

For applications in super capacitors, the high surface area of the porous material can offer a higher specific capacitance for energy storage (Lewandowski et al. 2012). The common materials include carbon fabric (Lewandowski et al. 2012), CuO foam (Li et al. 2012) and

porous silver (Brevnov et al. 2006). Compared with carbon materials, the usage of metals has an advantage of increased volumetric capacitance. The enhancement of volumetric capacitance is more significant in facilitating the loading to industrial products with limited space (Kobayashi et al. 2013).

Porous electrodes can be used for electrochemical recovery of heavy metals from a variety of industrial and laboratory model solutions (Bennion & Newman 1972, El-Deab et al. 1999, Gaunand et al. 1977, Podlaha & Fenton 1995, Saleh 2004, Soltan et al. 2003, Trainham & Newman 1977). The porous electrode forms a porous flow-through configuration providing a large surface area usually depleting the concentration of metal ions below 0.1 ppm (Nava et al. 2008). Therefore, porous materials are widely used as electrodes in electrochemical reactor systems for wastewater treatment due to their large specific surface area and permeability for flow fluid (Mattiusi et al. 2015, Doan et al. 2006, Li et al. 2011).

2.2 Production Methods and Techniques for Porous Metals

A range of manufacturing processes have been developed to achieve a wide variety of pore structures (closed-cell, open-cell, different pore sizes and porosities) and metal materials in order to achieve tailored properties for the applications. The characteristics of the nine classes of the main manufacturing processes for porous metals are summarized and listed in Table 2.1.

***Table 2.1**, Common manufacturing processes for porous metals.*

Process	**Relative cost**	**Pore size / Relative density**	**Cell topology**	**Metal foamed**	**References**
Melt gas injection	Low	5-20 mm / 0.03-0.1	Closed-cell	Al, Mg	(Ashby 2000)
Gas-releasing particle decomposition	Low	0.5-5 mm / 0.07-0.2	Closed-cell	Al	(Ashby 2000)
Casting using a polymer/wax template	Medium	1-5 mm / 0.05	Open-cell	Al, Mg, Ni-Cr, Stainless Steel, Cu	(Ashby 2000)
Metal deposition on cellular preforms	High	10-300 μm / 0.02-0.05	Open-cell	Ni, Ti	(Ashby 2000, Queheillalt et al. 2001)
Entrapped gas expansion	Medium -High	10-300 μm	Closed-cell	Ti	(Ashby 2000)
Hollow sphere structures	High	100 μm / 0.05	Closed-/ open-cell	Ni, Co, Ni-Cr	(Ashby 2000)
Casting of two materials	Low	10 μm – 10 mm / 0.3-0.5	Open-cell	Al	(Ashby 2000)
Gas-metal eutectic solidification	High	10 μm – 10 mm / 0.05-0.75	Closed-cell	Cu, Ni, Al	(Ashby 2000, Shapovalov 2007)
Space-holder	Low	50-1500 μm / 0.15-0.5	Open-cell	Cu, Ni, Al, Steel, Ti	(Zhao et al. 2001, Zhao et al. 2005)

2.2.1 Melt Gas Injection

The Melt Gas Injection (MGI) processes were developed simultaneously and independently by Alcan and Norsk Hydro in the late 1990s (Surace et al. 2009). The gas-injection processes are commonly used to manufacture porous aluminium alloys with closed-cell structures (Ashby 2000).

Fig. 2.2 shows a schematic illustration of the manufacture of porous Al by the melt gas injection method (CYMAT and HYDRO process) (Ashby 2000). A variety of gases (CO_2, O_2, inert gases and even water vapour) can be used to create bubbles within liquid aluminium. Bubbles form by this process float to the melt surface and liquid foam begins to solidify. The thermal gradient in the foam determines how long the foam remains liquid or semi-solid, and thus the extent of drainage (Ashby 2000).

The bubble size can be controlled by adjusting the gas flow rate and the propeller design (number of nozzles and their size) (Surace et al. 2009). By controlling the gas injection process and the cooling rate, the relative densities in the porous Al can be obtained in the range 0.03 to 0.1 and the closed cell pores can be controlled with diameters between 5 and 20 mm (Kenny & Thomas 1994, Sang et al. 1994).

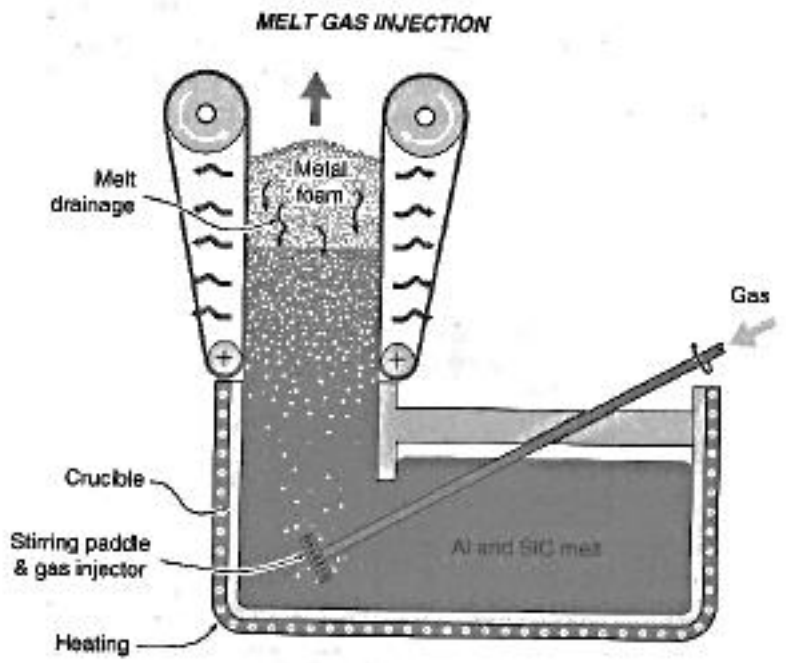

***Fig. 2.2**, A schematic illustration of the manufacture of porous Al by the melt gas injection method (CYMAT and HYDRO process). (Ashby 2000)*

2.2.2 Gas-Releasing Particle Decomposition in the Melt

Metals, such as Al and Al alloys, can be foamed by mixing into them a foaming agent that releases gas when heated. Titanium hydride (TiH_2) is widely used as the foaming agent. TiH_2 can be decomposed into Ti and gaseous H_2 when the temperature is about 465 °C (Speed 1976). For example, Fig. 2.3 shows the steps of Alporas process for porous Al manufacturing (Miyoshi et al. 2000). The process begins by melting Al and stabilizing the melt temperature between 670 and 690 °C. Then, 1%-2% of calcium is added in the melt. Ca can rapidly oxidize and form CaO and $CaAl_2O_4$ particles, which modify the viscosity of the Al. The melt is then aggressively stirred and 1%-2% of TiH_2 is added in the form of 5-20 μm diameter particles. The stirring system is withdrawn when the TiH_2 particles are dispersed in the melt in order for the foam to be formed. The foam is cooled to solidify and formed porous Al before the hydrogen escapes and the bubbles coalesce or collapse (Ashby

2000, Miyoshi et al. 2000). This technique can be used to manufacture porous metals with the pore size of 5 to 20 mm and relative densities of 0.03 to 0.1. (Ashby 2000)

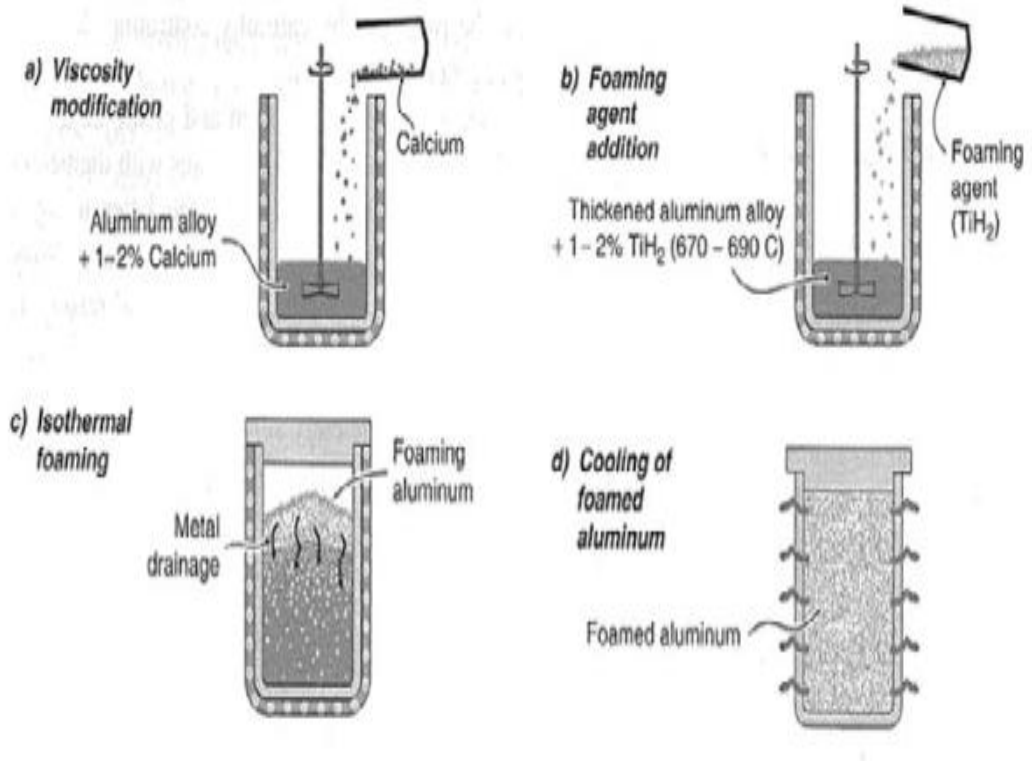

.

***Fig. 2.3**, The process steps used in the manufacture of porous Al by gas-releasing particle decomposition in the melt method (Alporas process). (Ashby 2000)*

2.2.3 Casting Using a Polymer/Wax Template

Investment casting in open-cell moulds has been used to manufacture open-cell porous metals. Fig. 2.4 schematically illustrates the DUOCEL process as an example of the investment casting method. An open-cell porous polymer/wax with the desired cell size and relative density is used as a template to create an investment-casting mould. The porous polymer/wax template is coated with a mould casting slurry which is then dried and embedded in casting sand. The casting slurry is then baked to harden and the polymer/wax template is decomposed at high temperature to produce a mould with open channels. The molten metal is then filled into the open channels. After the metal solidifies and the mould

material is removed, the open-cell porous metal is formed. A typical pore structure of the DUOCEL porous metal is shown in Fig. 2.4. This method is used to manufacture porous metals with pore size of 1-5 mm and relative densities as low as 0.05 (Ashby 2000, Harte et al. 1999).

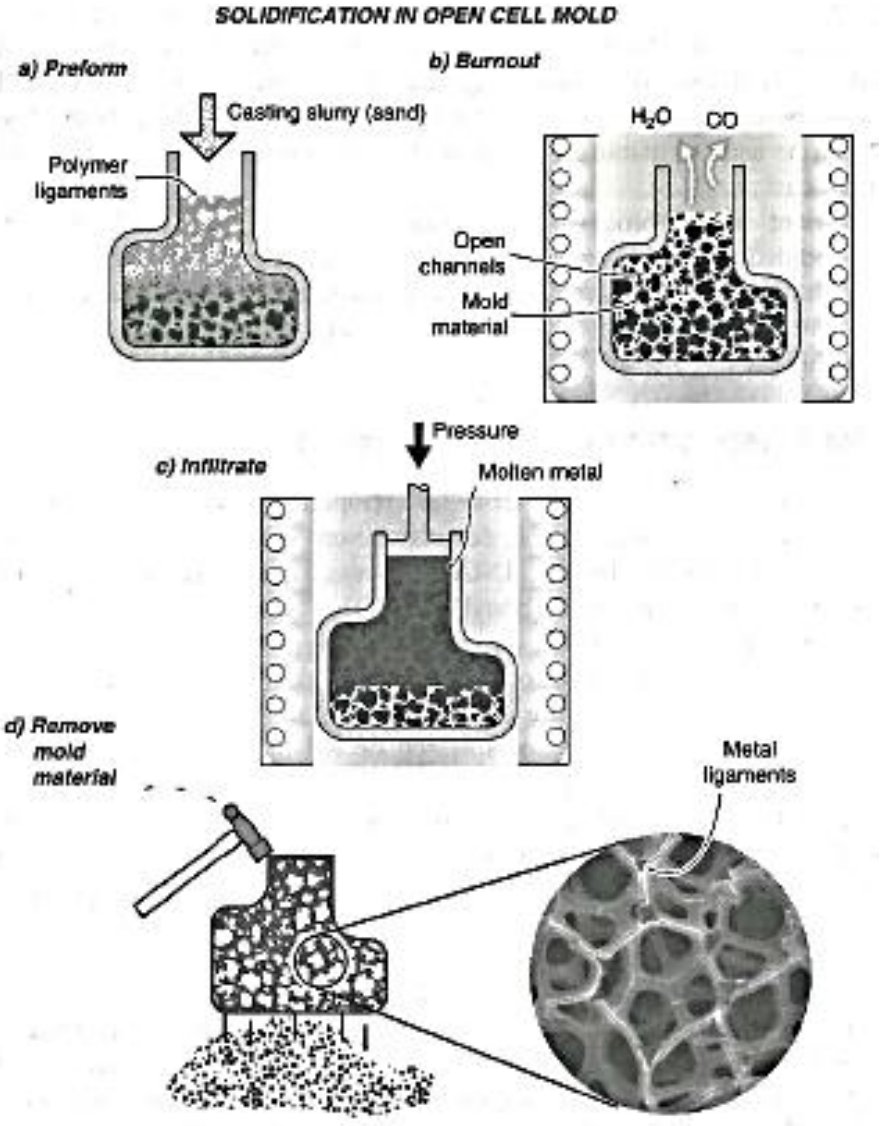

***Fig. 2.4**, Investment casting method used to manufacture open-cell porous metal (DUOCEL process). (Ashby 2000)*

2.2.4 Metal Deposition on Cellular Preforms

In the metal deposition method, metals are deposited on an open-cell porous polymer template by chemical vapour decomposition (CVD). In the INCO process, which is such a

vapour deposition method, Ni is deposited by the decomposition of nickel carbonyl, $Ni(CO)_4$. The detail of the process is shown in Fig. 2.5. An open-cell polymer is placed in a CVD reactor and $Ni(CO)_4$ is introduced. Then, gaseous $Ni(CO)_4$ decomposes into Ni and CO at the temperature of 100 °C and coats all the exposed heated surfaces within the reactor. The metal-coated porous polymer is removed from the CVD reactor after several tens of micrometres of the metal have been deposited. Finally, the porous Ni is formed after the polymer template is burnt out by heating in air (Babjak et al. 1990). This method is used in the manufacture of porous Ni and Ti and produces porous metals with the lowest relative density in the range of 0.02-0.05 and pore size in the range of 100-300 μm (Ashby 2000).

Fig. 2.6 shows the structure of INCO porous Ni. As an open-cell porous metal with high porosity, INCO porous Ni has great potential in electrochemical applications. This material is currently being studied for the electrode applications in alkaline fuel cells (Bidault et al. 2009) and solid oxide fuel cells (Corbin et al. 2009).

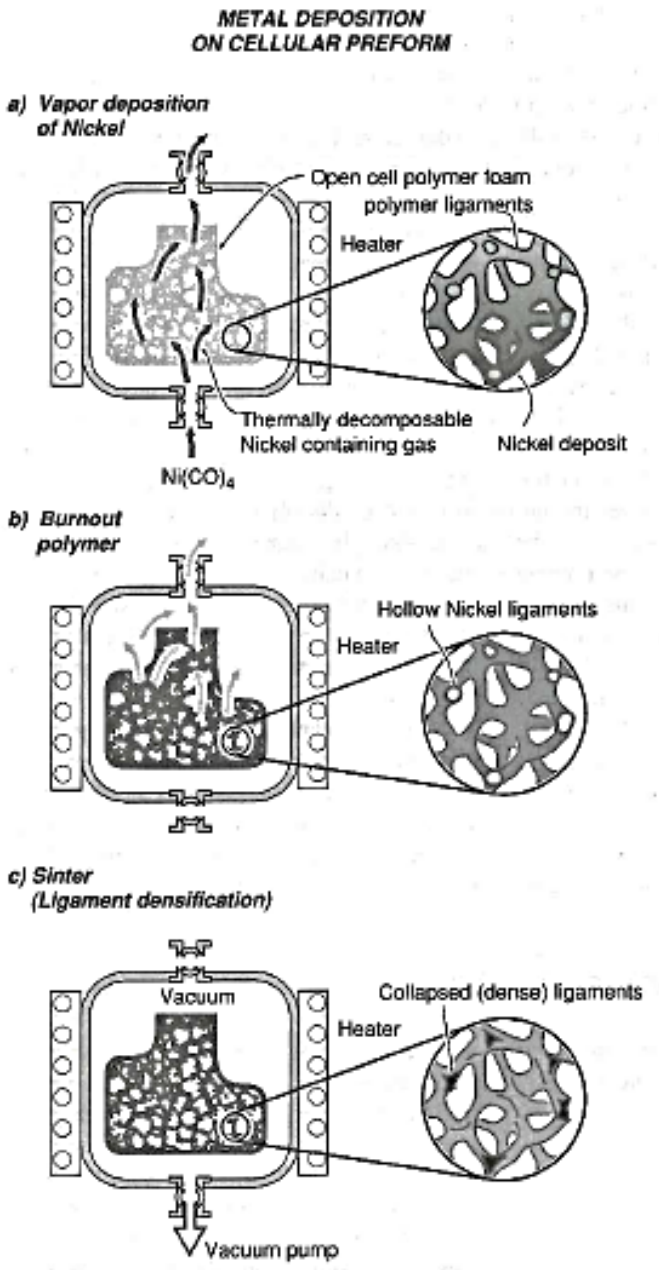

Fig. 2.5, *Schematic illustration of the CVD process used to create open-cell porous Ni (INCO process). (Ashby 2000)*

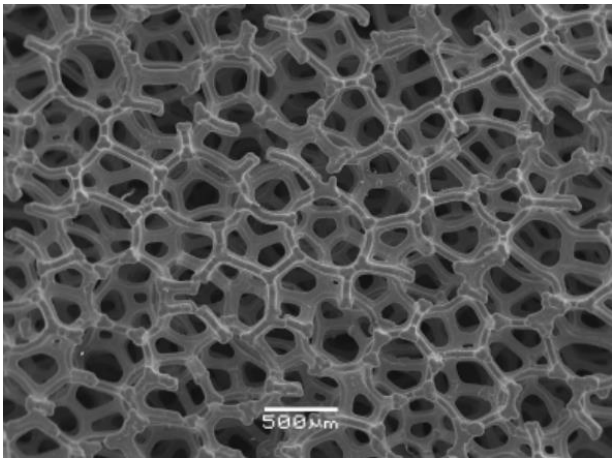

Fig. 2.6, *Open-cell structure of the INCO porous Ni. (Corbin et al. 2009)*

2.2.5 Entrapped Gas Expansion

The entrapped gas expansion method is used to manufacture closed-cell porous metals such as the low-density core (LDC) Ti-6Al-4V sandwich panels. Fig. 2.7 shows the process for manufacturing porous titanium alloy. Firstly, Ti-6Al-4V powder is sealed in a canister of the same alloy. The canister is evacuated to remove any oxygen and then backfilled with between 3 to 5 atmospheres of argon. Then, the canister is sealed and consolidated at 900 °C for 2 hours. The canister is then rolled at 900-940 °C resulting in void flattening and elongation in the rolling direction. Finally, the canister is expanded by heating at 900 °C for 20-30 hours. The high temperature raises the internal pore pressure causing creep dilation and a reduction in the overall density of the sample (Kawasaki 2015). This process gives the porous metal a porosity up to 0.5 and a pore size of 10-300 μm (Ashby 2000).

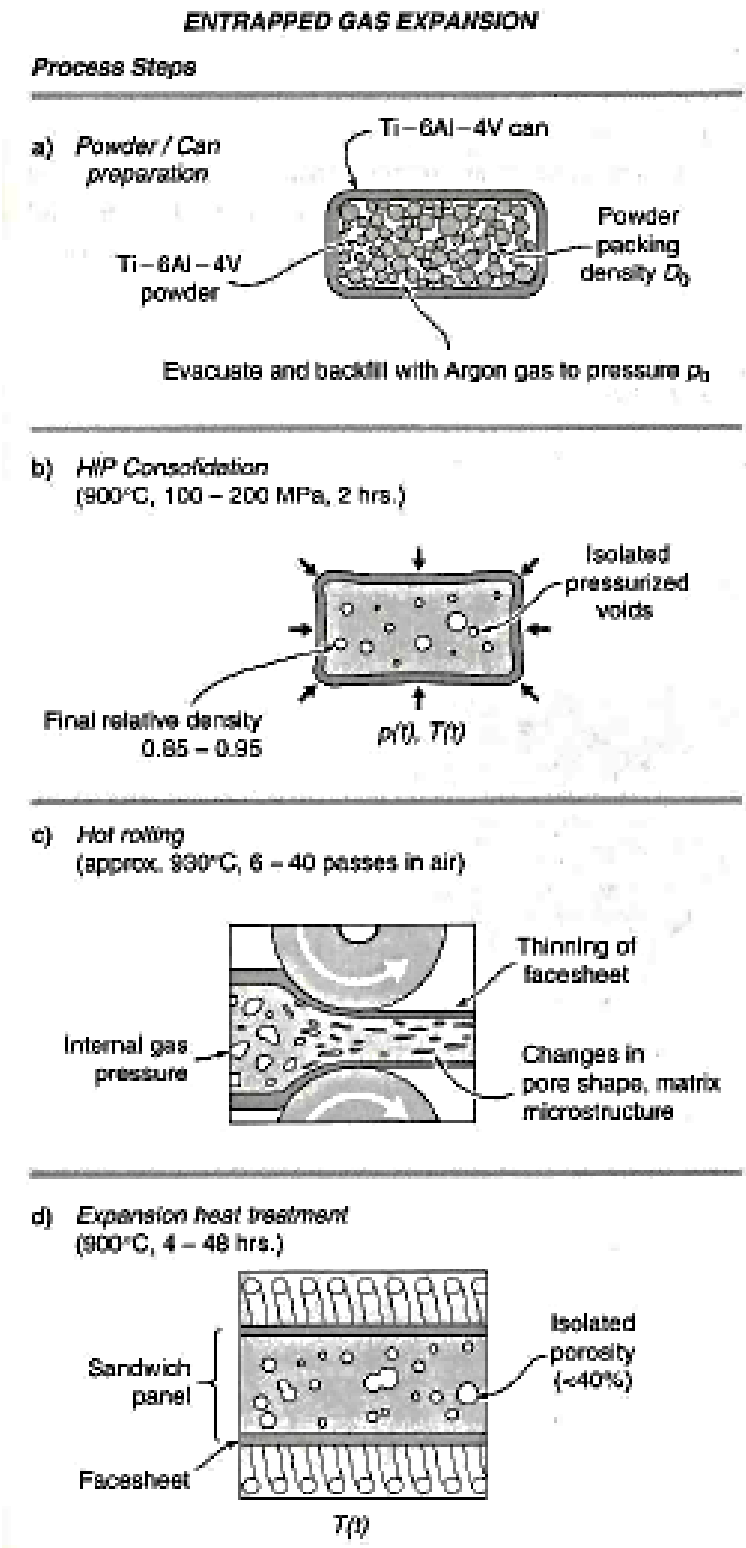

Fig. 2.7, *Process steps used to manufacture Ti alloy sandwich panels with highly porous closed-cell cores. (Ashby 2000)*

2.2.6 Hollow Sphere Structures

Hollow sphere methods have been commercially used to manufacture both open-cell and closed-cell porous metals (Ni superalloys and Ti-6Al-4V) with relative densities of 0.06 and pore size from 100 μm to several millimetres (Ashby 2000, Vida-Simiti et al. 2011). Fig. 2.8 shows the Georgia Tech route for creating hollow metal spheres. In this route, hollow spheres are formed from slurry composed of a decomposable precursor such as TiH_2, together with organic binders and solvents. The spheres are hardened by evaporation during their flight in a tall drop tower, heated to drive off the solvents and to volatilize the binder. The consolidation of the spheres without binder can form open or closed cells. A final heat treatment decomposes the metal hydride leaving hollow metal spheres (Kendall et al. 1981). This method can also be used to manufacture hollow stainless steel spheres by the oxide mixture of Fe_2O_3 and Cr_2O_3 (Lhuissier et al. 2009, Roy et al. 2011). Hollow spheres can be sintered to form a porous structure.

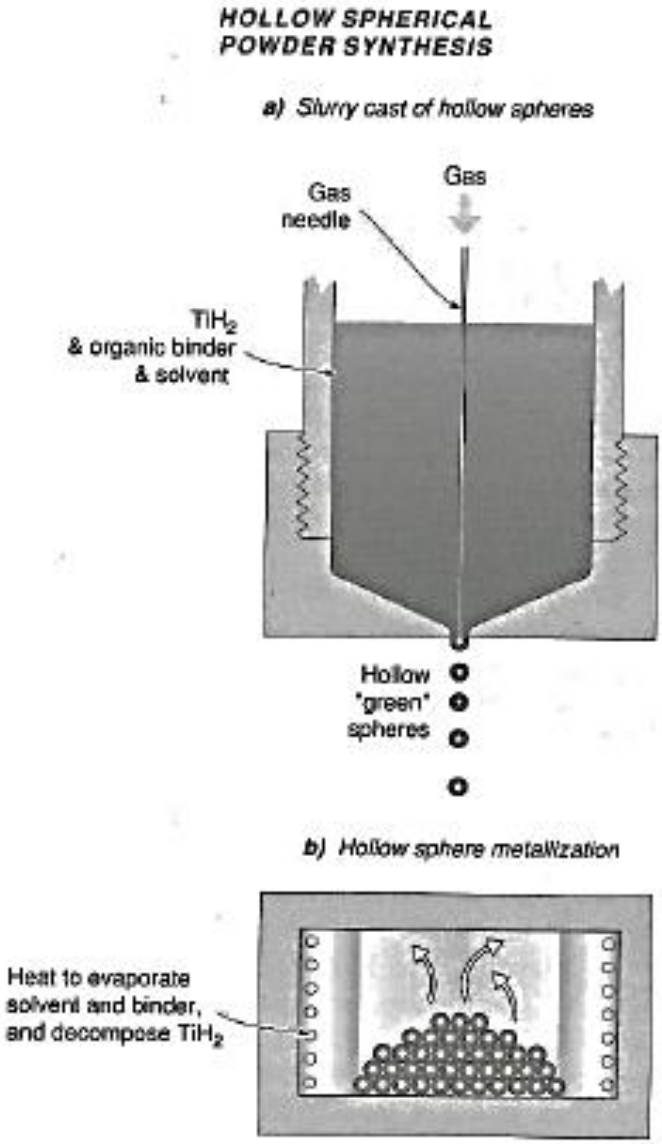

***Fig. 2.8**, Georgia Tech route for creating hollow metal spheres and their consolidation to create a porous metal with an open/closed-cell pore structure. (Ashby 2000)*

2.2.7 Casting of Two Materials

Open-cell porous metals (such as Al and its alloys) can be manufactured by casting of two materials. A salt powder is consolidated and used as a bed of leachable particles as shown in Fig. 2.9 (a). Then, the liquid metal (Al and its alloys) infiltrates into the bed. After the metal is solidified, the leached particles (salt) can be dissolved in a suitable solvent (e.g. water) leaving an open-cell pore structure. This method is used to manufacture porous metals with

relative densities of between 0.3 and 0.5. The pore size is determined by the powder particle size, and lies in the range 10 μm to 10 mm (Ashby 2000).

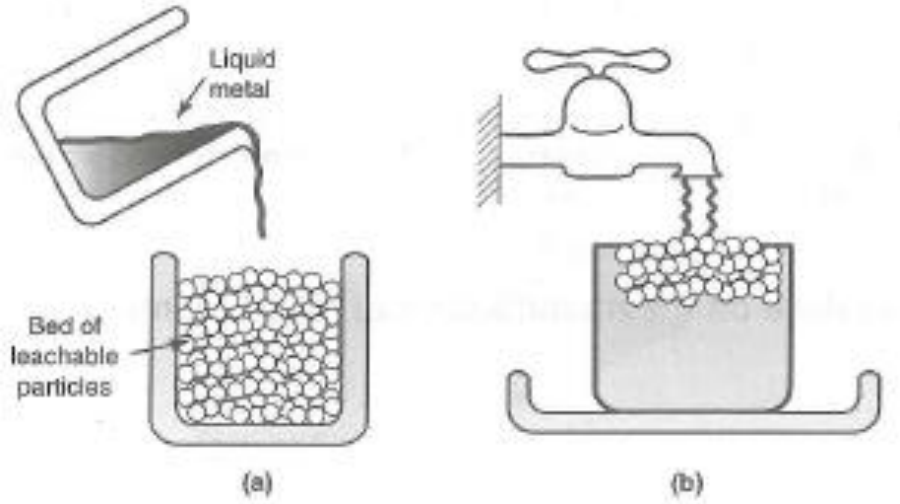

***Fig. 2.9**, (a) A bed of leachable particles (such as salt) is infiltrated with a liquid metal (such as Al or one of its alloys). (b) The particles are dissolved in a suitable solvent (such as water) leaving an open-cell foam. (Ashby 2000)*

2.2.8 Gas-Metal Eutectic Solidification

This method is used to manufacture porous metals (such as Al-, Be-, Cr-, Cu-, Fe-, Mg-, Mn- and Ni-based alloy) using the metal-hydrogen eutectic reaction characteristics and the directional solidification technique. This method is referred to as GASAR (Ashby 2000).

Fig. 2.10 shows a schematic diagram of the basic approach of gas-metal eutectic solidification. A furnace placed within a pressure vessel is used to melt an alloy under an appropriate pressure (5-10 atmospheres) of hydrogen. This melt is then poured into a mould where directional eutectic solidification is allowed to occur, achieving a volume fraction of pores (or porosity) up to 30%. The porosity and pore orientation are a sensitive function of alloy chemistry, melt over-pressure, melt superheat, the temperature field in the liquid during solidification, and the rate of solidification (Ashby 2000). Fig. 2.11 shows the

GASAR porous metal with largely elongated pores oriented in the direction of solidification (Shapovalov & Withers 2009).

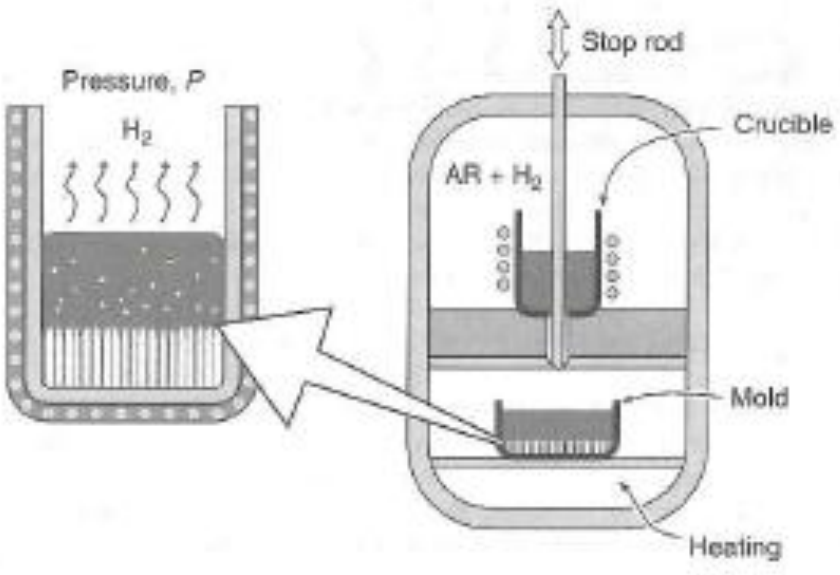

***Fig. 2.10**, Gas metal eutectic solidification for the manufacture of GASAR porous metals. (Ashby 2000)*

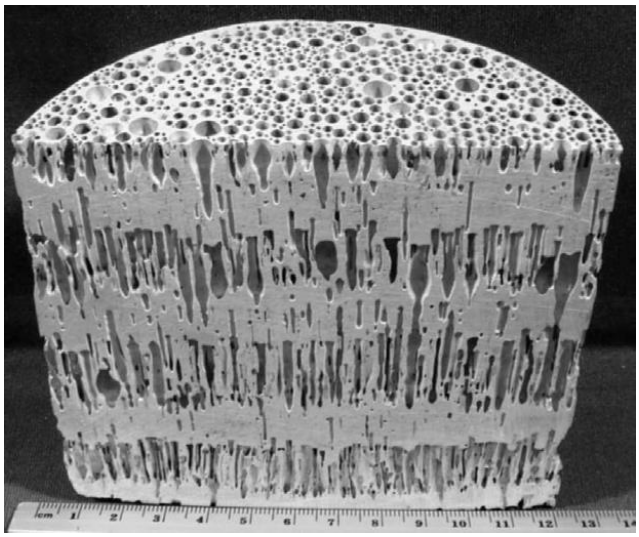

***Fig. 2.11,** Pore structure of GASAR porous metals. (Shapovalov & Withers 2009)*

2.2.9 Space-Holder Methods

Space holder methods are an important family of methods developed recently for manufacturing open cell porous metals. Two space-holder methods, Sintering Dissolution Process (SDP) and Lost Carbonate Sintering (LCS), developed at University of Liverpool are reviewed here.

2.2.9.1 Sintering Dissolution Process (SDP)

Sintering Dissolution Process (SDP) is a representative powder metallurgy based space holder method for manufacturing net-shape, open-cell porous metal (Zhao & Sun 2001). SDP consists of the mixing, compacting, sintering and dissolution stages as shown in Fig. 2.12. The raw materials of Al and NaCl powder are mixed at a pre-specified volume or weight ratio. The mixture of Al/NaCl is compacted into a net-shape preform under an appropriate pressure (200 MPa) by a hydraulic press and sealed in a mild steel tube. The preform is then sintered at an appropriate temperature (680 °C) above the melting point of Al (660 °C) but far below that of NaCl (801 °C) for 180 min. After the Al in the preform forms a well-bonded networked structure, the preform is cooled to room temperature. The leachable NaCl powder can be dissolved in hot water leaving an open cell structure in porous Al.

In SDP process, the pore size can be controlled by the size of the leachable particle, NaCl, in the range of 300-1000 μm. The two powders, Al and NaCl, are mixed thoroughly at different weight ratios to control the porosity in the range of 0.2-0.75. This method can also be used to manufacture other porous metals such as Cu, Ti, Ni, Fe and steel. SDP is capable of producing low-cost, net-shape porous metals with controlled pore morphology, size, distribution and porosity.

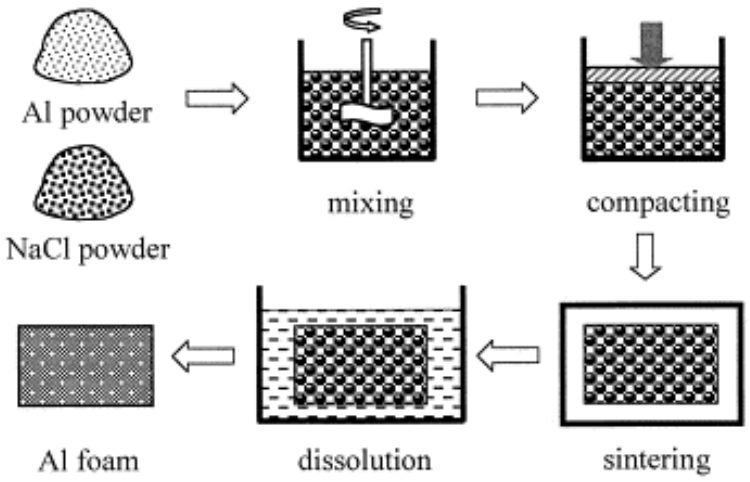

***Fig. 2.12**, Schematic of the sintering-dissolution process for manufacturing Al foams. (Zhao et al. 2001)*

2.2.9.2 Lost Carbonate Sintering (LCS)

Zhao and his colleagues improved the Sintering and Dissolution Process (SDP) and invented the Lost Carbonate Sintering (LCS) process (Zhao et al. 2005). SDP uses NaCl powder as the filler material, which is difficult to be removed completely and the residual NaCl can corrode metals (Zhao et al. 2005). LCS uses potassium carbonate as the filler material, which can be removed completely by decomposition or dissolution. LCS process is one of the leading technologies capable of manufacturing open-cell porous metals with controlled pore size and porosity (Zhao et al. 2005, Ma et al. 2005).

Fig. 2.13 shows the LCS process schematically. The raw materials used in LCS for manufacturing a porous metal are metal powder (such as Cu, Ni and Ti) and a carbonate powder. The metal and K_2CO_3 powders are mixed with a pre-specified volume ratio. Ethanol is used as the binder and added during mixing. The mixture of metal/K_2CO_3 is then compacted at 200 MPa by a hydraulic press. In some cases, the debinding is carried out at 200 °C for 1 hr in order to evaporate the ethanol in the preform. In others, the debinding is achieved by heating the samples slowly to the sintering temperature. After the ethanol is

evaporated, three different routes of sintering and carbonate removal can be chosen, as shown in Fig. 2.14. In route A, the preform is sintered at 850 °C for 4 hrs, cooled to room temperature and then placed in a running-water bath for 5 hrs to dissolve the carbonate. In route B, the preform is sintered at 850 °C for 4 hrs, heated at 950 °C for 0.5 hrs to melt and decompose the carbonate before being cooled to room temperature. In route C, the preform is heated to 950 °C directly and maintained at this temperature for 2 hrs and then cooled to room temperature (Zhao et al. 2005).

Although all of the sintering and carbonate removal routes, A, B and C, produce porous metal with acceptable quality, they show different characteristics. In route A, the K_2CO_3 particles remained solid during sintering and hold the metal particle network in place so that the preform shows very little shrinkage. The pores in the porous metal are virtually replicas of the K_2CO_3 particles after their dissolution. In route B, the space holder material, K_2CO_3, is decomposed after strong bonding is formed between the metal particles. The preform shrinks during the K_2CO_3 removal stage. However, the resultant porous metal is very clean and this route protects the porous metal from chemical attack during the dissolution of K_2CO_3. In route C, the preform is cleared of the K_2CO_3 particles before the metal particles are strongly bonded. The metal network often collapses to form large cavities and the resultant porous metal is often weak (Zhao et al. 2005).

The SEM image of a typical pore structure (pores, cell walls and sintering neck) of porous Cu produced by LCS process is shown in Fig. 2.15 (Zhao et al. 2005). The porosity of LCS porous metals can be up to 85%. The range of pore size of LCS porous metals is 50-1500 μm. All of these properties can be controlled (Zhao et al. 2005).

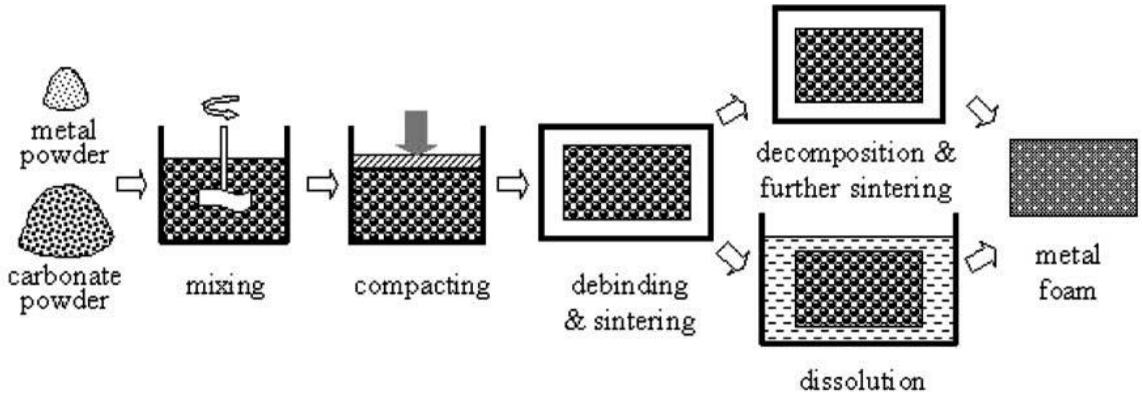

***Fig. 2.13**, Schematic of the LCS process for manufacturing porous metals. (Zhao et al. 2005)*

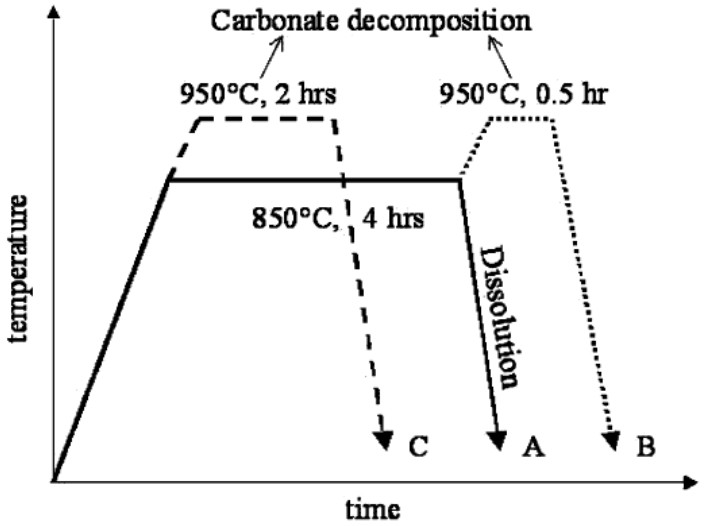

***Fig. 2.14**, Illustration of the three different sintering and carbonate removal routes. (Zhao et al. 2005)*

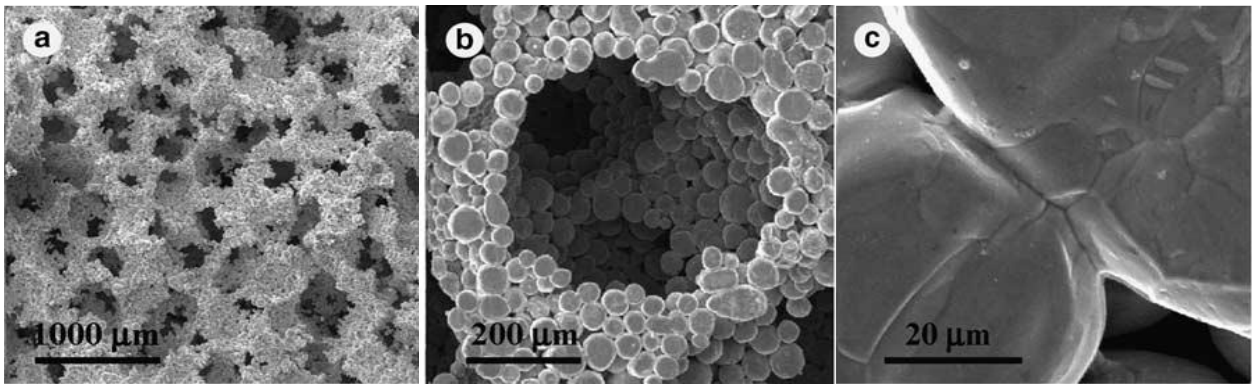

***Fig. 2.15**, SEM micrographs showing (a) typical structure of porous Cu, (b) a cell and its walls, and (c) bonding between the Cu particles. (Zhao et al. 2005)*

2.3 Fundamentals of Electrochemistry and Electrochemical Characterisation Techniques

In electrochemical processes, two liquid phase structures (Fig.2.16) (Scholz 2002) are formed on the electrode surface, double layer and diffusion layer. The double layer is an interface between electrode and electrolyte and formed by the ion adsorption onto the electrode surface, since the double layer can be viewed as a capacitor (Eaborn 1988). The diffusion layer is the region in the vicinity of an electrode and formed by the concentration gradient between electrode and bulk solution (Eaborn 1988). The thickness of the diffusion layer depends on the diffusion coefficient and scan rate in the voltammetric measurements, such as cyclic voltammetry.

2.3.1 Electrical Double Layer

The double layer includes a compact layer (inner Helmholtz layer) and diffuse layer (Gouy-Chapman layer) (Srinivasan 2006, Signorelli et al. 2009, Scholz 2002) and occupies a distance of about 1 nm from the electrode surface (Fig. 2.16) (Scholz 2002). The earliest double-layer model was attributed to Helmoltz in 1853 who assumed the presence of a compact layer of ions in contact with the charged metal surface (Scholz 2002). In this model, it is assumed that no faradaic process occur at the electrode (Fisher 1996). The next

model, of Gouy and Chapman, involves a diffuse layer in which the accumulated ions, due to the Boltzmann distribution, extend to some distance from the solid surface. Stern (1924) suggested that the electrified solid-liquid interface includes both the rigid Helmholtz layer and the diffuse layer of Gouy and Chapman. Graham (1947) pointed out that there is specific adsorption of ions at the metal surface (Scholz 2002).

The thickness of the double layer is usually given as being approximately 1.5 κ^{-1} (Scholz 2002), where κ^{-1} is the Debye-Huckel length:

$$\kappa^{-1} = (\varepsilon' \varepsilon_0' k_B T / 2 c z_i^2 e_0^2)^{1/2} \qquad (2.1)$$

where c is the bulk electrolyte concentration, ε' is the relative dielectric permittivity of the solvent, ε_0' is the permittivity of the vacuum, k_B is the Boltzmann constant, T is the temperature, z is the ion charge and e_0 is the elementary charge. For the electrolyte concentrations of 1×10^{-3}, 1×10^{-5} and 1×10^{-7} M, the double layer thicknesses are 15 nm, 150 nm and 1.5 μm, respectively (Scholz 2002).

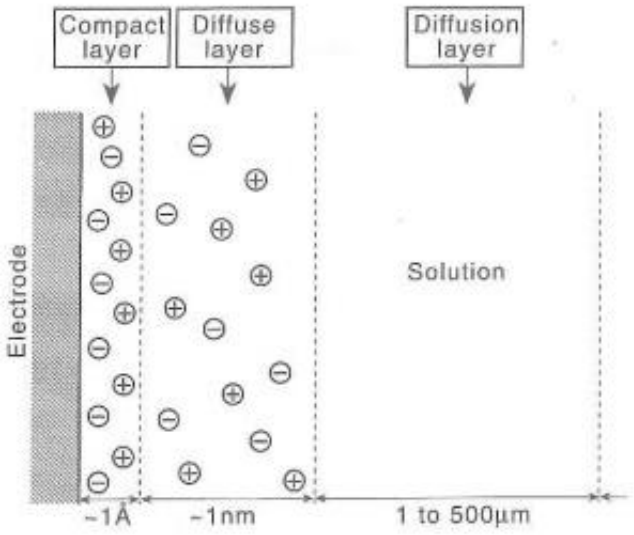

***Fig. 2.16**, Schematic representation of the composition of the solution phase in the vicinity of the electrode surface (not to scale). (Scholz 2002)*

2.3.2 Diffusion Layer

Diffusion layer, or Nernst's diffusion layer (Amatore et al. 2001), is defined as the region in the vicinity of an electrode where the concentrations are different from their value in the bulk solution (Eaborn 1988). Under most experiments, the size of the diffusion layer is several orders of magnitude larger than that of the double layer (Scholz 2002). For different experimental arrangement, the thickness of the diffusion layer can vary.

For a stationary electrode in Cyclic Voltammetry (CV) experiment, the thickness of the diffusion layer depends on the diffusion coefficient (D) of the analyte and the scan rate (v) in the voltammetric measurements. Generally, the diffusion layer thickness (δ) is expressed by (Gileadi 2011):

$$\delta = \sqrt{\frac{4Dt}{\pi}} \tag{2.2}$$

where t is time.

In CV, the thickness of the diffusion layer (δ_{peak}) at the time that the peak current is reached can be expressed by (Scholz 2002):

$$\delta_{peak} = \sqrt{\frac{DRT}{vnF}} \tag{2.3}$$

where *R* is gas constant, *F* is Faraday constant, and *n* is number of electrons in the reaction.

For a rotating disc electrode in CV experiment, the diffusion layer thickness is affected by fluid flow, caused by the rotation of the electrode, and can be expressed by (Gileadi 2011):

$$\delta = 1.61 D^{1/3} v^{1/6} {\omega_R}^{-1/2} \tag{2.4}$$

where ω_R is the rotation rate.

2.3.3 Cyclic Voltammetry (CV)

Cyclic voltammetry (CV) is a linear sweep method. It is frequently used in the analysis of electrochemical properties because it can offer a variety of experimental information in both the kinetic and thermodynamic details of chemical systems (Parsons 1990).

2.3.3.1 Experimental Setup and Voltammogram

A three-electrode cell set-up is used in the cyclic voltammetry experiment as shown in Fig. 2.17 (a) (Scholz 2002). The working electrode is the sample to be tested or the electrode to be studied. The counter electrode is used to form the current circuit and lets the current flow between the working and counter electrodes. The surface area of the counter electrode has to be larger than the working electrode (Scholz 2002). The reference electrode is used to measure and control the potential in the CV experiment. Argon gas is usually used to remove the oxygen in the electrolyte. A continuously time-varying potential is applied to the working electrode by a potentiostat (Fig. 2.17 (b)) (Scholz 2002). The potentiostat is also used to record the response of current at the same time. The plots of the potential applied in cyclic voltammetry experiment and the resulting current response are shown schematically in Fig. 2.18 (Scholz 2002).

Fig. 2.19 shows a typical cyclic voltammogram of a reversible reaction between $K_3Fe(CN)_6$ and $K_4Fe(CN)_6$ (Scholz 2002). The anodic and cathodic peak current data, I_{pa} and I_{pc}, and peak potentials, E_{pa} and E_{pc}, determine the anodic and cathodic processes at the working electrode, respectively. The anodic and cathodic reactions are expressed by Eqn. 2.5 and 2.6, respectively.

$$Fe(CN)_6^{4-} - e \rightarrow Fe(CN)_6^{3-} \tag{2.5}$$

$$Fe(CN)_6^{3-} + e \rightarrow Fe(CN)_6^{4-} \tag{2.6}$$

The peak current value (I_p) can be calculated by Randles-Sevcik equation, (Scholz 2002):

$$I_p = 2.69 \times 10^5 \times n^{\frac{3}{2}} \times A \times D^{\frac{1}{2}} \times c \times v^{\frac{1}{2}} \quad (2.7)$$

where I_p (I_p=I_{pa}=I_{pc}) is the forward peak-current (A), n is the number of electrons exchanged per molecule of reactant, A is the area of the electrode (m^2), D is the diffusion coefficient of reactant (m^2/s), c is the concentration of reactant (mol/L), n is the number of electrons in the reaction and v is the potential scan rate (V/s).

The reaction between $K_3Fe(CN)_6$ and $K_4Fe(CN)_6$, as a standard reversible reaction, is widely used in the CV experiment for studying the electrochemical properties of the electrode. Noble metals, such Au, Ag and Pt, are used as testing electrodes in the CV experiment because these metals are resistant to corrosion and oxidation and do not affect the reaction in the test (Scholz 2002, Fisher 1996, Compton & Sanders 2006). In some cases, carbon (Smith et al. 2015) and Ni (Recio et al. 2013) electrodes are also investigated by $K_3Fe(CN)_6$ and $K_4Fe(CN)_6$.

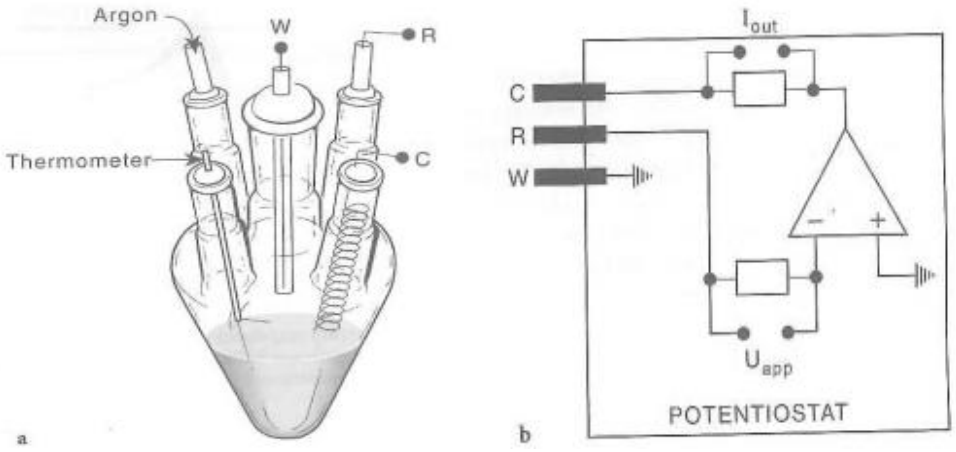

***Fig. 2.17**, (a) Cell for cyclic voltammetry (CV) experiments with three-electrode configuration (where W is working electrode, C is counter electrode and R is reference electrode). (b) Simplified circuit diagram for a three-electrode potentiostat system. (Scholz 2002)*

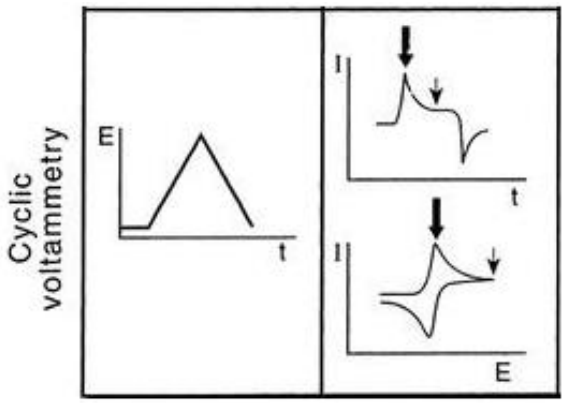

***Fig. 2.18**, Plots of the potential applied in cyclic voltammetry experiment and the resulting current response. (Scholz 2002)*

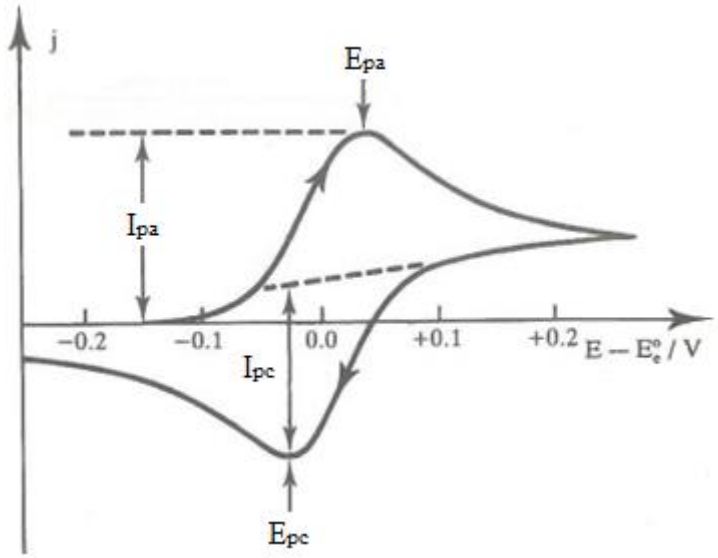

***Fig. 2.19**, Typical cyclic voltammogram. (Scholz 2002)*

2.3.3.2 Effect of Diffusion Layer

For a standard reversible redox reaction, the difference of the two peak potentials (E_{pc}-E_{pa}) is 59 mV in the CV in a fully diffusion controlled process (Pletcher 1991). When the reaction is not fully controlled by diffusion, this value would be lower than 59 mV. In porous media, the diffusion layer thickness may be greater than the diffusion space available in the porous media and the reaction may no longer be controlled by the diffusion of electro-active species. Fig. 2.20 shows the simulated cyclic voltammograms for an electrode with a surface area of 10 cm^2 and a pore radius, R_P, of 30 μm (the schematic diagram of the

electrode is shown in Fig. 2.21) in the given redox solution at scan rates of 0.1 and 0.01 V/s (Smith et al. 2015). At a high scan rate of 0.1 V/s, the difference of the peak potentials was around 59 mV, as shown in Fig. 2.20 (a). In this case, the reaction on the electrode is controlled by the diffusion of the reactant in the electrolyte, which can be considered as semi-infinite. With the decrease of scan rate, however, the thickness of the diffusion layer increases and become greater than the diffusion space (pores) in the porous material. The electrolyte cannot be considered as semi-infinite diffusion and the reaction starts to be controlled by thin-layer behaviour (Ward et al. 2013). In the transition from semi-infinite to thin-layer regime, the difference of the peak potentials becomes less than 59 mV. Fig. 2.20 (b) shows the cyclic voltammogram at a low scan rate of 0.01 V/s. In this case, the difference of the peak potential becomes almost 0, meaning that the reaction is fully controlled by thin-layer behaviour.

Davies et al. (2006) pointed out that when the controlling factor of the reaction in the CV experiment changes from semi-infinite to thin-layer, both the differences of peak potential and peak current become smaller. If the reaction is controlled by semi-infinite diffusion, the Randles-Sevcik equation (Eqn. 2.7) can be used to calculate the value of the peak current, which depends upon the electro-active surface area of the electrode. If the reaction is controlled by the thin-layer behavior, however, the peak current, I_p, does not depend on the electrode surface area any more but on the volume of the thin-layer and is expressed by (Davies et al. 2006):

$$I_p = \frac{n^2 F^2 v V c}{4RT} \tag{2.8}$$

where n is the number of electrons transferred, F is the Faraday constant, v is the scan rate, V is the volume of the thin layer, c is the initial concentration of redox species in the thin

layer, *R* is the molar gas constant and *T* is the temperature. Therefore, the peak current measured by CV experiment would be decreased with the increasing effect of the thin-layer.

Ward et al. (2013) studied the formation of the diffusion layer and found that the diffusion fields of neighbouring particles strongly overlap such that diffusion to the entire surface is essentially planar, as shown schematically in Fig. 2.22. As a consequence, if the diffusion layer is thicker than the scale of the roughness of electrode surface, the measured surface area would be lower than the real surface area (Ward et al. 2013).

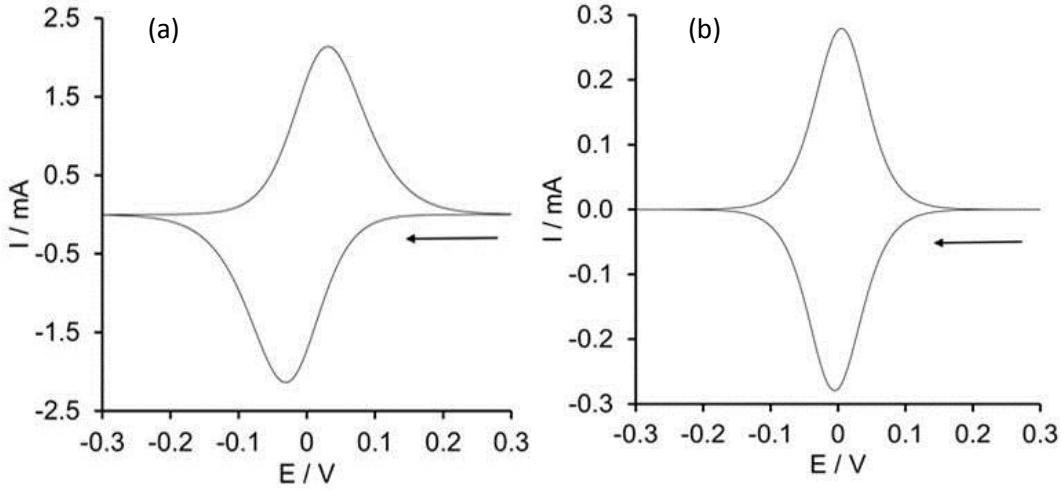

***Fig. 2.20**, Simulated cyclic voltammograms for a porous electrode of total surface area 10 cm^2 and average pore radius of 30 µm at scan rates of (a) 0.1 V/s and (b) 0.01 V/s. (Smith et al. 2015)*

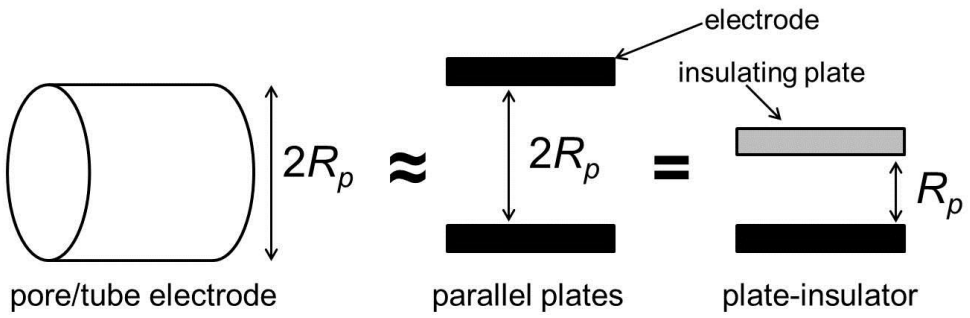

***Fig. 2.21**, Schematic diagram of a tube electrode approximating a pore, it can be approximated as a parallel plate electrode assembly, which is mathematically identical to a planar electrode below an insulating plate. (Smith et al. 2015)*

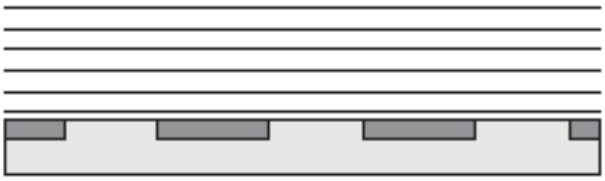

***Fig. 2.22**, Schematic of the diffusion demonstrated by simulated voltammetry. (Ward et al. 2013)*

2.3.3.3 Cyclic Voltammetry of Non-Noble Metals

The chemical reactions of non-noble metals without high resistance of corrosion and oxidation are very complex because these metals can participate in these reactions. Copper is a transitional element and can form a rich variety of compounds with oxidation states +1 and +2, i.e. cuprous and cupric, respectively.

Ambrose et al. (1973) studied the reactions of copper by cyclic voltammetry. Fig. 2.23 is the cyclic voltammogram of copper in 1.0 M potassium hydroxide electrolyte, with a sweep rate of 0.026 V/s. There are four significant anodic peaks (I, II, III and IV) and four cathodic peaks (V, VI, VII and VIII) in the cyclic voltammogram.

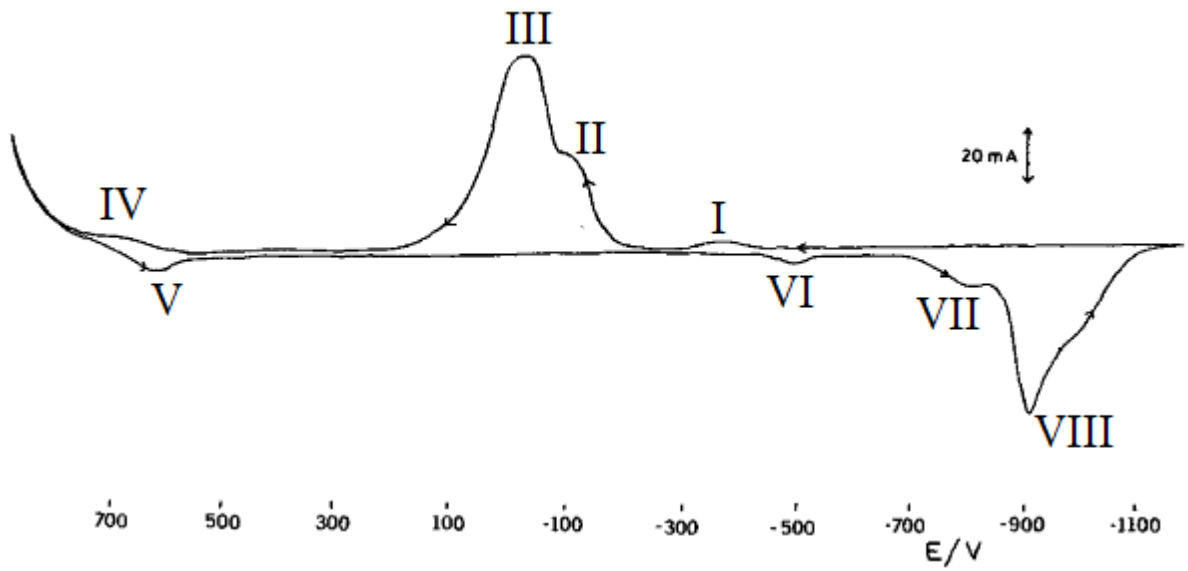

***Fig. 2.23**, Cyclic voltammogram of Cu in 1.0 M KOH at the scan rate of 0.026 V/s. (Ambrose et al. 1973)*

Ambrose et al. (1973) studied each peak of the anodic and cathodic processes in the CV experiment and identified their reactions as:

Peak (I):

$$2Cu + OH^- \rightarrow Cu_2O + H_2O + 2e \tag{2.9}$$

Peak (II):

$$Cu_2O + 6OH^- + H_2O \rightarrow 2Cu(OH)_4^{2-} + 2e \qquad initially \tag{2.10}$$

$$Cu + 4OH^- \rightarrow Cu(OH)_4^{2-} + 2e \qquad main\ reaction \tag{2.11}$$

Peak (III):

$$Cu + 2OH^- \rightarrow Cu(OH)_2 + 2e \tag{2.12}$$

$$Cu + 2OH^- \rightarrow CuO + H_2 + 2e \tag{2.13}$$

Peak (IV):

$$Cu(OH)_2 + 2OH^- \rightarrow Cu(OH)_4^- + e \tag{2.14}$$

$$CuO + H_2O + 2OH^- \rightarrow Cu(OH)_4^- + e \tag{2.15}$$

Peak (V):

$$Cu(OH)_4^- + e \rightarrow CuO + H_2O + 2OH^- \quad (2.16)$$

$$Cu(OH)_4^- + e \rightarrow Cu(OH)_2 + 2OH^- \quad (2.17)$$

Peak (VI):

$$2Cu(OH)_4^- + 2e \rightarrow Cu_2O + 6OH^- + H_2O \quad (2.18)$$

$$2Cu(OH)_2 + 2e \rightarrow Cu_2O + 2OH^- + H_2O \quad (2.19)$$

Peak (VII):

$$Cu_2O + H_2O + 2e \rightarrow 2Cu + 2OH^- \quad (2.20)$$

There is no conclusion for Peak (VIII) because this reaction is too complex (Ambrose et al. 1973).

On a clean copper surface, peak currents are controlled by the diffusion of OH^-. According to Delahay (1954), the current of peak (III) can be calculated by:

$$I_p = 3.67 \times 10^5 n^{\frac{3}{2}} AcD^{\frac{1}{2}} v^{\frac{1}{2}} \quad (2.21)$$

where *n* is the number of electrons in the reaction, *A* is the electrode surface area, c is the bulk concentration of OH^- in mol/cm^3, *D* is the diffusion coefficient of OH^- ion, and *v* is the scan rate in V/s. However, Delahay equation cannot be used directly to calculate the surface area of the Cu electrode due to passivation on the Cu electrode surface (Ambrose et al. 1973).

For the CV experiment of Cu in alkaline solution, peak III predominates at slow scan (v = 0.015-0.026 V/s) (Ambrose et al. 1973). The I_p values for peak III is proportional to the square root of scan rate ($I_p \propto v^{1/2}$). However, at scan rates below 0.015 V/s the I_p values for peak III cannot be fitted to either an $I_p \propto v^{1/2}$ or $I_p \propto v$ relationship (Ambrose et al. 1973).

Therefore, the CV experiment for Cu electrode cannot operate at very low scan rates (<0.015 V/s).

The cathodic processes are affected by the range of potential applied at the working electrode (Droog et al. 1980). No equations are available to calculate the current values of cathodic peaks of copper in CV experiment.

2.3.4 Double Layer Capacitance

In section 2.3.1, it has been described that a very thin double layer (thickness < 15 nm when concentration > 0.001 M) can form on the surface of the electrode. A large amount of electrical charge can be stored in the double layer (Lewandowski et al. 2012, Wan et al. 2015). The double layer capacitance is dependent on the real surface area of the electrode. Therefore, the real surface area of the solid metal electrode can be estimated by the measurement of the double layer capacitance (Lewandowski et al. 2012, Brevnov 2006). CV experiment in the non-faradaic region is a common method for the measurement of the double layer capacitance.

Faradaic current is generated by the oxidation and reduction of the chemical substance on the electrode surface. Non-faradaic region means that no redox reaction occurs on the electrode surface and the current is generated only because of the charge/discharge of the double layer capacitor. Fig. 2.24 shows an ideal cyclic voltammogram of the CV experiment in the non-faradaic region. The current density in charge (j_a) and discharge (j_b) would be the same (Gileadi 2011).

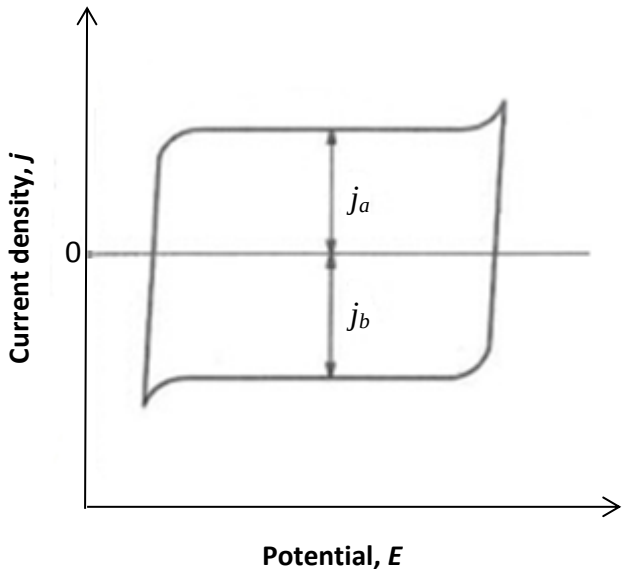

***Fig. 2.24**, Ideal cyclic voltammogram for the capacitance measurement. (Gileadi 2011)*

However, in practice, it is very hard to obtain a voltammogram with the rectangle shape as shown in Fig. 2.24. For a real electrode in CV experiment, the shape of the voltammogram deviates from the rectangle as shown in Fig. 2.25 (a), especially at high scan rates (Lewandowski et al. 2012). Fig. 2.25 (b) shows the linear relationship between charging current and scan rate (Brevnov et al. 2006), which can be used for capacitance calculation as follows (Arulepp et al. 2004):

$$C = \frac{I}{v} \tag{2.22}$$

where C is capacitance, I is charge current and v is scan rate.

Fig. 2.26 shows the current difference, Δj, in the voltammogram, which can be expressed by (Gileadi 2011):

$$\Delta j = j_a - j_b \tag{2.23}$$

where j_a and j_b are the current in the charge and discharge phases, respectively ($|j_a| = |j_b|$). The charge current, I, is therefore (Gileadi 2011):

$$I = \frac{\Delta j}{2} \tag{2.24}$$

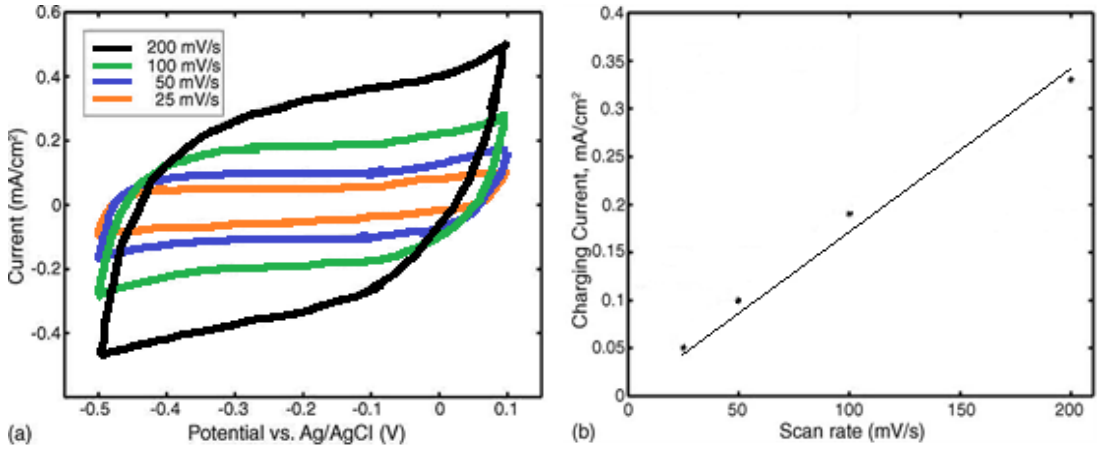

***Fig. 2.25**, (a) Cyclic voltammograms obtained for silver particles/aluminium/copper electrode and (b) charging current dependence upon the scan rate. (Brevnov et al. 2006)*

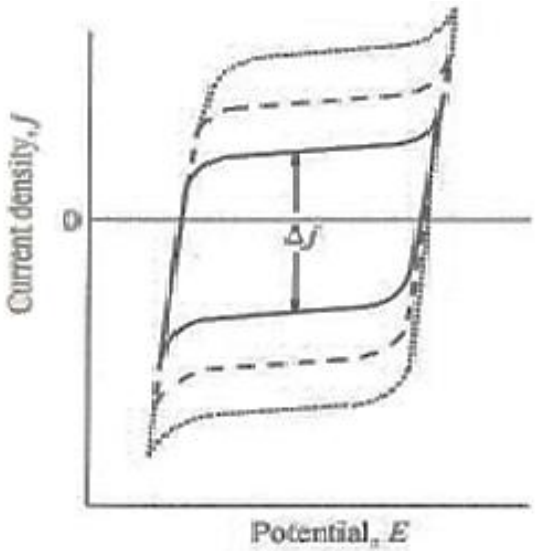

***Fig. 2.26**, Current difference in the j/E plots obtained at different scan rates. (Gileadi 2011)*

2.3.5 Linear Sweep Voltammetry (LSV)

Linear Sweep Voltammetry (LSV) is a potentiostatic technique used to control the change of the potential in the test. The potential is changed at a constant rate, and the resulting current is followed as a function of time (Gileadi 2011).

As well the CV experiment, LSV is used to investigate the electrochemical redox reaction on the electrode surface. In CV, the potential is swept forward and backward between two fixed values so that the current measured at a particular potential on the anodic sweep can readily be compared with that measured at the same potential on the cathodic sweep. In LSV, however, the potential is often swept only in one direction for studying the anodic (or cathodic) reaction on the electrode surface (Gileadi 2011).

LSV experiment is commonly carried out at very slow sweeps. When the sweep rate is very low (0.1-5 mV/s), the measurement is conducted under quasi-steady-state conditions. In this case, the sweep rate does not play any role in the reaction, except that the sweep rate must be slow enough to ensure that the reaction is effectively at a steady state along the course of the sweep. LSV is widely used in corrosion, passivation and fuel cell reaction studies (Gileadi 2011). In mass transfer coefficient measurements, LSV is commonly used to measure the limiting current generated on the electrode, which will be described in 2.5.2.

2.4 Techniques for Surface Area Measurements

2.4.1 Introduction

High surface area is often desirable for many functional applications. In electrochemical applications, for instance, the reaction surface area of an electrode is the most important characteristic (Scholz 2002) because high surface area means high energy density and thus better performance.

Surface area of porous metals is generally characterised either by geometric area or by true area, which can be different by more than two orders of magnitude. The active or effective surface area for a particular application depends on the length scale at which the surface plays a role. It is often greater than the geometric area but lower than the true area. Taking porous electrodes as an example, real surface area is the key parameter for applications such

as super capacitors (Li et al. 2012, Lewandowski et al. 2012). In applications involving electrochemical reactions, however, the electro active surface area, which depends on how well the electrolyte accesses the pores, is the key parameter, and the magnitude of the diffusion or Nernst layer in the electrolyte and the surface roughness of the electrode are also important (Davies et al. 2005, Ward et al. 2013).

Surface area of porous metals is very sensitive to the manufacturing method. For example, for similar pore size of 600 μm and porosity of 0.95-0.99, the INCO porous Ni produced by CVD has a real surface area of 292 cm^2/g (Bidault et al. 2009), while the Mitsubishi porous Ni produced by the slurry foaming method has a surface area of 19,710 cm^2/g (Đukić et al. 2013) (both measured by BET).

This section reviews the different techniques used to measure surface areas of porous materials and discusses their applicability.

2.4.2 Quantitative Stereology

The Quantitative Stereology (QS) method attempts to interpret the three-dimensional structures in minerals, metals and other materials from their two-dimensional cross sections. This method can measure internal surfaces, such as boundaries between space-filling cells and the interfaces between particles and matrix, and external surfaces, such as the jagged irregular surface of an oxidized wire, a fracture surface and the surface of an isolated particle (Underwood 1970).

The basic equation for obtaining the area of surfaces in a volume is (S. A. Saltykov 1958, S. A. Saltykov 1967):

$$S_V = 2P_L \tag{2.25}$$

where S_V is the specific surface area (area to volume ratio) and P_L is the number of intersections with surfaces per unit length of test line. This equation applies to the systems of interconnected, discontinuous, separated and bounded surfaces. In order to evaluate the extent of boundary areas in space, a simple intersection (P_L) count with boundary traces on a section plane is only required (Underwood 1970).

For example, Fig. 2.27 shows a 2D plane of dispersed particles of α-phase in a matrix phase. This structure is very similar to the pore structure in porous materials, if pores take place of the particles of α-phase. In this diagram, the number of the intersections (P_L) on the testing line (L_T), with length of 0.1 cm, is 8, giving a specific surface area (or surface-to-volume ratio) of 16 mm^{-1} (Underwood 1970).

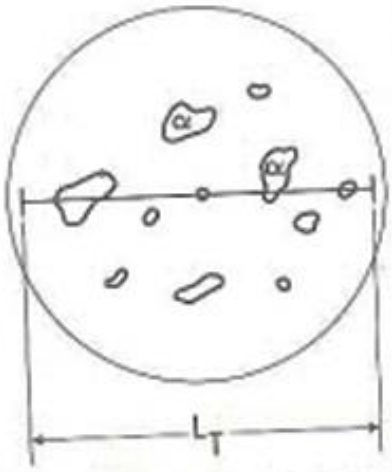

Fig. 2.27, *2D plane of dispersed particles of α-phase in a matrix phase. (Underwood 1970)*

2.4.3 Brunauer-Emmett-Teller Method

Brunauer-Emmett-Teller (BET) method was first reported in 1938 (Brunauer et al. 1938). It was developed from Langmuir's monolayer theory (Park & Seo 2011). The BET's equation has been used to determine the monolayer volume of adsorbed gas and thus the specific surface area of the adsorbents. The BET's equation is derived on the basis of three hypotheses (Park & Seo 2011):

(1) The surface is energetically homogeneous, i.e., all adsorption sites on the bare surface have the same adsorption energy;

(2) There is no lateral interaction between adsorbed molecules;

(3) The adsorption energies in the second and all higher layers are equal to the condensation energy of the adsorptive.

BET theory can be used for a series of discrete layers on the testing surface as shown in Fig. 2.28 (Park, Seo 2011).

BET method is commonly used to measure the specific surface area of porous materials such as rocks (Lai et al. 2015), cement (Odler 2003) and porous metals (Wan et al. 2015, Nersisyan et al. 2013). In practice, BET method can also be used to analyse other pore parameters, such as pore size and porosity, by analysis of the nitrogen adsorption isotherms.

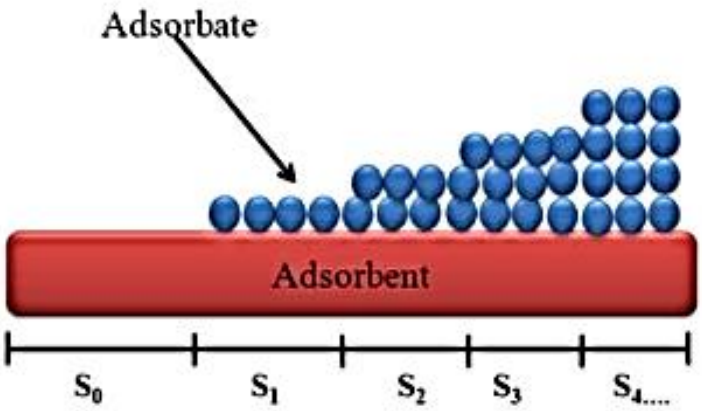

***Fig. 2.28**, BET model of adsorption. (Park & Seo 2011)*

2.4.4 Electrochemical Method

The performances of batteries, catalysts and solid-state sensors depend on the surface area and active interfacial sites of the electrodes (Xu et al. 2014, Du et al. 2013, Wang et al.

2011, Rydén & Magnus 1975, Leion & Henrik 1976). It is important to measure the electro-active surface area by electrochemical methods in these electrochemical applications.

According to the Randles-Sevcik equation, the value of the peak current is affected by the surface area of the electrode. If the other factors affecting the peak current do not change, there will be a linear relation between the surface area of the working electrode and the value of the peak current. Therefore, it is possible to apply the CV experiment to measure the surface area of the working electrode.

Some researchers (Fragkou et al. 2012, Estudillo-Wong et al. 2011, Cao et al. 2009, Guo et al. 2005, Tan et al. 2012) have used CV to measure the surface area of porous metals. For example, Tan et al. (2012) used CV to measure the surface area of nano-porous gold, as shown in Fig. 2.29. The values of their measurements, as compared to the values obtained by BET are listed in Table 2.2. As Table 2.2 shows, the electrochemically active surface area is lower than the surface area measured by the BET method. This is because the permeability of gases is higher than that of liquid solutions and the BET method can explore the areas in which ions in the solution cannot enter (Tan et al. 2012).

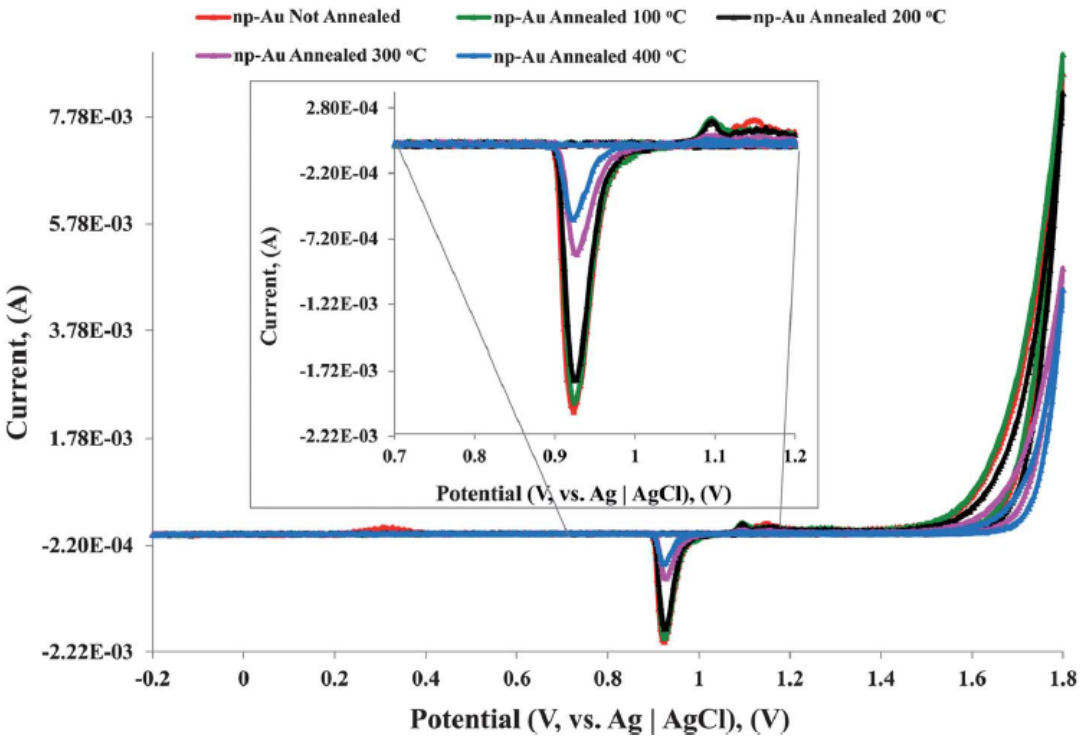

***Fig. 2.29**, Cyclic voltammograms of nanoporous gold. (Tan et al. 2012)*

***Table 2.2**, Electroactive surface area of nanoporous gold samples. (Tan el at. 2012)*

Nanoporous Gold annealing T/°C	np-Au Substrate Mass,[a] (g)	Electrochemically active Surface Area, (m^2 g^{-1})	Surface Area S_{BET}, (m^2 g^{-1})
room temperature	0.256804	5.34	6.4
100	0.268556	4.85	6.35
200	0.230166	4.34	5.34
300	0.265356	3.92	4.57
400	0.249948	1.65	1.79

2.5 Measurement of Mass Transfer Coefficient

2.5.1 Introduction

Mass transport is a very important electrochemical property for the study and application of electrodes. A high and uniform rate of mass transport of material to or from the electrode surface is important in the following four areas of flow cell reactor performance (Walsh 1993):

(1) Current density: A high current density results in high fractional conversion, and high yield;

(2) Current efficiency: The current density should be uniform over the electrode surface in order to minimise secondary reactions and hence maintain the current efficiency. This is only possible if the mass transport regime is uniform over the whole electrode surface;

(3) Kinetics of the desired reaction: The composition of the reaction layer at the electrode surface should be maintained at a value close to that in the bulk solution to prevent unwanted chemical reactions. Otherwise, the processes may hinder the kinetics of the desired reaction;

(4) Cost of fluid movement: Mass transport is related to fluid velocity conditions. It will affect the cost involved in facilitating fluid movement in order to improve reactor performance.

2.5.2 Measurement Technique

Fig. 2.30 (Bard, Faulkner 2001) shows two types of flow electrolytic cells for mass transfer coefficient measurement for porous materials of glassy carbon granule (Fujinaga & Kihara 1977) and Reticulated Vitreous Carbon (Strohl & Curran 1979), respectively. The electrolyte flows through the flow cell by a pump with a controlled flow rate. The working, counter and reference electrodes are connected to a potentiostat for supplying voltage. The potentiostat is also used to record the change of the current generated in the Linear Sweep Voltammetry (LSV) experiment, which is used to measure the limiting current of the testing (working) electrode. A typical LSV voltammogram is shown in Fig. 2.31 (Coñizares et al. 2006). In the middle region of the LSV voltammogram, the current does not change with

potential because the reaction on the electrode surface is controlled by the mass transfer (Recio et al. 2013). This stable current is called limiting current.

The mass transfer coefficient (k) is related to the limiting current (I_L) in the LSV experiment by (Coñizares et al. 2006):

$$k = \frac{I_L}{nFAc} \tag{2.26}$$

where n is the number of electrons transferred, F is Faraday constant, A is the surface area of electrode and c is bulk concentration of the electrolyte.

For measuring the mass transfer coefficient of Ni electrode, it is common to use the reaction between potassium ferricyanide and potassium ferrocyanide on the surface of the Ni electrode in the alkaline solution (Recio et al. 2013, Brown et al. 1993) in a LSV experiment. The reaction in the measurement is expressed by:

$$Fe(CN)_6^{3-} \rightarrow Fe(CN)_6^{4-} - e \tag{2.27}$$

Fig. 2.32 shows a typical LSV voltammogram for the reaction (Eqn. 2.27) on a Ni electrode (Recio et al. 2013). Three characteristic zones, the mixed control region, mass transfer control region and hydrogen evolution region, can be clearly distinguished. The limiting current can be obtained from the mass transfer control region, from which the mass transfer coefficient on the Ni electrode can be calculated using Eqn. 2.26.

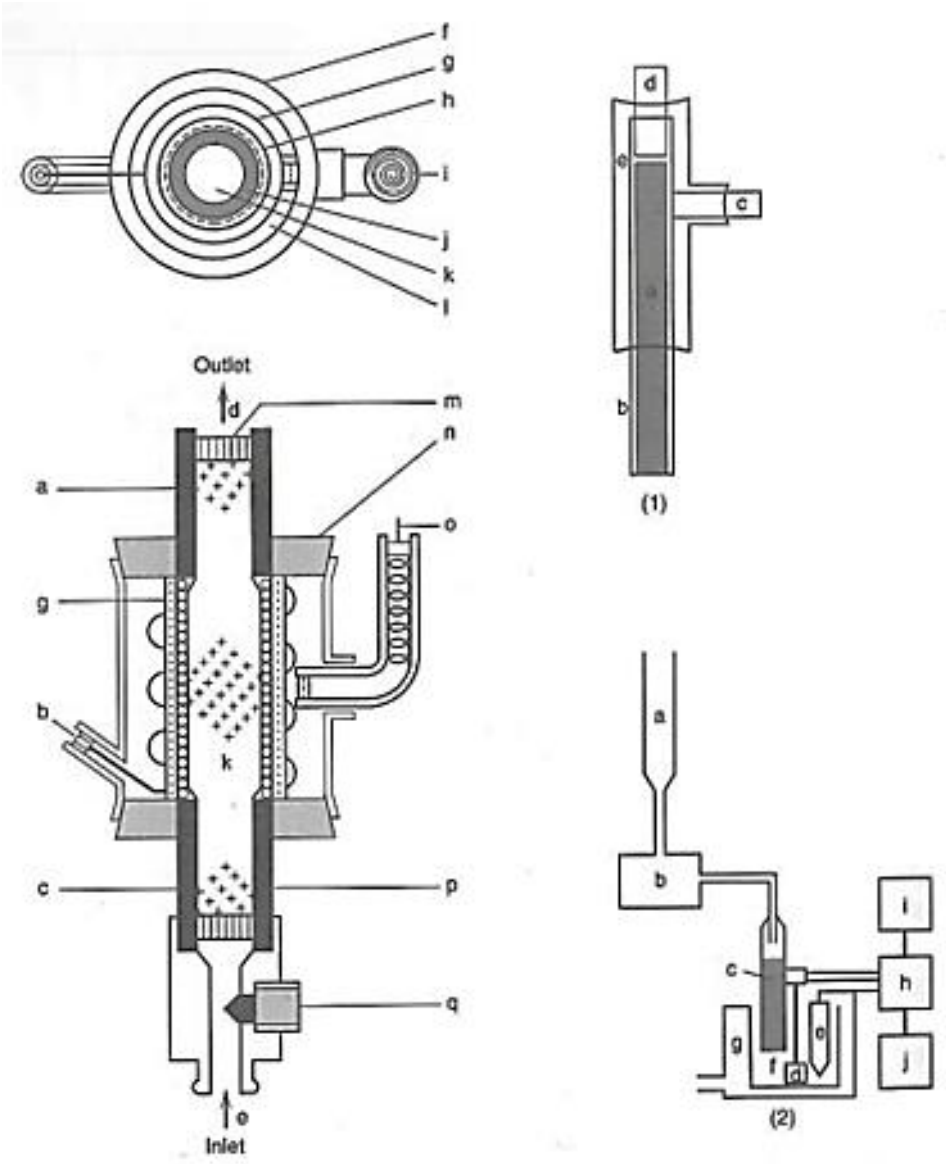

***Fig. 2.30**, Flow electrolytic cells. Left: Cell utilizing glassy carbon granule. (k) Working electrode of glassy carbon granule, (g) silver counter electrode, (o, i) Ag/AgCl reference electrode with (h) porous glass separator. Other components are (a, c) lead for working electrode; (b) lead to counter electrode; (d) solution outlet; (e) solution inlet; (f) glass or plastic tube; (j, p) porous carbon tube; (l) saturated KCl solution; (m) silicone rubber. Top right: Schematic of flow cell for Reticulated Vitreous Carbon (RVC) (a) RVC cylinder, (b) heat-shrink tubing, (c) graphite rod sidearm, (d) glass tube, (e) glass and epoxy support. Bottom right: Schematic diagram of complete apparatus. (a) Solution reservoir, (b) pump, (c) RVC electrode, (d) platinum electrode, (e) SCE reference electrode, (f) downstream reservoir, (g) runover collector, (h) potentiostat, (i) recorder, (j) digital voltmeter. (Bard, Faulkner 2001)*

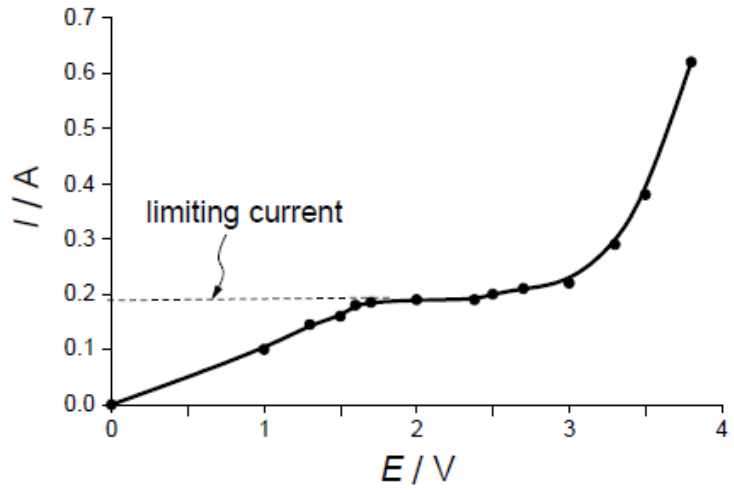

Fig. 2.31, *Typical Linear Sweep Voltammetry (LSV) voltammogram for limiting current measurement. (Coñizares et al. 2006)*

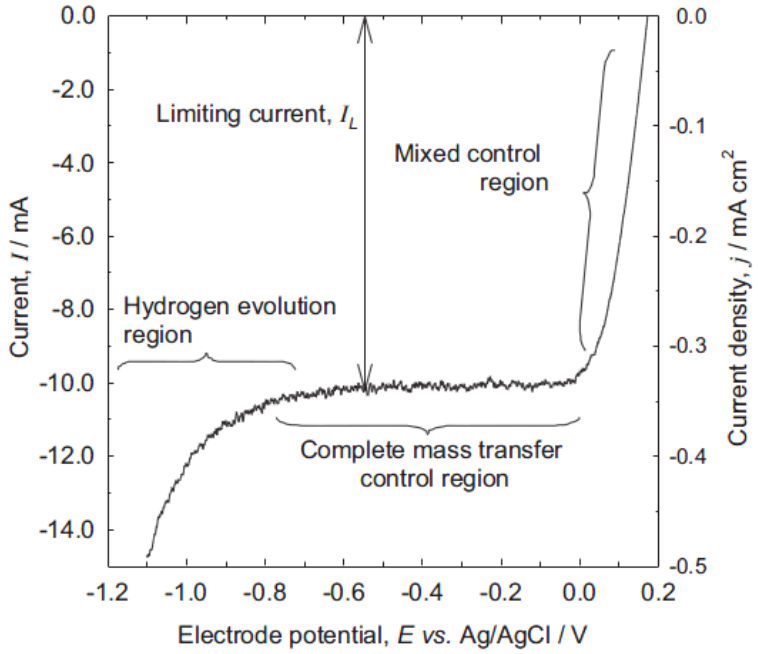

Fig. 2.32*, Typical LSV voltammogram for the reduction of* $Fe(CN)_6^{3-}$ *in 0.001 mol/L* $K_3Fe(CN)_6$ *+ 0.001 mol/L* $K_4Fe(CN)_6$ *+ 0.1 mol/L* Na_2CO_3 *at a nickel electrode with an electrolyte velocity of 38 cm/s. (Recio et al. 2013)*

2.5.3 Dimensionless Numbers for Mass Transport

In electrochemical engineering, it is common to use the dimensionless groups related to the mass transport as defined in Table 2.3 (Walsh 1993). The number of such groups used in a correlation is given by the Buckingham π theorem of dimensional analysis (Walsh 1993).

***Table 2.3**, Common dimensionless groups used in electrochemical mass transport. (Walsh 1993) (k* is mass transfer coefficient, *l* is characteristic length, *D* is diffusion coefficient, *U* is characteristic velocity, v is kinematic viscosity, μ_0 is dynamic viscosity, ρ is fluid density, *g* is acceleration due to gravity, and *L* is length of electrode)

Dimensionless Group	**Definition**	**Significance**
Sherwood number, *Sh*	$Sh = \frac{kl}{D}$	Mass transport under forced convective flow conditions
Stanton number, *St*	$St = \frac{k}{U}$	Ratio of mass transferred into a fluid to fluid velocity under forced convective flow conditions
Reynolds number, *Re*	$Re = \frac{Ul}{v}$	Fluid flow condition in forced convection
Grashof number, *Gr*	$Gr = \frac{L^3 g\rho}{\mu_0^2}\Delta\rho$	Mass transport under natural convection flow conditions
Schmidt number, *Sc*	$Sc = \frac{v}{D}$	Ratio of the momentum diffusivity and mass diffusivity

Three correlations are commonly used to provide expressions for mass transport (via *Sh*) in terms of the fluid flow conditions (via *Re* or *Gr* or both) and the transport properties of the electrolyte (via *Sc*).

In the general case of convective diffusion, the mass transport correlation can be expressed as (Walsh 1993):

$$Sh = a'Re^{b'}Gr^{d'}Sc^{c'} \quad (2.28)$$

where *a'*, *b'*, *c'* and *d'* are fitting parameters.

If only free convection is present, the expression becomes (Walsh 1993):

$$Sh = a'Gr^{d'}Sc^{c'} \quad (2.29)$$

If forced convection predominates, the mass transport correlation can be written as (Walsh 1993):

$$Sh = a'Re^{b'}Sc^{c'} \quad (2.30)$$

For Eqn. 2.30, the values of *a'* depends upon both electrode geometry and flow conditions. The value of *b'* is sensitive to flow conditions and tends to be greater in turbulent flow than in laminar flow. The value of *c'* is 1/3 which can be obtained by hydrodynamic theory (Walsh 1993).

2.5.4 Effect of Porosity

To study the effect of porosity on mass transfer of porous metal electrodes, Zhou et al. (2015) measured three porous copper samples with different porosities (70%, 80% and 90%). Compared with 70% and 90% porosity samples, the sample with 80% porosity had better performance in mass transfer in methanol conversion. For the porous electrode with a high porosity (90%), the reactant can easily pass through the electrode with low pressure drop and short residence time due to its high porosity. Consequently, the reaction cannot be fully carried out on the surface of electrode (Zhou et al. 2009). When the porous metal with a low porosity (70%) is used as electrode, a much longer residence time was obtained for the reactant. However, the amount of effective surface area which participates in the reaction was decreased because the pores in the porous metal with low porosity were easily

blocked. Therefore, porous metal electrodes with too high or too low porosity exhibited poor performance in mass transfer (Zhou et al. 2015).

2.6 Techniques for Tortuosity Measurements

2.6.1 Introduction to Tortuosity

Tortuosity characterizes the convoluted pathways (or channels) formed by pores through porous media. In the fluid mechanics of porous media, tortuosity is the ratio of the length of a streamline, a flow line or path, between two points to the straight-line distance between those points which is shown in Fig. 2.33. In a porous medium, a large tortuosity is caused by the decreased area of available cross-section and increased path length (Currie 1960). The tortuosity influences the diffusion (Currie 1960), permeability (Khayargoli et al. 2005) and dynamic specific surface area (Montillet et al. 1993) in the porous material. It is an important property of porous metals, especially for fluid behaviour in porous metals.

Tortuosity is defined as the ratio of the average length of pathways in porous material to the sample length (Epstein 1989):

$$\tau = \frac{\overline{L_e}}{L} \tag{2.31}$$

where $\overline{L_e}$ is the average length of pathways and L is sample length.

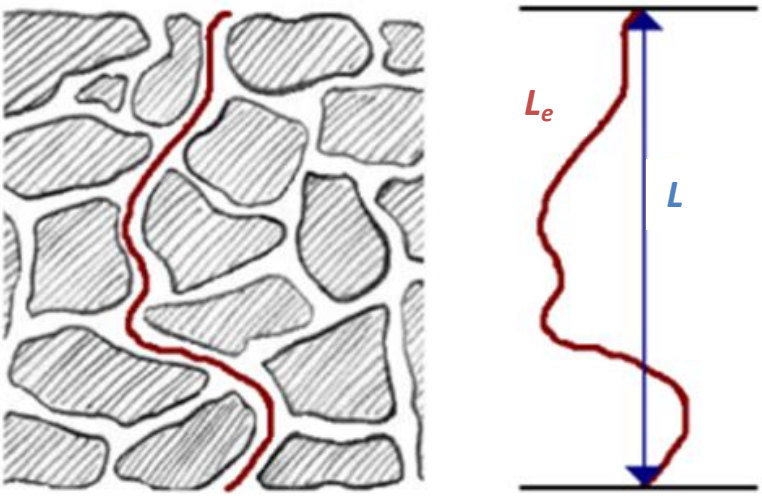

Fig. 2.33, *Schematic of the tortuosity in a porous media*

2.6.2 X-ray Computed Tomography

X-ray computed tomography (CT) scan is commonly used to generate a three-dimensional image of the inside of the object from a large series of two-dimensional radiographic images (Herman 2009). CT scan has been used to obtain the 3D porous structure in porous material samples (Fig. 2.34 (a)) and to analyse the characteristics of the pore structure, such as porosity, pore size, surface area and tortuosity (Rehder et al. 2014, Shanti et al. 2014).

The tortuosity can be obtained by the path length ratio (PLR) method from the 3D image. The PLR method uses the simple relationship (Epstein 1989):

$$\tau = L_0/L' \tag{2.32}$$

where τ is tortuosity, L_0 is the length of a pore channel (geodesic length), and L' is the end-to-end length of the pore channel (Euclidean length). L_0 and L can be measured directly from skeletonized networks in the 3D image as shown in Fig. 2.34 (d). The skeletonized network was numerically converted to a matrix of nodes (idealized point intersections of two or more pore channel pathways). The shortest path between nodes through the pore network (L_0) can be found by Dijkstra algorithm (Dijkstra 1959). The end-to-end distance

(*L*) between these two nodes was calculated directly from the 3D image. The tortuosity was then calculated by taking the ratios of these values (Shanti et al. 2014).

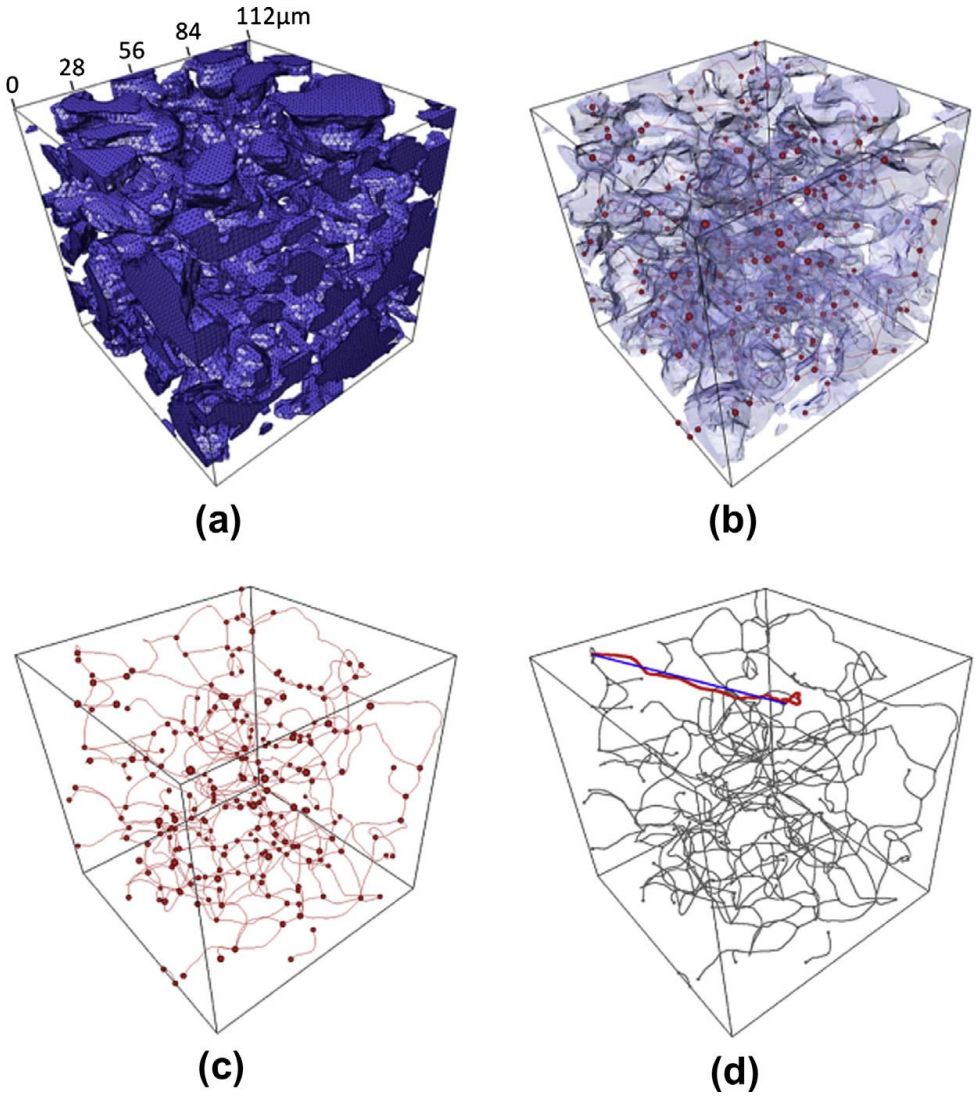

***Fig. 2.34**, Schematic of skeletonization process for an Al_2O_3 sample produced with 49.5% porosity: (a) 3D µCT reconstruction; (b) skeleton overlaid on 3D reconstruction; (c) skeleton showing nodes (red dots) and channels (red lines); (d) skeleton with a single pore channel (lenth L_0, shown in red) and corresponding straight line path (length L, shown in blue) highlighted. (Shanti et al. 2014).*

2.6.3 Acoustic Method

The tortuosity of porous media can also be estimated from the acoustic absorption curves of the porous media by the analytical solution and extrapolation approach (Panneton & Olny 2006, Kino 2015, Allard & Atalla 2009, Rogerio & d'Andrade 2012).

The acoustic tests of the porous media are conducted in an impedance tube (Fig. 2.35) to obtain the acoustic curves (acoustic absorption coefficient vs. frequency), as shown in Fig. 2.36 (Rogerio & d'Andrade 2012). The tortuosity ($\mathcal{T}$) can be obtained from the Johnson-Champoux-Allard model which is based on the work by Johnson, Koplik and Dashen to describe visco-inertial dissipative effects inside the porous media and the work by Champoux and Allard to describe the thermal dissipative effects (Kino 2015):

$$\rho(\omega')_{J-A} = \rho\tau[1 + \frac{\sigma\varepsilon}{\sqrt{-1}T\rho_0\omega'}G_J(\omega')] \tag{2.33}$$

$$G_J(\omega') = (1 + \frac{4\sqrt{-1}T^2\eta\rho_0\omega'}{\sigma^2L^2\varepsilon^2})^{1/2} \tag{2.34}$$

where ρ is the density of the air, ω' is the angular frequency, f is the frequency, η is the viscosity of the air, σ is static air flow resistivity, ε is porosity and L is characteristic length (Kino 2015).

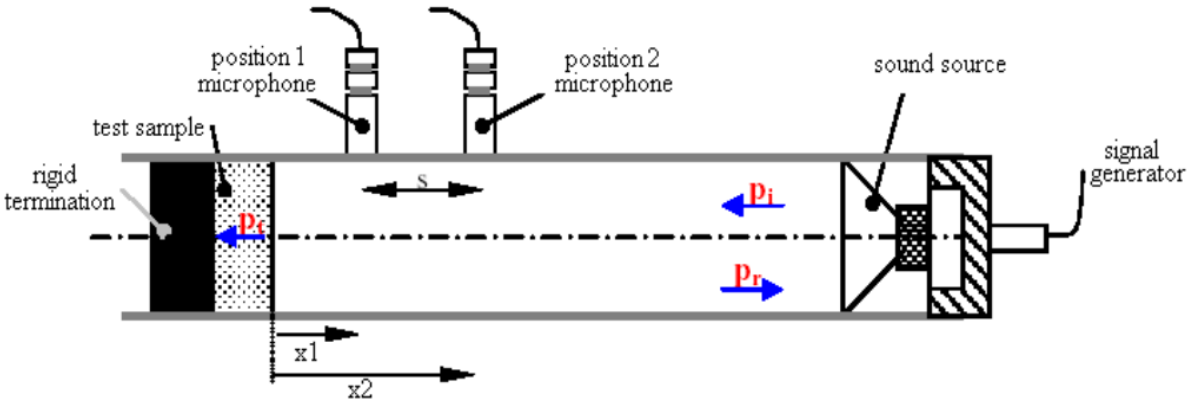

***Fig. 2.35**, Schematic of impedance tube. (Rogerio & d'Andrade 2012)*

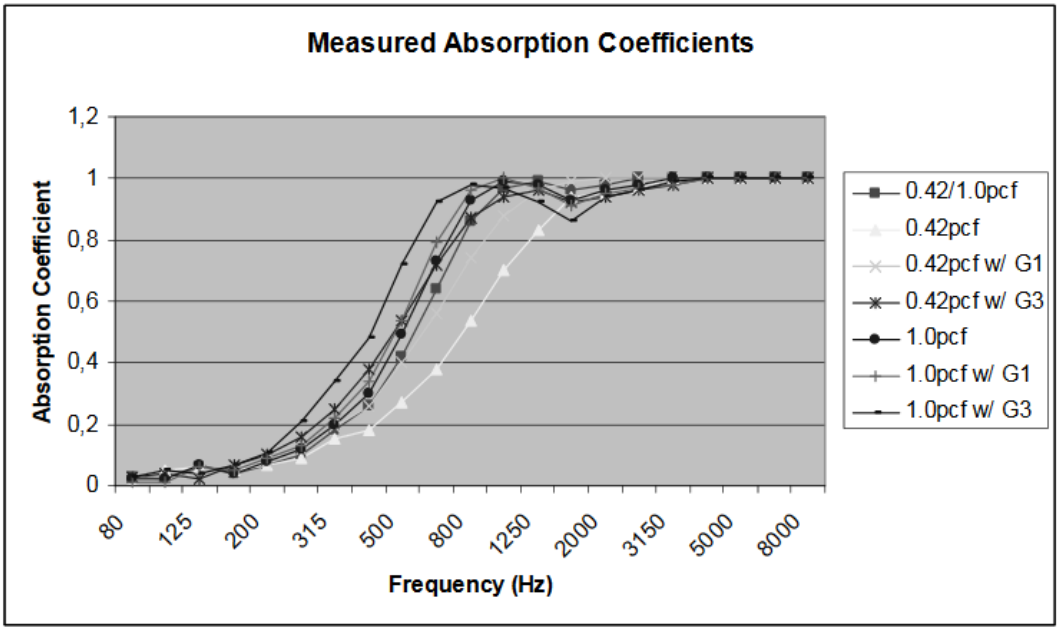

***Fig. 2.36**, Typical acoustic curves. (Rogerio & d'Andrade 2012)*

2.6.4 Diffusion Method

A common method of measuring the tortuosity is to measure the gas or liquid diffusion coefficient in the porous media. The relationship between tortuosity ($\mathcal{T}$) and diffusion coefficient can be expressed as (Currie 1960):

$$\tau = \sqrt{\frac{D_0}{D_e}} \tag{2.35}$$

where D_e is effective diffusion coefficient and D_0 is standard diffusion coefficient.

The effective diffusion coefficient can be measured in a diaphragm cell as shown in Fig. 2.37 (Cussler 1984). Porous material samples are fixed in the middle of the diaphragm cell. Liquids or gases with different concentrations are filled into the top and bottom compartments, respectively. In the experiment, the solutes or gases diffuse through the porous material sample from the high concentration compartment to the low concentration compartment. The effective diffusion coefficient can be obtained from measuring the concentrations in the top and bottom compartments by (Cussler 1984):

$$D = \frac{1}{\beta t} \ln[\frac{c_{b,i} - c_{t,i}}{c_{b,t} - c_{t,t}}] \quad (2.36)$$

where β (in cm^2) is a diaphragm cell constant, t is the time, $c_{b,i}$ and $c_{t,i}$ is the solute concentration in the bottom and top compartment at initial, and $c_{b,t}$ and $c_{t,t}$ is the solute concentration in the bottom and top compartment at time t, respectively. β can be expressed by (Cussler 1984):

$$\beta = \frac{A}{l}(\frac{1}{V_t} + \frac{1}{V_b}) \quad (2.37)$$

where A is the area available for diffusion, l is the effective thickness of the sample, and V_t and V_b are the volumes of the two cell compartments.

A few points deserve emphasis in applying the diffusion method. Firstly, the calculation of the diffusion coefficient requires accurate knowledge of the concentration differences, not the concentrations themselves. Secondly, the experiments need to run over a long period of time in order to obtain accurate results. Finally, the diffusion should always take place vertically (Cussler 1984).

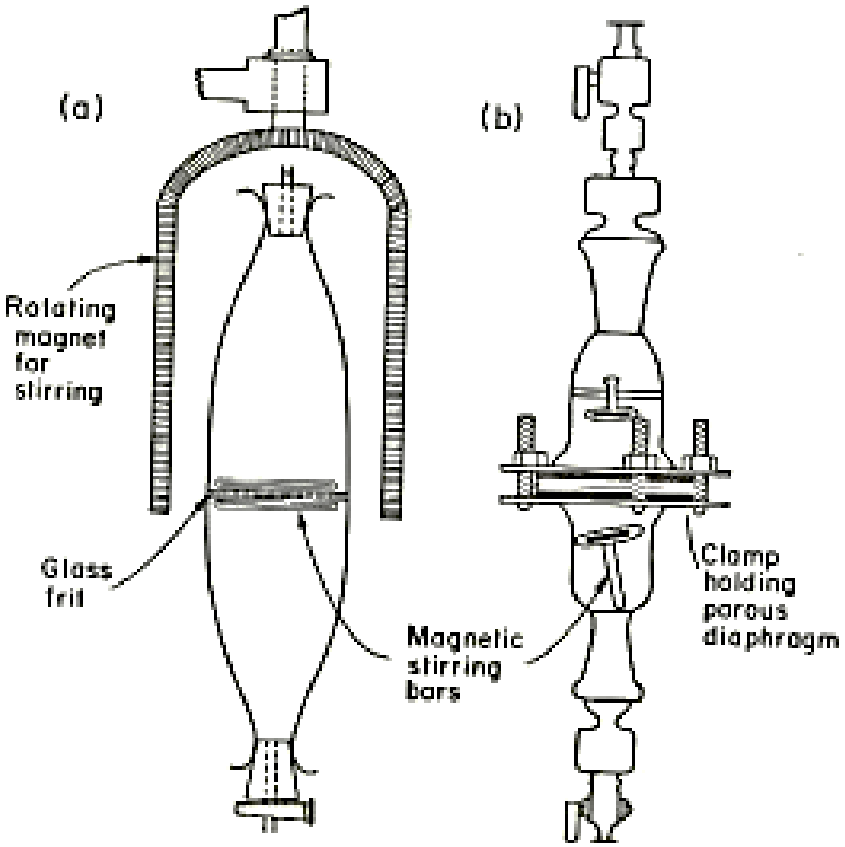

***Fig. 2.37**, Schematic of two diaphragm cells. (Cussler 1984)*

2.7 Summary

Open-cell porous metals can be used as porous electrodes for electrochemical applications, such as fuel cells, flow batteries and wastewater treatment, because of their high surface area and good permeability. The high surface area can provide a high current density and the good permeability allows the electrolyte to flow through the porous electrode.

In most previous studies on porous metals, only geometric or real surface area was characterised. The geometric surface area depends upon the pore size and porosity of the porous metal. A porous metals with similar pore size and porosity have similar geometric surface areas. The real surface area of a porous metal is commonly one to two orders of

magnitude higher than its geometric surface area and is very sensitive to the manufacturing method because of the different resultant surface roughness of the cell walls.

The electro-active surface area is a very important property of a porous metal electrode because it determines the current density depends. The electro-active surface area is affected by the diffusion of the electro-active species in the electrolyte. It is considerably lower than the real surface area if the diffusion layer thickness is greater than the scale of the roughness of the electrode surface. However, very little research has been conducted to date to understand the characteristics of the electro-active surface area of porous metals and the effects of pore size and diffusion layer thickness.

Mass transport is a very important property for the performance of a porous electrode in flow cell applications. The increase of surface roughness and the presence of turbulence promoter both can increase the mass transfer coefficient. Porous metals are good turbulence promoters because the tortuous pathways (or channels) can lead to a high level of turbulence. However, there has been very little research on the mass transport of porous metals manufactured by the space-holder methods.

Tortuosity is an important structural property of porous metals for fluid flow application. The tortuosity normally decreases with porosity. Although high high tortuosity can provide high level of turbulence which can improve the mass transport performance of the porous metals for use in a flow cell, the high tortuosity leads to high pressure drop and low permeability.

Chapter 3 Experimental

Porous metal samples with different porosities, pore sizes and materials (copper and nickel) were fabricated by the LCS process developed by Zhao and his colleagues (Zhao et al. 2005). Two sintering routes (dissolution and decomposition) can be used in LCS, as described in the literature review. In this project, the decomposition route was used to manufacture both porous copper and porous nickel samples for the investigations of their structural characteristics (particle size, pore size, porosity and geometric surface area) and electrochemical properties (electro-active surface area, real surface area and mass transfer coefficient). The dissolution route was used to fabricate the porous copper samples for tortuosity measurement.

3.1 Preparation of Test Samples by LCS

The LCS process was developed by Zhao and his colleagues (Zhao et al. 2005), which is based on sintering a compact of metal powder incorporating removable salt particles. LCS uses K_2CO_3 powder as the filler material, which can be eliminated by decomposition or dissolution. The relatively high melting temperature (890°C) of potassium carbonate permits a high sintering temperature, ensuring strong bonding between the metal particles before the filler material melts or decomposes. Therefore, the LCS process can be used for manufacturing a wide variety of porous metals with high sintering temperatures, such as Cu, Ni, Fe and Ti. The porous metal samples manufactured by LCS have controlled pore structure, including porosity, pore size and pore shape. Both porous Cu and porous Ni samples with different pore sizes (75-1500 μm) and porosities (0.5-0.8) were manufactured by the LCS process either in a vacuum furnace (Vacua-Therm Sales Ltd., UK) or in a conventional furnace (Vecstar Ltd., UK).

3.1.1 Raw Materials

Two types of porous metals (Cu and Ni) were fabricated. Commercially pure Cu powder with a particle size of 50-120 μm was used in manufacturing porous Cu samples. The Cu powder had a purity of 99.5% and was supplied by Ecka Granules Metal Powder Ltd, UK. Pure Ni powder with a purity of 99% and particle size smaller than 90 μm, supplied by Ecka Granules Metal Powder Ltd, was used in the manufacture of porous Ni samples.

Food grade K_2CO_3 powder (E&E Ltd, Australia) with a purity of 99% was used as the filler material in the manufacture of both porous Cu and Ni samples. The K_2CO_3 powder was sieved into five different particle size ranges: 75-150 μm, 250-425 μm, 425-710 μm, 710-1000 μm and 1000-1500 μm.

3.1.2 Mixing and Compaction

K_2CO_3 powder was mixed with the metal powder at a pre-specified volume ratio according to the target porosity, using ethanol as a binder. The required masses of the metal powder (M_{Metal}) and the K_2CO_3 powder ($M_{K_2CO_3}$) can be calculated by:

$$M_{Metal} = (1 - \varepsilon)V\rho_{Metal} \tag{3.1}$$

$$M_{K_2CO_3} = \varepsilon V\rho_{K_2CO_3} \tag{3.2}$$

where ρ_{Metal} is the density of the metal (8.96 g/cm^3 for Cu and 8.91 g/cm^3 for Ni), $\rho_{K_2CO_3}$ is the density of K_2CO_3 (2.3 g/cm^3), ε is the target porosity and V is the target volume of the sample. A moderate amount of ethanol (about 0.1 ml ethanol for 1 cm^3 target volume of sample) was used as a binder to mix the metal and carbonate powders evenly. Less ethanol could lead to layering and separation between metal and carbonate powders and more ethanol could lead to the agglomeration of the metal powder.

After the metal and carbonate powders were fully stirred by a stick and mixed with ethanol, the mixture was filled into a mild steel mould (for decomposition route) or tube (for dissolution route). For electrochemical measurements of electro-active and real surface areas and mass transfer coefficient, the mixture was compacted into a cuboid preform of 0.5 cm × 2 cm × 3 cm under a pressure of 200 MPa for approximately 10 seconds by a hydraulic press (Moore Hydraulic Press, UK), as shown in Fig. 3.1. The compacts were removed from the mould and placed in a desiccator with silica gel to prevent potassium carbonate from taking up moisture.

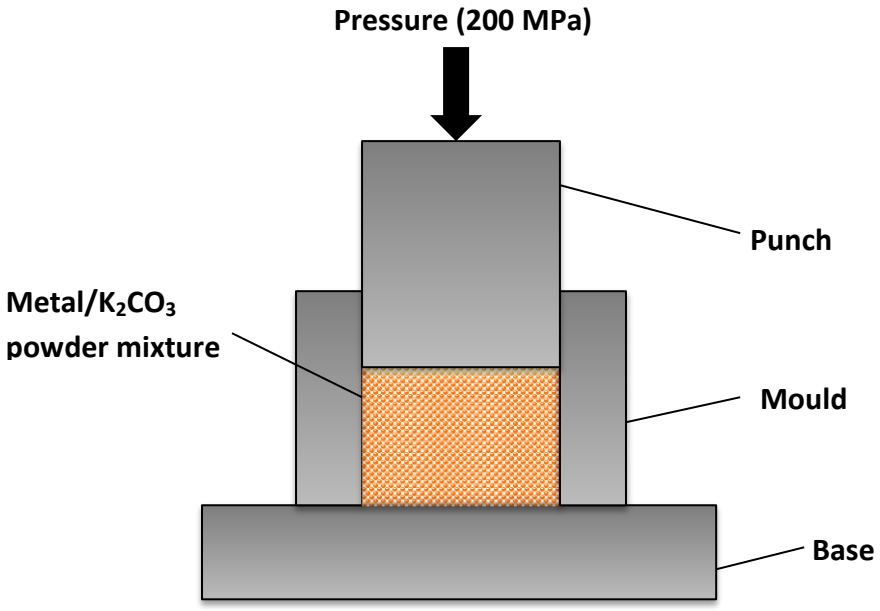

***Fig. 3.1**, Schematic of the compaction process for metal/carbonate powder mixture.*

For tortuosity measurements, the compacts were manufactured into cylinders of Ø 5 cm × 1 cm and sealed in a mild steel tube, as shown schematically in Fig. 3.2. Before compaction, both ends of the tube were sealed by steel powder in order to prevent the green samples from being oxidized during sintering. The potassium carbonate powder was used to separate the metal/K_2CO_3 mixture and steel sealing powder. The powders were compacted in the tube under a pressure of 200 MPa.

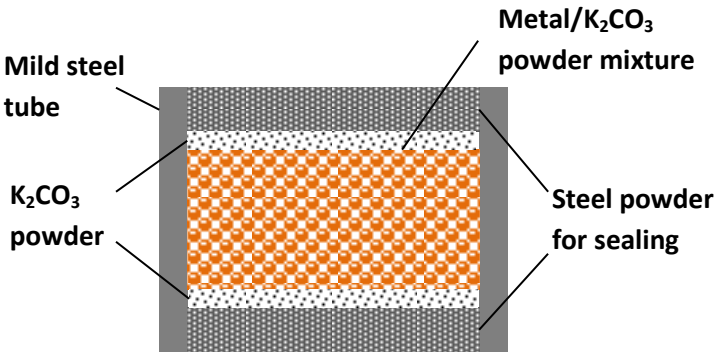

***Fig. 3.2**, Schematic of the copper/carbonate powder mixture in a steel tube.*

3.1.3 Sintering

In this project, the decomposition route was used to fabricate most test samples, because of the simplicity of the manufacture procedure. This route can also provide better mechanical properties and well controlled micro-pore structure. The dissolution route was only used to manufacture the porous Cu samples for tortuosity measurement. By using this route, the potassium carbonate particles were ensured to remain in the pores of the sample after sintering, so that the sample can be cut and ground to the correct size and shape without damaging the pore structure.

In manufacturing samples by the decomposition route, the preforms (green samples) were placed on a stainless steel plate with a piece of alumina paper separating the samples and the plate, which was then placed in the centre of the VTS vacuum furnace. In order to prevent the samples from oxidization, the heating of the furnace started after the chamber pressure was evacuated to lower than 0.7 mbar. Debinding was carried out at 200°C for 30 minutes in order to evaporate the ethanol in the preforms. The preforms were pre-sintered at 800 °C for 30 minutes in the vacuum environment in order to prevent the samples from collapse. In order to achieve strong bonding between metal particles, the preforms were further sintered at 950 °C for 2 hours. In the sintering stage, the potassium carbonate was decomposed as the melting point of K_2CO_3 is 891 °C, at which it also started to decompose and was completely

removed from the samples, resulting in open-cell porous metal samples with fixed porosities and pore sizes. After sintering, the porous samples were cooled rapidly in an Argon environment to prevent the samples from oxidization. The sintering and carbonate removal procedure is shown schematically in Fig. 3.3.

In manufacturing samples by the dissolution route, the preforms (green samples sealed in mild steel tubes) were placed in a conventional furnace. Debinding was carried out at 200°C for 30 minutes in order to evaporate the ethanol in the preforms. The green samples were then sintered at 850°C for 4 hours (the sintering process is shown schematically in Fig. 3.4). After the samples were cooled to room temperature and removed from the tubes, they were cut and ground to the correct sizes and shapes with potassium carbonate particles still inside. Finally, the potassium carbonate was dissolved in boiled water, resulting in open-cell porous Cu samples.

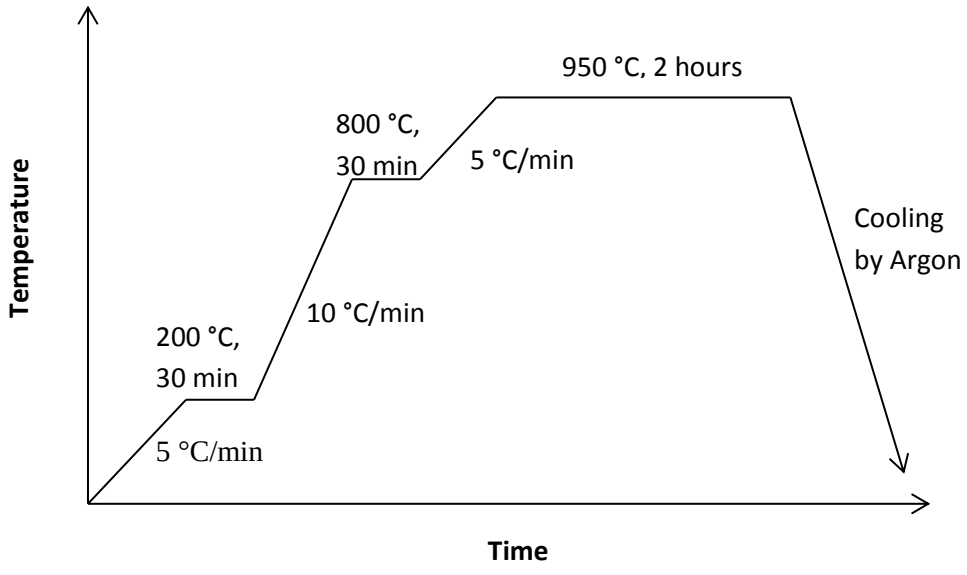

Fig. 3.3, Schematic of the sintering and carbonate removal process in the decomposition route.

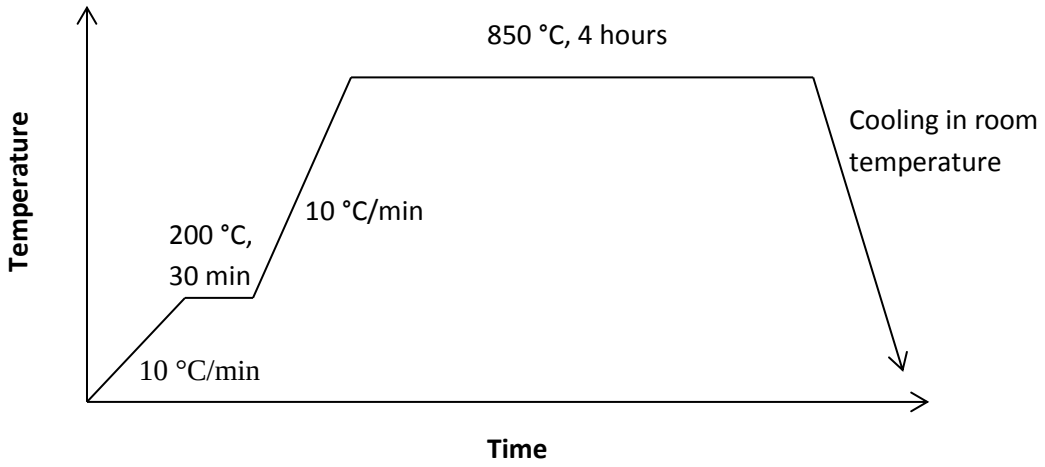

***Fig. 3.4**, Schematic of the sintering process in the dissolution route.*

3.2 Structural Characterisation

The Cu, Ni and K_2CO_3 powders were analysed by a particle size analyser (Malvern Mastersizer 2000) in order to obtain the mean particle size and distribution. For Cu and Ni powders, the powder was stirred in a container with distilled water added with a small amount of detergent. The detergent was used to reduce the surface tension of the distilled water so that the metal particles were not agglomerated. During the particle size analysis, a liquid circulation system was used to flow the metal powder passing the lens for laser light scattering analysis. The particle size of the K_2CO_3 powder was measured in ethanol instead of distilled water, because potassium carbonate dissolves in water.

The porous Cu and Ni samples were observed by SEM (JSM-6610) to characterise the microstructure, such as pores, cell walls and sintering necks between metal particles. The energy-dispersive X-ray spectroscopy on the SEM (JSM-6610) was used to analyse the purity of the porous metal samples.

The porosity of each porous sample was obtained by measuring its density. The mass of the sample was obtained by an electronic balance (Ohaus Scout Pro Portable Balance,

resolution: 0.01 g). The length, width and height of the sample were measured by a calliper (Electronic Digital Calliper, Maplin) to obtain the volume of the sample. In order to improve the accuracy of the measurements, the length, width and height were measured five times at different positions of the sample and the average values were used. The porosity, ε, was calculated by:

$$\varepsilon = 1 - \frac{M}{V\rho_{Metal}} \tag{3.3}$$

where M and V are the mass and volume of the porous metal sample, respectively, and ρ_{Metal} is the density of the metal.

3.3 Measurement of Geometric Surface Area and Primary Porosity by Quantitative Stereology

Two kinds of pores exist in the LCS porous metals: primary and secondary pores. The primary pores are open pores randomly distributed in the metal matrix and interconnected through small windows. They are formed by the removal of the K_2CO_3 particles. Secondary pores are the small interstices or voids between the metal particles resulting from partial sintering. The geometric surface area and primary porosity take into account the surface area and volume of the primary pores formed by the K_2CO_3 particles, excluding the secondary pores.

In this project, the quantitative stereology (QS) method was used to measure these two structural properties of the porous metal samples with different porosities and pore sizes by an optical microscope (Veho VMS-004, 20-400x Magnication USB Digital Microscope Camera). Specifically, the QS method was used in the determination of the geometric specific surface area and primary porosity in porous Cu and Ni samples with various pore sizes of 250-1500 μm and porosities of 0.55-0.75. The samples with pore size smaller than

250 μm were not analysed because of the difficulty in differentiating the primary and secondary pores.

As a common method to analyse the pore structure of porous materials, QS characterizes quantitatively the geometrical features of the microstructure. In this method, a three-dimensional object (porous material) is cut by a sectioning plane to obtain a two-dimensional structure. The three-dimensional structural quantities can be obtained by measuring the lines and points on the two-dimensional plane.

In these measurements, the porous metal sample was cut to a small size about $1.5\times1.5\times0.5$ cm^3 and immersed in an epoxy resin (CHEMSET ES 8103), so that the resin filled all the pores. After the epoxy resin was solidified, one surface of the porous metal sample was ground and polished to form a flat surface. The pores at the surface were not enlarged, filled or smeared during preparation, because of the existence of the resin. The micrograph of the carefully-prepared flat surface of each porous metal (Cu or Ni) sample was taken by an optical microscope and a counting grid was superimposed onto the micrograph by ImageJ (Schindelin et al. 2012), as shown in Fig. 3.5.

The geometric surface area was obtained by counting the intercepts between the grid lines and the pore perimeters on the micrograph (Fig. 3.5). The volumetric specific geometric surface area, S_{VG}, is the total internal surface area of the primary pores per unit volume of the sample and was obtained by (Underwood 1970):

$$S_{VG} = \frac{2P}{L_T} \tag{3.4}$$

where P is the number of intercepts between the grid lines and the primary pore perimeters and L_T is the total length of the grid lines.

The gravimetric specific geometric surface area can be obtained from its volumetric surface area by:

$$S_{MG} = \frac{S_{VG}}{(1-\varepsilon)\rho} \tag{3.5}$$

where ε is the porosity of the sample and ρ is the density of the solid metal.

Primary porosity, ε_p, was obtained by counting the number of points falling in the pores. The primary porosity is equal to the ratio of the points falling in the pores to the total grid points by (Underwood 1970):

$$\varepsilon_p = \frac{P_{pore}}{P_{total}} \tag{3.6}$$

where P_{pore} is the number of points in the pores and P_{total} is the total grid points in the test area.

Fig. 3.6 shows the standard deviation of the intercept points on the grid line in the different grid size from 0.15 mm to 0.6 mm. When the grid size is smaller than 0.3 mm, the decrease of standard deviation becomes not significant and the value of standard deviation approaches to 15%. Therefore, the grid size of 0.3 mm was chosen and used in the measurements of geometric surface area and primary porosity.

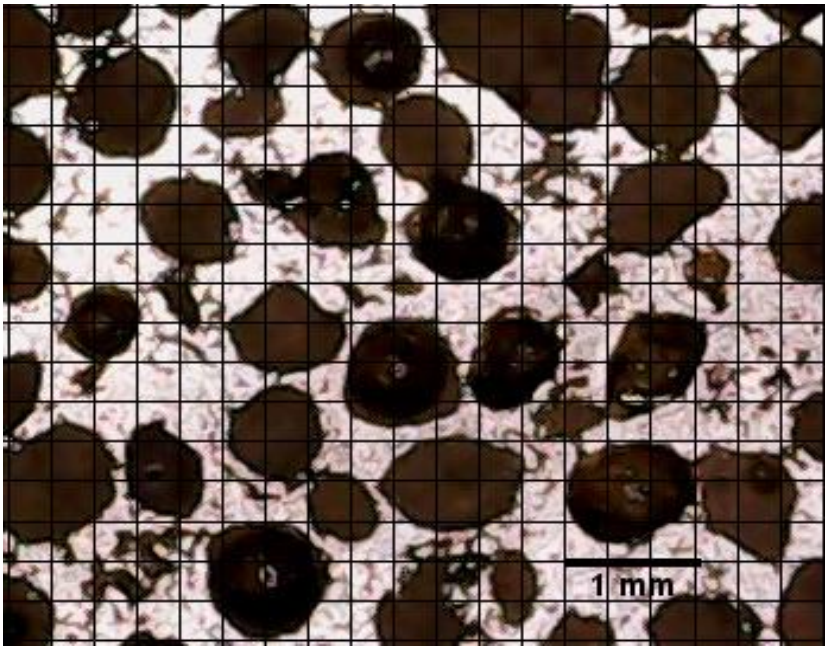

***Fig. 3.5**, Optical micrograph of a porous Ni sample superimosed with a counting grid.*

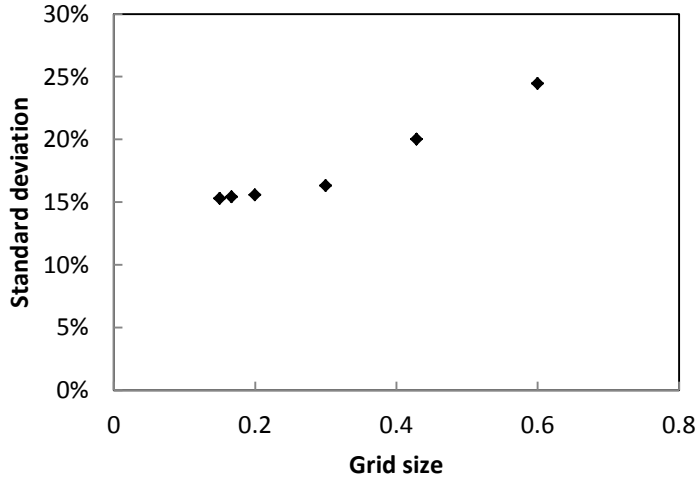

***Fig. 3.6,** Variations of standard deviation of intercept points on the grid line with grid size*

3.4 Measurement of Tortuosity by the Diffusion Method

Tortuosity is an important parameter of the porous metal which depends on the pore structure and has a significant influence on the fluid flow in the porous metal. In this project, a diaphragm cell was used to measure the diffusion of a species in the porous metal. As the diffusion coefficient of a certain species in a certain liquid is a constant and the flux in a

channel depends on the cross-sectional area and length of the channel, the average true length of the channels in the porous metal sample can be obtained by measuring the change of the concentration of the species in the diaphragm cell. The tortuosity of the sample is simply the ratio of the average true channel length and the sample thickness.

3.4.1 Experimental Apparatus

A purpose-built diaphragm cell was used to measure the diffusion of salt (NaCl) in water through the LCS porous Cu sample as shown schematically in Fig. 3.6. The top compartment was filled with pure distilled water and the bottom compartment was filled with 1.75 mol/L aqueous solution salt (NaCl). The circular porous Cu sample sat in the middle of the cell between the two compartments. The circumferential side of the sample was sealed by PTFE and PVA tapes, so that the solute (NaCl) can only diffuse through the porous Cu sample from the bottom compartment to the top compartment. To minimise the concentration difference within the top and bottom compartments, the two compartments were stirred by two stirrers at 60 rpm using two rotating magnets placed outside the two ends of the cell. Filter papers were used to cover both sides of the sample to prevent forced flow within the sample due to stirring in the compartments.

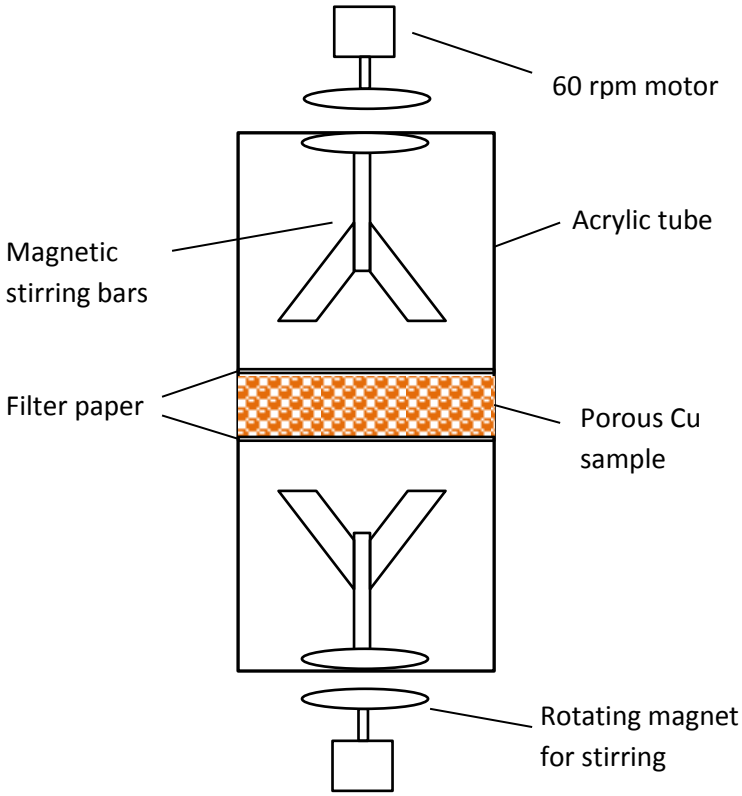

***Fig. 3.6**, Schematic of the diaphragm cell used in the measurement of tortuosity.*

3.4.2 Sample Preparation and Test Procedure

The porous Cu samples for tortuosity measurement were manufactured by the dissolution route. After dissolution of the potassium carbonate in boiled water, the porous Cu sample was cut into a circular disc with 4.8 cm diameter and 1 cm thickness by an EDM machine (WMT ONA E250), which has a precision better than 0.1 mm. The sample was cleaned in the 10% hydrochloric acid (HCl) and then soaked and immersed in distilled water in order to obtain a clean surface and to ensure that water penetrates all pores or channels. The sample was inserted in the middle of the diaphragm cell as shown in Fig. 3.6. The top and bottom compartments were then filled with pure water and the salt solution, respectively.

The experiment was conducted in an incubator (Thermo Scientific, USA) at a constant temperature of 25°C for three days in order to improve the accuracy. To measure the concentrations of the solutions in the two compartments, 50 ml of each solution was placed

into a two-beaker cell (Fig. 3.7) and heated in a furnace at 220°C to evaporate the water and crystallize the salt (NaCl). Specifically, the solution was poured into the small beaker which was placed in a large beaker and covered with a lid. The arrangement prevented the solution from splashing and ensured that all of the solute remained in the two-beaker cell. The molar concentrations of the solutions in the top and bottom compartments were obtained by weighing the dried salt by an Ohaus Scout Pro Portable Balance with the resolution of 0.01 g.

***Fig. 3.7**, Two-beaker cell for salt crystallization.*

The tortuosity, τ, of the porous Cu sample was calculated by the equation (Cussler 1984):

$$\tau^2 = DAt\left(\frac{1}{V_t} + \frac{1}{V_b}\right)/\left\{L \times \ln\left[\frac{c_{b,i} - c_{t,i}}{c_{b,t} - c_{t,t}}\right]\right\} \quad (3.7)$$

where D (1.481×10^{-5} cm^2/s) is the standard diffusion coefficient (Riquelme et al. 2007), t is the time, L is the thickness of the sample, V_t and V_b are the volumes of the top and bottom cell compartments, respectively, and c_t and c_b are the molar concentrations of the solutions

in the top and bottom compartments, respectively. *A* is the cross-sectional surface area of the open channels, which can be calculated by:

$$A = A_{disc} \times \varepsilon \tag{3.8}$$

where A_{disc} is the cross-sectional area of the circular disc sample and ε is the porosity of the sample.

3.5 Measurement of Surface Area by Cyclic Voltammetry

Cyclic voltammetry (CV) experiment was used to measure the electro-active surface area of porous Cu and Ni using a redox reaction on the sample surface. According to the Randles-Sevcik and Delahay equations, there exists a linear relation between peak current (*I*) and electro-active surface area (*A*) in the CV experiment (Scholz 2002, Delahay 1954, Ambrose et al. 1973). In this project, linear relations between *I* and *A* for Cu and Ni surfaces were obtained using a series of Cu and Ni plates with known surface areas. Based on these linear relations, the electro-active surface area of porous Cu or Ni can be determined by CV experiment.

CV experiment in the non-Faradaic (no redox reaction) region was used to estimate the real surface area of the porous Cu samples. Here, the change of current in the experiment occurs because of the double layer capacitance on the porous Cu sample, which depends on its real surface area. Therefore, the real surface area can be obtained by the measurement of the double layer capacitance.

3.5.1 Experimental Apparatus

A three-electrode cell system was used in the CV experiments. Fig. 3.8 shows a schematic diagram of the three-electrode electrochemical cell used for porous Cu tests as an example. The three-electrode cell system consisted of a computerized potentiostat (Autolab

PGSTAT101), working electrode (porous metal), counter electrode (Pt plate for solid metal plate samples and Pt coil for porous metal samples) and reference electrode (SCE). The counter electrode is used to form an electronic circuit with the working electrode and the reference electrode is used to obtain the potential on the working electrode so that the potential can be controlled. The porous metal, as a working electrode, was connected to the potentiostat by two metal wires (Cu wires for porous Cu and Ni wires for porous Ni) coated with resin, which is shown in the inset photo in Fig. 3.8.

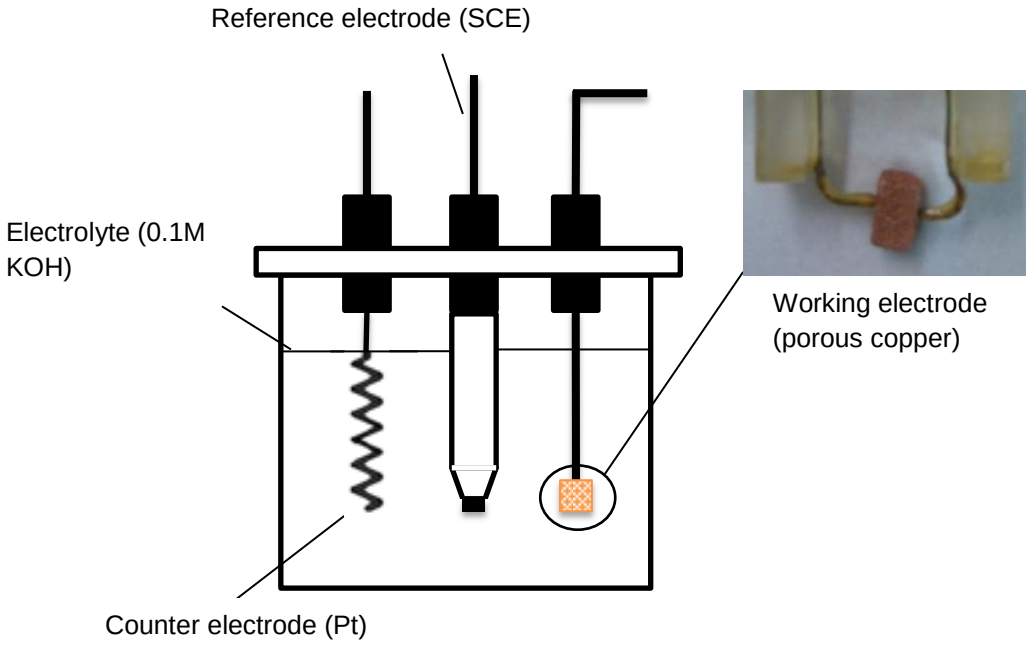

***Fig. 3.8**, Schematic of the three-electrode electrochemical cell used for the CV measurements. The inset figure shows a porous copper working electrode, which is clipped by two copper wires.*

3.5.2 Preparation of Samples

3.5.2.1 Cu and Ni Plates

The proportional relationship between the electrode surface area and peak current was obtained by using solid metal (Cu and Ni) plates with known surface areas. The Cu and Ni plate electrodes were cut into squares and the geometric surface areas were measured by a calliper. The metal plate was fixed onto a nylon block and connected to a steel wire

embedded in the nylon block. The edges of the metal plate were sealed by resin, as shown in Fig. 3.9. The steel wire was used to connect the metal plate to the potentiostat. The steel wire does not affect the accuracy and stability of the CV experiment, because it is not in contact with the electrolyte.

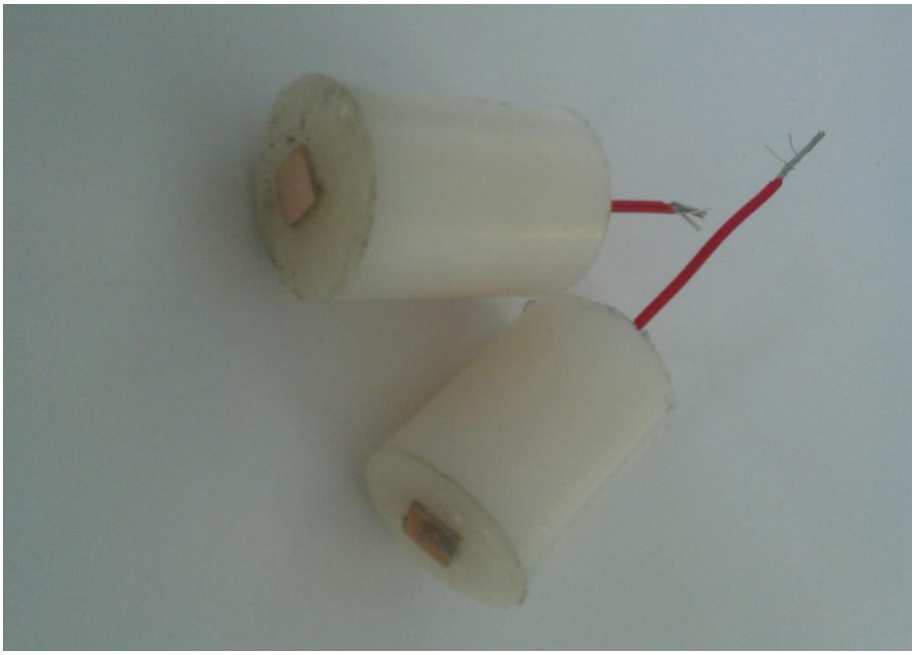

***Fig. 3.9**, Copper plate electrode fixed in resin.*

The surfaces of the Cu and Ni plate electrodes were polished to a 1 micron finish because of the diffusion layer >30 μm in the experiment. The Cu plate electrode was washed by 10% hydrochloric acid and then cleaned by distilled water. The Ni plate was simply cleaned by distilled water because Ni can react with the acid.

3.5.2.2 Porous Cu and Ni Samples

A series of porous Cu and Ni samples with different pore sizes and porosities were used as working electrodes for surface area measurement. Each porous Cu or Ni sample was cut to dimensions of 0.3 cm × 0.4 cm × 0.5 cm. The porous Cu sample was washed by 10% HCl and cleaned by ultrasonic treatment (Professional Ultrasonic Cleaner, GT Sonic). The porous Ni sample was cleaned by ultrasonic treatment in distilled water without acid

treatment. Before the CV experiment began, the porous Cu and Ni samples were immersed in stirred electrolyte to ensure that complete infiltration of the sample by the electrolyte was achieved during the measurement.

3.5.3 Test Procedure

3.5.3.1 Electro-Active Surface Area of Porous Cu

The electrolyte used for the porous Cu electro-active surface area measurement was 0.1 M potassium hydroxide (KOH). The oxygen in the electrolyte was removed by bubbling Nitrogen or Argon for at least 10 minutes (Kihlman 1958).

The potential was swept from -1.55 V to 0.8 V with a scan rate of 0.026 V/s. Three anodic peaks appeared in the voltammogram (Fig. 3.10). The third current peak with the reaction of $Cu+2OH^- \rightarrow CuO+H_2+2e$, which is the predominant reaction at slow scan rate, was used to determine the electro-active surface area of porous Cu samples. An overvoltage of -1.55 V was used in order to remove the residual CuO or Cu_2O on the porous Cu surface.

For a redox reaction controlled by the diffusion of OH^-, the anodic or cathodic peak current in the cyclic voltammogram corresponding to the reaction can be expressed by the Delahay equation (Ambrose et al. 1973):

$$I_p = 3.67 \times 10^5 n^{\frac{3}{2}} A c D^{\frac{1}{2}} v^{\frac{1}{2}} \quad (3.9)$$

where I_p is the peak current, n is the number of electrons in the reaction, A is the surface area of the electrode, c is bulk concentration of OH^-, D is the diffusion coefficient of OH^- and v is the scan rate of the electrode potential.

The Delahay equation cannot be used directly to calculate the surface area of the Cu electrode due to passivation. However, the peak current for a redox reaction is still

proportional to the electrode surface area, although the proportionality coefficient may be different from that in Eqn. 3.9. In the current work, the proportional relationship (Eqn. 3.10) between the electrode surface area and the peak current was calibrated using solid Cu plates with known surface areas and was then used to determine the electro active surface area of a porous metal electrode from the experimental value of I_p.

$$I_p = YA \tag{3.10}$$

where Y is the correlation coefficient.

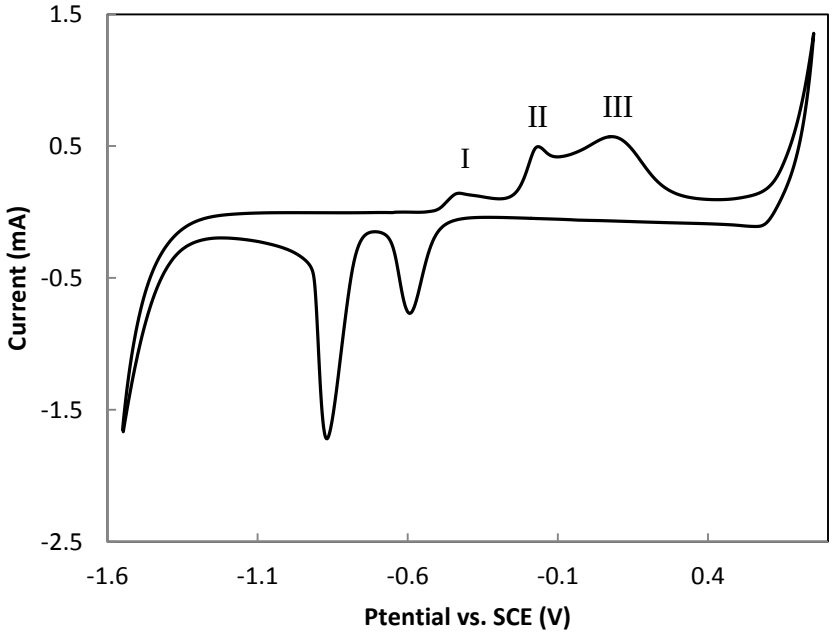

***Fig. 3.10**, Typical cyclic voltammogram of copper electrode in 0.1 mol/L KOH.*

3.5.3.2 Electro-Active Surface Area of Porous Ni

The electrolyte used for the porous Ni electro-active surface area measurement was 1 mM potassium ferricyanide ($K_3Fe(CN)_6$) and 1mM ferrocyanide ($K_4Fe(CN)_6$) in 0.1 M potassium hydroxide (KOH). The oxygen in the electrolyte was removed by bubbling Nitrogen or Argon for at least 10 minutes (Kihlman 1958).

In order to investigate the effect of diffusion layer thickness on the electro-active surface area, the potential was swept from -0.2 V to 0.3 V at a series of scan rates (0.005 V/s, 0.01 V/s, 0.05 V/s, 0.1 V/s, 0.2 V/s and 0.3 V/s). The current peak (Fig. 3.11) with the reaction of $Fe(CN)_6^{4-}$ - e→$Fe(CN)_6^{3-}$ was used to determine the electro-active surface area of the porous Ni samples.

In the electrochemical experiment, the reaction between $Fe(CN)_6^{3-}$ and $Fe(CN)_6^{4-}$ is a typical reversible reaction. In this case, the Randles-Sevcik equation (Eqn. 3.11) can be used to express the relationship between the value of the peak current and the electro-active surface area of the electrode (Bard & Faulkner 2001):

$$I_p = 2.69 \times 10^5 \times A \times D^{\frac{1}{2}} \times n^{\frac{3}{2}} \times v^{\frac{1}{2}} \times c \qquad (3.11)$$

where I_p is the peak current, A is the electro-active surface area of the electrode, n is the number of electrons in the reaction, v is the scan rate and c is the bulk concentration of the reactant. D is the diffusion coefficient of the reactant which was calibrated by a series of solid Ni plates with known surface areas. The electro-active surface area of porous Ni was calculated from the experimental value of I_p using Eqn. 3.11.

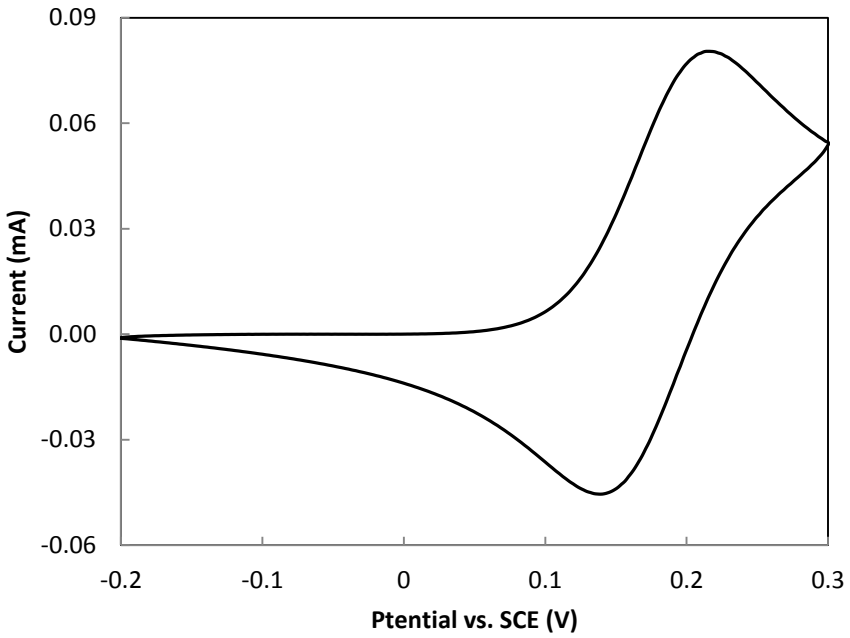

***Fig. 3.11**, Typical cyclic voltammogram of Ni in 1 mM $Fe(CN)_6^{3-/4-}$.*

3.5.3.3 Actual Surface Area of Porous Cu

The electrolyte used for the porous Cu actual surface area measurement was the same as that used for its electro-active surface area measurement. The CV experiment was conducted in the non-Faradaic region (no redox reaction) of -1 V to -0.75 V in order to measure the double layer capacitance on the porous Cu, as shown in Fig. 3.12.

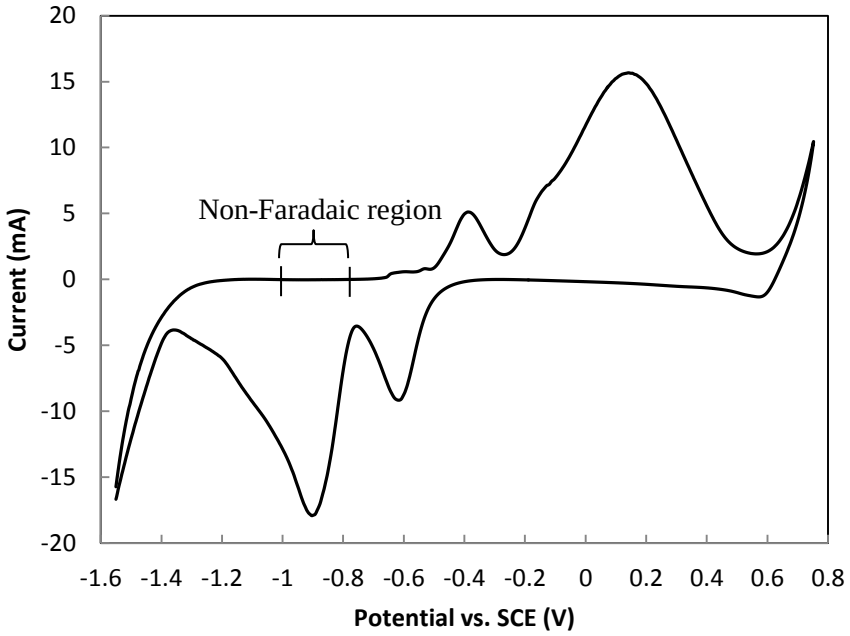

***Fig. 3.12**, Non-Faradaic region in the typical cyclic voltammogram of porous Cu.*

A series of scan rates from 0.001 V/s to 0.5 V/s were used to obtain the ratio of current change and scan rate. In the CV experiment, the double layer capacitance, *C* (mF), in the non-Faradaic region with different scan rates can be determined by (Lewandowski et al. 2012):

$$C = \frac{I}{v} \tag{3.12}$$

where *I* (mA) is the current, which is generated in the charge or discharge process and equals to half of the difference between the currents (ΔI) in the charge and discharge (Gileadi 2011), as Fig. 3.13 shows, and *v* (V/s) is the scan rate.

Lukomska and Sobkowski (2004) have shown that the specific capacitance of the Cu/electrolyte interface is approximately 0.02 mF/cm^2, so the real surface area of porous Cu electrode, A_R (cm^2), can be estimated by:

$$A_R = \frac{C}{0.02} \tag{3.13}$$

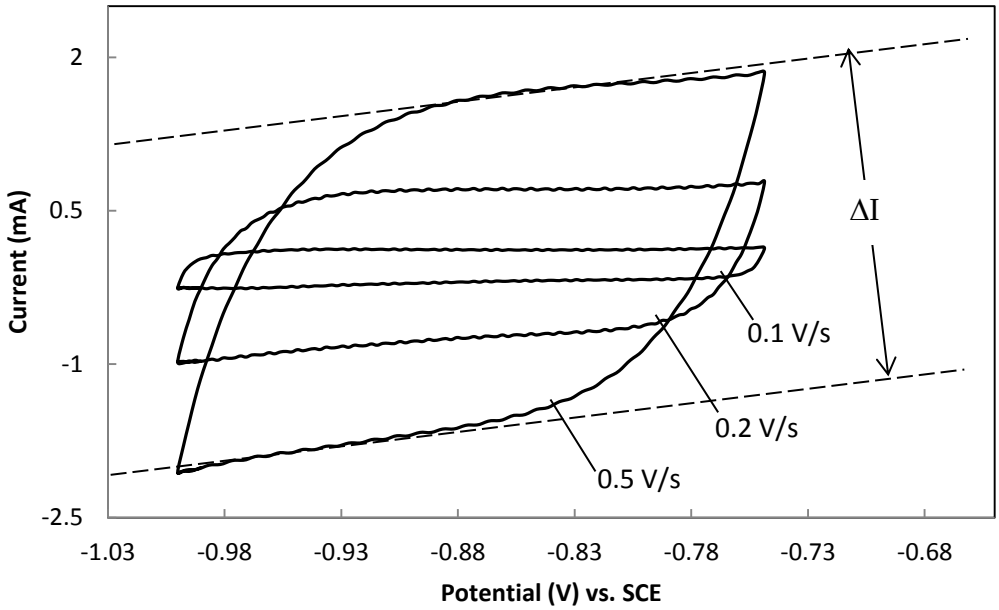

***Fig. 3.13**, Voltammograms of a porous Cu sample in the non-Faradaic region with different scan rates.*

3.6 Measurement of Mass Transfer Coefficient by Linear Sweep Voltammetry

Mass transfer is a very important factor for electrochemical performance of electrodes because the electrochemical reaction rate is often limited by it. In this project, the mass transfer coefficients in the porous Ni samples with different pore sizes and porosities were measured in a flow cell by linear sweep voltammetry (LSV). The LSV experiment was used to measure the limiting current in the test sample, which was then used to obtain the mass transfer coefficient.

3.6.1 Experimental Apparatus

The mass transfer coefficient measurement of LCS porous nickel was implemented by measuring the limiting current in a flow cell as shown in Fig. 3.14. A computerized potentiostat (Autolab PGSTAT101) was used to control the potential in the LSV experiment. The electrolyte was forced to flow through the porous nickel working electrode (Fig. 3.14 e) by a peristaltic pump (Masterlex L/S Computer-Compatible Digital Pump)

(Fig. 3.14 b) from the electrolyte reservoir (Fig. 3.14 a) and exhausted by a solution outlet (Fig. 3.14 i). A saturated calomel electrode (SCE) and a platinum coil were used as the reference electrode (Fig. 3.14 f) and the counter electrode (Fig. 3.14 g), respectively. The measurement of the limiting current was carried out by the potentiostat (Fig. 3.14 h). In the experiment, the porous Ni sample (Fig. 3.14 j) was cut into a disc 6 mm in diameter and 5 mm in length. The sample was placed in a heating shrink tubing (Fig. 3.14 k) which was in turn connected with an acrylic tube (Fig. 3.14 m) and sealed by water proof heating tubing with glue (Fig. 3.14 n) to prevent it from liquid leakage. The sample (working electrode) was connected to the potentiostat by a nickel wire (Fig. 3.14 l).

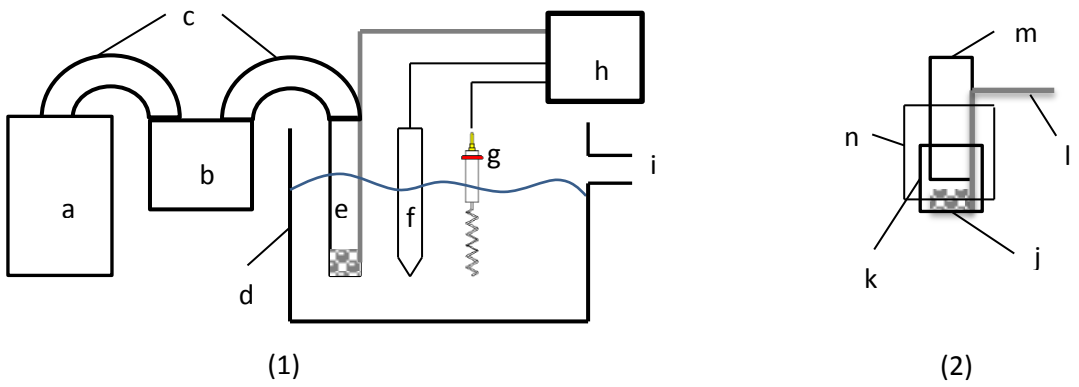

***Fig. 3.14**, Flow electrolytic cell. (1) Schematic diagram of complete apparatus: (a) solution reservoir, (b) pump, (c) pipes, (d) beaker, (e) working electrode, (f) reference electrode, (g) counter electrode, (h) potentiostat and (i) solution outlet. (2) Schematic diagram of working electrode: (j) porous nickel sample, (k) heating shrink tubing, (l) nickel wire, (m) acrylic tube and (n) water proof heating shrink tube with glue.*

3.6.2 Test Procedure

In the experiment, the porous Ni samples with different pore sizes and porosities were cut and ground into discs with the diameter of 0.6 cm and the thickness of 0.5 cm. They were soaked and rinsed in distilled water to obtain a clean surface. The disc was fixed into the end of the Acrylic tube as shown in Fig. 3.14.

The mass transfer coefficient was measured in an electrolyte of 1 M Na_2CO_3, 1 mM $K_3Fe(CN)_6$ and 1 mM $K_4Fe(CN)_6$. The Oxygen in the electrolyte was removed by bubbling Nitrogen before the implementation of the measurement. The LSV was carried out between 0.2 V and -1.1 V vs. SCE at a linear potential sweep rate of 5 mV/s. A series of flow rates (from 0.24 mL/s to 2.8 mL/s) were used to investigate the influence of flow conditions.

Fig. 3.15 shows a typical current vs. potential curve for the reduction of $Fe(CN)_6^{3-}$ ion at the nickel electrode. Three characteristic zones, mixed controlled region, mass transfer controlled region and hydrogen evolution region, can be clearly distinguished in the voltammogram (Fig. 3.15). In the mass transfer controlled region, the current is not changed by the potential and has a fixed value. This fixed current value is called the limiting current. In Fig. 3.15, the mass transfer controlled region occurred in the potential range between -0.35 V to -0.95 V. The fluctuation of the current value was due to the vibration of the fluid from the peristaltic pump. Therefore, the limiting current (I_L) was obtained by the average value of current in the mass transfer controlled region. The mass transfer coefficient, *k*, can be calculated by (Recio et al. 2013):

$$kA = \frac{I_L}{nFc} \tag{3.14}$$

where *A* is the geometric surface area of electrode, *n* is the number of electrons exchanged in the reaction, *F* is the Faraday constant and *c* is the bulk concentration of the electrolyte.

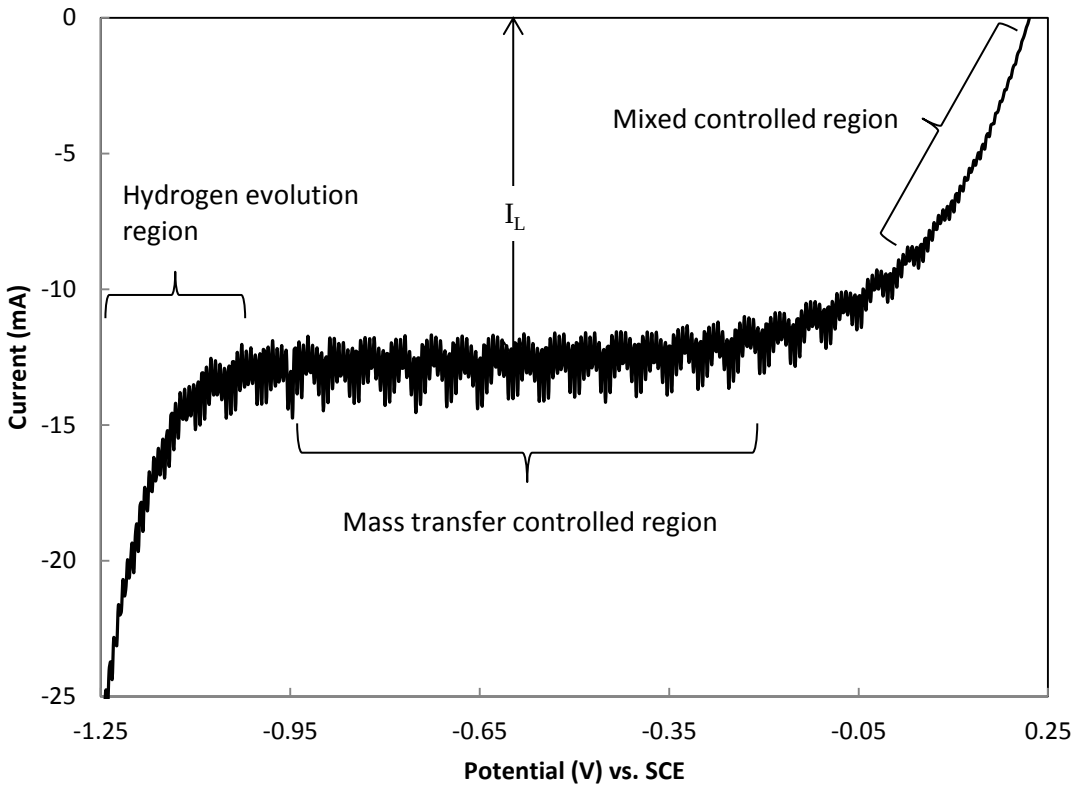

***Fig. 3.15**, Typical linear sweep voltammogram of porous Ni in the mass transfer measurement.*

Chapter 4 Structural Characteristics of Porous Metals

4.1 Particle Sizes of Metal and K_2CO_3 Powders

Fig. 4.1 shows the particle size distributions of the copper and nickel powders measured by a particle size analyser (Malvern Mastersizer 2000). The copper powder has a relatively broad particle size distribution. Most copper particles are in the range of 60-100 μm. The Ni powder has finer particles in the range of 20-40 μm and contains some smaller nickel particles (<5 μm).

In the general linking of particle size distribution, it is advised to use some form of weighted mean diameter which relate to the parameters of interest in the property function in the application, for example, weighted mean particle diameter is used in the applications where the surface area is the determining factor (Merkus 2009).

Table 4.1 lists the surface and volume weighted mean particle diameters of the Cu and Ni powders. The surface weighted mean diameter, *D[3,2]*, is determined by (Merkus 2009):

$$D[3,2] = (\sum n_i D_i^3)/(\sum n_i D_i^2) \tag{4.1}$$

D[3,2] is used in the geometric, electro-active and real surface areas estimations of the porous Cu and Ni.

The volume weighted mean diameter, *D[4,3]*, is determined by (Merkus 2009):

$$D[4,3] = (\sum n_i D_i^4)/(\sum n_i D_i^3) \tag{4.2}$$

D[3,2] is useful for applications where the volume is the determining factor, e.g., the measurement of tortuosity.

The surface and volume weighted mean particle diameters are 72 μm and 109 μm, respectively, for the Cu particles and 20 μm and 25 μm, respectively, for the Ni particles.

***Table 4.1**, Surface and volume weighted mean particle sizes of the Cu and Ni powders.*

Metal	**Surface weighted mean diameter, *D[3,2]* (μm)**	**Volume weighted mean diameter, *D[4,3]* (μm)**
Copper	72	109
Nickel	20	25

Figs. 4.2 (a-e) show the particle size distributions of the K_2CO_3 powder sieved in the particle size ranges of 1000-1500 μm, 710-1000 μm, 425-710 μm 250-425 μm and 75-150 μm. The particle sizes measured by the particle size analyser are different from those classed by the sieve. The particle size ranges measured by the particle size analyser are 500-1500 μm, 400-1200 μm, 300-900 μm, 200-600 μm and 70-250 μm, for the sieve classed sieve ranges of 1000-1500 μm, 710-1000 μm, 425-710 μm, 250-425 μm and 75-150 μm, respectively. Table 4.2 shows the surface and volume weighted mean particle diameters of the K_2CO_3 powders in different particle size ranges classed by a sieve. For the sieve classed particle size ranges of 1000-1500 μm, 710-1000 μm, 425-710 μm, 250-425 μm and 75-150 μm, the surface weighted mean particle diameters are 1290 μm, 936 μm, 623 μm, 341 μm and 122 μm, respectively, and the volume weighted mean particle diameters are 1500 μm, 1010 μm, 653 μm, 367 μm and 134 μm, respectively.

Table 4.2, *Surface and volume weighted mean particle sizes of the potassium carbonate powder.*

Particle size range (μm)	**Surface weighted mean diameter, *D[3,2]* (μm)**	**Volume weighted mean diameter, *D[4,3]* (μm)**
1000-1500	1290	1500
710-1000	936	1010
425-710	623	653
250-425	341	367
75-150	122	134

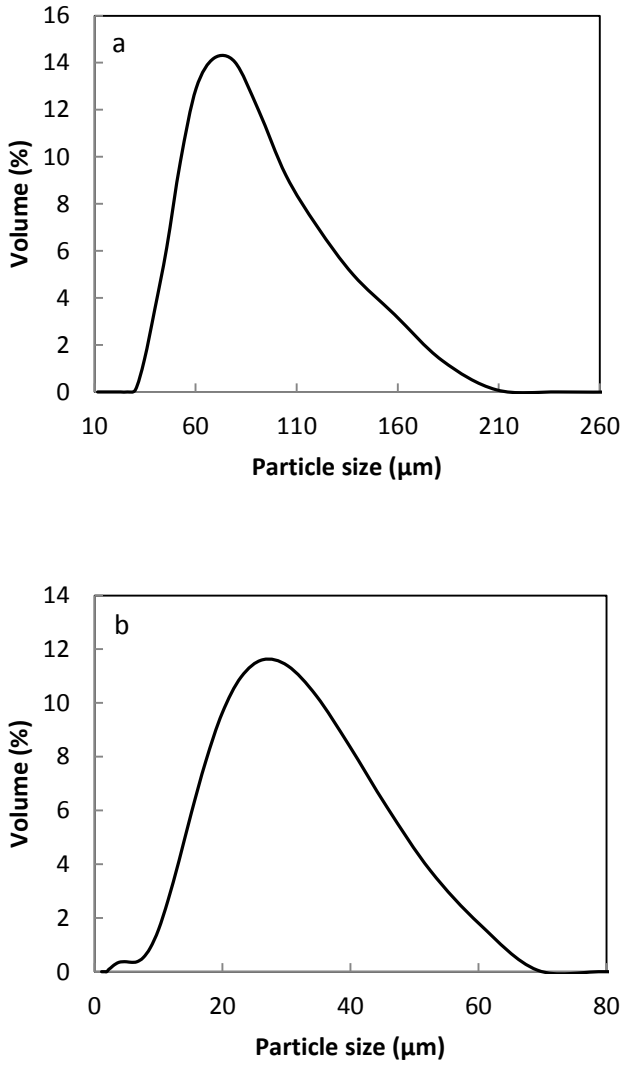

Fig. 4.1*, Particle size distributions of (a) copper powder and (b) nickel powder measured by Malvern Mastersizer 2000.*

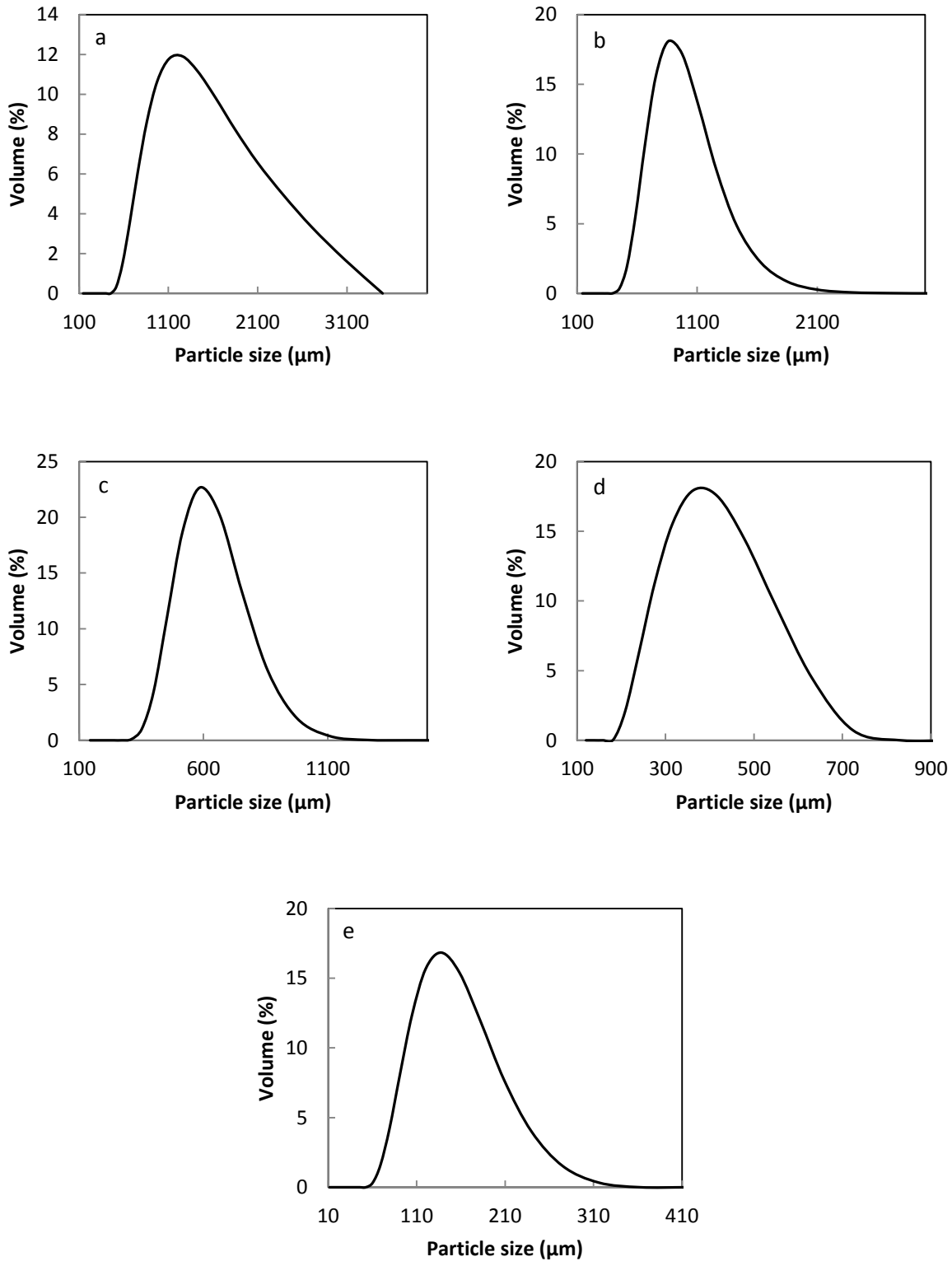

***Fig. 4.2**, Particle size distributions of the potassium carbonate powder in the particle size ranges of (a) 1000-1500 µm, (b) 710-1000 µm, (c) 425-710 µm, (d) 250-425 µm and (e) 75-150 µm, measured by Malvern Mastersizer 2000.*

4.2 Pore Structure

Fig. 4.3 shows the typical porous structure of the porous Cu samples, obtained by SEM (JSM-6610). The large pores (primary pores) are negative replicas of the K_2CO_3 particles and are largely spherical, as shown in Fig. 4.3 (a) and (b). The primary pores are all interconnected to form an open cell network. Fig. 4.3 (b) also shows that the cell walls are formed by the sintering of Cu particles and have a structure characteristic of sintered materials, i.e., metal particles connected by sintering necks and interspersed with micro-voids (secondary pores). The particle size of the Cu powder particles is relatively uniform and most Cu particles detected by SEM have particle sizes in 70-80 μm. Fig. 4.3 (c) shows the sintering necks between the Cu particles.

Fig. 4.4 shows the typical porous structure of the porous Ni samples, obtained by SEM (JSM-6610). As well the porous Cu samples, the large pores (primary pores) are negative replicas of the K_2CO_3 particles and form an open cell network as shown in Fig. 4.4 (a) and (b). The cell walls are formed by the sintering of the nickel particles. However, the nickel particles have mixed particle sizes from 2 μm to 60 μm as shown in Fig. 4.4 (c). The mixed particle sizes decreased the size and volume of the secondary pores (formed by the interstices and micro-voids interspersed in the cell walls) in porous Ni.

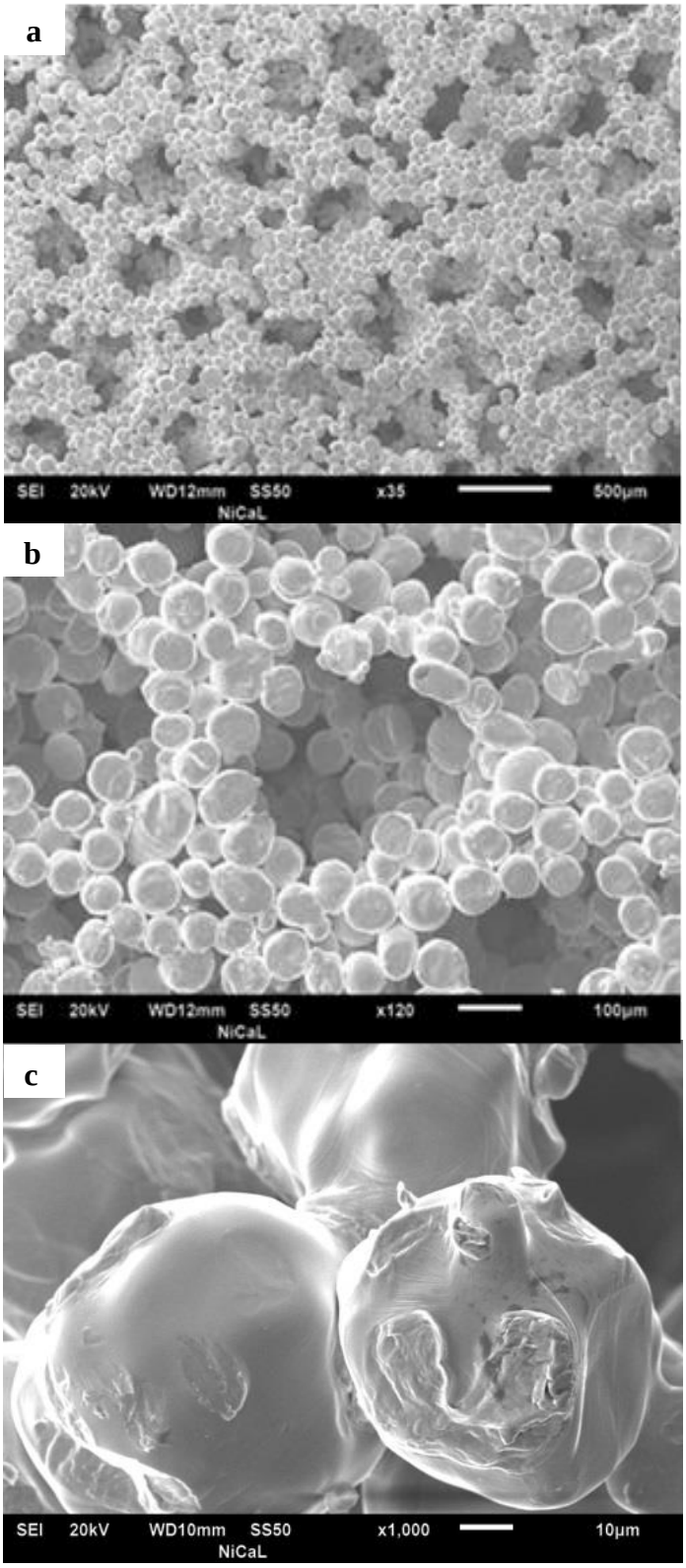

***Fig. 4.3**, Microstructure of porous Cu: (a) a global view, (b) morphology of pores and cell walls, and (c) sintering necks between copper particles.*

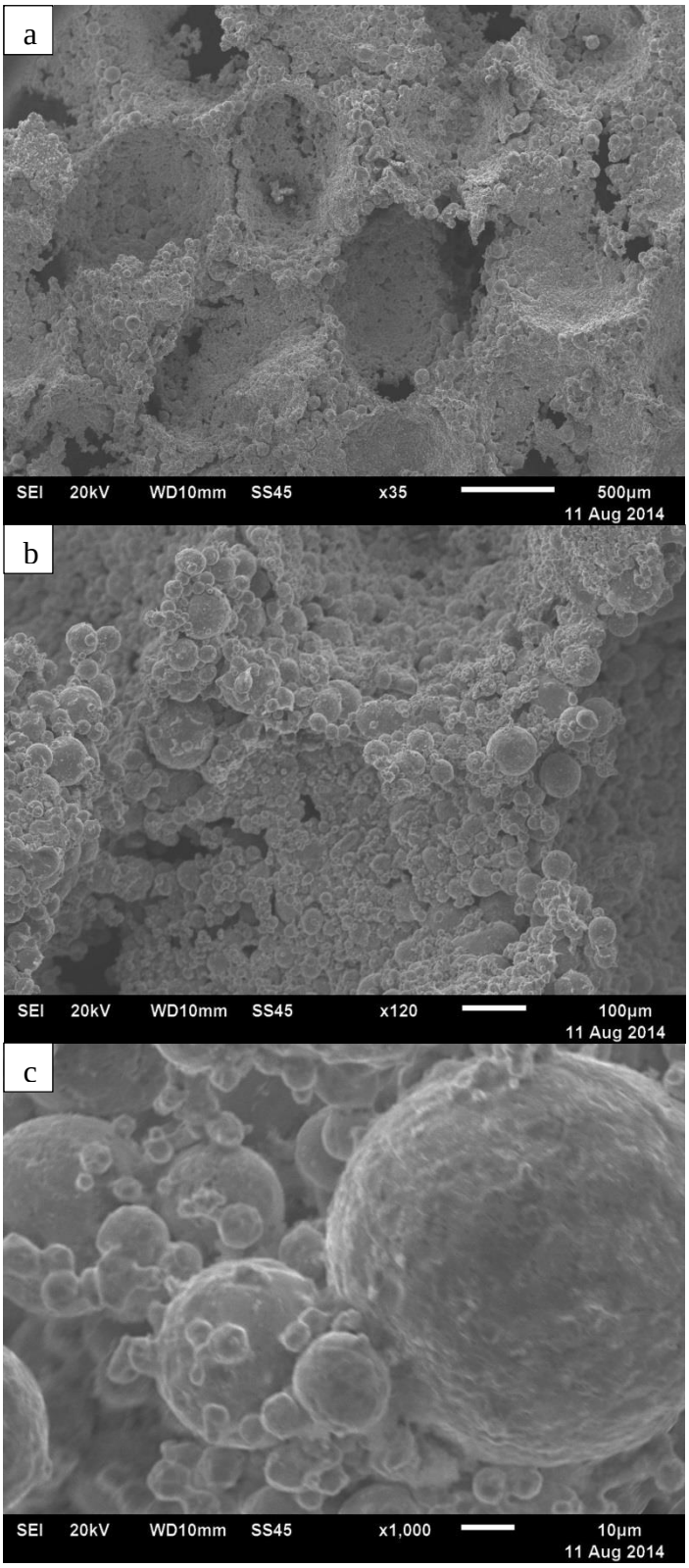

***Fig. 4.4**, Microstructure of porous Ni: (a) a global view, (b) morphology of pores and cell walls, and (c) sintering necks between nickel particles.*

4.3 Porosity

Table A4.3 (see Appendixes) shows the dimensions and porosities of the porous Cu samples with different pore size and porosity (Cu01 to Cu30) used for electro-active and real surface area measurements. Table A4.4 (see Appendixes) shows the dimensions and porosities of the porous Cu samples with different pore size and porosity (S01 to S20) used for geometric surface area and primary porosity measurements. Table A4.5 (see Appendixes) shows the dimensions and porosities of the porous Ni samples with different pore size and porosity (Ni01 to Ni24) used in the measurements of geometric surface area, primary porosity, electro-active surface area and real surface area. Table A4.6 (see Appendixes) shows the porosities of the porous Cu samples with different pore size and porosity (T01 to T18) used in the tortuosity measurement. Porous Cu samples T01 to T18 were cut by EDM and have the same dimensions: 4.8 cm in diameter and 1 cm in thickness. The porosities of all the samples shown in Tables A4.3-A4.6 (see Appendixes) were determined by measuring their densities.

4.4 Purity of Metal Matrix

Energy-dispersive X-ray spectroscopy (EDX) investigations were conducted on a porous Cu sample and a porous Ni sample to analyse their compositions.

Fig. 4.5 shows the EDX results acquired from the porous Cu sample surface without cleaning. In general a high level of Cu can be detected with a smaller amount of oxygen (about 6.83%), because the copper would have been oxidized in air. In order to reduce the effect of oxide on the electrochemical experiments, the porous Cu samples were cleaned in 10% HCl by ultrasonic treatment to remove the copper oxide on the surface. Fig. 4.6 shows the EDX results acquired from the porous Cu sample surface after it had been washed in 10% HCl. It shows that the copper oxide had been completely removed and a surface of a high level purity of Cu was obtained.

Fig. 4.7 shows the EDX results acquired from the surface of a porous Ni sample cleaned by distilled water. It shows that high purity of nickel was obtained on the surface of the sample. Nickel is highly corrosion resistant and is not easy to oxidize. Therefore, the porous Ni sample soaked and rinsed in distilled water was sufficient to obtain a clean surface.

The minimum detection limit for the elements can be achieved is about 0.1% using EDX (Goodhew et al. 2001). However, the minimum detection limit also depends on the material. For particles and rough surfaces, the error in the EDX can be up to 5%. Therefore, some trace contaminants, such as K, C and Cl, which would be left in the manufacturing process, cannot be detected by EDX. The trace contaminant of K on the porous Cu surface is much lower than the element of K in the electrolyte (0.1 mol/L KOH). The trace contaminants of C and Cl are not reacted in the electrochemcial experiments. Therefore, traces contaminants will not affect the experiments.

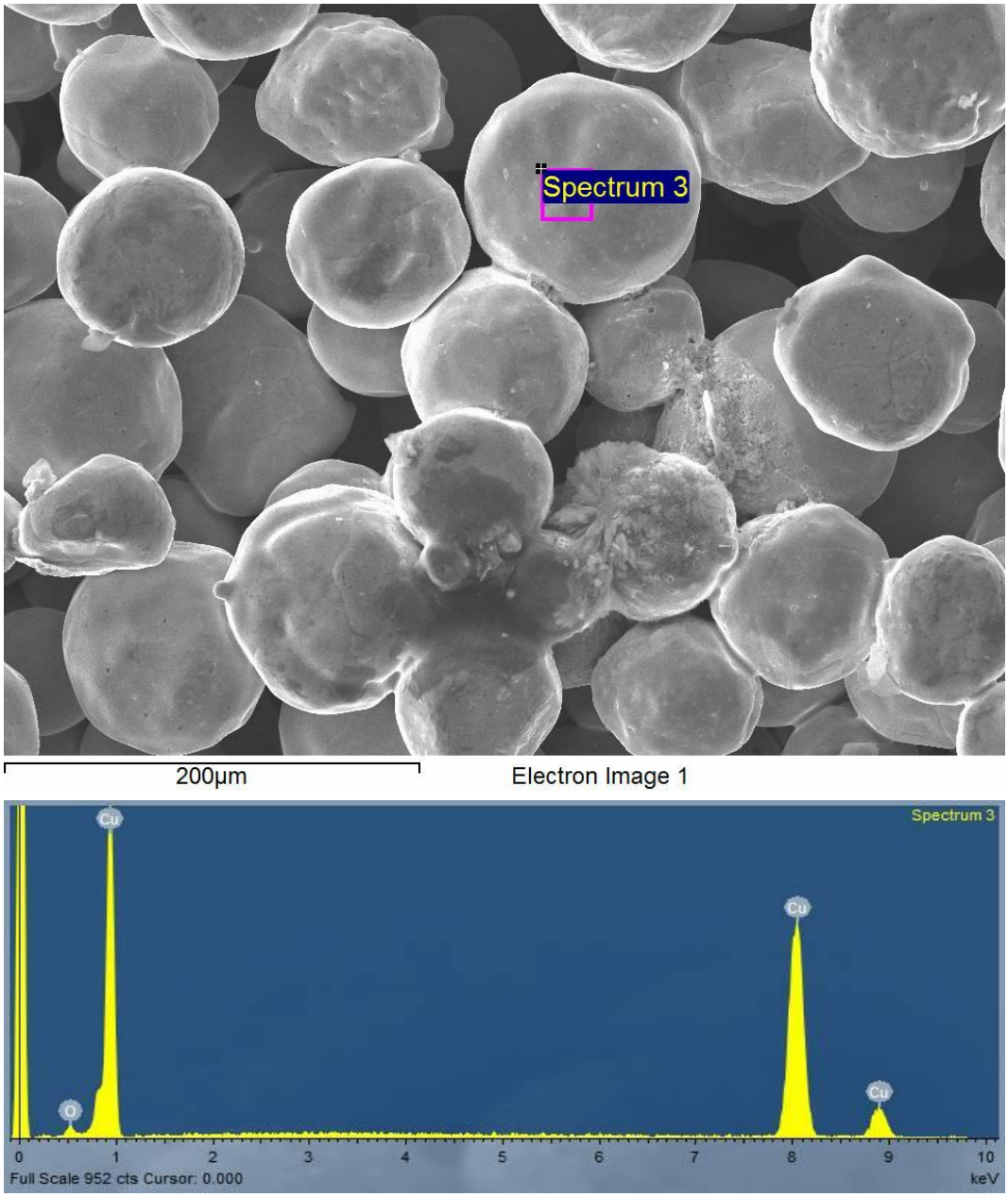

***Fig. 4.5**, EDX spectrum of the surface of a porous copper sample before washed by 10% HCl.*

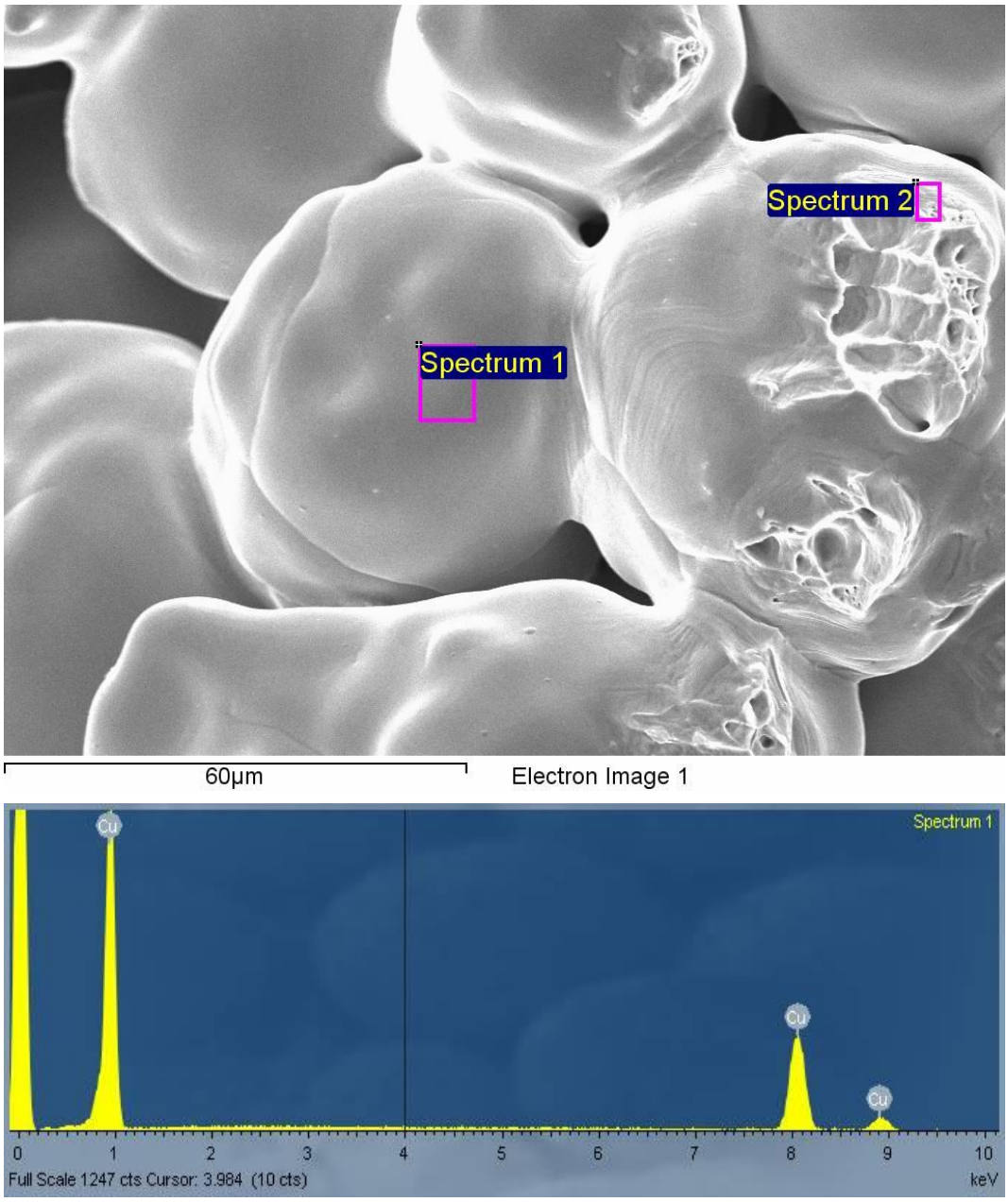

***Fig. 4.6**, EDX spectrum of the surface of the porous copper sample after washed by 10% HCl.*

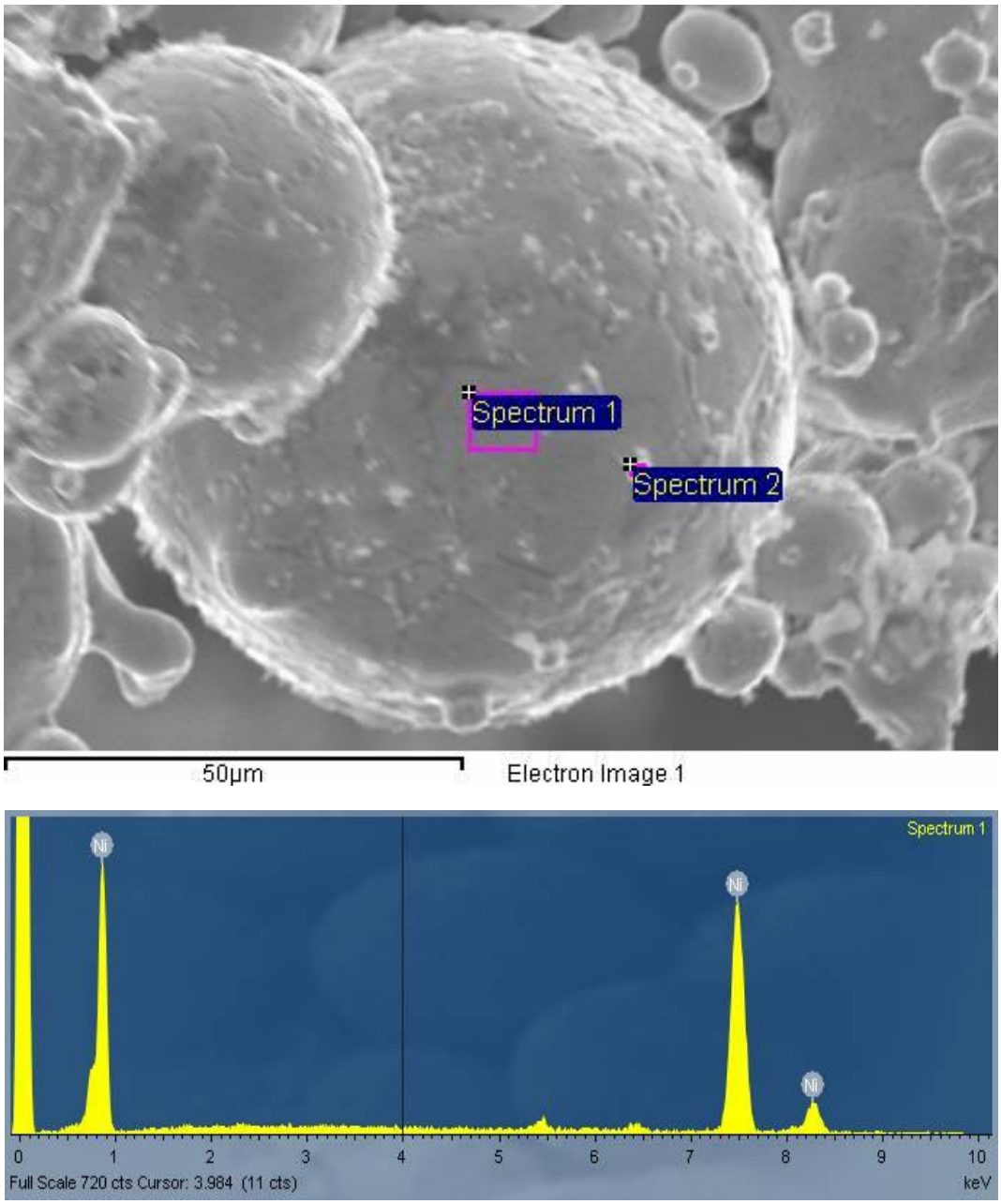

Fig. 4.7, EDX spectrum of the surface of a porous nickel sample.

4.5 Primary Porosity

The primary porosities of porous Cu and Ni samples with different pore size and porosity (S01 to S20 and Ni01 to Ni24) determined by QS are listed in Tables A4.7 and A4.8 (see Appendixes), respectively.

Different from total porosity, the primary porosity of porous metals is the porosity contributed by the primary pores only. In Fig. 3.5, for example, the micrograph shows the primary pores clearly. In QS method, the primary porosity, ε_p, was represented by the point fraction, $P_P = P_{pore}/P_{total}$, for the primary pores, ignoring the secondary pores, and was calculated from Eqn. 3.6. P_{pore} is the number of points (the cross points of the gridlines on the micrograph as shown in Fig. 3.5) falling in the primary pores in the test area and P_{total} is the total points in the test area which was 180. Column 4 in Tables A4.7 and A4.8 (see Appendixes) show the numbers of the testing points falling in the primary pores in the porous Cu and Ni samples, respectively.

The variations of the ratio between primary porosity (ε_P) and total porosity (ε) of porous Cu and Ni samples as a function of porosity and pore size are shown in Fig. 4.8. The total porosity (ε) was determined by their densities. For porous Cu, in the porosity range 0.59-0.75 and pore size range 250-1500 μm, $\varepsilon_P/\varepsilon$ increased with porosity and decreased with pore size. In other words, the total porosity of the samples with low porosity and large pore size have more contributions from secondary pores. The error of the sample with small pore size (250-425 μm) is higher than other samples. It is because it is hard to separate some of secondary pores from primary pores in the samples with small pore size. For porous Ni, in the porosity range 0.62-0.81 and pore size range 250-1500 μm, the primary porosities of these samples are only slightly lower than their total porosities. The $\varepsilon_P/\varepsilon$ did not change

with porosity or pore size. The contribution of secondary pores to the total porosities is small.

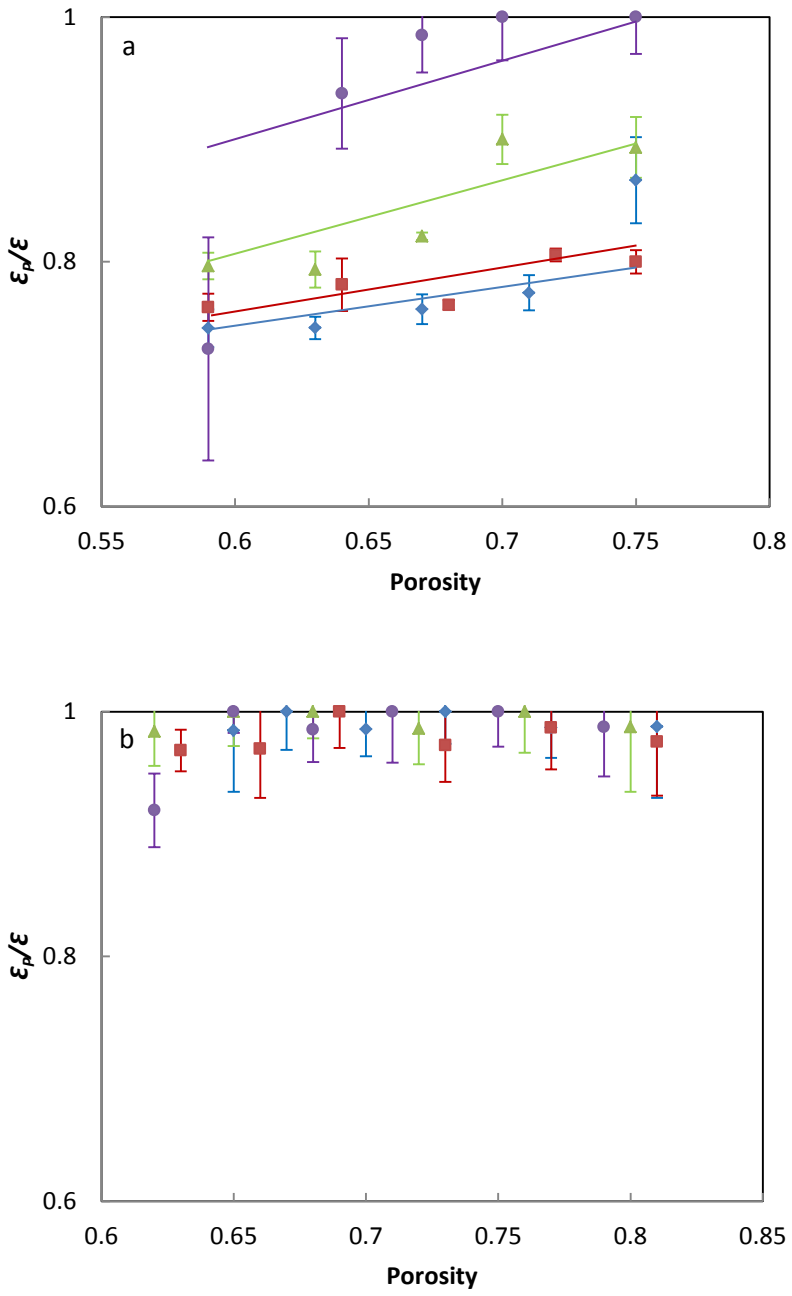

***Fig. 4.8**, Variations of the ratio between primary porosity (ε_p) and total porosity (ε) for (a) porous Cu and (b) porous Ni with porosity at different pore sizes (● 250-425 µm, ▲ 425-710 µm, ■ 710-1000 µm, ◆ 1000-1500 µm).*

4.6 Primary and Secondary Porosities

Two kinds of pores are formed in the LCS porous metal, primary and secondary pores. The primary pores are the large pores in the porous metal formed by the removal of K_2CO_3 particles. They are randomly distributed in the metal matrix, interconnected through small windows and form an open cell network. The primary pores are negative replicas of the potassium carbonate particles, so their shapes, sizes and quantity are well defined and are the same as the leachable K_2CO_3 particles, in the range of 75-1500 μm. The secondary pores are the small interstices or voids between the metal particles resulting from partial sintering. The sizes of the secondary pores are just several to ten odd microns. The separation of primary and secondary pores can be made by an optical microscope. At a low magnification (200 ×), only primary pores can be clearly observed on the optical micrographs and the primary porosity, contributed by the primary pores, can be obtained by the QS method.

The secondary porosity contributed by the secondary pores, ε_S, can be obtained by:

$$\varepsilon_S = \varepsilon - \varepsilon_P \tag{4.1}$$

where ε is total porosity (measured by the density of the sample) and ε_P is primary porosity.

Tables A4.9 and A4.10 (see Appendixes) show the values of secondary porosity, ε_S, in the porous Cu and prous Ni samples, respectively. The variations of the ratio of secondary porosity to total porosity as a function of total porosity of porous Cu and porous Ni samples with different pore sizes are shown in Fig. 4.9. For porous Cu, $\varepsilon_S/\varepsilon$ decreased with porosity and increased with pore size. The effect of porosity and pore size on $\varepsilon_S/\varepsilon$ can be explained by the relative quantities of Cu particles in the interior and exterior regions in the solid matrix. With the increase of porosity and decrease of pore size, more Cu particles are located in the surface region and the number of Cu particles residing in the interior region is

reduced. Therefore, more Cu particles contribute to the formation of primary pores and their contribution to the secondary porosity decreases. However, this situation only happens if the metal particles are large and have a uniform size.

For porous Ni, $\varepsilon_S/\varepsilon$ was very small and did not change with porosity or pore size significantly. This is because the porous Ni samples were produced from a Ni powder with small and mixed particle sizes. The small Ni particles can fill into the interstices or voids between the bigger Ni particles and reduce the volume of the secondary pores.

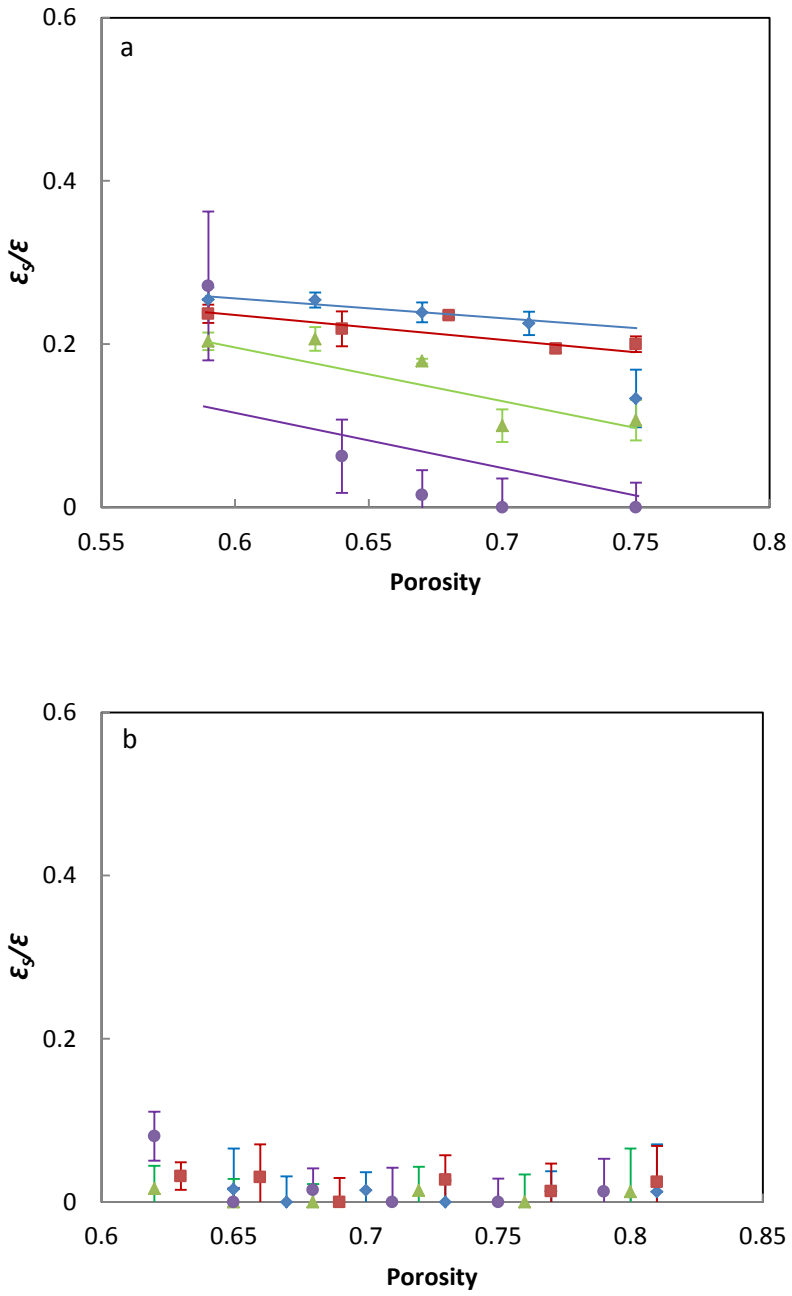

***Fig. 4.9**, Variations of the ratio between secondary porosity (ε_s) and total porosity (ε) with total porosity of (a) porous Cu and (b) porous Ni with different pore sizes (● 250-425 µm, ▲ 425-710 µm, ■ 710-1000 µm, ◆ 1000-1500 µm).*

Chapter 5 Tortuosity of Porous Cu

5.1 Standard Diffusion Coefficient of NaCl

In the diaphragm cell for the tortuosity by measurement, filter papers were used to cover both sides of the porous sample to prevent forced flow within the sample caused by the stirring bars in the compartments. However, the thin filter papers could not stop the forced flow between the two compartments and the thick filter papers would reduce the flux diffusing through the sample, effectively reducing the diffusion coefficient.

In order to analyse the effect of the filter paper on the diffusion coefficient, initial experiments were carried in a 5 cm inner diameter and 1 cm length acrylic tube to measure the diffusion coefficient without any sample. Both sides of the tube were covered by either one piece or two pieces of No.1 filter paper. Table 5.1 shows that the experimental values of the diffusion coefficient (D) of NaCl in an open channel for one piece of No.1 filter paper and two pieces of No.1 filter paper are 2.023×10^{-5} cm^2/s and 1.474×10^{-5} cm^2/s, respectively.

When one piece of No.1 filter paper was used, the diffusion coefficient was much higher than the standard diffusion coefficient of NaCl in water, which is 1.481×10^{-5} cm^2/s (Riquelme et al. 2007). It seems that one piece of filter paper cannot prevent the forced flow in the channel. When two pieces of filter paper were used, the measured diffusion coefficient was close to the reference value. It means that the solute (NaCl) passed through the channel mainly by diffusion. Therefore, in the measurements, two pieces of No.1 filter paper were used to cover both sides of the circular disc porous Cu samples.

Table 5.1, *Diffusion coefficient (D) of NaCl obtained using one piece and two pieces of No.1 filter paper.*

	V_t (cm^3)	V_b (cm^3)	$c_{t,t}$ (mol/L)	$c_{b,t}$ (mol/L)	D (cm^2/s)
One piece	114.08	111.20	0.31	1.26	2.023×10^{-5}
Two pieces	114.08	111.20	0.19	1.31	1.474×10^{-5}

5.2 Tortuosity of Porous Cu Samples

In the determination of the tortuosity of the porous Cu samples, 1.481×10^{-5} cm^2/s was used as the standard diffusion coefficient of NaCl (1.75mol/L, 25°C). The measured values of the molar concentration of the solutions in the top ($c_{t,t}$) and bottom ($c_{b,t}$) compartments are listed in Table A5.2 (see Appendixes). The tortuosity values of the porous Cu samples with different pore sizes (250-1500 μm) and porosities (0.56-0.84) were calculated from Eqn. 3.7 and are listed in Table A5.2 (see Appendixes).

The variations of tortuosity as a function of porosity and pore size are shown in Fig. 5.1. In the porosity range 0.56-0.84 and pore size range 250-1500 μm, the tortuosity is in the range of 1.33-1.78. In general, the tortuosity of the porous Cu increased with pore size and decreased with porosity. A good linear relationship between tortuosity and porosity can be obtained when the samples have the same pore size.

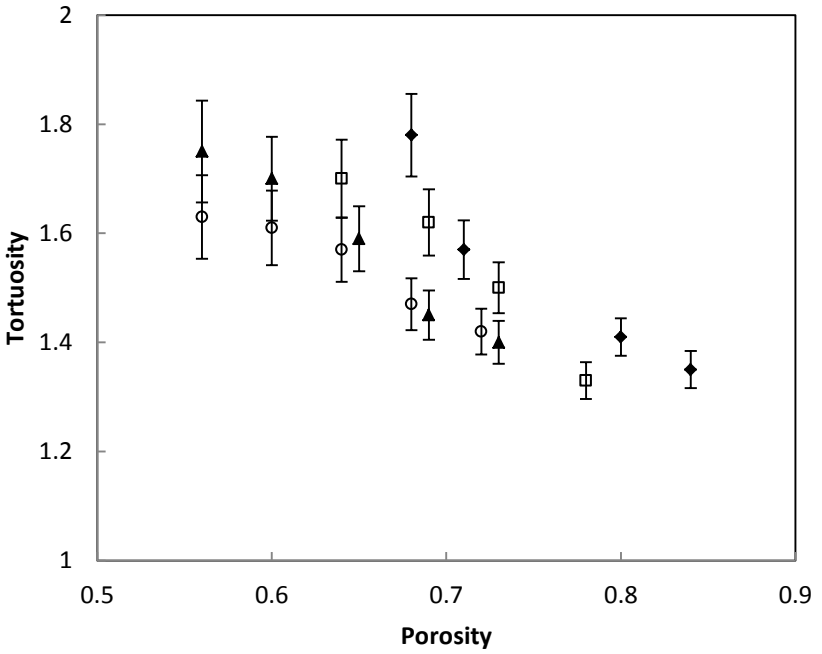

***Fig. 5.1**, Variations of tortuosity with porosity for samples with different pore sizes: (○ 250-425 µm, ▲ 425-710 µm, □ 710-1000 µm, ◆ 1000-1500 µm).*

5.3 Uncertainty Analysis

The tortuosity of porous Cu was determined by measuring the flux of NaCl diffusing through the sample in a diaphragm cell. The flux was obtained from the measurement of the concentrations of the solutions in the top and bottom compartments. The errors in the concentration measurements would affect the accuracy of the determination of the tortuosity. Therefore, it is essential to analyse the uncertainties in the concentration and tortuosity measurements.

In error and uncertainty analysis, arithmetic mean, deviation and standard deviation are usually used for statistical analysis of experimental data obtained by a large number of measurements (may be > 20) (Holman 2001). In the measurement of tortuosity, however, a sample needs to be tested for at least three days to obtain an acceptable accuracy. Due to the time constraint, the quantity of data obtained for one sample is very limited. Therefore, propagation of uncertainty is used to estimate the uncertainty in the experimental results.

In the analysis of the propagation of uncertainty (Kline & McClintock 1953), a result R is a given function of the independent variables x_1, x_2, x_3,…, x_n. Thus,

$$R = R(x_1, x_2, x_3, \dots, x_n) \tag{5.1}$$

If ω_1, ω_2, ω_3,…, ω_n are the uncertainties in the independent variables x_1, x_2, x_3,…, x_n, respectively, the uncertainty in the result can be expressed by (Kline & McClintock 1953):

$$\omega_R = [(\frac{\partial R}{\partial x_1}\omega_1)^2 + (\frac{\partial R}{\partial x_2}\omega_2)^2 + \cdots + (\frac{\partial R}{\partial x_n}\omega_n)^2]^{1/2} \tag{5.2}$$

Let us first analyse the error in the preparation of the initial solution (1.75 mol/L NaCl). The molar concentration of the solution, c, can be expressed by:

$$c = \frac{M}{58.44 \times V} \tag{5.3}$$

where M is the weight of NaCl, V is the volume of the salt water and 58.44 g/mol is the molar mass of NaCl. The uncertainty of molar concentration (ω_c) can be obtained by:

$$\omega_c = [\left(\frac{\partial c}{\partial M}\omega_M\right)^2 + (\frac{\partial c}{\partial V}\omega_V)^2]^{1/2} \tag{5.4}$$

where ω_M is the uncertainty in weighing the NaCl mass (±0.01 g) and ω_V is the uncertainty in volume measurement of the solution (±0.005 L). As 71.59 g NaCl was weighed and added to 0.7 L water in a 700 ml beaker, the uncertainty of the molar concentration (ω_c) was 0.0125 mol/L in the preparation of the initial aqueous salt solution.

The uncertainty of the initial concentration difference between the top ($c_{t,i}$) and bottom ($c_{b,i}$) compartments can be expressed by:

$$\omega_{c_{b,i}-c_{t,i}} = [{\omega_{c_{b,i}}}^2 + {\omega_{c_{t,i}}}^2]^{1/2} \tag{5.5}$$

Beacuse the initial solution in the top compartment was pure distilled water, $c_{t,i}$ is 0 mol/L and the uncertainty $\omega_{c_{t,i}}$ is also 0. Therefore, the uncertainty of the initial concentration difference was ±0.0125 mol/L.

The uncertainty of the molar concentration difference between the top and bottom compartments after the completion of the measurements can also be obtained in the same manner. The concentration differences ($c_{b,t}$-$c_{t,t}$) and their uncertainties are listed in Table. A5.3 (see Appendixes). The uncertainties in the concentration differences after completion of measurements were around ±0.03 mol/L.

The tortuosity was calculated by:

$$\tau^2 = \frac{DAt(\frac{1}{V_t}+\frac{1}{V_b})}{L\times\ln(\frac{c_{b,i}-c_{t,i}}{c_{b,t}-c_{t,t}})} \tag{5.6}$$

where D is the standard diffusion coefficient of NaCl (1.481×10^{-5} cm^2/s), A is the cross-sectional area of the sample, t is time, L is the thickness of the sample, V_t and V_b are the volumes of the top and bottom compartments, respectively. All these constants are fixed in the experiment, so their uncertainties are negligible. Each experiment was carried out for 3 days and the error for time, t, was controlled within 10 minutes (259200±600 s).

For the purpose of uncertainty analysis Eqn. 5.7 can be simplified as:

$$\tau^2 = \frac{\alpha t}{ln} \tag{5.7}$$

where α is the product of the constants (D, A, $1/V_t$, $1/V_b$ and $1/L$), t is time, and ln is used to represent $ln[(c_{b,i}-c_{t,i})/(c_{b,t}-c_{t,t})]$.

The uncertainty of natural logarithm of the concentration difference ratio can be expressed by (Harris 2003):

$$\omega_{\ln[(c_{b,i}-c_{t.i})/(c_{b,t}-c_{t,t})]} = \frac{\omega_{[(c_{b,i}-c_{t.i})/(c_{b,t}-c_{t,t})]}}{(c_{b,i}-c_{t.i})/(c_{b,t}-c_{t,t})} \quad (5.8)$$

The values of the uncertainties for different samples are listed in Table A5.3 (see Appendixes).

Based on Eq. 5.7, the uncertainty of τ^2 can be expressed by:

$$\omega_{\tau^2} = \sqrt{(\frac{a}{ln}\omega_t)^2 + (-\frac{at}{ln^2}\omega_{ln})^2} \quad (5.9)$$

and the uncertainty of tortuosity (ω_τ) can be expressed by:

$$\omega_\tau = \sqrt{(\frac{1}{2} \times (\tau^2)^{\frac{1}{2}} \times \omega_{\tau^2})^2} \quad (5.10)$$

The values of uncertainties of tortuosity in the porous Cu samples are listed in Table A5.3 (see Appendixes). The uncertainties of the tortuosity values are around 2.5% to 4.7% in the experiments.

Fig. 5.1 shows the tortuosity as a function of porosity for porous Cu samples with different pore sizes with error bars.

5.4 Effects of Pore Size and Porosity

Koponen et al. (1996) (Koponen, Kataja et al. 1996) obtained an empirical correlation between tortuosity (τ) and porosity (ε) by solving the flow equations for a porosity range from 0.5 to 1 using the Lattice Gas Automata (LGA) method:

$$\tau - 1 = p(1 - \varepsilon) \quad (5.11)$$

where τ is tortuosity, p is a fitting parameter and ε is porosity. When the porosity is 1, there is no metal particle as barrier in the porous metal and the fluid flows through the channel straight so that the tortuosity is 1.

Fig. 5.2 (a) shows the values of (τ-*1*) as a function of (*1*-ε) at different pore sizes. The lines are obtained by fitting the empirical correlation (Eqn. 5.11) between (τ-*1*) and (*1*-ε).

Fig. 5.2 (a) shows that the results obtained in this work agree well with the correlation Eqn. 5.11. The values of the fitting parameter, *p*, obtained from the slopes in Fig. 5.2 (a), increase with pore size as shown in Fig. 5.2 (b). According to the stochastic modelling (section 6.2), the number of K_2CO_3/K_2CO_3 contacts on a single K_2CO_3 particle decreases with pore size. It decreases the length of the channels which formed by pores through the porous metal.

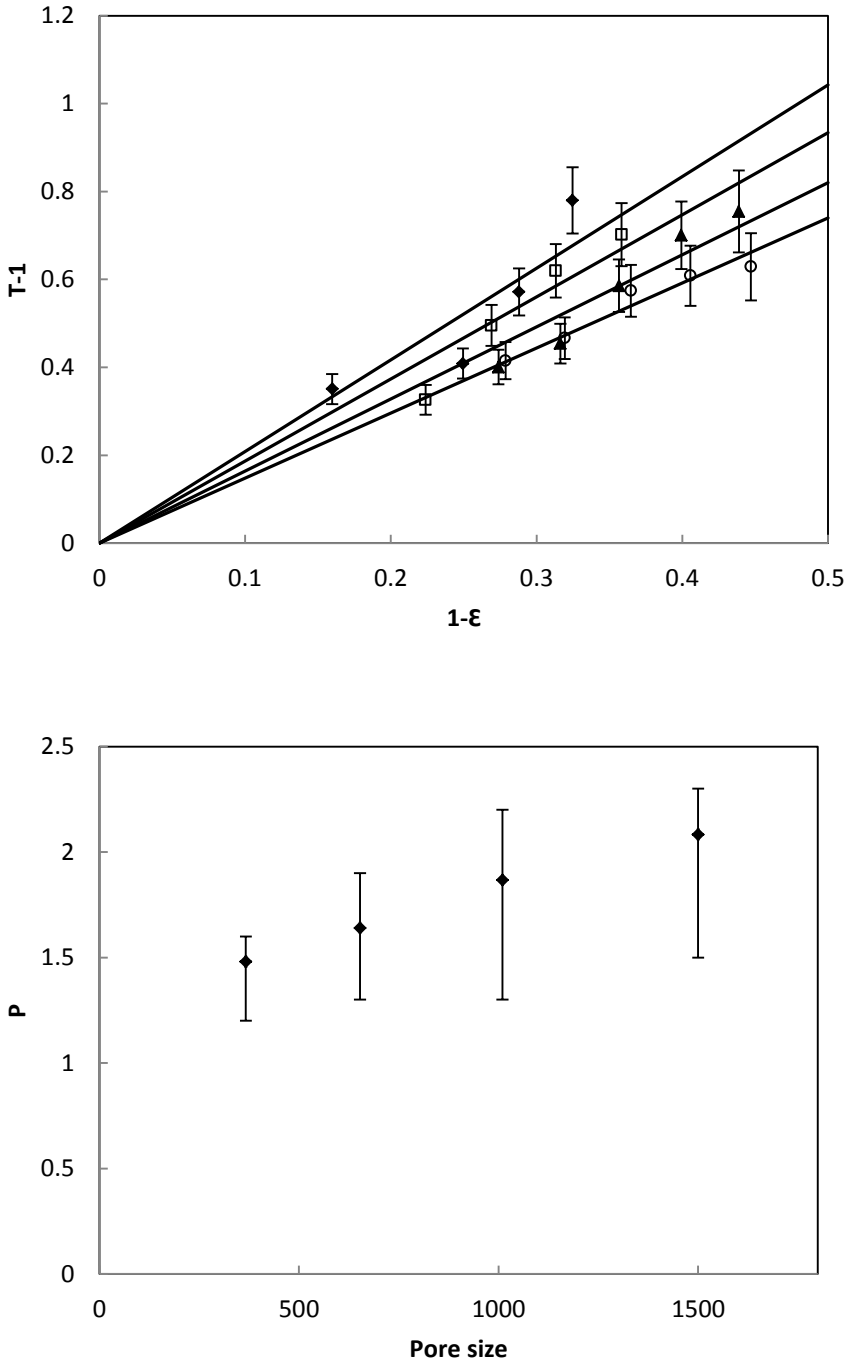

***Fig. 5.2**, (a) Variations of (T-1) with (1-Ɛ) at different pore sizes: (○250-425 µm, ▲425-710 µm, □ 710-1000 µm, ◆ 1000-1500 µm). (b) Variation of fitting parameter, p, with pore size.*

Chapter 6 Geometric Surface Area

6.1 Quantitative Stereology

The geometric surface area of LCS porous metal (Cu and Ni) is only contributed by the primary pores formed by the removal of potassium carbonate particles. It was measured by quantitative stereology (QS) using an optical microscope with a low magnification (×100) in order to remove the effect of secondary pores. The volumetric specific geometric surface area (S_{VG}) of was calculated by the number of intercepts between the grid lines and the pore perimeters of the optical micrograph from Eqn. 3.4. The length of each grid line (L_T) was fixed at 7.2 cm. The gravimetric specific geometric surface area (S_{MG}) of porous Cu samples was converted from S_{VG} by Eqn. 3.5.

The volumetric specific geometric surface area (S_{VG}) and the gravimetric specific geometric surface area (S_{MG}) of porous Cu samples with different pore size and porosity (S01 to S20) are listed in Table A6.1 (see Appendixes). The number of intercepts (P) in the micrograph of each sample was listed in Column 5 of Table A6.1 (see Appendixes). Variations of the S_{VG} and S_{MG} of porous Cu with porosity at different pore sizes are shown in Figs. 6.1 (a) and (b), respectively.

In the porosity range 0.59-0.75 and pore size range 250-1500 μm, the volumetric and gravimetric specific geometric surface areas are in the ranges of 18-88 cm^{-1} and 5-40 cm^2/g, respectively. Both volumetric and gravimetric specific geometric surface areas increase with porosity and decrease with pore size.

The volumetric specific geometric surface area (S_{VG}) and the gravimetric specific geometric surface area (S_{MG}) of porous Ni samples with different pore size and porosity (Ni01 to Ni24) are listed in Table A6.2 (see Appendixes). Variations of the S_{VG} and S_{MG} of porous Ni with porosity at different pore sizes are shown in Figs. 6.3 (a) and (b), respectively.

In the porosity range 0.62-0.81 and pore size range 250-1500 μm, the volumetric and gravimetric specific geometric surface areas of porous Ni are in the ranges of 26-110 cm^{-1} and 8-57 cm^2/g, respectively. Both volumetric and gravimetric specific geometric surface areas increase with porosity and decrease with pore size. Compared to porous Cu, the volumetric specific geometric surface area of porous Ni is less sensitive to porosity.

6.2 Stochastic Modelling

Geometric surface area is the total surface area of the cell walls of the primary pores in the porous sample. Because primary pores are in effect negative replicas of the K_2CO_3 particles used in the fabrication process, geometric surface area can be approximated by the total surface area of the K_2CO_3 particles less the area of the necks formed between the adjacent K_2CO_3 particles.

Zhao (2003) analysed the connectivity of the NaCl particle network in an Al/NaCl compact used for manufacturing porous aluminium by the SDP process. Although the analysis was developed using SDP as an example, it is applicable to all powder metallurgy based space-holder methods, because these methods use the same principle to generate the porous structure. The analysis can be applied directly to LCS by substituting K_2CO_3 for NaCl and Cu or Ni for Al.

The direct contact between two spherical K_2CO_3 particles in the metal/K_2CO_3 preform will form a neck, which will result in a window between the two resultant primary pores in the porous metal sample. The magnitude of the neck depends on the relative sizes of the K_2CO_3 and the metal particles. The area of the sphere crown on the K_2CO_3 particle corresponding to the neck, A_c, can be calculated by (Zhao 2003):

$$A_c = \frac{\pi}{2} d_p^2 \left(1 - \frac{\emptyset+2}{\sqrt{\emptyset^2+6\emptyset+5}}\right) \quad (6.1)$$

where d_p is the diameter of the K_2CO_3 particle (effectively, the pore size) and $\emptyset$ is the K_2CO_3-to-metal particle size ratio, i.e., the ratio between the diameters of the K_2CO_3 and the metal particles, d_p and d_M, respectively.

The average number of K_2CO_3/K_2CO_3 contacts on a single K_2CO_3 particle in the metal/K_2CO_3 powder mixture, μ, depends not only on the K_2CO_3-to-metal particle size ratio, $\emptyset$, but also on the volume fraction of the K_2CO_3 in the mixture (which is effectively the porosity of the resultant porous Cu or Ni, ε) and can be calculated by (Zhao 2003):

$$\mu = \frac{2}{(1-\frac{\emptyset+2}{\sqrt{\emptyset^2+6\emptyset+5}})(1-\emptyset+\frac{\emptyset}{\varepsilon})} \tag{6.2}$$

The surface area of each pore is therefore the surface area of the K_2CO_3 particle less the total area of the sphere crowns forming the necks. The volumetric specific geometric surface area of the porous metal, i.e., the total surface area of the primary pores per unit volume, can thus be calculated by:

$$S_{VG} = \frac{A_p-\mu A_c}{V_p/\varepsilon} = \frac{6}{1/\varepsilon+1/[(1-\varepsilon)\emptyset]} = \frac{6}{d_p/\varepsilon+d_M/(1-\varepsilon)} \tag{6.3}$$

where A_p and V_p are the surface area and volume of a K_2CO_3 particle, respectively. The gravimetric specific geometric surface area can be calculated accordingly by:

$$S_{MG} = \frac{S_{VG}}{(1-\varepsilon)\rho} = \frac{6}{\rho[d_M+d_p(1-\varepsilon)/\varepsilon]} \tag{6.4}$$

Eqs. (6.3) and (6.4) show that the volumetric specific surface area of LCS porous metal is a function of porosity, ε, K_2CO_3 particle size or pore size, d_p, and metal particle size, d_M. The gravimetric specific surface area is also a function of the density of the metal, ρ. Although the particles of the K_2CO_3, Cu and Ni powders used in this experiment have a size range

instead of a uniform size, it is possible to estimate the volumetric and gravimetric specific surface areas using mean particle sizes.

6.3 Comparison of Calculated and Experimental Values

The calculated values of the volumetric and gravimetric surface areas for the porous Cu samples are shown in Fig. 6.3 (a & b) alongside the experimental values, measured by the QS method. The calculations were carried out using Eqs. (6.3) and (6.4) with the following input values: density of Cu ρ = 8.96 g/cm^3, mean Cu particle diameter d_{Cu} = 72 μm, and surface weighted mean diameters of K_2CO_3 particles, d_p: 338 μm, 568 μm, 855 μm and 1250 μm for the particle size ranges 250-425 μm, 425-710 μm, 710-1000 μm and 1000-1500 μm, respectively. In the porosity range 0.59-0.75 and pore size range 250-1500 μm, the volumetric and gravimetric specific geometric surface areas of porous Cu are in the ranges of 26-112 cm^{-1} and 7-50 cm^2/g, respectively. Fig. 6.1 shows that the experimental values generally follow the trends predicted by this model, indicating that the model gives a reasonable quantitative description of the major controlling factors for surface area. However, the calculated values are higher than the measured results. This is likely due to the approximations of the broad particle size ranges of the K_2CO_3 and Cu powders by single particle sizes. If the porosity was modified to the primary porosity, the stochastic modelling can fit the experimental value very well which is shown in Fig. 6.2. It is because both the geometric surface area and primary porosity are contributed by the primary pores.

The variations of volumetric (S_{VG}) and gravimetric (S_{MG}) specific geometric surface areas, measured by the QS method, as a function of porosity for porous Ni with different pore sizes are shown in Fig. 6.3 (a & b). The calculations were carried out using Eqs. (6.3) and (6.4) with the following input values: density of Ni ρ = 8.908 g/cm^3, mean Ni particle diameter d_{Cu} = 20 μm, and surface weighted mean diameters of K_2CO_3 particles the same as

used for porous Cu. In the porosity range 0.63-0.81 and pore size range 250-1500 μm, the volumetric and gravimetric specific geometric surface areas of porous Ni are in the ranges of 29-114 cm^{-1} and 9-60 cm^2/g, respectively. Both volumetric and gravimetric specific geometric surface areas increase with porosity and decrease with pore size. However, volumetric specific geometric surface area is less sensitive to porosity. Due to the small size of the secondary pores in porous Ni, the porosity was mainly contributed by the primary pores. The experimental data obtained by QS fitted very well to the values obtained by stochastic modelling.

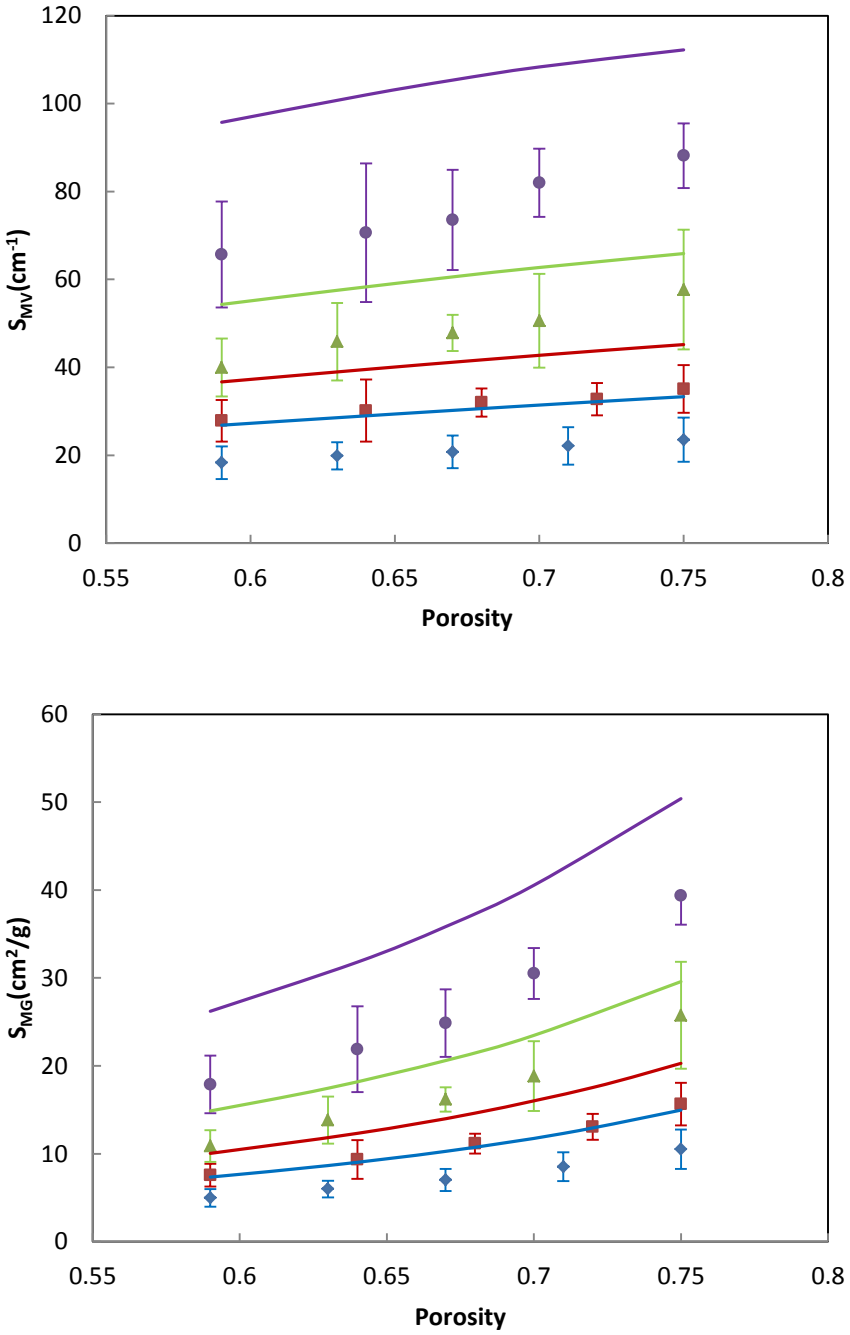

***Fig. 6.1**, Variations of (a) volumetric (S_{VG}) and (b) gravimetric (S_{MG}) specific geometric surface areas with porosity at different pore sizes: experimental (● 250-425 µm, ▲ 425-710 µm, ■ 710-1000 µm, ◆ 1000-1500 µm); modelling (—— 250-425 µm, —— 425-710 µm, —— 710-1000 µm, —— 1000-1500 µm).*

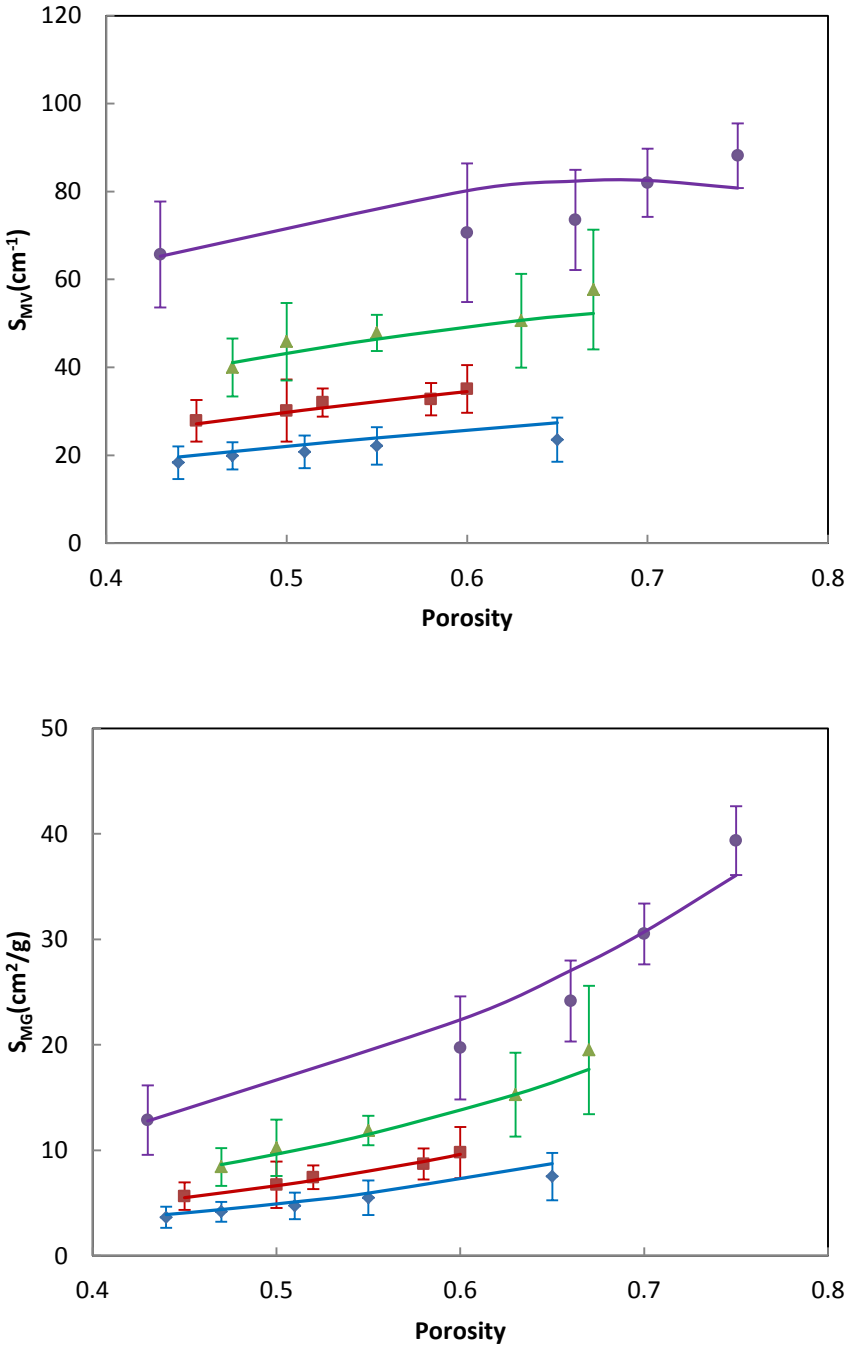

***Fig. 6.2**, Variations of (a) volumetric (S_{VG}) and (b) gravimetric (S_{MG}) specific geometric surface areas with primary porosity at different pore sizes: experimental (● 250-425 µm, ▲ 425-710 µm, ■ 710-1000 µm, ◆ 1000-1500 µm); modelling (—— 250-425 µm, —— 425-710 µm, —— 710-1000 µm, —— 1000-1500 µm).*

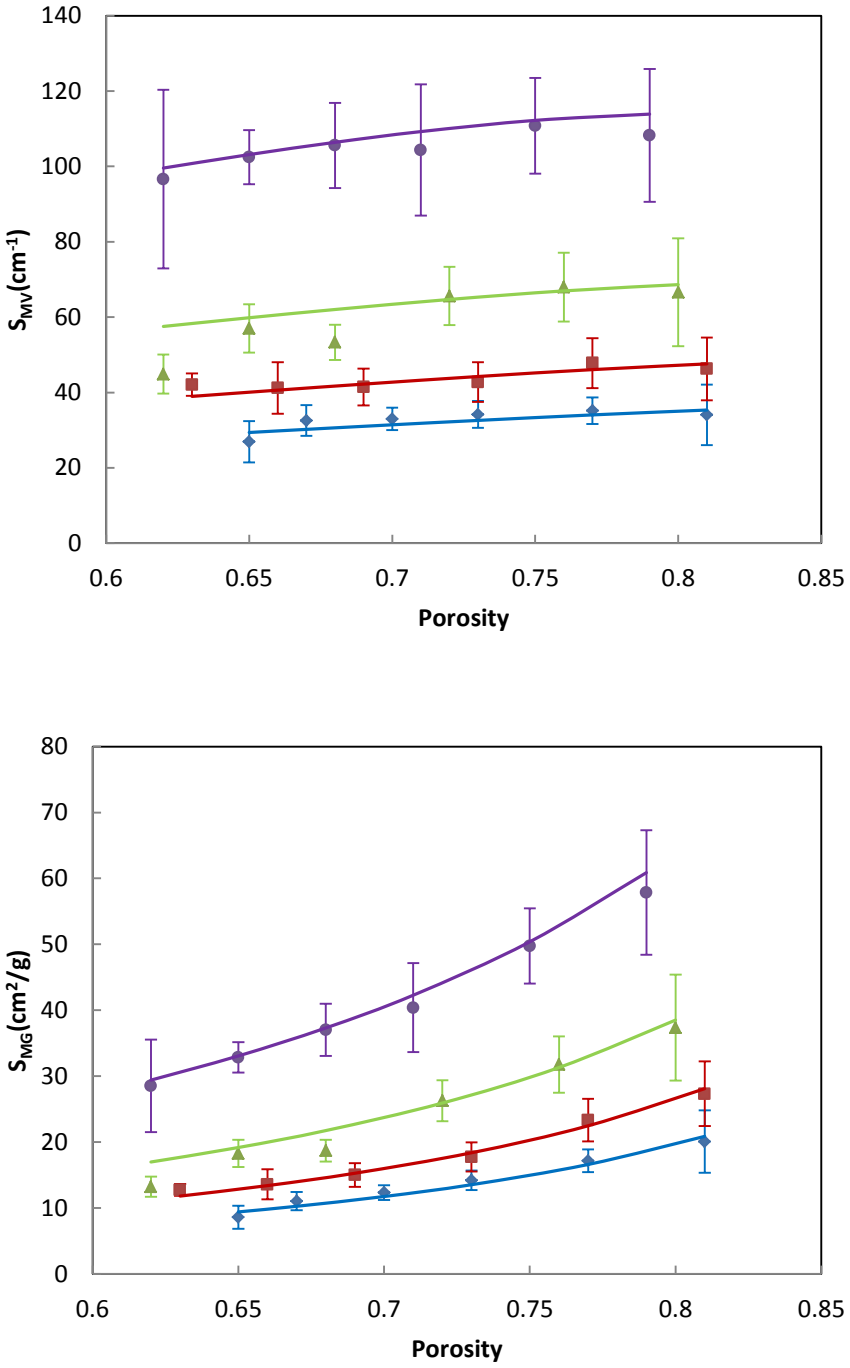

***Fig. 6.3**, Variations of (a) volumetric (S_{VG}) and (b) gravimetric (S_{MG}) specific geometric surface areas with porosity at different pore sizes: experimental (● 250-425 µm, ▲ 425-710 µm, ■ 710-1000 µm, ◆ 1000-1500 µm); modelling (—— 250-425 µm, —— 425-710 µm, —— 710-1000 µm, —— 1000-1500 µm).*

Chapter 7 Electro-active Surface Area of Porous Cu

7.1 Calibration of Electro-active Surface Area by Cu Plates

Because Delahay equation cannot be used directly to calculate the surface area of Cu electrode due to passivation, a series of solid copper plates with known surface areas were used to calibrate and obtain the linear relation between surface area and peak current.

Fig. 7.1 shows the cyclic voltammograms of solid Cu plates with different surface areas. Fig. 7.2 shows that the peak current value of Peak III is directly proportional to the surface area of the Cu plate, so peak III was used in this work for the determination of the electro-active surface area of porous Cu samples. The coefficient of determination, R^2, is very close to 1 which means linear regression is relatively high. The relationship between the electro-active surface area, A_E (cm^2), and peak current, I_p (mA), for the Cu plates can be reliably expressed by:

$$A_E = 2.60 \times I_p \quad (R^2 = 0.9791) \tag{7.1}$$

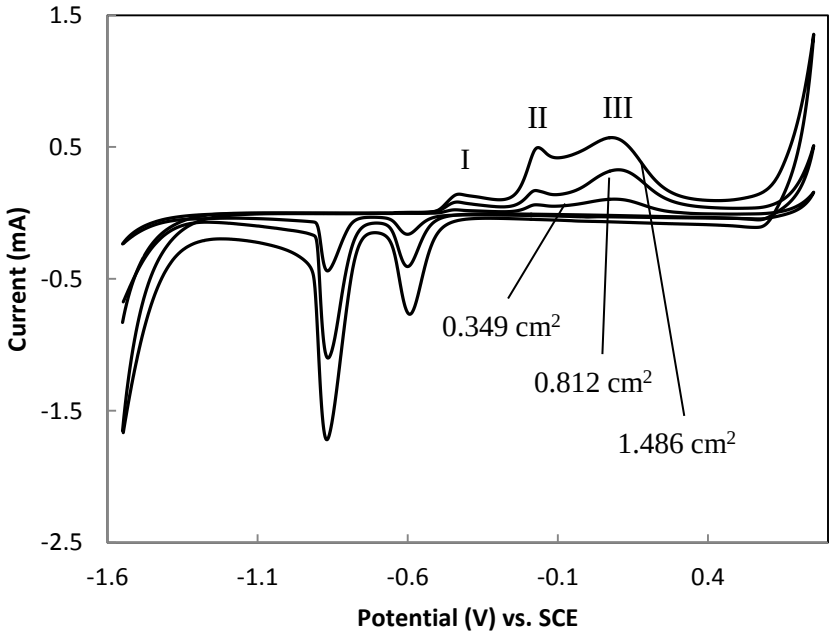

***Fig. 7.1**, Cyclic voltammograms of copper plate electrodes with different surface areas.*

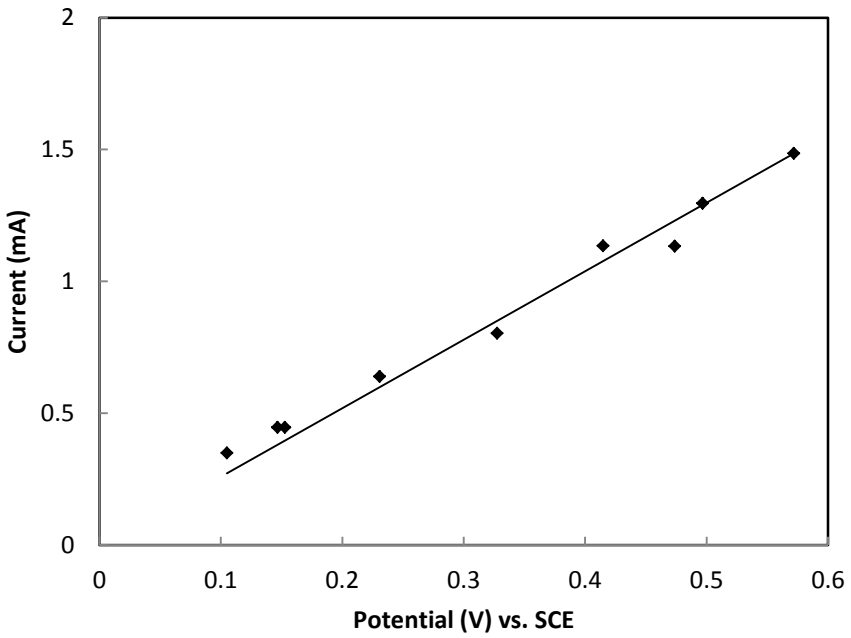

***Fig. 7.2**, Linear relation between Cu plate surface area and current of peak III.*

7.2 IR Compensation in CV Experiment

Fig. 7.3 shows the cyclic voltammogram of a porous Cu sample obtained without IR compensation, in comparison to the voltammogram of a solid Cu plate. The main factor which leads to the IR drop is the resistance of the electrolyte. The effect of electrolyte resistance to the potential in the experiment can be expressed by:

$$u = ir \tag{7.2}$$

where u is potential, i is current and r is electrolyte resistance. High electrolyte resistance can lead to the increase of potential in the experiment. Electrolyte resistance increases with the distance between the working electrode and the reference electrode. In order to reduce the effect of electrolyte resistance to the measurement, the working electrode was placed as near the reference electrode as possible. Large electrode surface area can lead to a high current (i in Eq. 7.2), which can also cause a peak potential higher than the standard potential and would lead to low accuracy and reliability in the experiment. Fig. 7.3 shows

that the potential of peak III the of porous Cu sample was much higher than the standard potential (around 0.1 V vs. SCE) measured by the Cu plate with a low surface area (0.349 cm^2), where a low current was generated in the experiment (about 0.1 mA).

Therefore, the porous Cu samples had to be tested with IR compensation so that the peak potential in the cyclic voltammogram was the standard potential (0.1 V vs. SCE). A series of IR compensation values from 1 to 15 Ω were used to fit until the peak potential appeared in the standard potential. The value of IR compensation was set to be about 12 Ω in the CV experiments. However, the IR compensation cannot be over 12 Ω, because over compensation can lead to scattered experimental results in the cyclic voltammogram as shown in Fig. 7.4.

Fig. 7.5 shows the cyclic voltammogram of a porous Cu sample with the IR compensation, of which the anodic peak potential was the same as that of the standard Cu plate. The voltammograms of the porous Cu and solid Cu plate have the same shapes, indicating that the electrochemical processes at the surface of porous Cu is the same as those at the surface of solid Cu. The relation in Eqn. 7.1 should also be applicable to porous Cu.

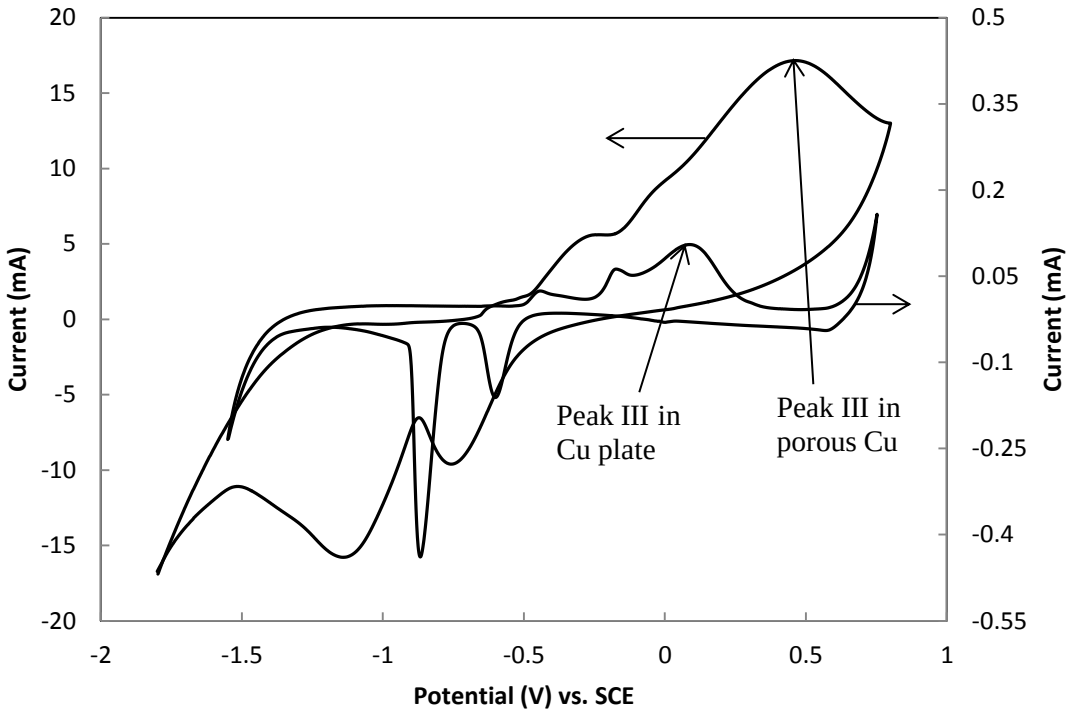

***Fig. 7.3**, Cyclic voltammograms of Cu plate and porous Cu without IR compensation.*

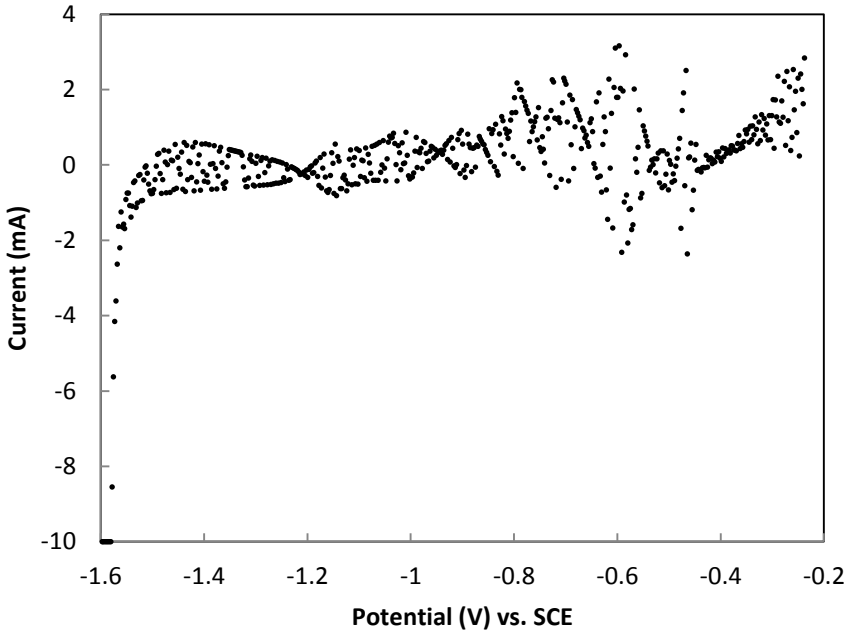

***Fig. 7.4**, Cyclic voltammogram of a porous copper sample tested with excessive IR compensation.*

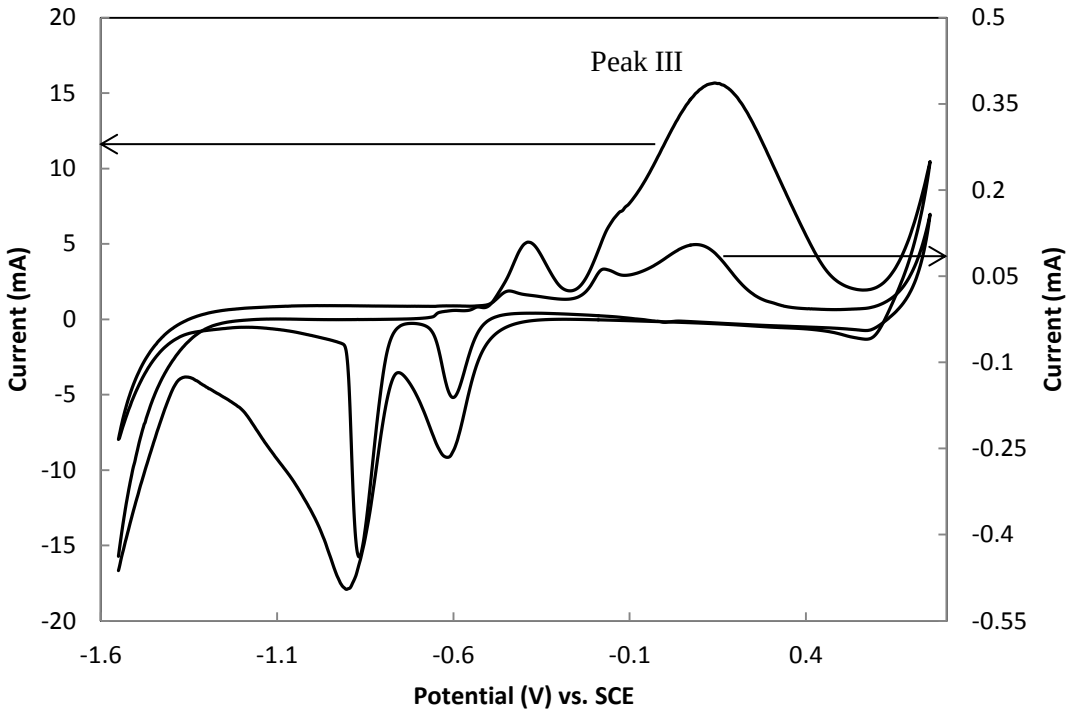

***Fig. 7.5**, Cyclic voltammogram of a porous copper sample after IR compensation, compared to that of a solid Cu plate.*

7.3 Cyclic Voltammograms and Electro-Active Surface Area of Porous Cu

Fig. 4.17 shows the cyclic voltammograms of the porous Cu samples (Cu01 to Cu30) with the porosity range of 0.56 to 0.74 and the pore size ranges of 1000-1500 µm, 710-1000 µm, 425-710 µm, 250-425 µm and 75-150 µm. In Fig. 4.17, current density, the current generated per unit mass of sample, was used. The peak current density (I_P), obtained in Fig. 7.6, was used to calculate the gravimetric electro-active surface area by Eqn. 7.1, which was converted to volumetric specific electro-active surface areas by Eqn. 3.5. The values of peak current (I_P), the volumetric specific geometric surface area (S_{VE}) and the gravimetric specific geometric surface area (S_{ME}) of these samples are listed in Table A7.1 (see Appendixes).

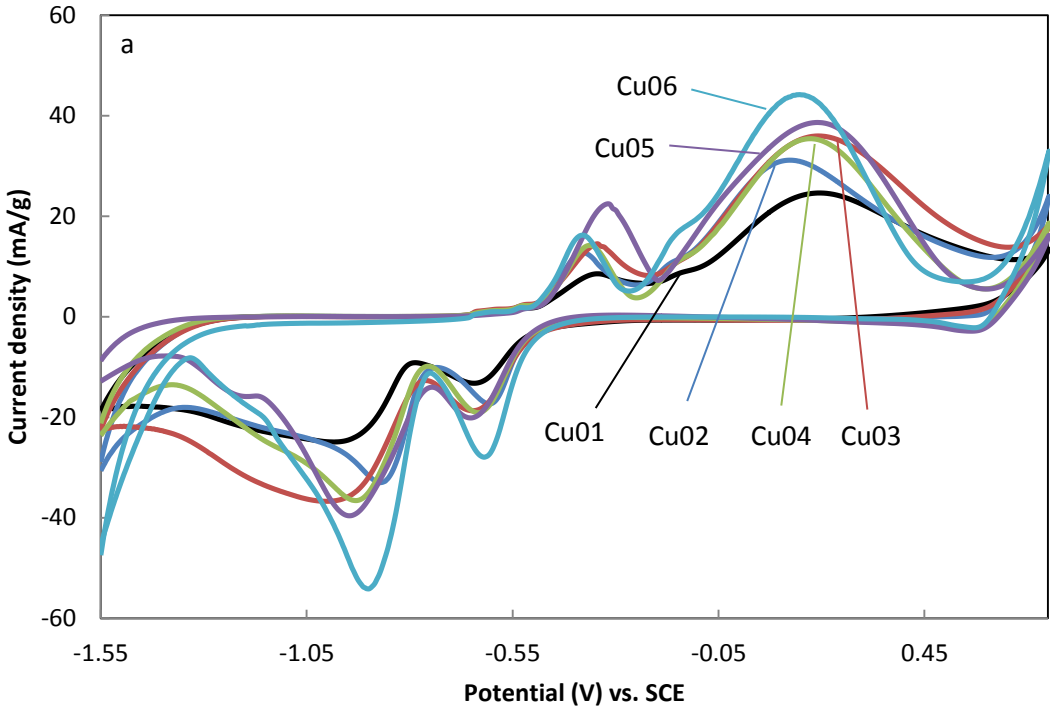

***Fig. 7.6**, Cyclic voltammograms of porous Cu samples with the pore size ranges of (a) 1000-1500 µm (Cu01 to Cu06); (b) 710-1000 µm (Cu07 to Cu12); (c) 425-710 µm (Cu13 to Cu17); (d) 250-425 µm (Cu19 to Cu24); (e) 75-150 µm (Cu25 to Cu30).*

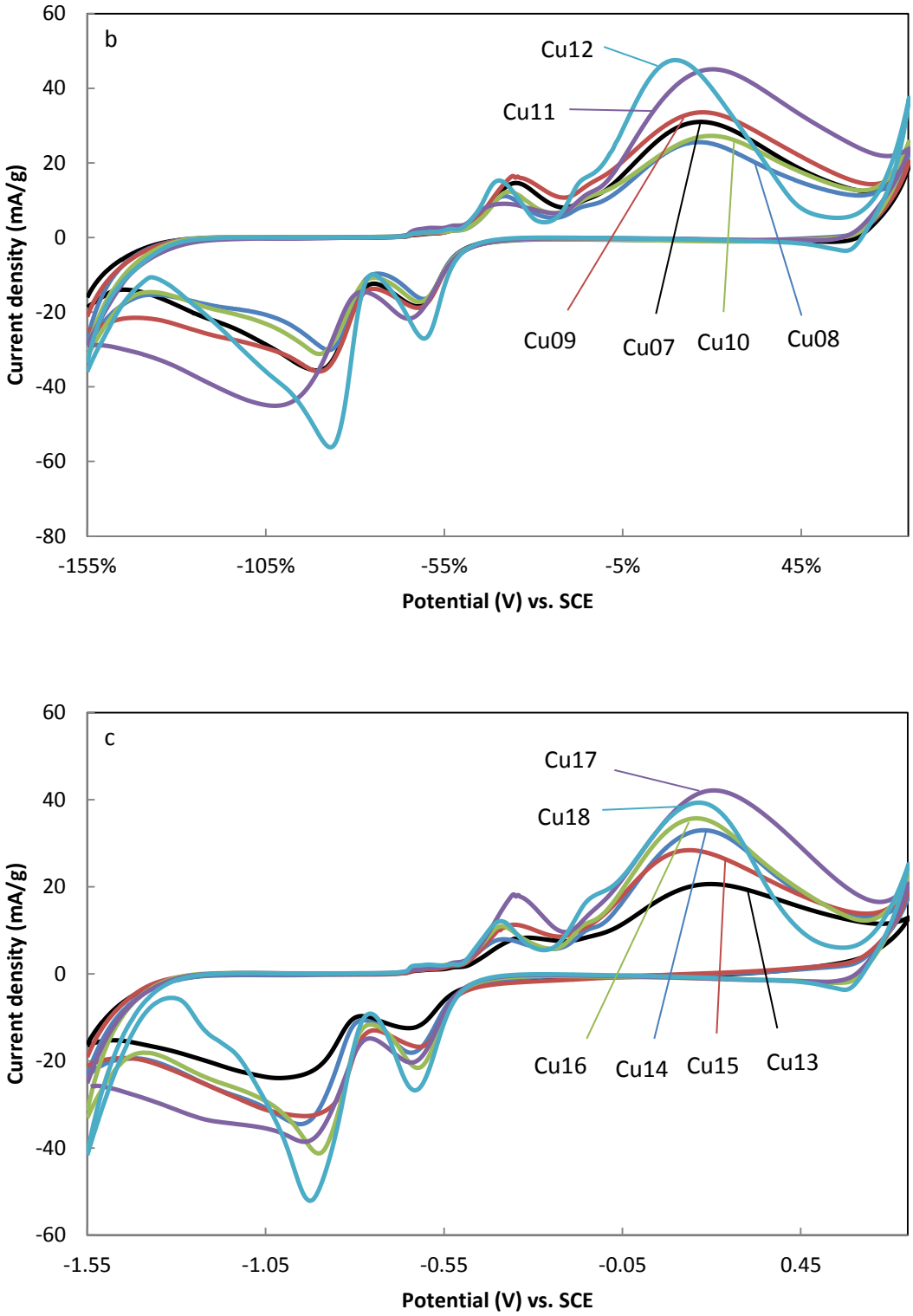

***Fig. 7.6**, Cyclic voltammograms of porous Cu samples with the pore size ranges of (a) 1000-1500 µm (Cu01 to Cu06); (b) 710-1000 µm (Cu07 to Cu12); (c) 425-710 µm (Cu13 to Cu17); (d) 250-425 µm (Cu19 to Cu24); (e) 75-150 µm (Cu25 to Cu30).*

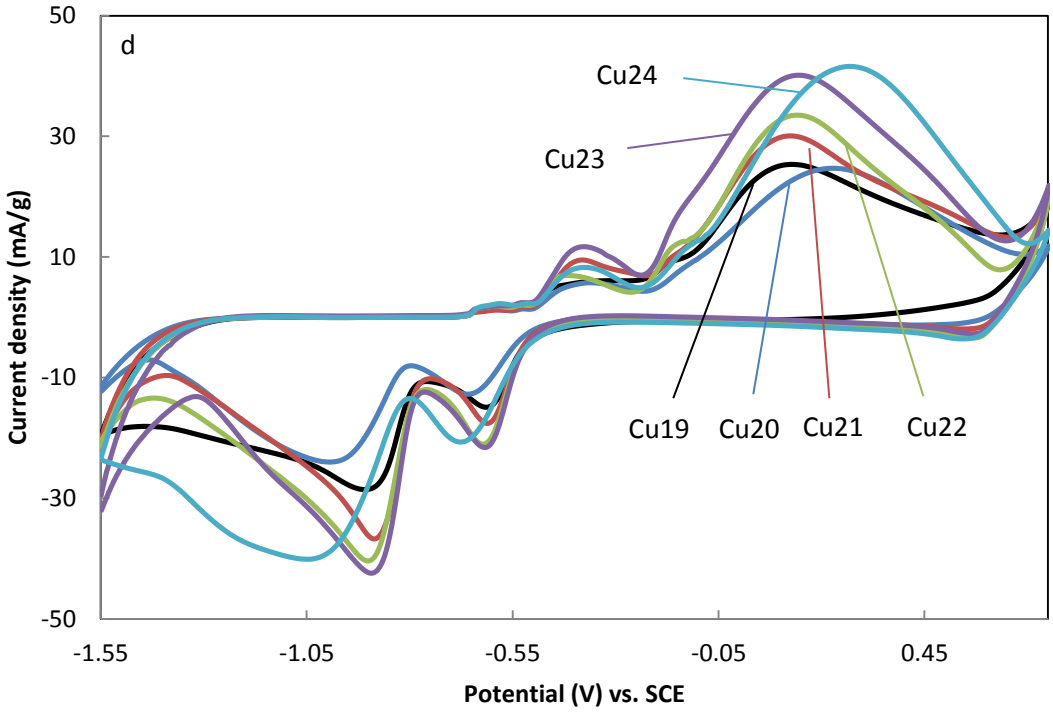

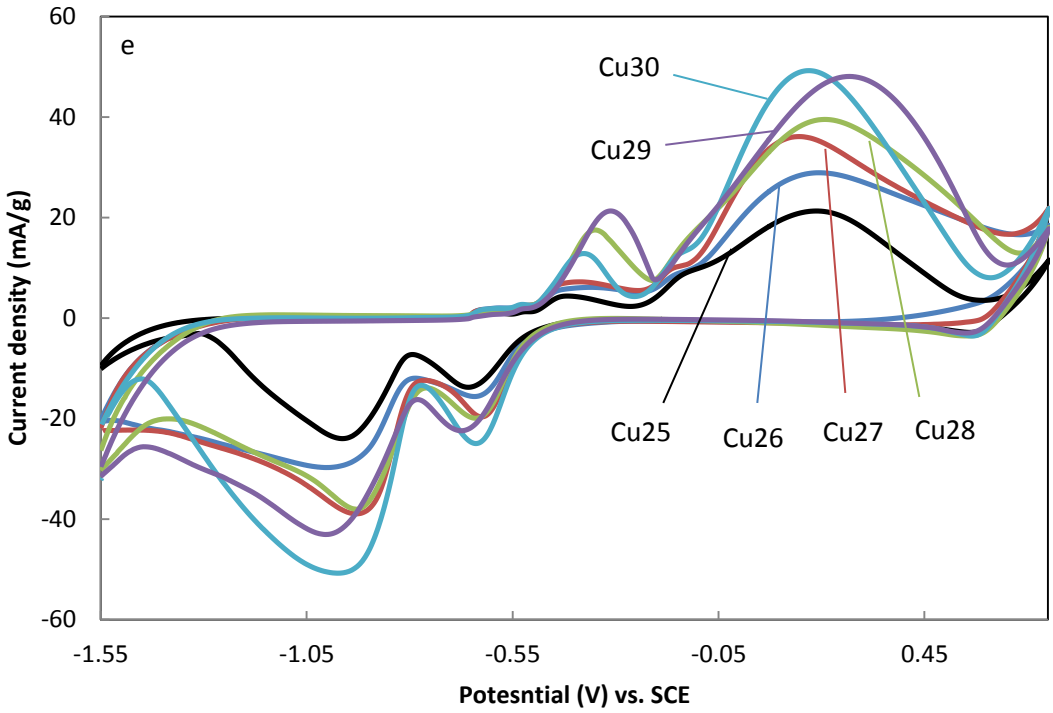

***Fig. 7.6**, Cyclic voltammograms of porous Cu samples with the pore size ranges of (a) 1000-1500 µm (Cu01 to Cu06); (b) 710-1000 µm (Cu07 to Cu12); (c) 425-710 µm (Cu13 to Cu17); (d) 250-425 µm (Cu19 to Cu24); (e) 75-150 µm (Cu25 to Cu30).*

7.4 Effects of Porosity and Pore Size

The variations of volumetric (S_{VE}) and gravimetric (S_{ME}) specific electro active surface areas with porosity and pore size are shown in Figs. 7.7 (a) and (b), respectively. In the porosity range 0.53-0.75 and pore size range 75-1500 μm, the volumetric and gravimetric specific electro active surface areas are in the ranges of 206-369 cm^{-1} and 53-128 cm^2/g, respectively. The specific electro active surface area is nearly one order of magnitude higher than the geometric surface area. In general, both volumetric and gravimetric specific electro active surface areas decrease with pore size; the gravimetric specific electro active surface area increases with porosity; the effect of porosity on the volumetric specific electro active surface area is not pronounced. The trends of the effects of porosity and pore size on electro active surface area are less clear than those on the geometric surface area.

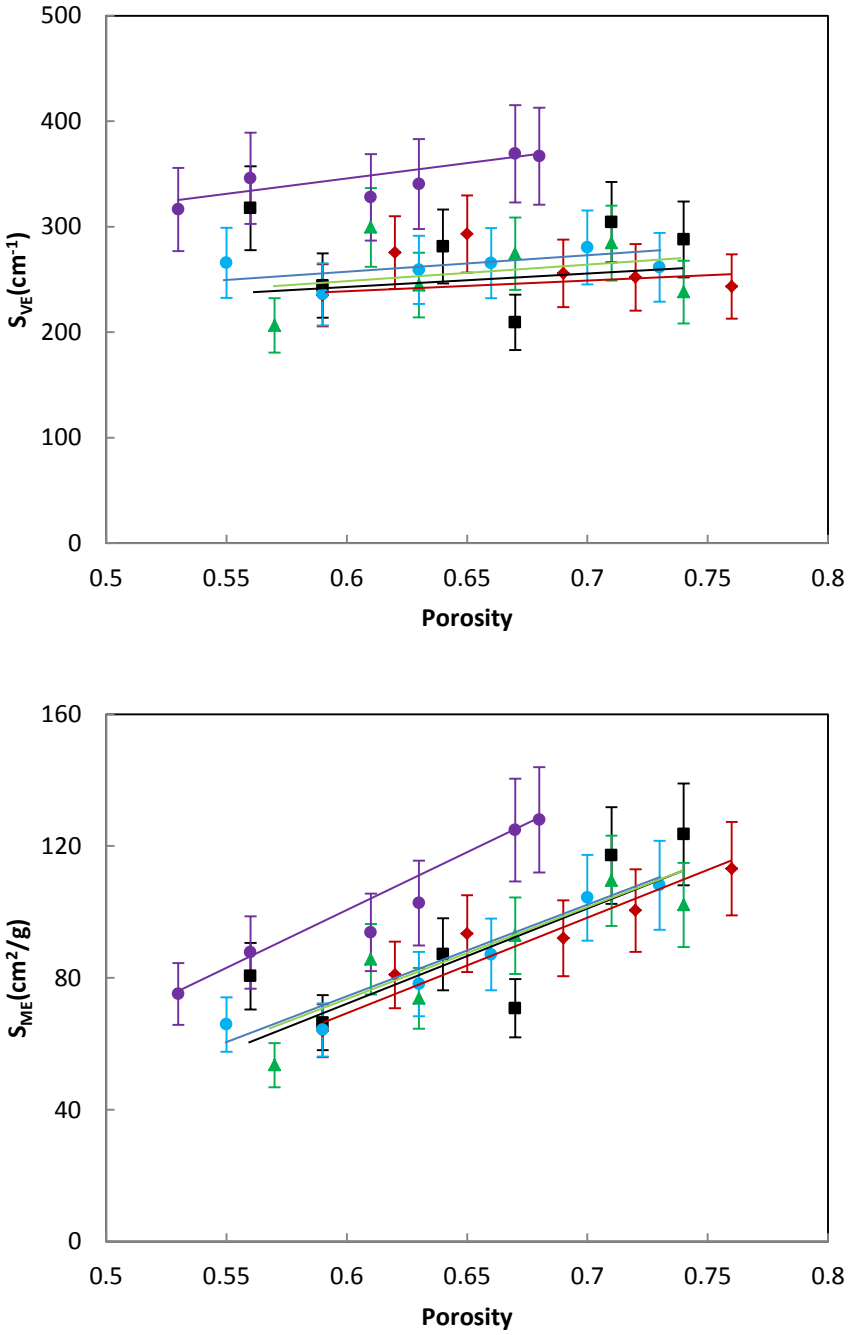

***Fig. 7.7**, Variations of (a) volumetric (S_{VE}) and (b) gravimetric (S_{ME}) specific electro active surface areas with porosity at different pore sizes: ● 75-150 µm, ● 250-425 µm, ▲ 425-710 µm, ■ 710-1000 µm, ◆ 1000-1500 µm.*

7.5 Discussion

The variations of both the geometric (Fig. 6.1) and electro-active (Fig. 7.7) surface areas with porosity have similar trends. It seems the electro-active surface area is proportional to the geometric surface area.

Fig. 7.8 shows the ratio of electro-active (A_E) to geometric (A_G) surface areas (same for volumetric and gravimetric, i.e., $\theta = A_E/A_G = S_{VE}/S_{VG} = S_{ME}/S_{MG}$), as a function of mean pore size at different porosities. Because the samples used for the QS and CV measurements had slightly different porosities, the ratio values could not be obtained directly from the experimental data. For each sample with a measured volumetric specific electro active surface area shown in Fig. 7.7 (a), the volumetric specific geometric surface area was obtained by interpolation of the data in Fig. 6.1 (a) based on the porosity of the sample. The ratio was simply the former divided by the latter.

The volumetric specific geometric surface areas of the samples with the smallest pore size range 75-150 μm were calculated using Eqn. (6.3), because no experimental data were available. Table A7.2 (see Appendixes) lists the values of the electro active (S_{VE}) and geometric (S_{VG}) surface areas and the surface area ratio (θ).

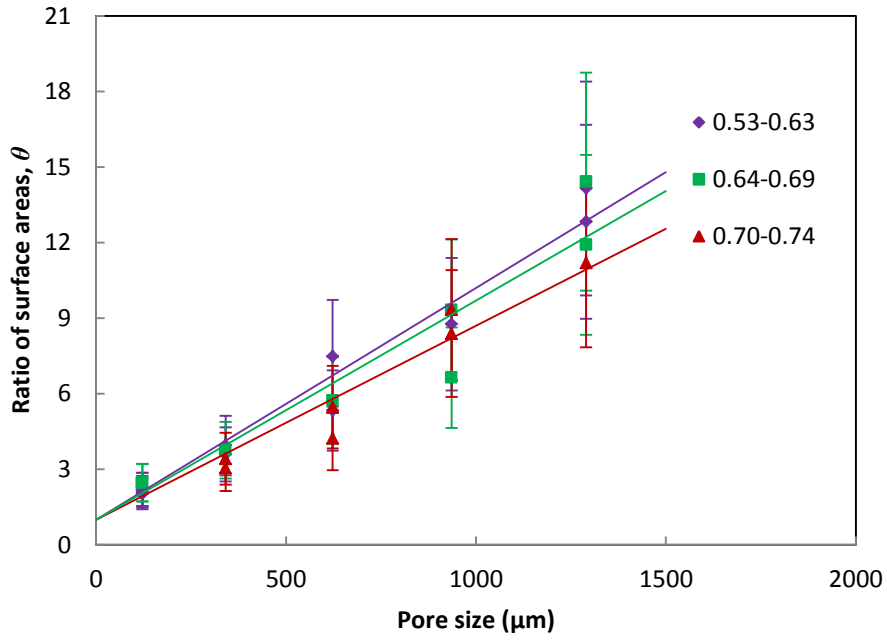

***Fig. 7.8**, Variations of the ratio between the electro active (A_E) and geometric (A_G) surface areas, θ, with mean pore size at different porosities.*

Fig. 7.8 shows that the ratio of electro active to geometric surface areas increases nearly linearly with mean pore size and generally increases with decreasing porosity. An especially interesting characteristic of the trendlines is that their intercepts at the vertical axis are all unity, indicating that there are more surfaces contributing to the electrochemical reactions and peak current than the geometric surface area. If the primary pore size is 0, only secondary pores are in the porous metal and can provide the surface area. Therefore, the electro-active surface area would equal to geometric surface area in this case. The electro active surface area can be separated into two parts: contribution from the primary porosity (geometric surface area) and contribution from the secondary porosity, i.e., the voids or interstices inside the Cu matrix. The contribution to the electro active surface area from the secondary porosity can be significantly greater than the geometric surface area (up to 15 times as shown in Fig. 7.8). This high contribution is due to the numerous small voids or interstices in the Cu matrix as a consequence of incomplete densification of Cu particles during sintering. The network formed by these voids, i.e., the secondary porosity, can be

penetrated by the electrolyte and therefore make significant contributions to the electro active surface area.

It can be seen from Fig. 7.8 that the contribution to the electro active surface area from the secondary porosity is proportional to pore size and decreases with porosity. The effect of porosity on the ratio between electro active and geometric surface areas can be explained by the relative quantities of Cu particles in the interior and exterior regions in the solid matrix. For a fixed pore size, increasing porosity means more Cu particles are located in the surface region and the number of Cu particles residing in the interior region is reduced. Relative to the contribution of the primary porosity to the electro active surface area (i.e., geometric surface area), the contribution of the second porosity decreases. Therefore, the ratio between electro active and geometric surface areas decreases with porosity. The effect of pore size is likely a manifestation of the effect of the diffusion layer on the concentration distribution of the electro active species.

The diffusion layer thickness (δ) for the diffusion of OH^- towards Cu electrode can be calculated by (Scholz 2002):

$$\delta = \sqrt{\frac{DRT}{nFv}} \tag{7.3}$$

where D ($2\times10^{-5}cm^2/s$) is the diffusion coefficient of OH^-, R is the gas constant (8.134 J/K mol), T is the temperature (298K), n is the number of electronic transfer (2 for reaction 4c), F is the Faraday constant (96485 C/mol) and v is the scan rate (0.026 V/s in this work). Under the current experimental conditions, the diffusion layer thickness for a flat surface is calculated to be about 31 μm. This is about 1/2 to 1/20 of the pore radius. The actual thickness of the region with low concentrations of electro active species is even greater and occupies a significant portion of the pores.

For small pores with a radius comparable to the diffusion layer thickness, a large proportion of the electrolyte is within the diffusion layer. Only a small reservoir of electrolyte in the central region of the pore has the initial concentration of the electro active species. The electro active species in the electrolyte is consumed rapidly during the CV measurement. In addition, acute curvature associated with small pores also leads to a greater actual diffusion layer than that predicted for a flat surface. All these factors reduce the concentrations of the electro active species in the region next to the electrode surface, leadings to a reduced peak current and thus a reduced electro active surface area.

With increasing pore size, the reservoir of electrolyte with the initial concentration of the electro active species becomes bigger. The diffusion layer thickness also approaches that predicted for a flat surface due to reduced curvature. As a consequence, the region of depleted electro active species next to the pore walls is reduced, leadings to an increased peak current and thus an increased electro active surface area.

Chapter 8 Electro-Active Surface Area of Porous Ni

8.1 Calibration of Electro-Active Surface Area by Ni Plates

Fig. 8.1 shows the voltammograms of Ni plates with known surface areas at a scan rate of 0.5 V/s. Fig. 8.2 shows that there is a linear relation between the surface area of nickel electrode and the peak current, which agrees with the Randles-Sevcik equation (Eqn. 3.11).

Fig. 8.3 shows the voltammograms of the nickel plate with the surface area of 1.33 cm^2 at various scan rates. The peak current was proportional to $v^{1/2}$, as shown in Fig. 8.4, which also agrees with the Randles-Sevcik equation (Eqn. 3.11). Therefore, the diffusion coefficient of $Fe(CN)_6^{3-/4-}$ can be determined to be 2.08×10^{-5} cm^2/s in this experiment. The potentials of the current peaks remain approximately constant (~0.22 V vs. SCE) for all surface areas and scan rates.

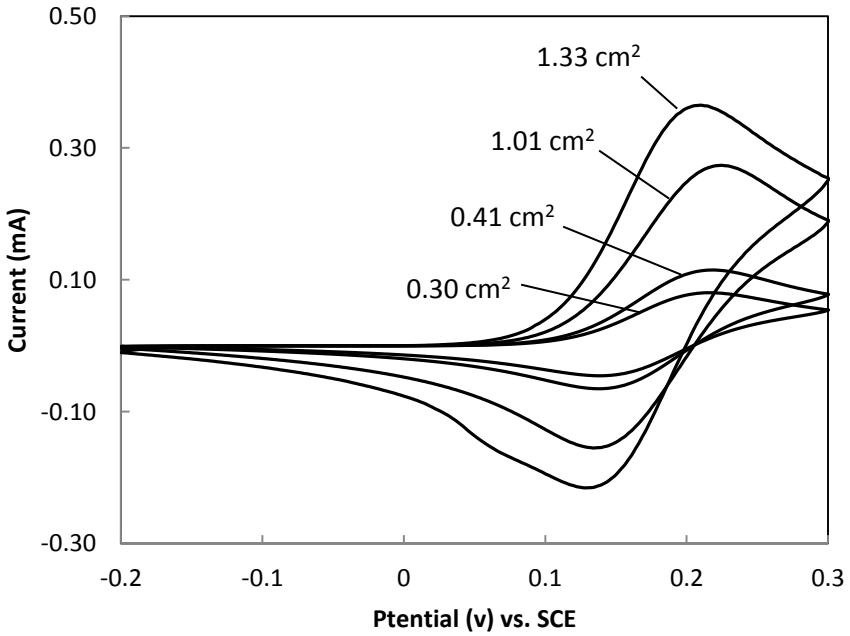

***Fig. 8.1**, Cyclic voltammograms of Ni plates with different surface areas.*

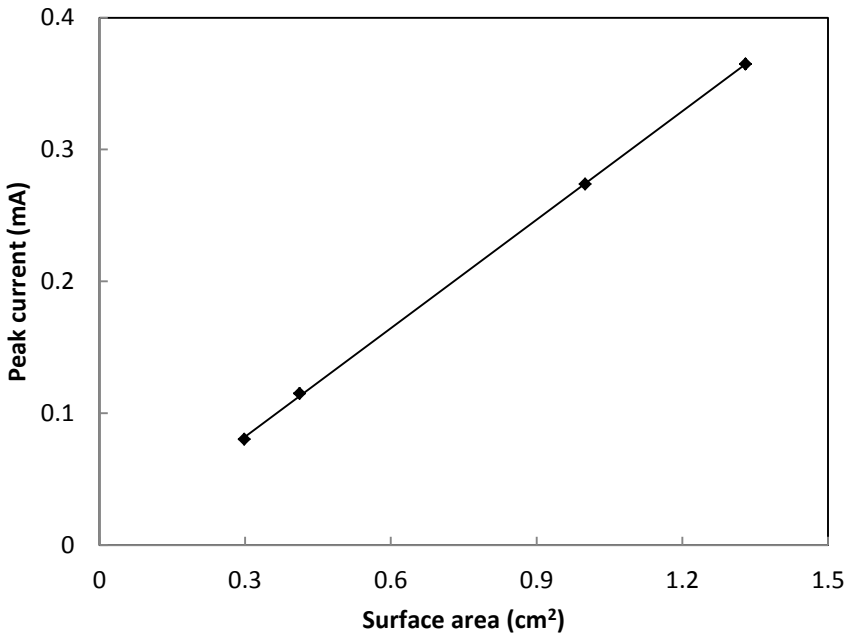

***Fig. 8.2**, Linear relation between Ni plate surface area and anodic peak current.*

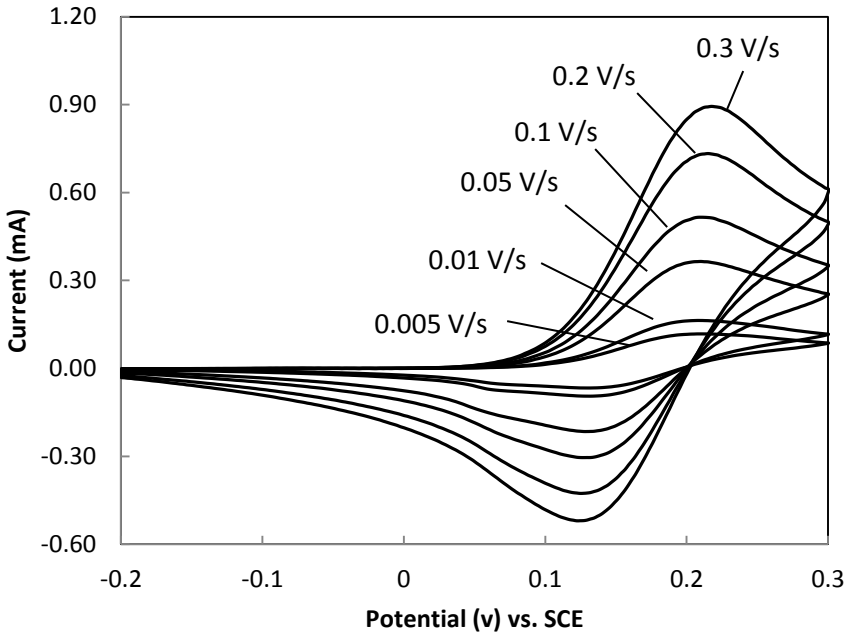

***Fig. 8.3**, Cyclic voltammograms of a Ni plate with the surface area of 1.33 cm^2 at different scan rates.*

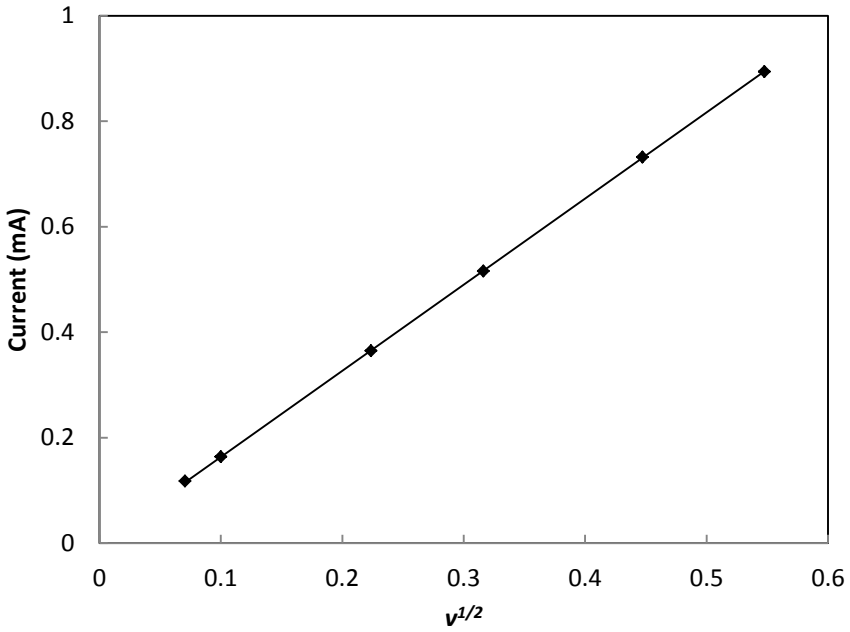

***Fig. 8.4**, Linear relation between anodic peak current and square root of scan rate.*

8.2 IR Compensation

In the electro-active surface area measurements for porous Ni, high currents were generated because of the high surface areas. Similar to the porous Cu measurement, this would lead to the increase of the peak potential. Fig. 8.5 shows the cyclic voltammogram of a porous Ni sample without IR compensation, which shows no anodic peak. This is because the peak potential was higher than the standard potential and beyond the potential range in the CV experiment.

The standard peak potential was obtained using a Ni plate with a low surface area (0.3 cm^2). Due to the low current generated in the test (< 0.1 mA), IR compensation was not needed and did not affect the experimental result significantly. The standard peak potential was determined to be around 0.22 V. IR compensation was necessary for the other Ni plates with higher surface areas used in the calibration so that the peak potential appeared around 0.22 V.

IR compensation in the CV of porous Ni was operated at a high scan rate. According to the Randles-Sevcik equation (Eqn. 3.11), the higher the scan rate the higher the current generated in the experiment, which leads to a high level of IR compensation. The value of IR compensation can be determined more accurately at a high scan rate. After IR compensation, the peak potential in the cyclic voltammograms of the porous Ni samples was maintained at around the standard potential (0.22 V) as shown in Fig. 8.6.

The IR compensation was about 11 Ω in the current experiment. However, due to the high surface area in the porous Ni samples, the effect of IR drop cannot be eliminated completely. In some samples, the peak potential cannot be calibrated to the standard potential and was a bit higher than 0.22 V at high scan rates as shown in Fig. 8.7. However, a higher IR compensation would lead to scatter of data as shown in Fig. 8.8. Therefore, the value of IR compensation cannot be higher than 11 Ω.

After IR compensation, the cyclic voltammograms of the porous Ni samples have the same shape as those of solid Ni both in the literature and in the current tests (Fig. 8.6), indicating that the electrochemical processes at the surface of porous Ni are the same as those at the surface of solid Ni. The relation in Eqn. 3.11 should also be applicable to porous Ni.

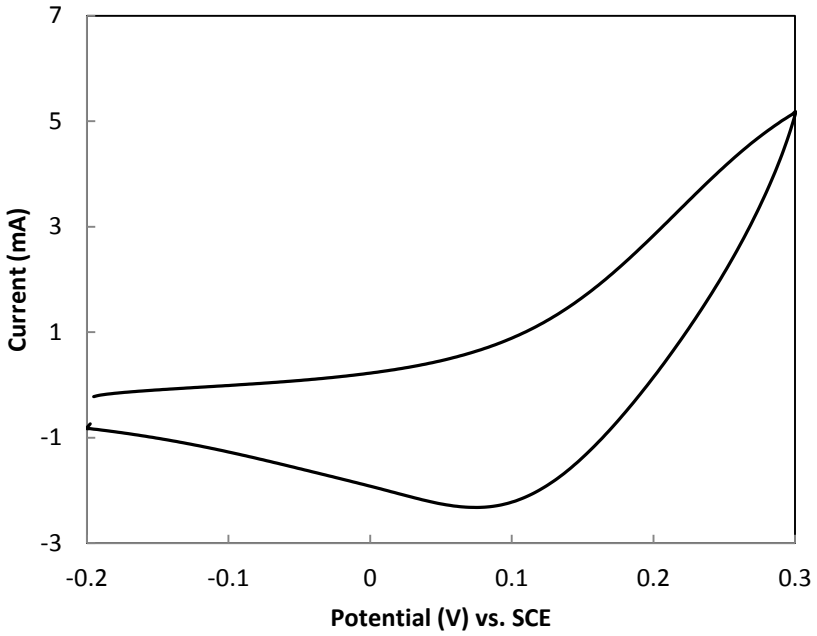

***Fig. 8.5**, Cyclic voltammogram of porous nickel without IR compensation.*

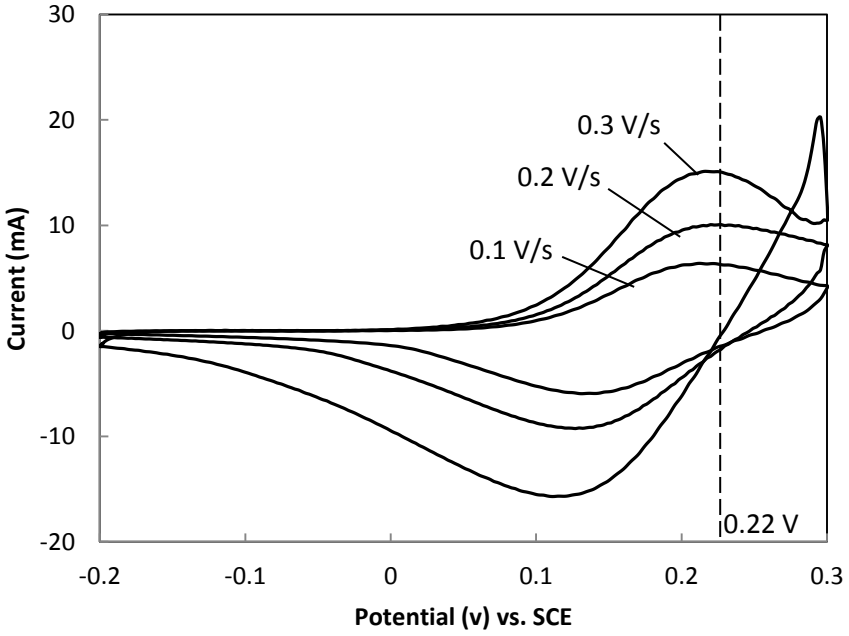

***Fig. 8.6**, Cyclic voltammograms of a porous nickel sample at different scan rates with IR compensation.*

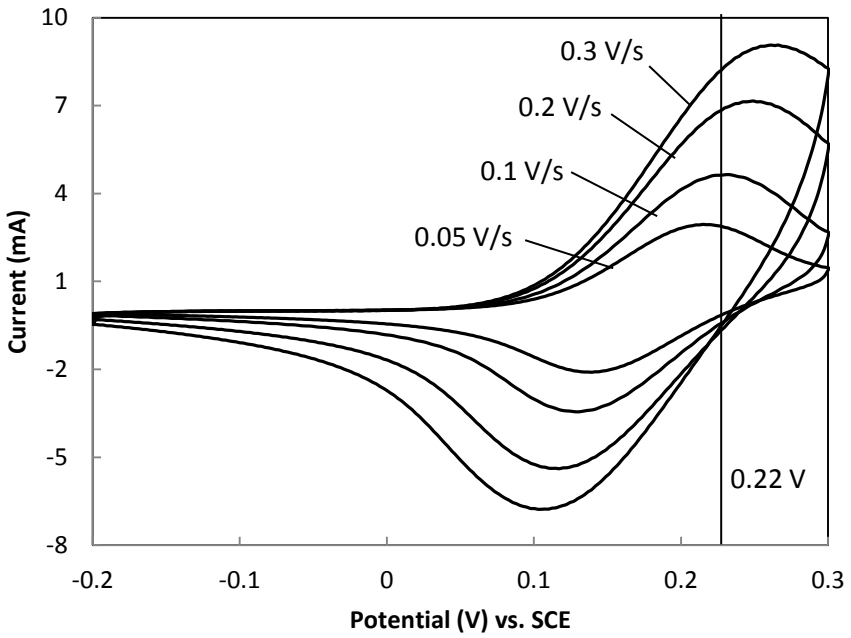

Fig. 8.7, *Cyclic voltammogram of porous nickel at different scan rates with IR compensation.*

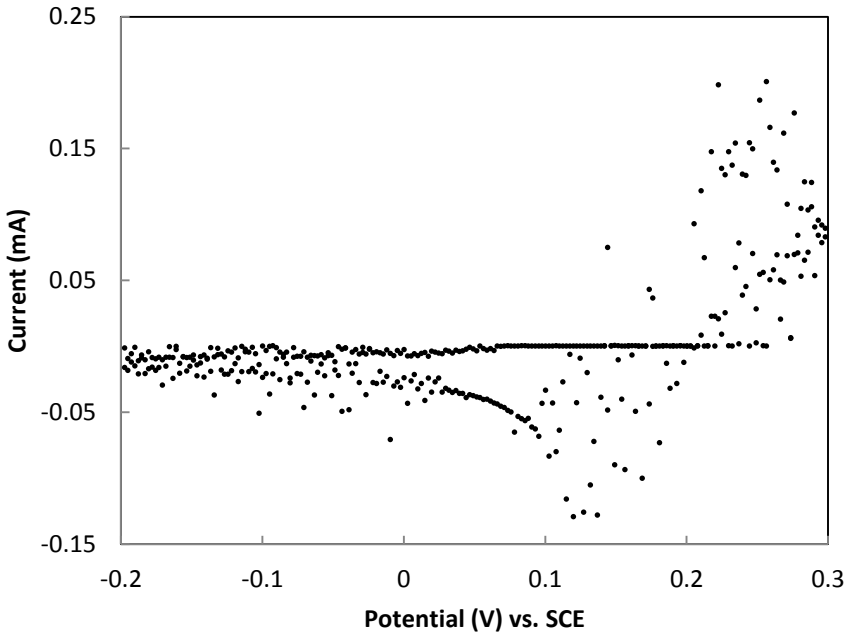

Fig. 8.8*, Cyclic voltammogram of porous nickel with excessive IR compensation.*

8.3 CV voltammograms and Electro-Active Surface Area for Porous Ni

Fig. 8.9 shows the cyclic voltammograms of the porous Ni samples with the pore size of 1000-1500 μm and porosities of 0.65 to 0.81 in an electrolyte of 1 mM potassium ferrocyanide and potassium ferricyanide with 0.1 M potassium hydroxide. In order to analyse the effect of diffusion layer on electro-active surface area, each sample was tested at a series of scan rates from 0.005 V/s to 0.3 V/s. As shown in Fig. 8.9 (a), the current peaks appeared at the potential of 0.22 V (standard peak potential) when the scan rate was higher than 0.1 V/s. When the scan rate was lower than 0.05 V/s, the peak potential moved to lower than 0.2 V.

The diffusion layer thickness as a function of scan rate can be predicted by (Scholz 2002):

$$\delta = \sqrt{DRT/nFv} \tag{8.1}$$

where v is scan rate, D is diffusion coefficient, R is ideal gas constant, T is temperature, n is the number of electronic transfer and F is the Faraday constant. The diffusion layer thicknesses in the CV experiment were calculated to be 102, 72, 32, 23, 16 and 13 μm at the scan rates of 0.005, 0.01, 0.05, 0.1, 0.2 and 0.3 V/s, respectively. A higher scan rate leads to a lower diffusion layer thickness. For all samples, when the scan rate was higher than 0.05 V/s (δ < 32 μm), the potential corresponding to the current peak appeared around the standard peak potential of 0.22 V (measured by pure nickel plates) or slightly higher than 0.22 V because of the high electrolyte resistance at high scan rates. When the scan rate was lower than 0.05 V/s (δ > 32 μm), however, the potential corresponding to the current peak appeared at or below 0.2 V. With the increase of diffusion layer thickness, the reaction on the surface of porous nickel was no longer controlled by fully semi-infinite diffusion and thin-layer behaviour became predominant. The decrease of the anodic peak potential was associated with the transition from semi-infinite to thin-layer controlled diffusion.

Figs. 8.10, 8.11 and 8.12 show the cyclic voltammograms of porous nickel samples with the pore size ranges of 710-1000 μm, 425-710 μm and 250-425 μm, respectively. The porosity of these porous Ni samples were from 0.62 to 0.81. In the CV experiment, the peak current increased with scan rate. The experimental values of peak current of the porous Ni samples with the pore size of 250-1500 μm and porosity of 0.62-0.81 at different scan rates are listed in Table A8.1 (see Appendixes).

The gravimetric and volumetric specific surface areas (S_{MR} and S_{VR}) for porous Ni samples with the pore size of 250-1500 μm and porosity of 0.62-0.81 at different scan rates are listed in Tables A8.2 and A8.3 (see Appendixes), respectively. The gravimetric specific electro-active surface area (S_{ME}) was calculated from its peak current in the cyclic voltammogram by Eqn. 3.11. The volumetric specific electro-active surface area (S_{VE}) was converted by Eqn. 3.5.

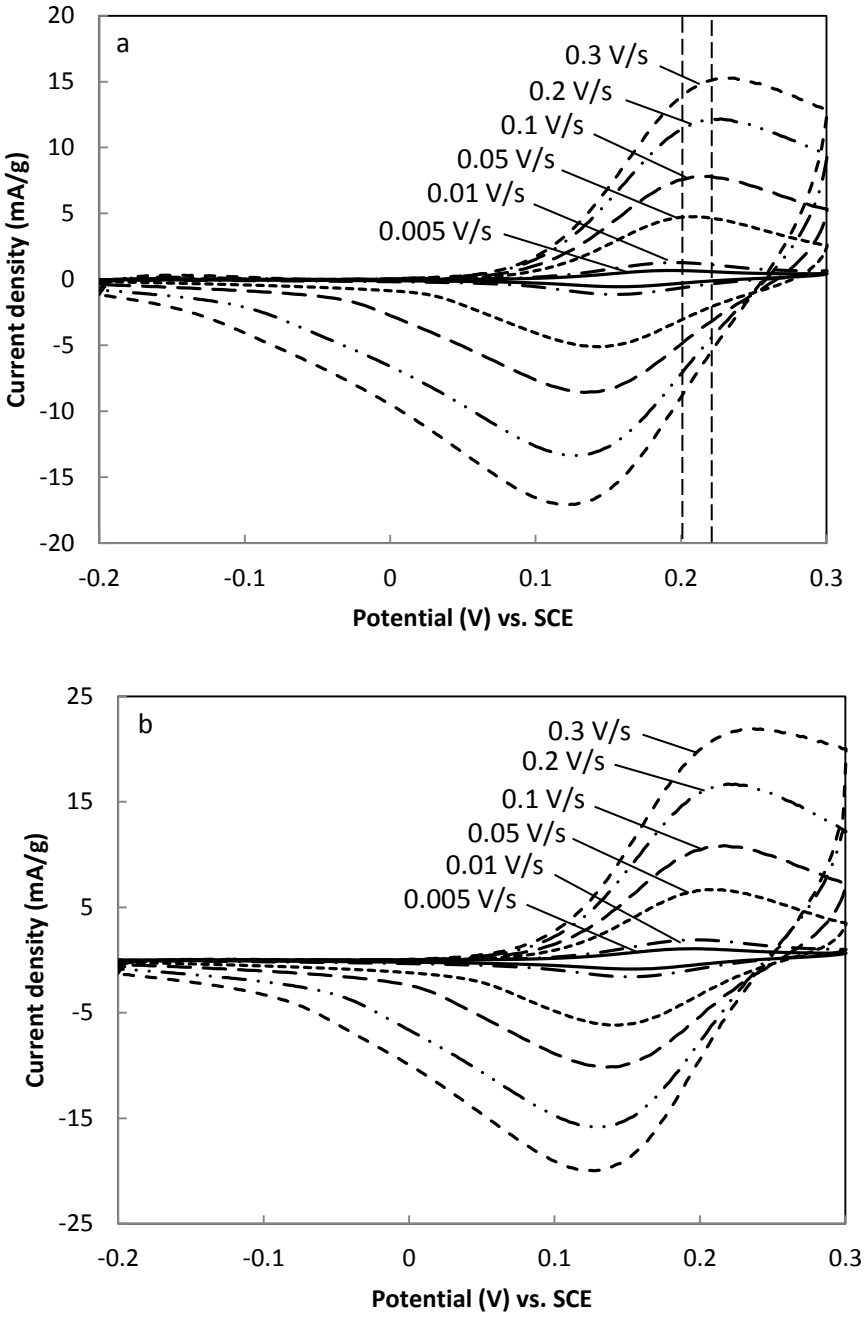

***Fig. 8.9**, Cyclic voltammograms of Ni samples with the pore size of 1000-1500 µm and porosity of (a) 0.65, (b) 0.67, (c) 0.70, (d) 0.73, (e) 0.77 and (f) 0.81 with different scan rates.*

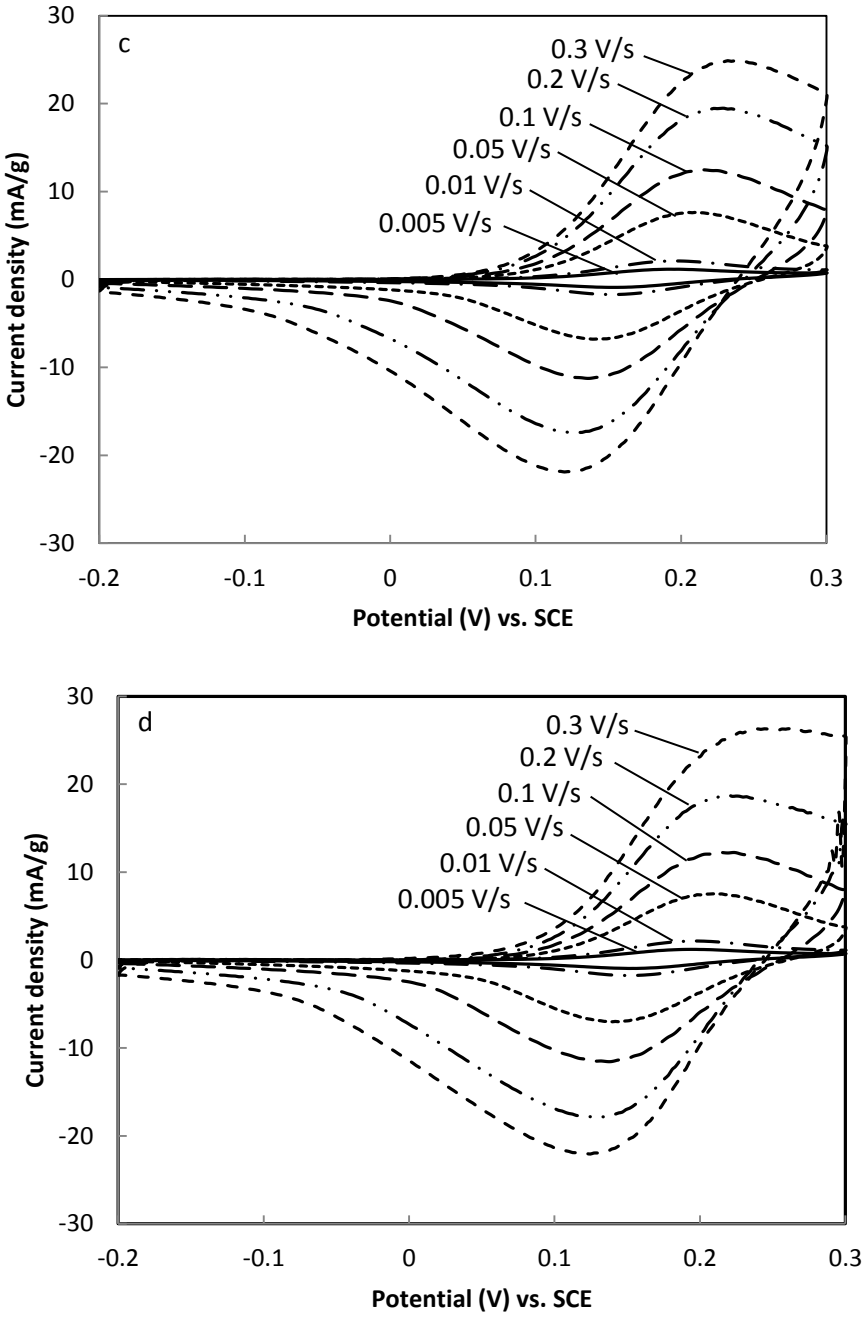

***Fig. 8.9**, Cyclic voltammograms of Ni samples with the pore size of 1000-1500 µm and porosity of (a) 0.65, (b) 0.67, (c) 0.70, (d) 0.73, (e) 0.77 and (f) 0.81 with different scan rates.*

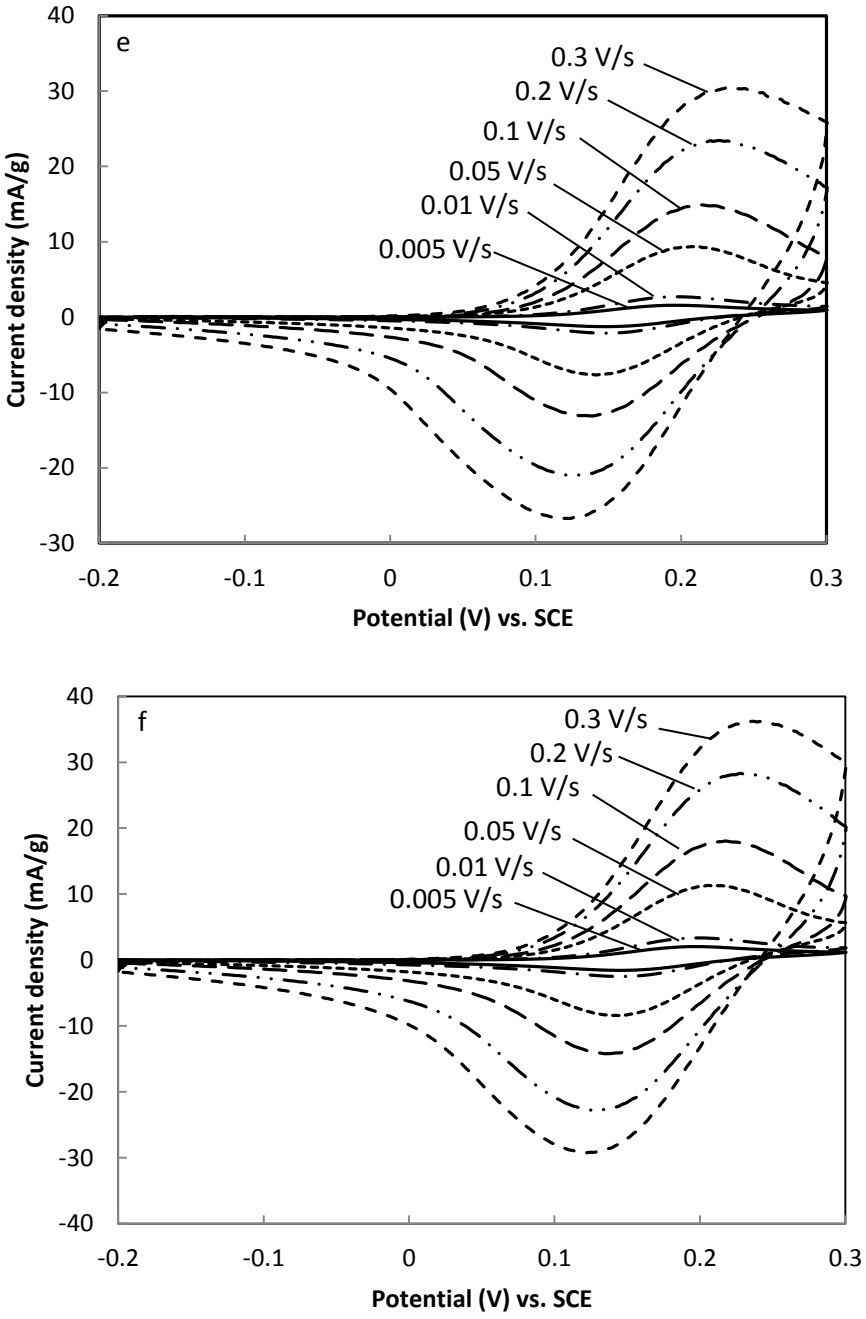

***Fig. 8.9**, Cyclic voltammograms of Ni samples with the pore size of 1000-1500 µm and porosity of (a) 0.65, (b) 0.67, (c) 0.70, (d) 0.73, (e) 0.77 and (f) 0.81 with different scan rates.*

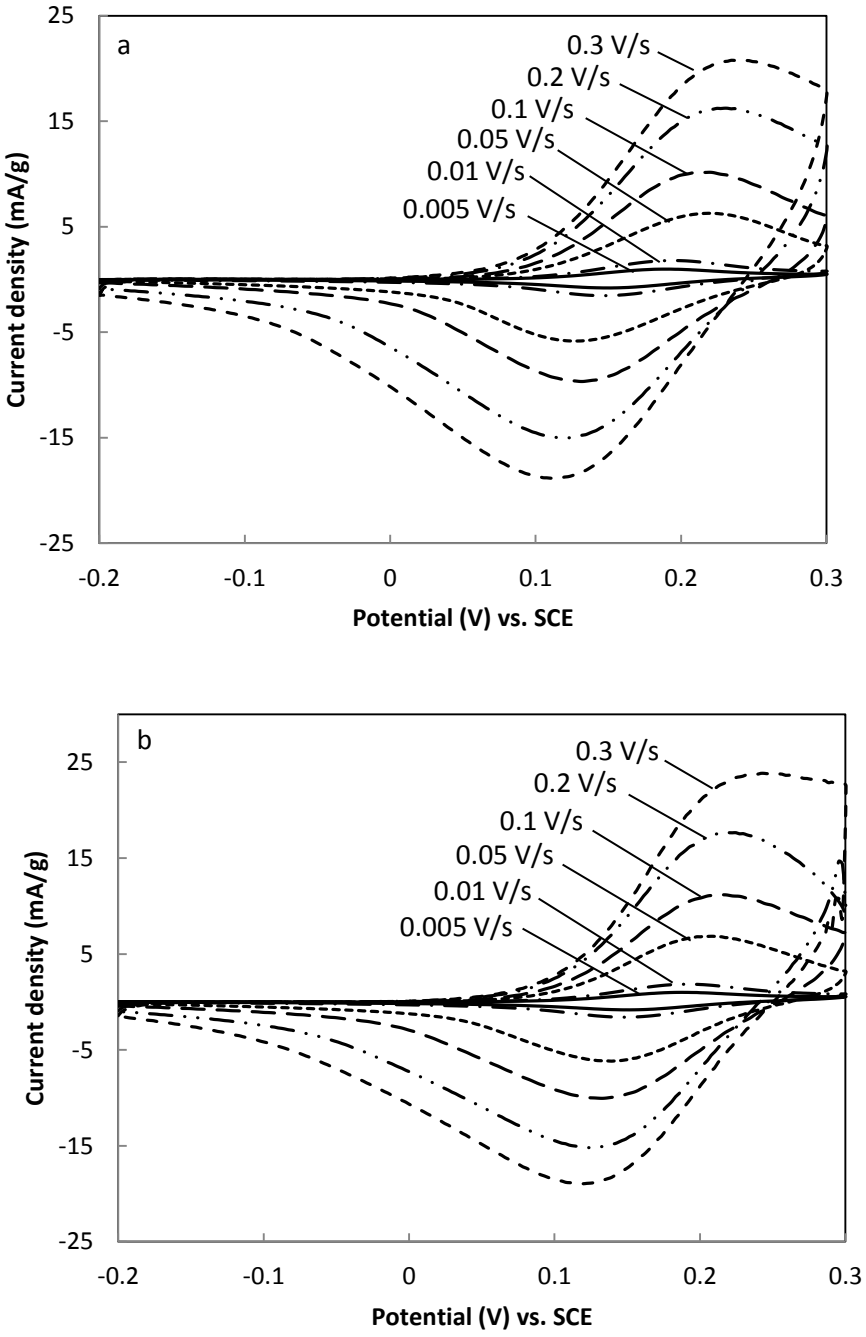

***Fig. 8.10**, Cyclic voltammograms of Ni samples with the pore size of 710-1000 µm and porosity of (a) 0.63, (b) 0.66, (c) 0.69, (d) 0.73 and (e) 0.81 with different scan rates.*

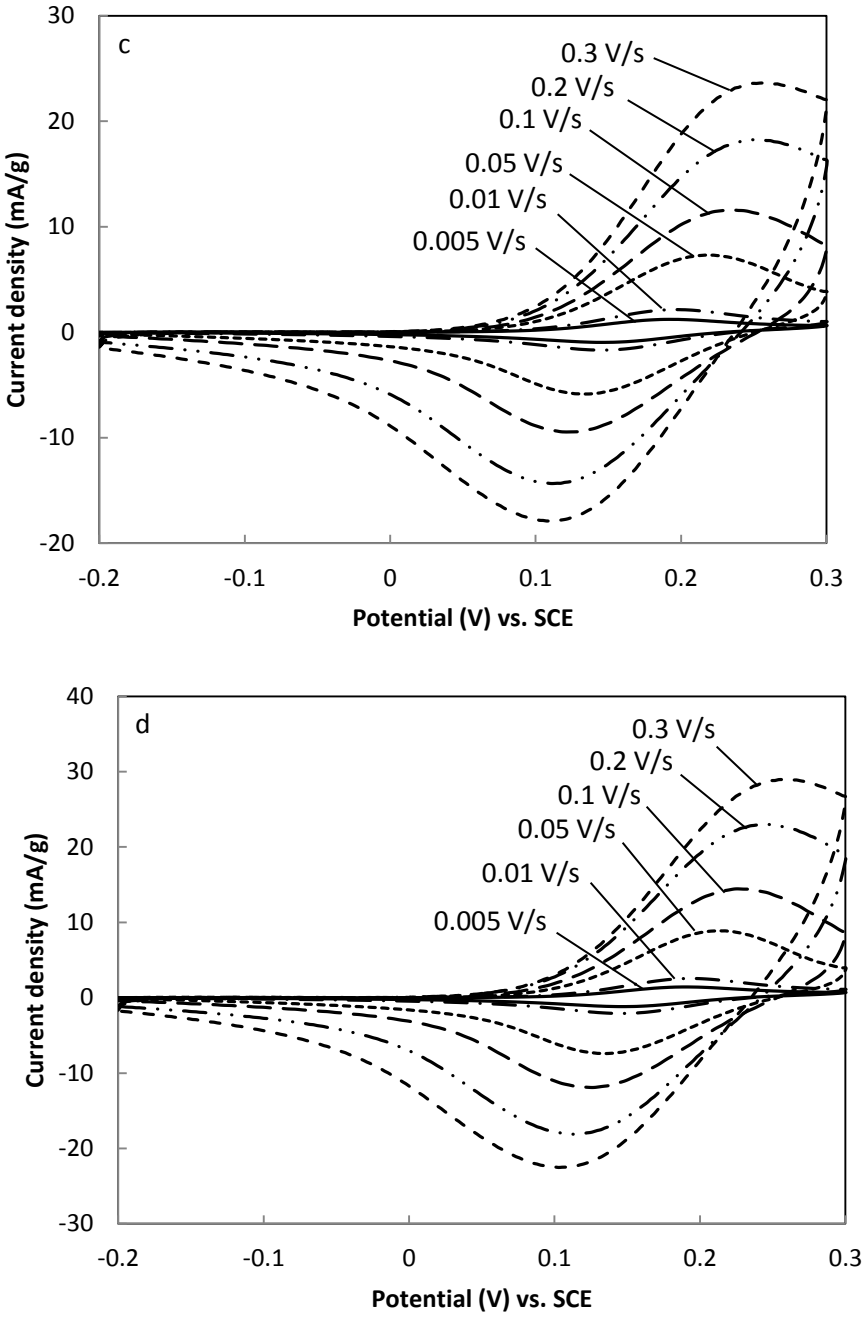

***Fig. 8.10**, Cyclic voltammograms of Ni samples with the pore size of 710-1000 µm and porosity of (a) 0.63, (b) 0.66, (c) 0.69, (d) 0.73 and (e) 0.81 with different scan rates.*

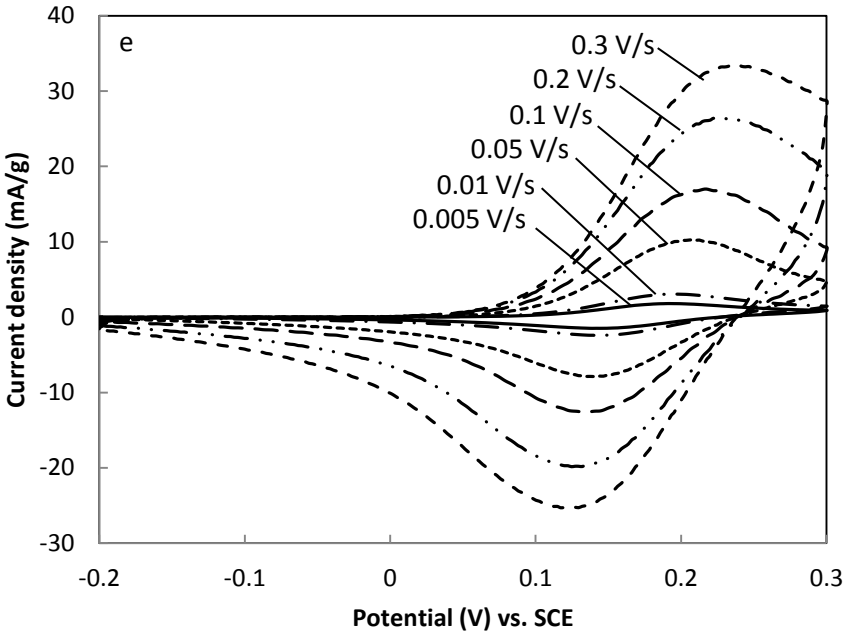

***Fig. 8.10**, Cyclic voltammograms of Ni samples with the pore size of 710-1000 µm and porosity of (a) 0.63, (b) 0.66, (c) 0.69, (d) 0.73 and (e) 0.81 with different scan rates.*

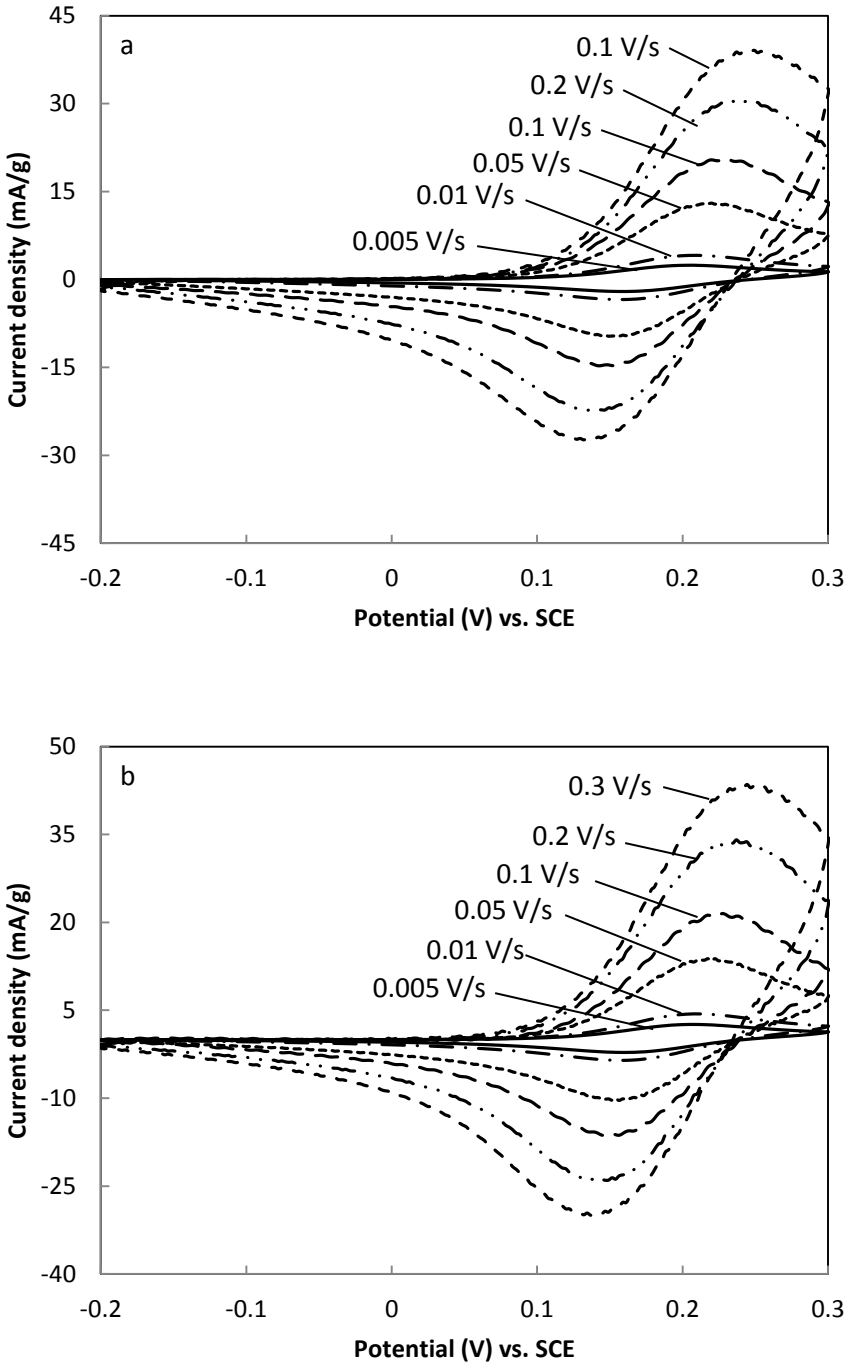

***Fig. 8.11**, Cyclic voltammograms of Ni samples with the pore size of 425-710 µm and porosity of (a) 0.75 and (b) 0.81 with different scan rates.*

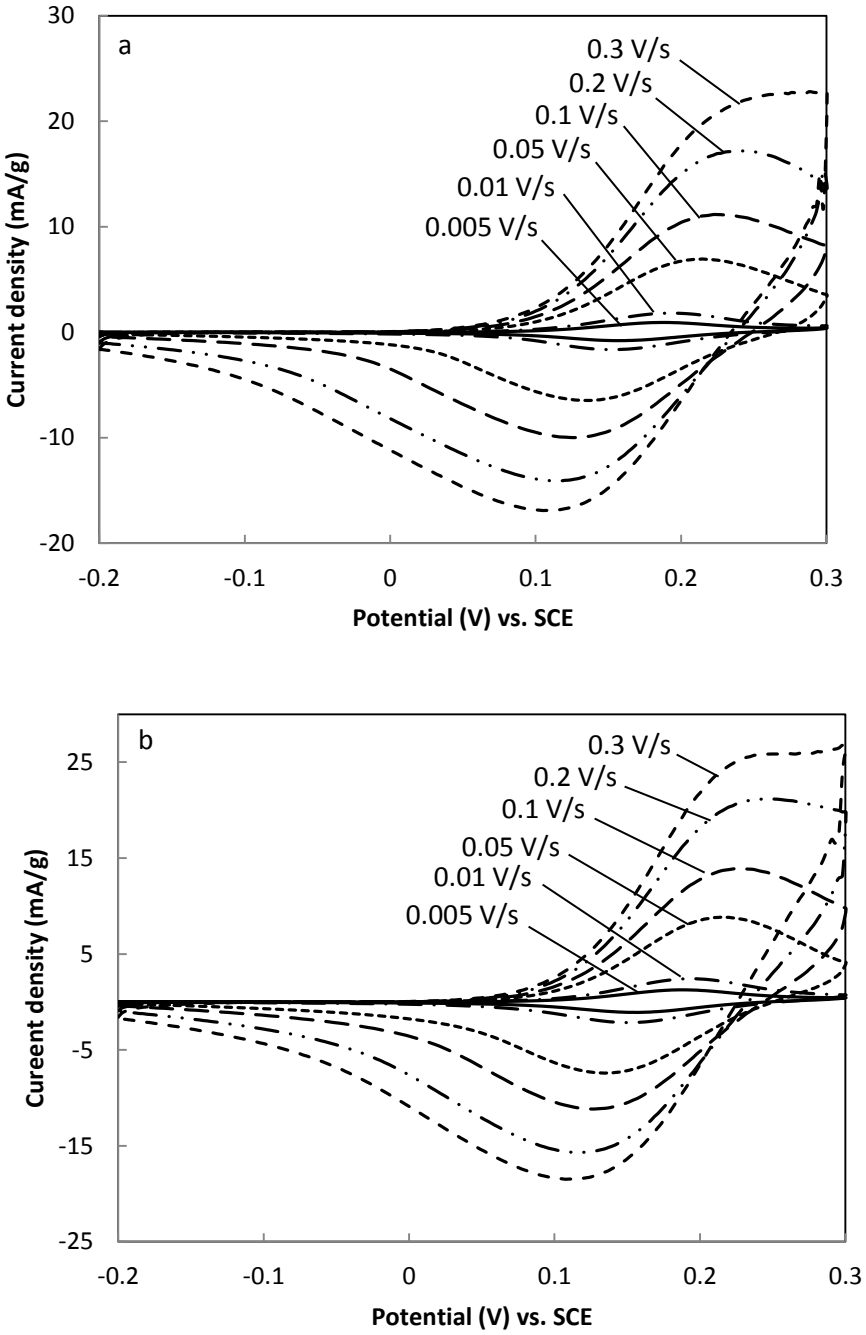

Fig. 8.12, *Cyclic voltammograms of Ni samples with the pore size of 250-425 µm and porosity of (a) 0.62, (b) 0.65, (c) 0.68, (d) 0.71, (e) 0.75 and (f) 0.79 with different scan rates.*

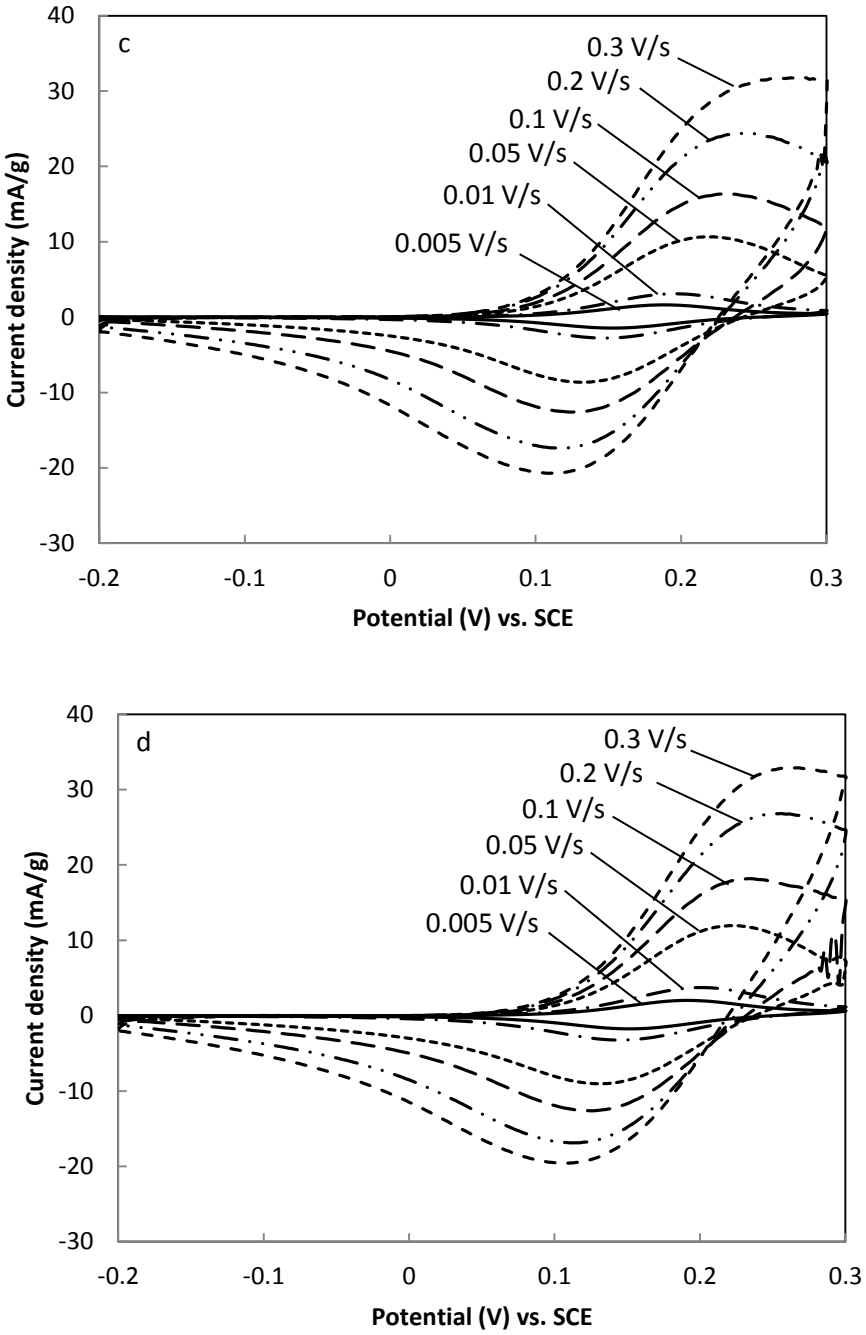

Fig. 8.12, *Cyclic voltammograms of Ni samples with the pore size of 250-425 µm and porosity of (a) 0.62, (b) 0.65, (c) 0.68, (d) 0.71, (e) 0.75 and (f) 0.79 with different scan rates.*

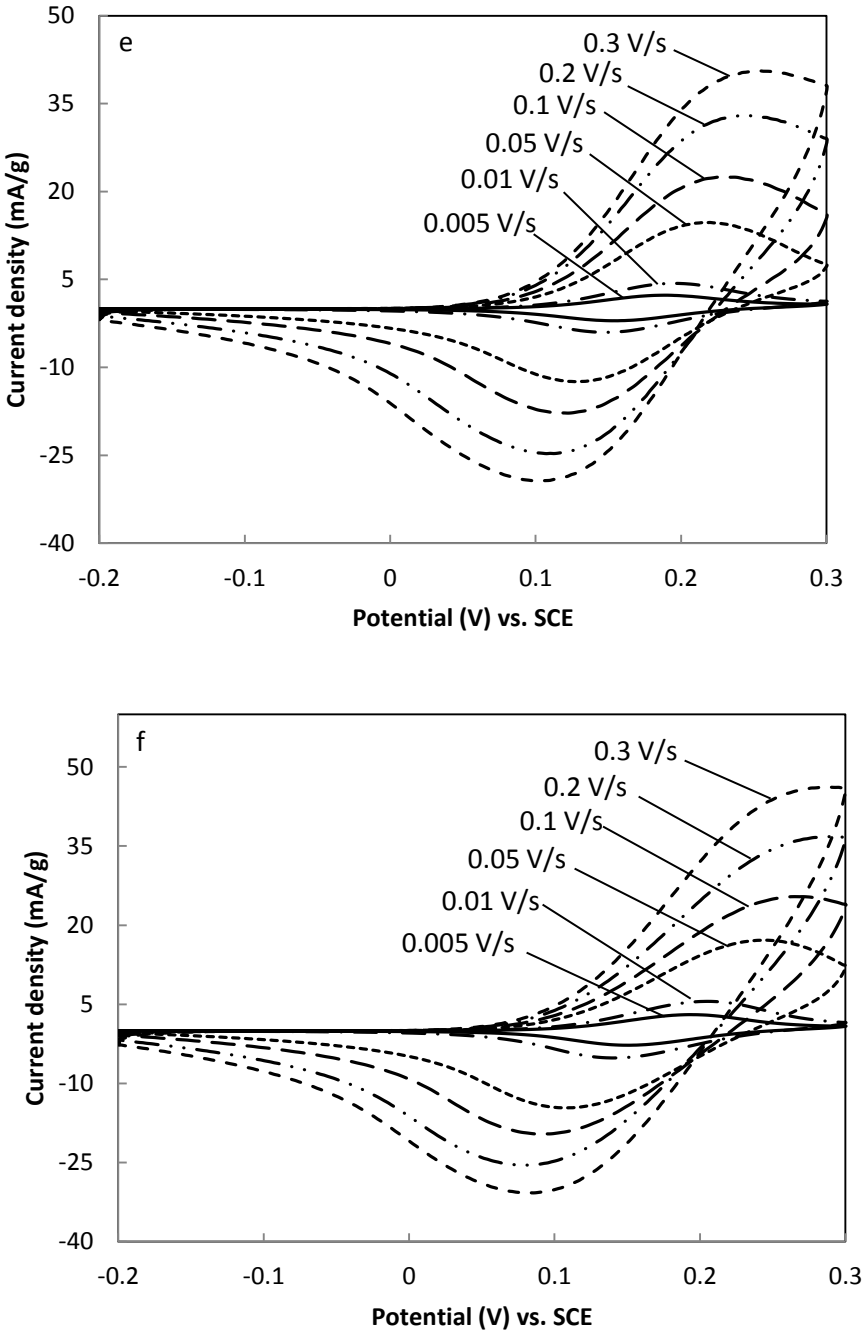

Fig. 8.12, *Cyclic voltammograms of Ni samples with the pore size of 250-425 µm and porosity of (a) 0.62, (b) 0.65, (c) 0.68, (d) 0.71, (e) 0.75 and (f) 0.79 with different scan rates.*

8.4 Effect of Scan Rate

Figs. 8.13 (a-d) and 8.14 (a-d) show the gravimetric and volumetric specific electro-active surface areas, respectively, of porous nickel samples measured at different scan rates, porosity and pore size. Both the gravimetric and volumetric specific electro-active surface areas increased with scan rate. The decrease in electro-active surface area at low scan rates was because low scan rate leads to a thick diffusion layer. The features smaller than the diffusion layer, such as the secondary pores, become difficult to be detected. According to Eqn. 8.1, the relationship between diffusion layer thickness and scan rate can be expressed by $\delta \propto \sqrt{1/v}$. Therefore, the thickness of diffusion layer increases rapidly when the scan rate < 0.05 v/s. Figs. 8.13 (a-d) and 8.14 (a-d) show the electro-active surface area decreases rapidly when the scan rate < 0.05 v/s. The experimental data fit to the change of the diffusion layer thickness at different scan rates. In addition, the transition from semi-infinite to thin-layer controlled diffusion at low scan rates can also lead to decrease of peak current.

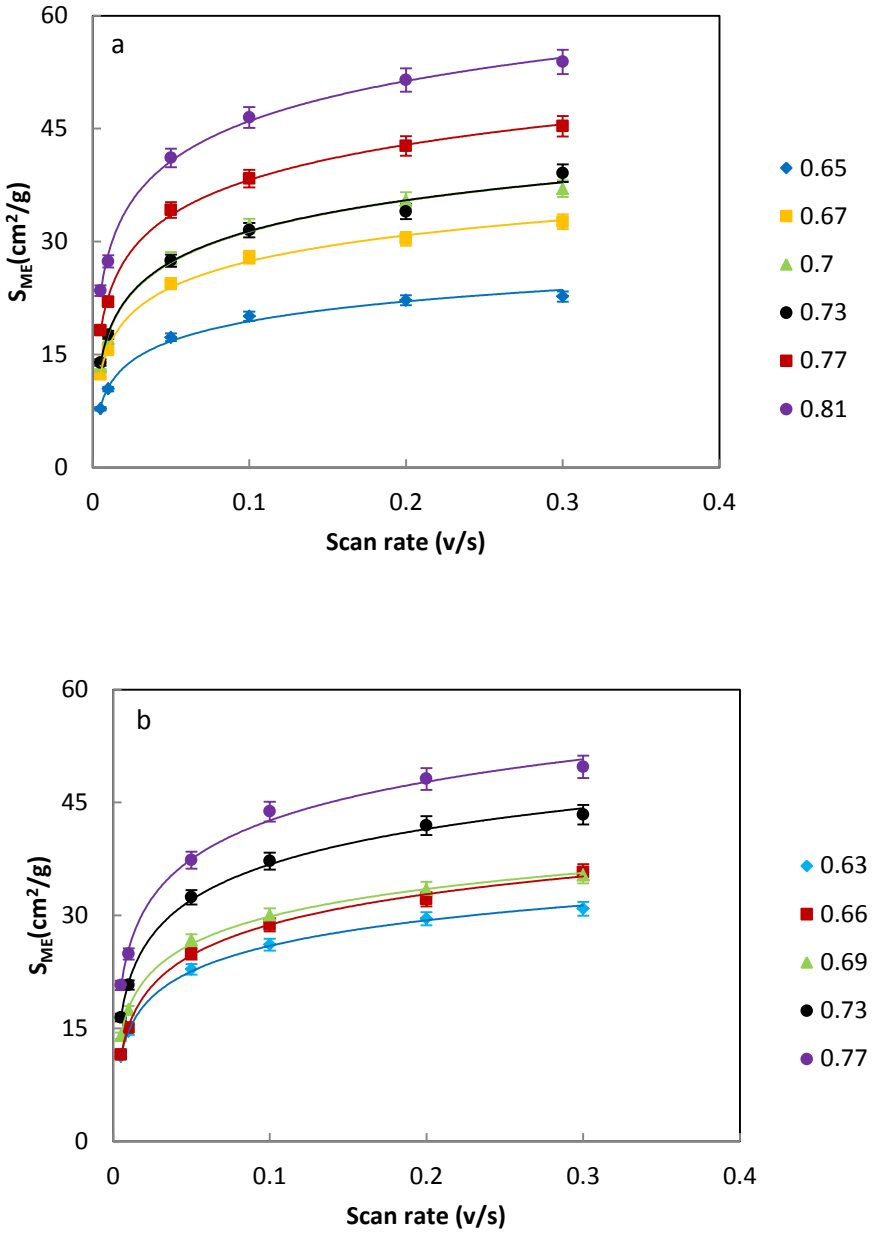

***Fig. 8.13**, Variations of gravimetric electro active surface areas (S_{ME}) with scan rate at different porosities and pore sizes of (a) 1000-1500 µm, (b) 710-1000 µm, (c) 425-710 µm and (d) 250-425 µm.*

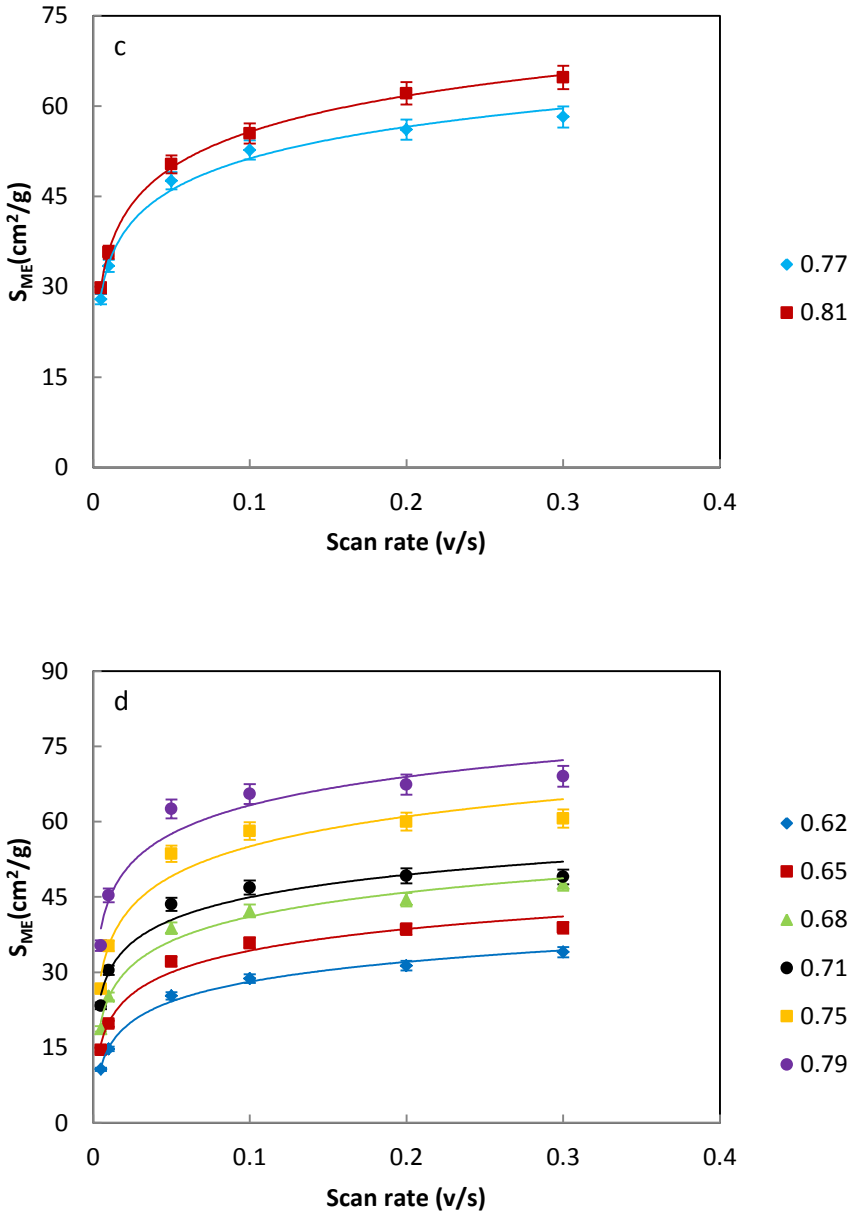

***Fig. 8.13**, Variations of gravimetric electro active surface areas (S_{ME}) with scan rate at different porosities and pore sizes of (a) 1000-1500 µm, (b) 710-1000 µm, (c) 425-710 µm and (d) 250-425 µm.*

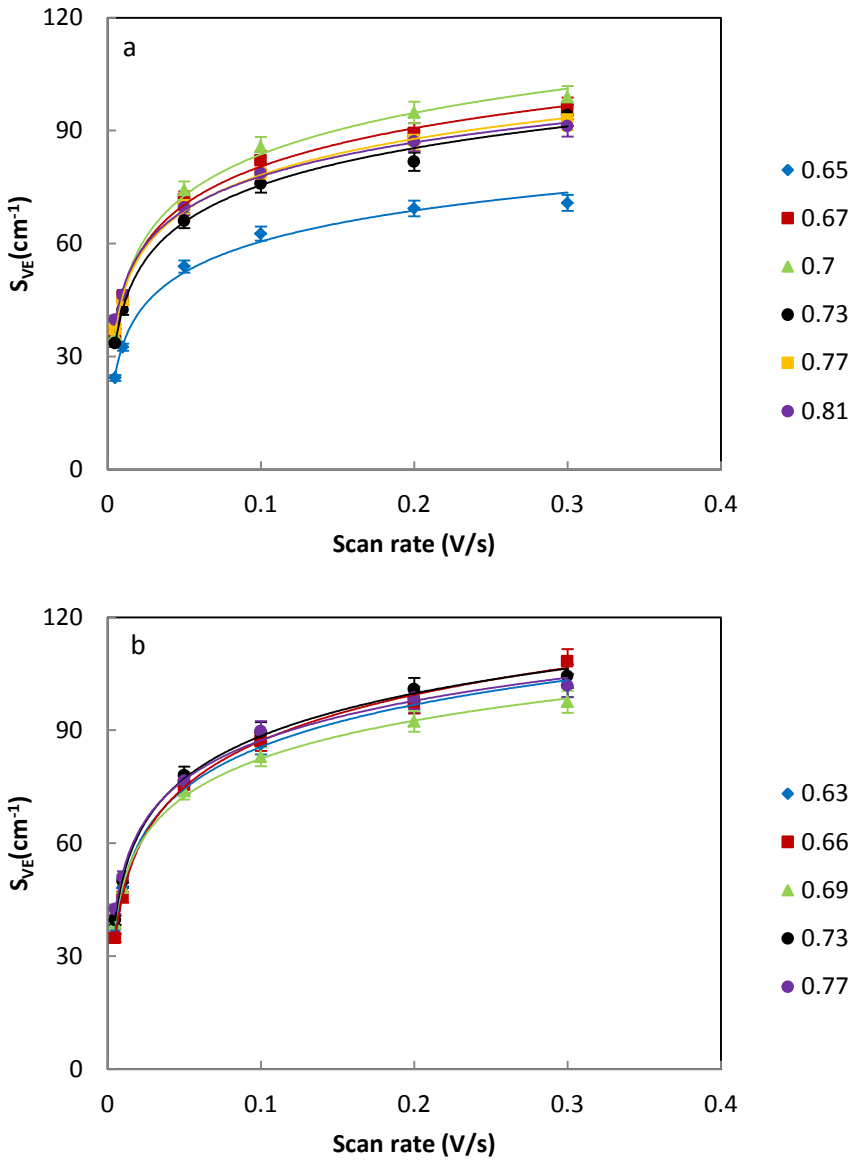

***Fig. 8.14**, Variations of volumetric specific electro active surface areas (S_{VE}) with scan rate at different porosities and pore sizes of (a) 1000-1500 µm, (b) 710-1000 µm, (c) 425-710 µm and (d) 250-425 µm.*

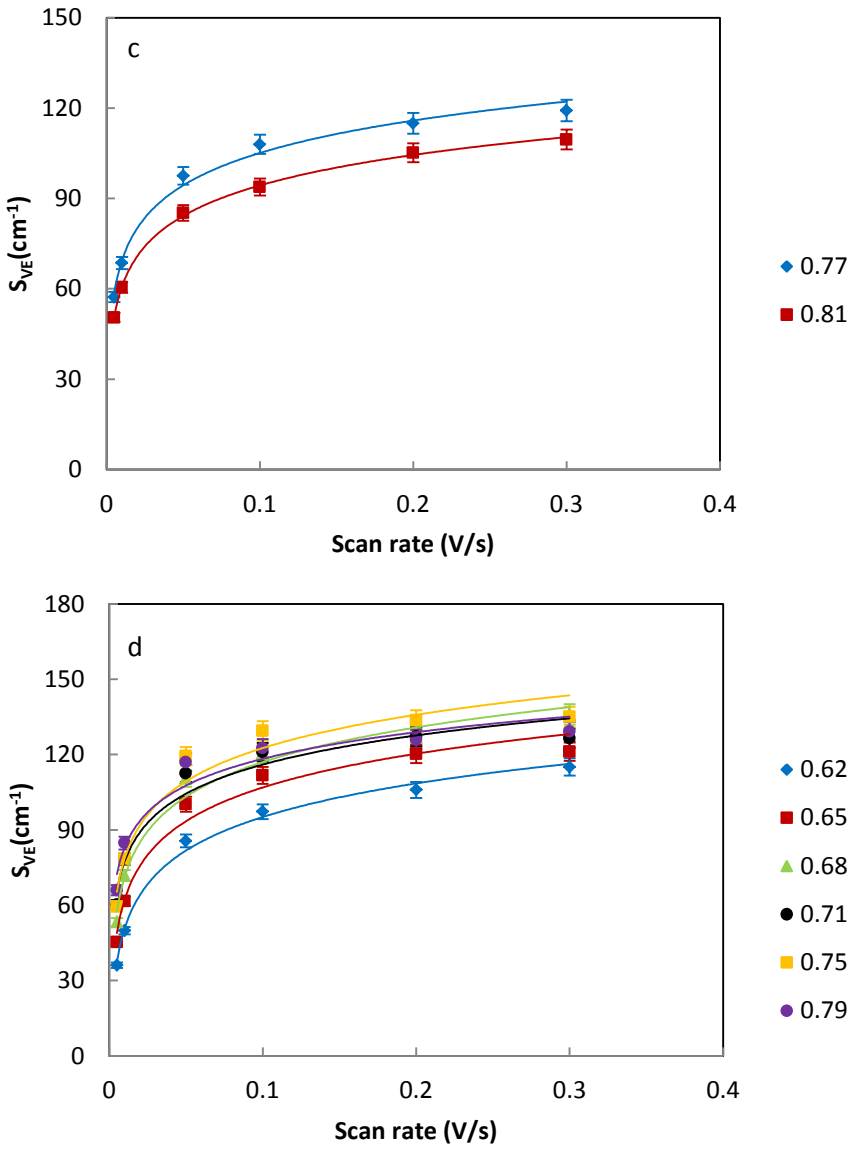

***Fig. 8.14**, Variations of volumetric specific electro active surface areas (S_{VE}) with scan rate at different porosities and pore sizes of (a) 1000-1500 µm, (b) 710-1000 µm, (c) 425-710 µm and (d) 250-425 µm.*

8.5 Effects of Porosity and Pore Size

The variations of gravimetric and volumetric specific electro active surface areas, measured by the CV, as a function of porosity at different pore sizes and scan rates are shown in Figs. 8.15 (a-f) and 8.16 (a-f), respectively.

The gravimetric specific electro active surface areas of the samples are in the range of 8-35 cm^2/g, 10-45 cm^2/g, 17-63 cm^2/g, 20-65 cm^2/g, 22-67 cm^2/g and 23-69 cm^2/g at the scan rate of 0.005 V/s, 0.01 V/s, 0.05 V/s, 0.1 V/s, 0.2 V/s and 0.3 V/s, respectively. For all scan rates, the gravimetric specific electro active surface area increased with porosity and decreased with pore size.

The volumetric specific electro-active surface areas of these samples are in the range of 24-66 cm^{-1}, 32-85 cm^{-1}, 54-120 cm^{-1}, 63-130 cm^{-1}, 69-134 cm^{-1} and 70-135 cm^{-1} at the scan rate of 0.005 V/s, 0.01 V/s, 0.05 V/s, 0.1 V/s, 0.2 V/s and 0.3 V/s, respectively. For all scan rates, the volumetric specific electro-active surface area increased with porosity and decreased with pore size. However, the trend of the effect of porosity on the volumetric specific electro active surface area is not pronounced.

In Figs. 8.15 & 8.16, the trend of the effect of porosity on electro-active surface area is very similar to the change of the calculated value of geometric surface area by Stochastic modelling at different porosities (Fig. 6.3). When the calculated value of geometric surface area multiplies a fitted constant in the range from 0.5 to 2.9, the calculated value can be fitted with the experimental data of electro-active surface area very well which is shown in Figs. 8.15 & 8.16.

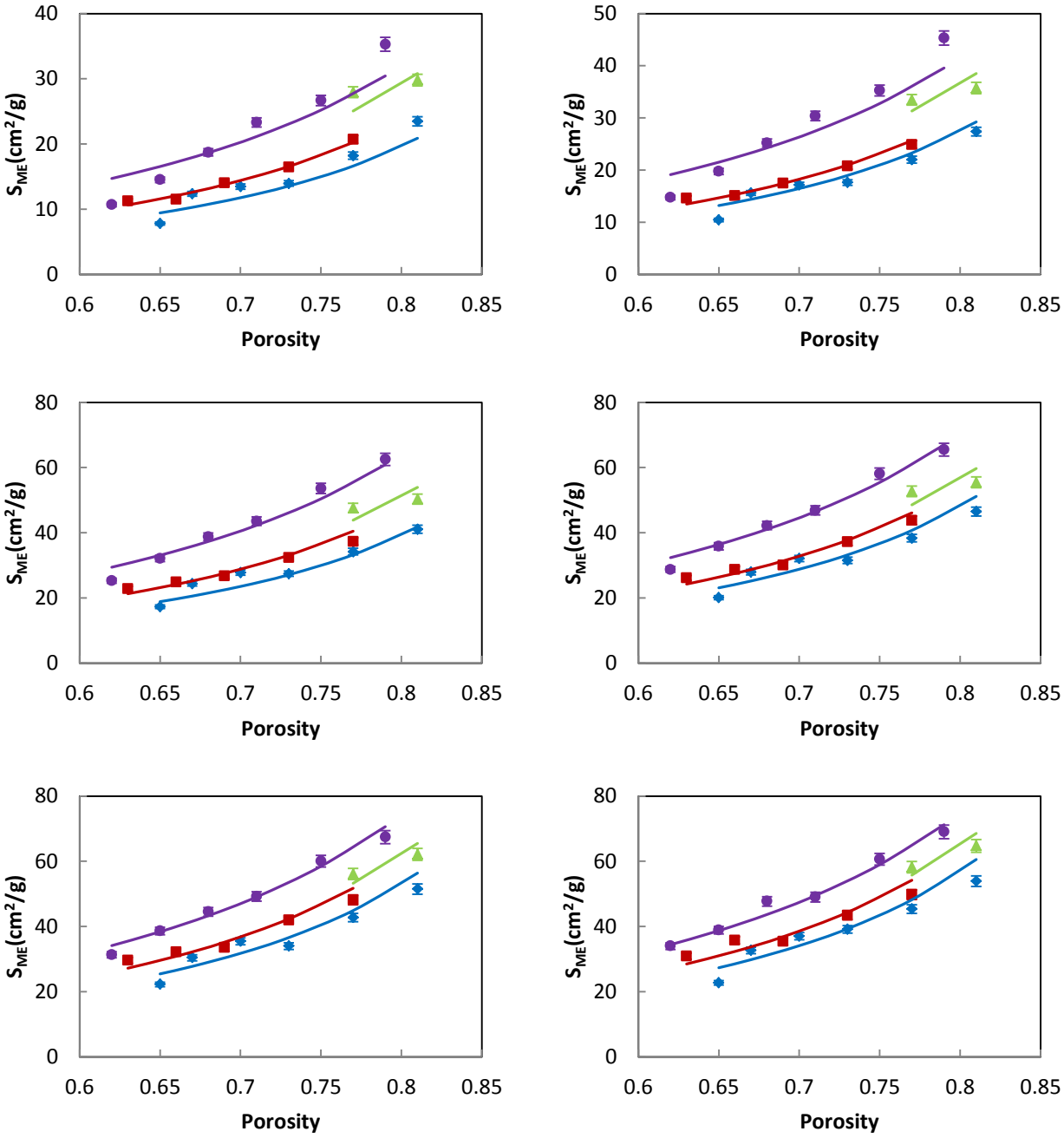

***Fig. 8.15**, Variations of gravimetric specific geometric surface areas (S_{VE}) with porosity for porous Ni with different pore sizes: (●250-425 µm, ▲425-710 µm, ■710-1000 µm, ◆1000-1500 µm) and at different scan rates: (a) 0.005 V/s, (b) 0.01 V/s, (c) 0.05 V/s, (d) 0.1 V/s, (e) 0.2 V/s and (f) 0.3 V/s.*

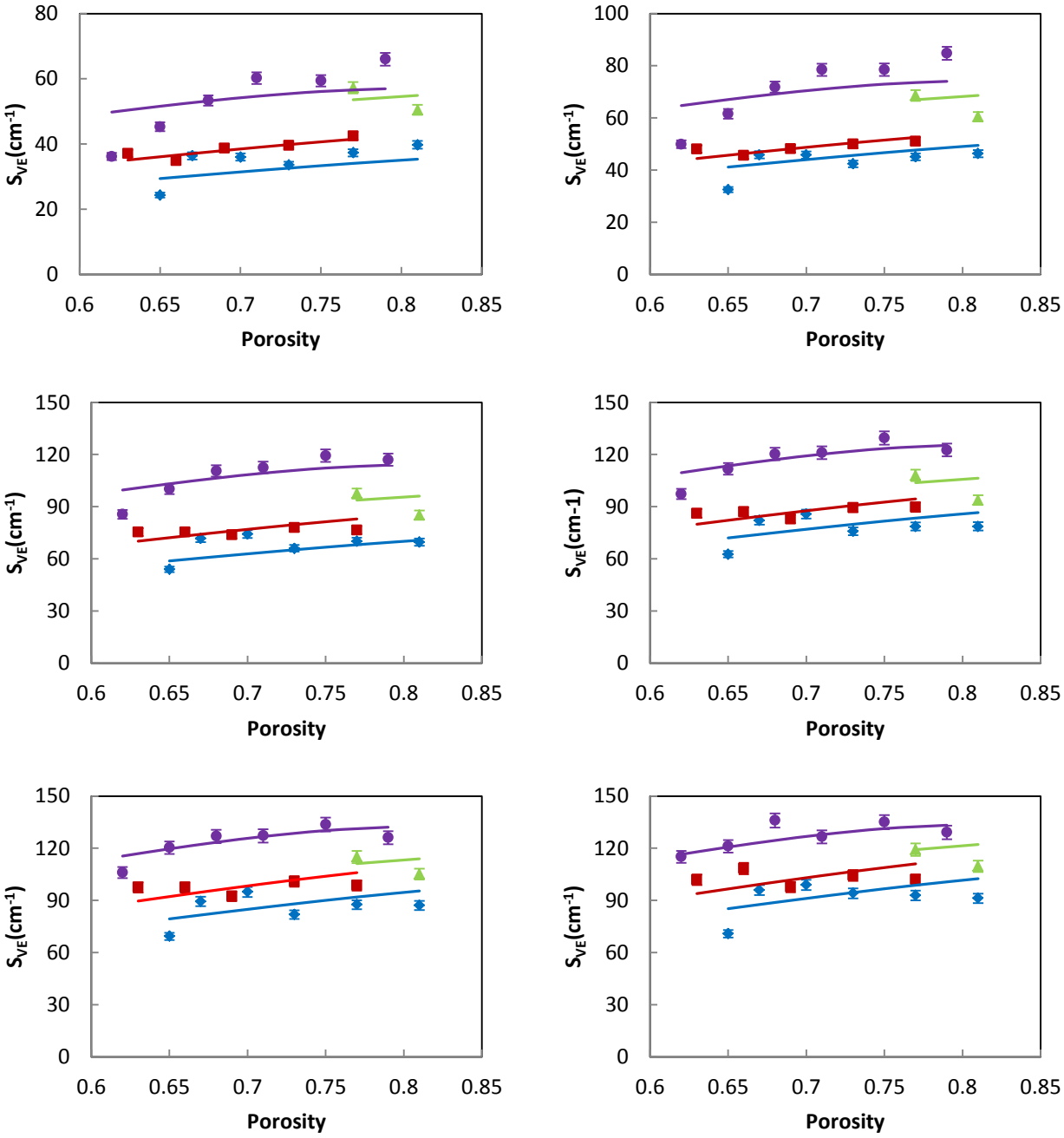

***Fig. 8.16**, Variations of volumetric specific geometric surface areas (S_{VE}) with porosity for porous Ni with different pore sizes: (●250-425 µm, ▲425-710 µm, ■710-1000 µm, ◆1000-1500 µm) and at different scan rates: (a) 0.005 V/s, (b) 0.01 V/s, (c) 0.05 V/s, (d) 0.1 V/s, (e) 0.2 V/s and (f) 0.3 V/s.*

8.6 Discussion

Table A8.4 (see Appendixes) shows the values of the ratio between electro-active and geometric surface areas (θ) for the porous Ni samples with different pore sizes and porosities at different predicted diffusion layer thickness (δ), which was calculated from Eqn. 7.3 for a series of scan rates (0.005 V/s, 0.01 V/s, 0.05 V/s, 0.1 V/s, 0.2 V/s and 0.3 V/s). The ratio of electro-active to geometric surface areas as a function of predicted diffusion layer thickness is shown in Fig. 8.17. The ratio between electro-active and geometric surface areas decreased with diffusion layer thickness because a thicker diffusion layer means that less surface features on the sample can be detected by CV.

Fig. 8.18 shows the variations of the reciprocal of the ratio between electro-active and geometric surface areas ($1/\theta$) as a function of predicted diffusion layer thickness (δ). For each pore size in semi-infinite, $1/\theta$ increases with δ nearly linearly for $\delta \lesssim 32$ μm and is not very sensitive to porosity. However, deviations from linear relations occurred when δ >32 μm due to the thin-layer effect and the reaction cannot be controlled by diffusion, especially in the samples with small pore size (250-425 μm).

Figs. 8.13 and 8.14 show that the electro-active surface area increased with scan rate. At a very high scan rate, the diffusion layer thickness becomes infinitesimal. The electro-active surface area detected by CV would approach a fixed value representative of the maximum electro-active surface area of the porous Ni sample. The ratio between the maximum electro-active surface area and the geometric surface area, θ_M, can be obtained from the plot of $\frac{1}{\theta}$ vs. δ at δ=0.

Fig. 8.19 shows that θ_M increased with the surface weighted mean pore size of the samples. θ_M is always greater than one, indicating that more surfaces than the geometric surface area

are contributing to the electrochemical reactions and peak current. The effect of pore size is in agreement with the results for porous Cu. The electro active species in the electrolyte is consumed more rapidly with the decrease of pore size during the CV measurement. It leads to a greater actual diffusion layer than that predicted for small pores. In samples with large pores, the reservoir of electrolyte with the initial concentration of the electro active species is bigger. The actual diffusion layer approaches the predicted value.

An especially interesting characteristic of the trendline is that the intercept at the vertical axis is approximately 1. It is because the electro-active surface area would equal to geometric surface area when primary pore size is 0 and surface area is only provided by secondary pores. This shows that the electro-active surface area converges to the geometric surface area when pore size approaches zero.

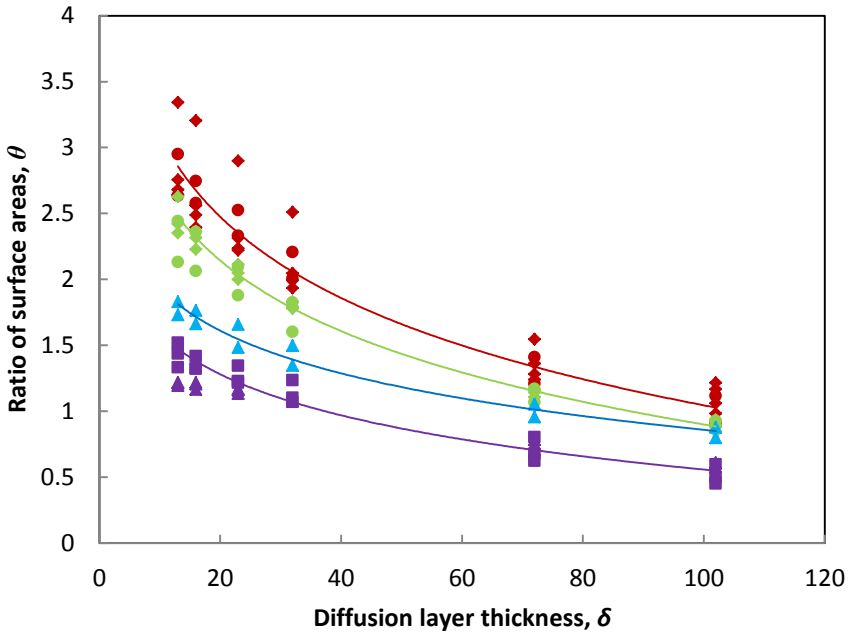

***Fig. 8.17**, Variations of the ratio between the electro active (S_{VE}) and geometric (S_{VG}) surface areas with predicted diffusion layer thickness at different porosities and pore sizes: (◆) 1000-1500 µm, <0.7 porosity, (●) 1000-1500 µm, >0.7 porosity, (◆) 710-1000 µm, <0.7 porosity, (●) 710-1000 µm, >0.7 porosity, (▲) 425-710 µm, >0.7 porosity, (■) 250-425 µm, <0.7 porosity and (▲) 250-425 µm, >0.7 porosity.*

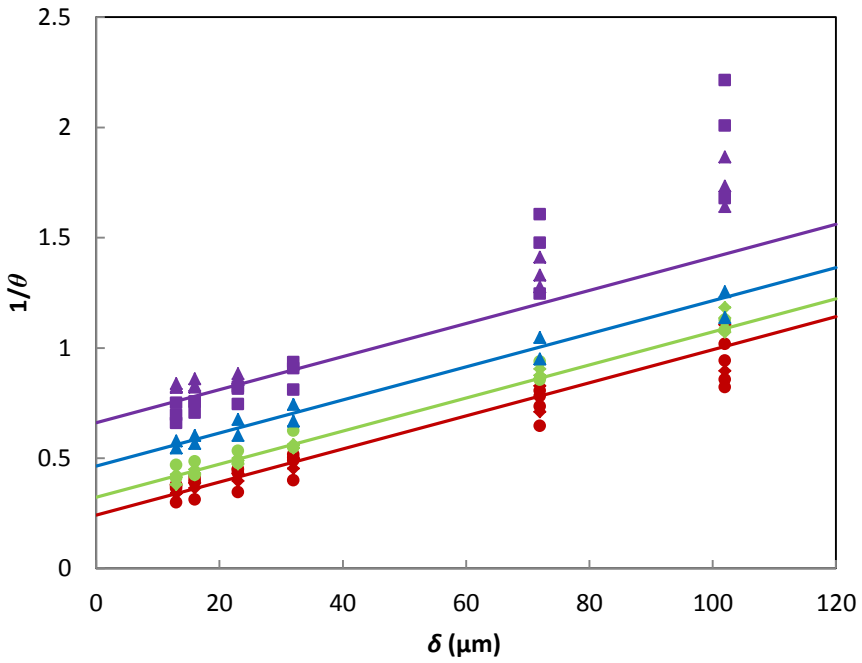

Fig. 8.18, *Variations of the reciprocal of the ratio between electro active (A_E) and geometric (A_G) surface areas ($1/\theta$) with predicted diffusion layer thickness (δ) at different porosity and pore sizes: (◆) 1000-1500 µm, <0.7 porosity, (●) 1000-1500 µm, >0.7 porosity, (◆) 710-1000 µm, <0.7 porosity, (●) 710-1000 µm, >0.7 porosity, (▲) 425-710 µm, >0.7 porosity, (■) 250-425 µm, <0.7 porosity and (▲) 250-425 µm, >0.7 porosity.*

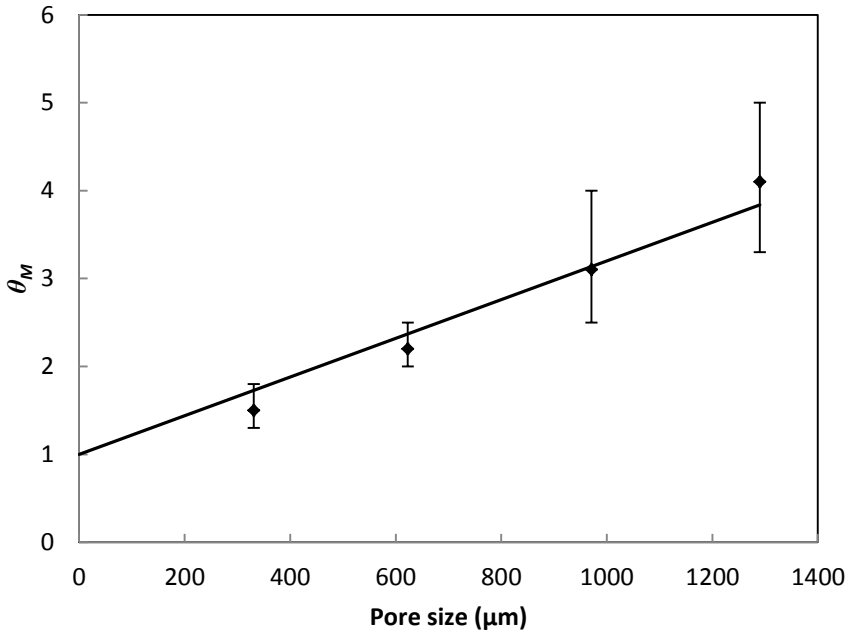

Fig. 8.19*, Linear relation between the maximum ratio, θ_M, and surface weighted mean pore size of the porous Ni (measured by Malvern Mastersizer 2000).*

Chapter 9 Real Surface Area of Porous Cu

9.1 Voltammograms, Capacitance and Real Surface Area

Figs. 9.1 – 9.5 show the cyclic voltammograms of porous copper samples with different porosities (0.50-0.80) at different scan rates (0.05 V/s, 0.07 V/s, 0.1 V/s, 0.2 V/s, 0.3 V/s, 0.4 V/s and 0.5 V/s) for pore size ranges of 1000-1500 μm, 710-1000 μm, 425-710 μm, 250-425 μm and 75-150 μm, respectively.

The change in current in the charge/discharge cycle (ΔI) increased with scan rate. Linear relations between the ΔI and v (scan rate) in the samples can be obtained and are shown in Figs. 9.6 – 9.10. All the linear relations had a coefficient of determination (R^2) greater than 0.9, as shown in Column 5 of Table A9.1 (see Appendixes). The double layer capacitances (C) in the porous Cu samples are listed in Table A9.1 (see Appendixes) which were obtained from the ratios between ΔI and v, according to Eqn. 3.12. The gravimetric specific real surface areas (S_{MR}) of porous Cu samples were calculated by Eqn. 3.13 and the volumetric specific real surface areas (S_{VR}) were converted by Eqn. 3.5. Both S_{MR} and S_{VR} are listed in Table A9.1 (see Appendixes).

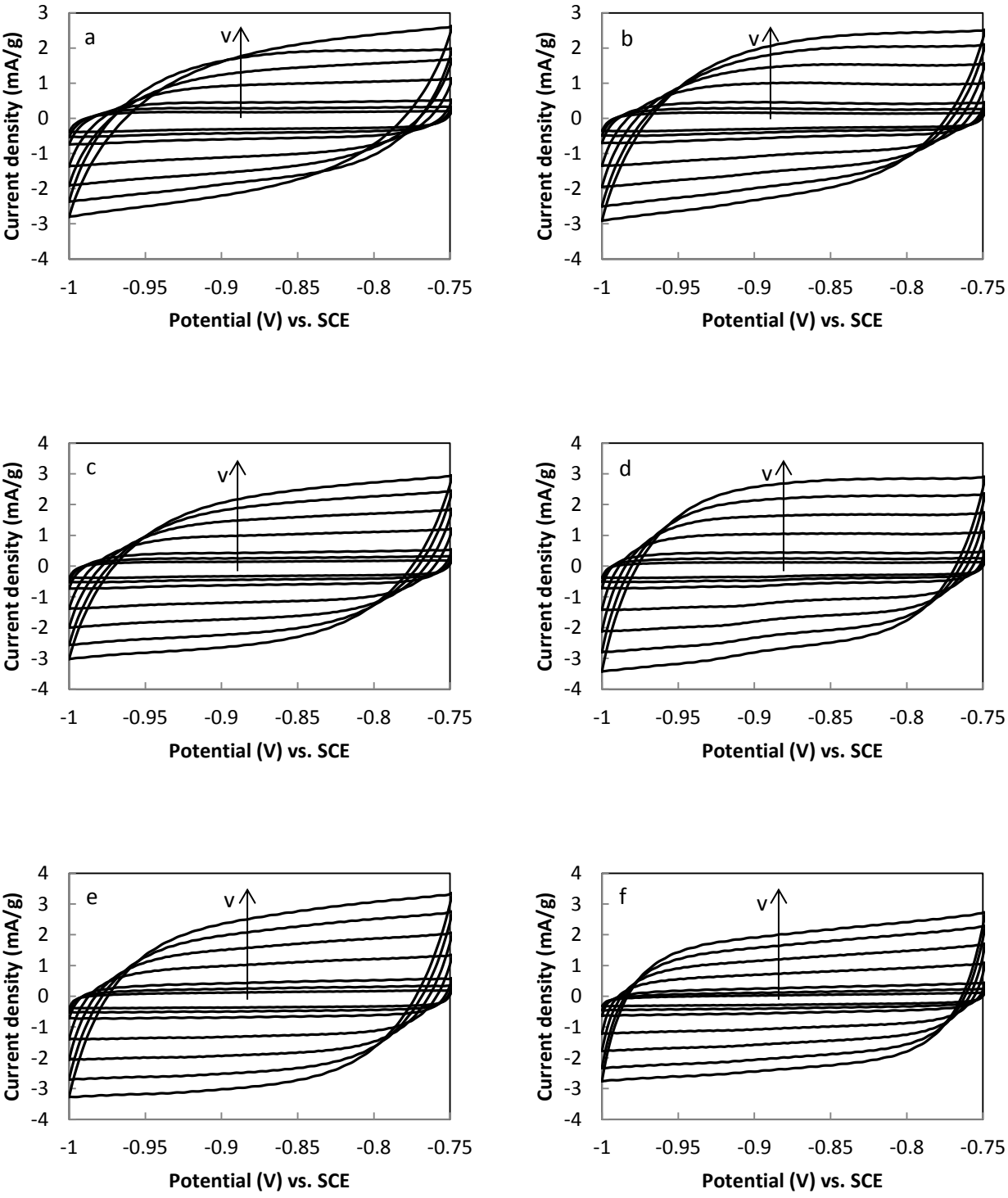

Fig. 9.1 *Cyclic voltammograms of porous Cu samples with the pore size of 1000-1500 µm and porosity of (a) 0.59, (b) 0.62, (c) 0.65, (d) 0.69, (e) 0.72 and (f) 0.76 at various scan rates (from 0.05 V/s to 0.5 V/s).*

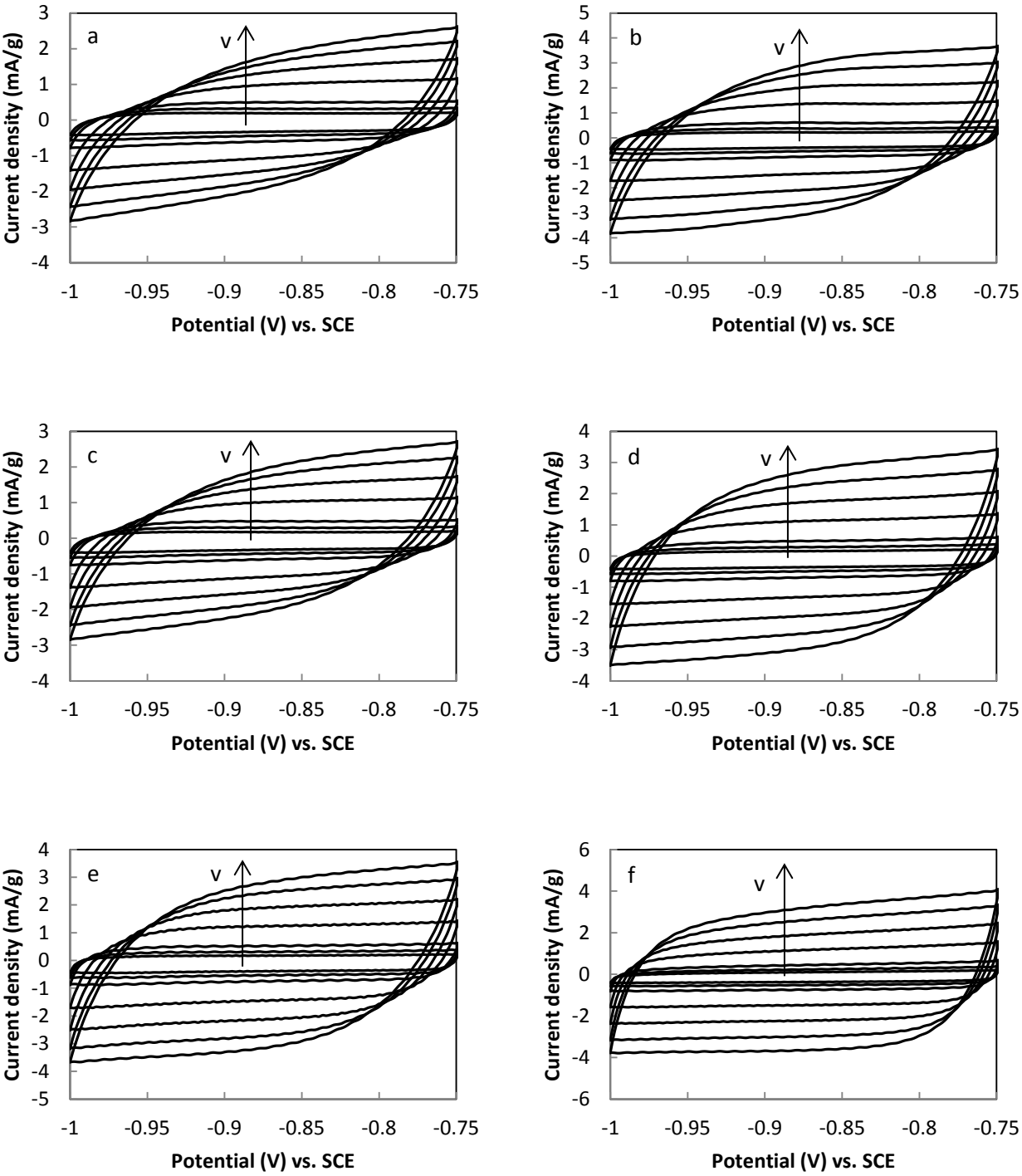

***Fig. 9.2**, Cyclic voltammograms of porous Cu samples with the pore size of 710-1000 µm and porosity of (a) 0.56, (b) 0.59, (c) 0.64, (d) 0.67, (e) 0.71 and (f) 0.74 at various scan rates (from 0.05 V/s to 0.5 V/s).*

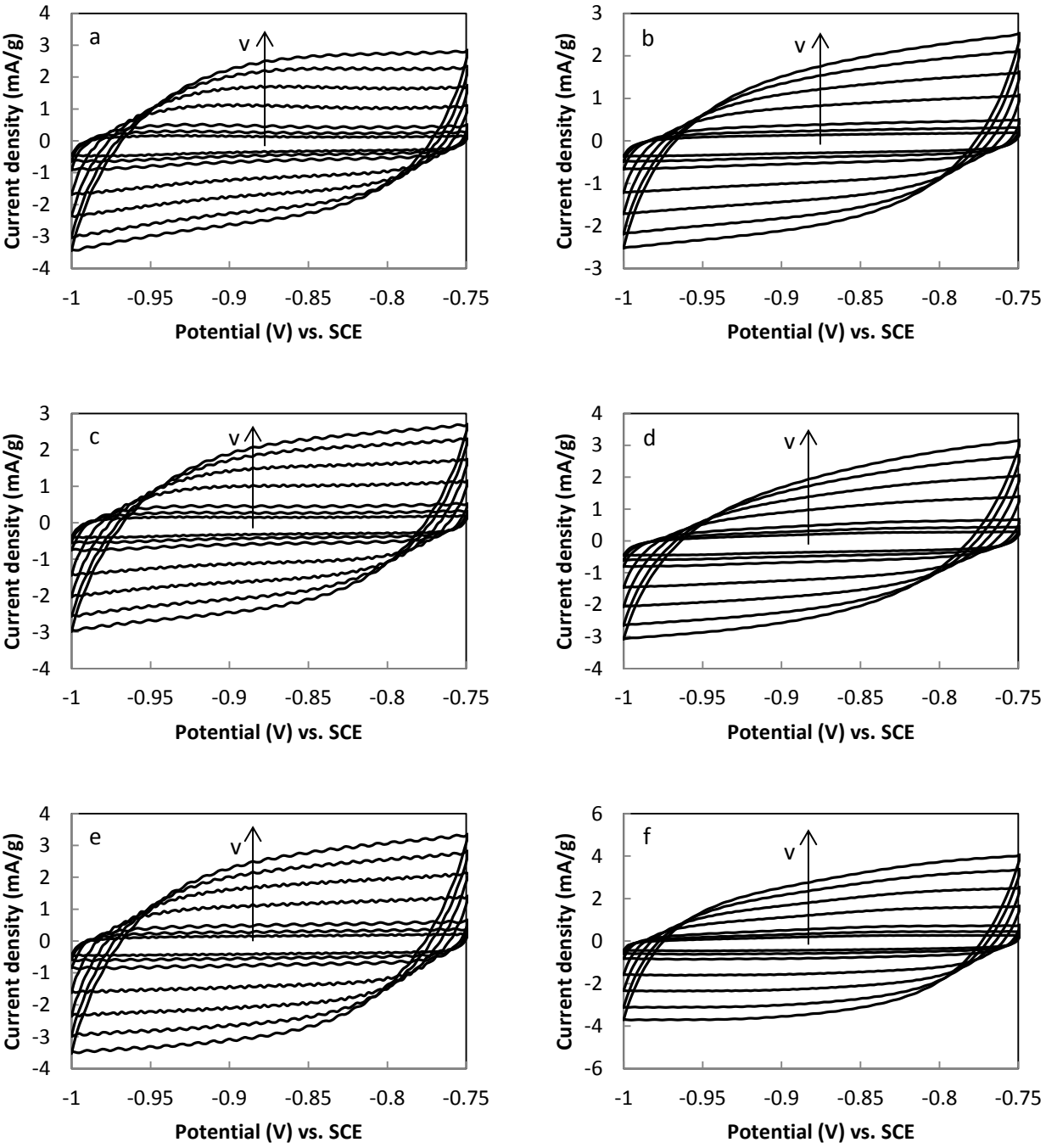

***Fig. 9.3**, Cyclic voltammograms of porous Cu samples with the pore size of 425-710 µm and porosity of (a) 0.57, (b) 0.61, (c) 0.63, (d) 0.67, (e) 0.71and (f) 0.74 at various scan rates (from 0.05 V/s to 0.5 V/s).*

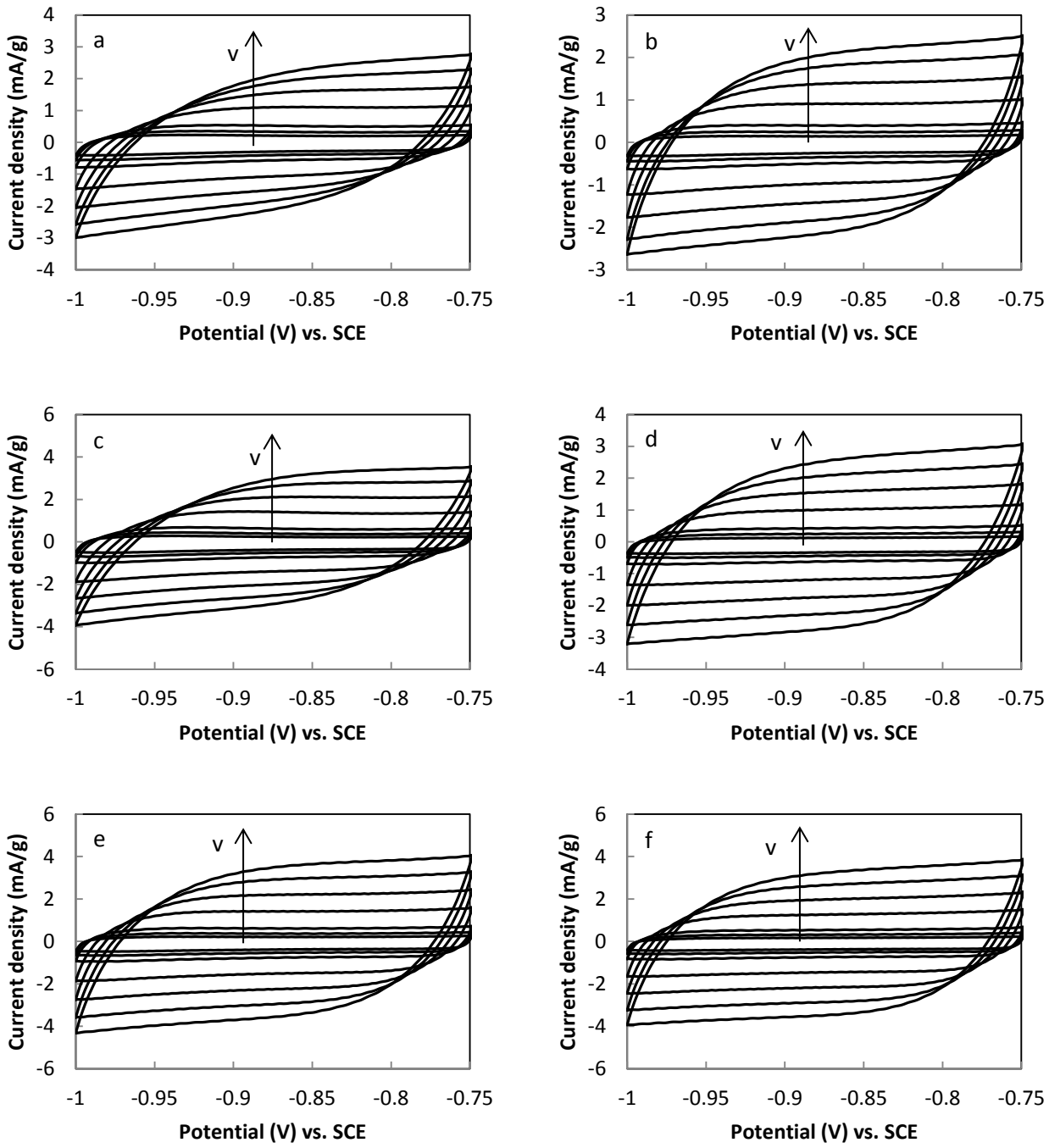

***Fig. 9.4**, Cyclic voltammograms of porous Cu samples with the pore size of 250-425 µm and porosity of (a) 0.55, (b) 0.59, (c) 0.63, (d) 0.66, (e) 0.70 and (f) 0.73 at various scan rates (from 0.05 V/s to 0.5 V/s).*

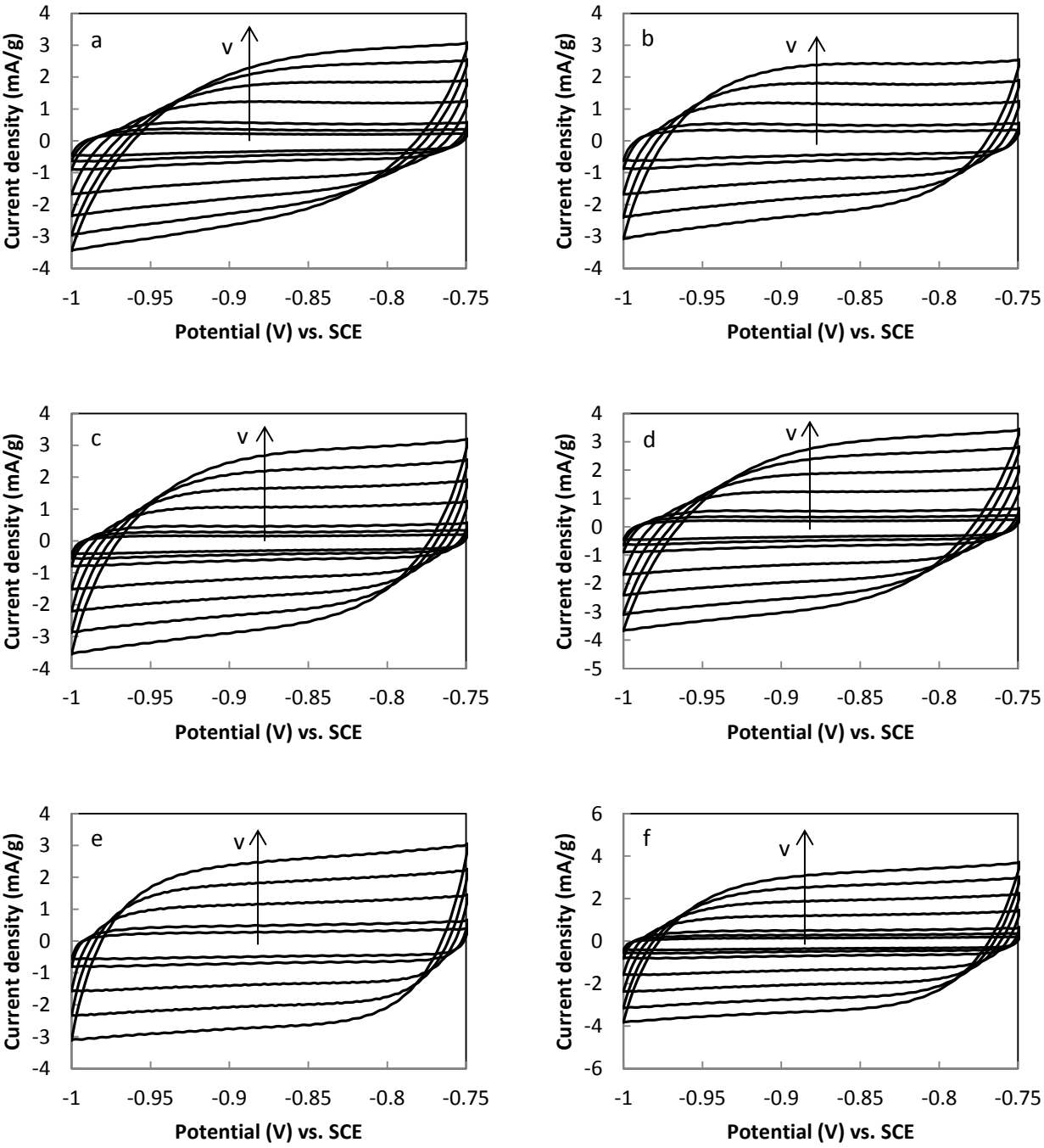

***Fig. 9.5**, Cyclic voltammograms of porous Cu samples with the pore size of 75-150 µm and porosity of (a) 0.53, (b) 0.56, (c) 0.61, (d) 0.63, (e) 0.67 and (f) 0.68 at various scan rates (from 0.05 V/s to 0.5 V/s).*

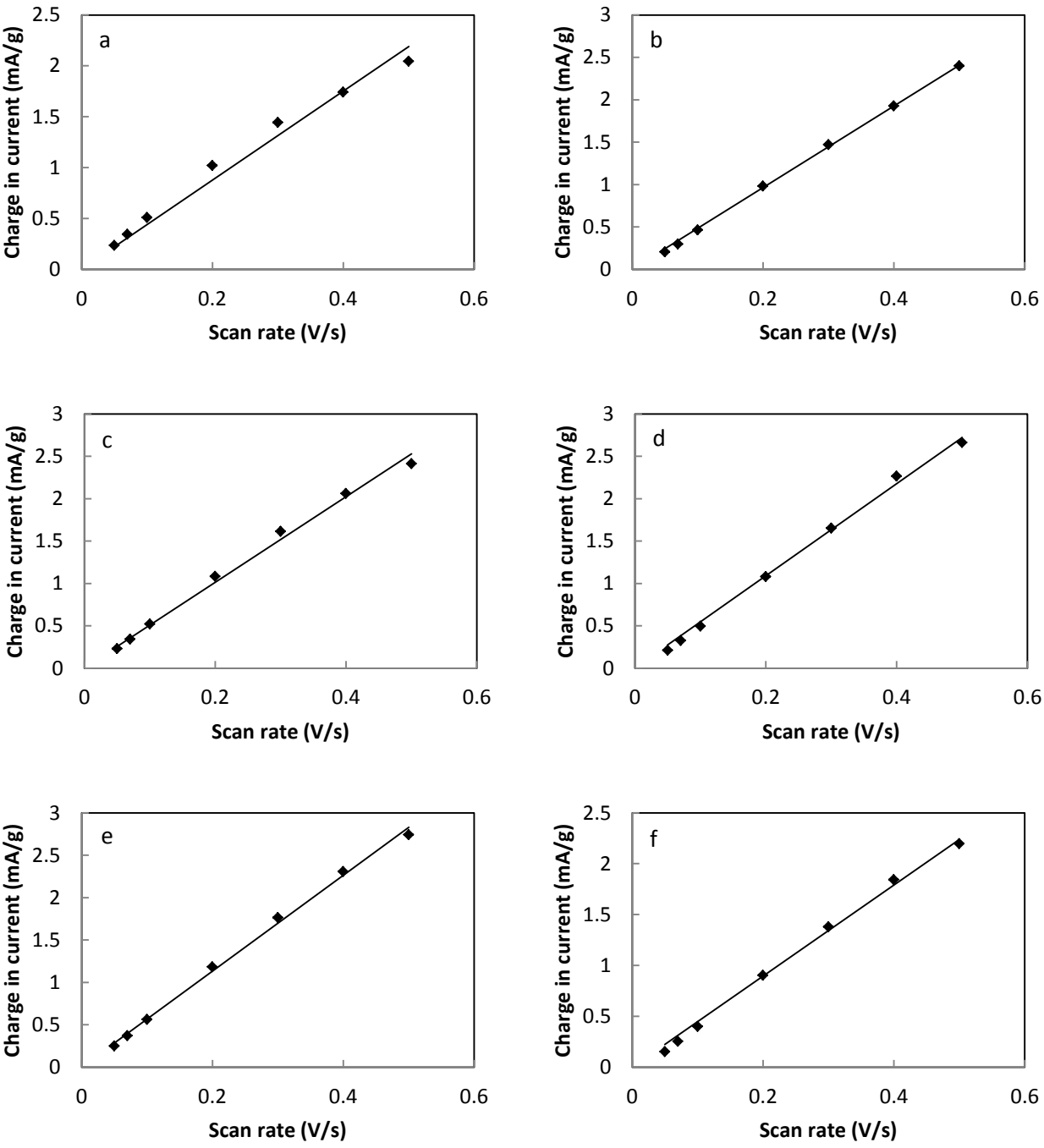

***Fig. 9.6**, Linear relations between the change in current and scan rate for the porous Cu samples with the pore size range of 1000-1500 µm and porosities of (a) 0.59, (b) 0.62, (c) 0.65, (d) 0.69, (e) 0.72 and (f) 0.76.*

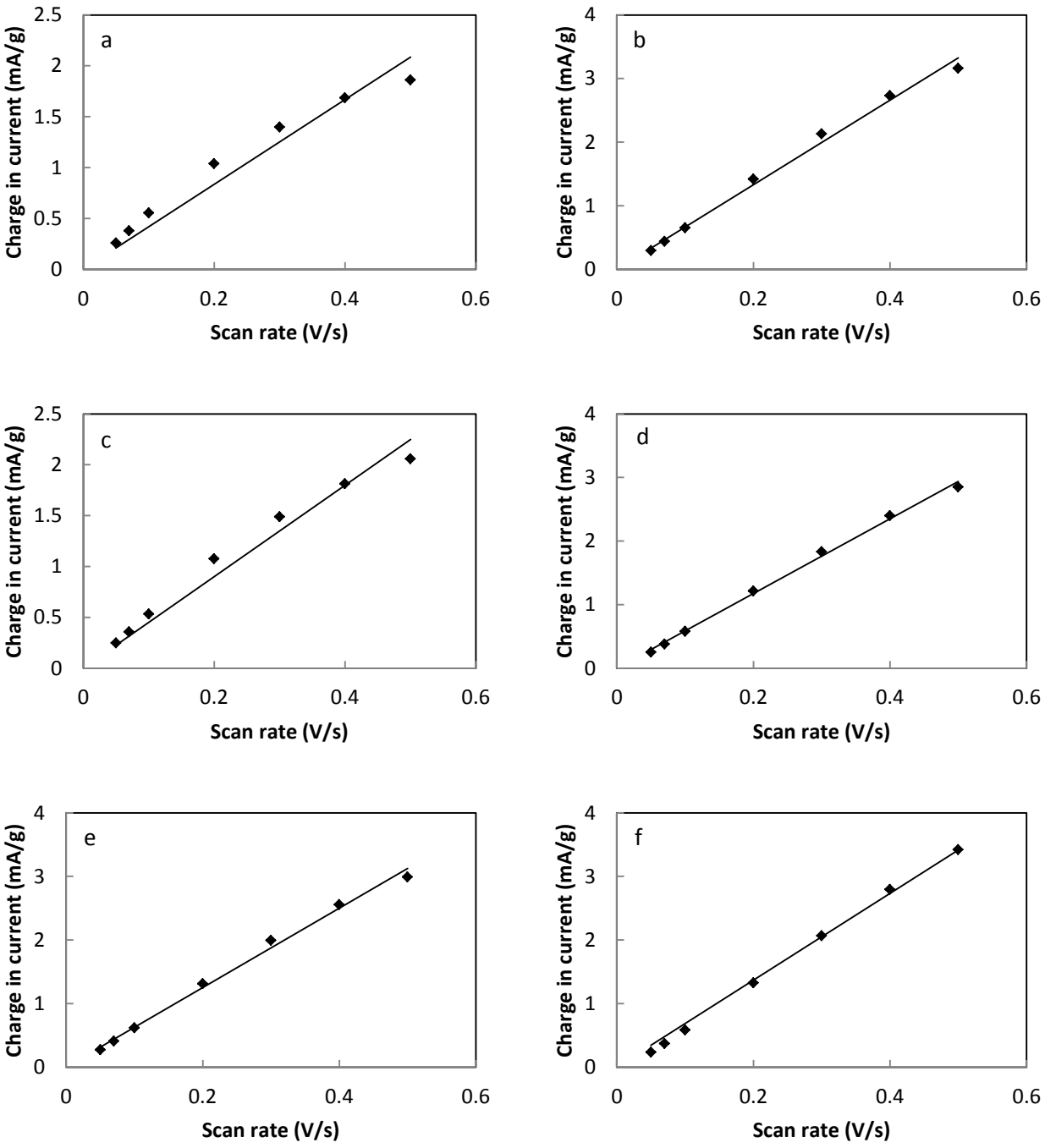

***Fig. 9.7**, Linear relations between the change in current and scan rate for the porous Cu samples with the pore size range of 710-1000 µm and porosities of (a) 0.56, (b) 0.59, (c) 0.64, (d) 0.67, (e) 0.71 and (f) 0.74.*

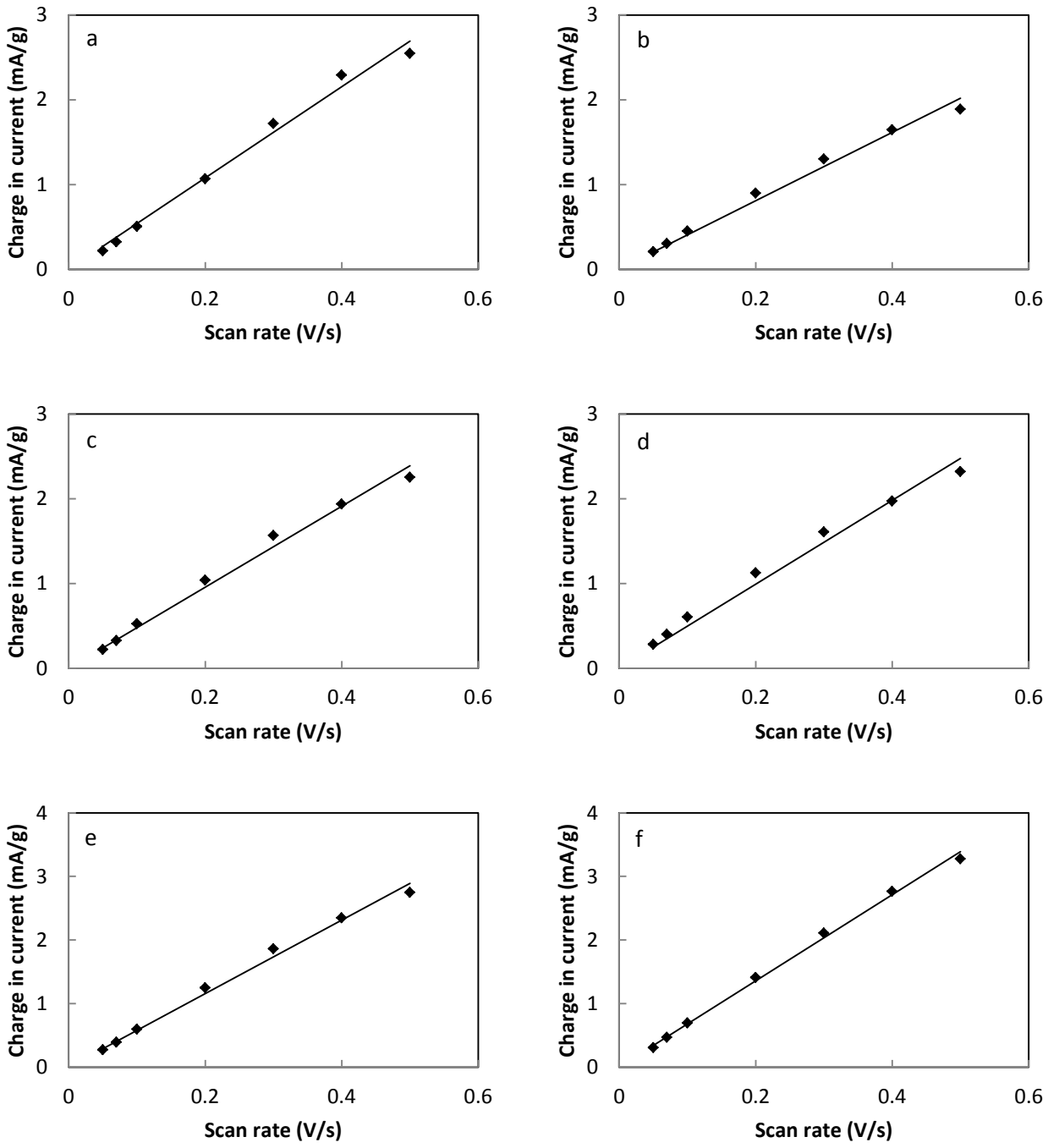

***Fig. 9.8**, Linear relations between the change in current and scan rate for the porous Cu samples with the pore size range of 425-710 µm and porosities of (a) 0.57, (b) 0.61, (c) 0.63, (d) 0.67, (e) 0.71 and (f) 0.74.*

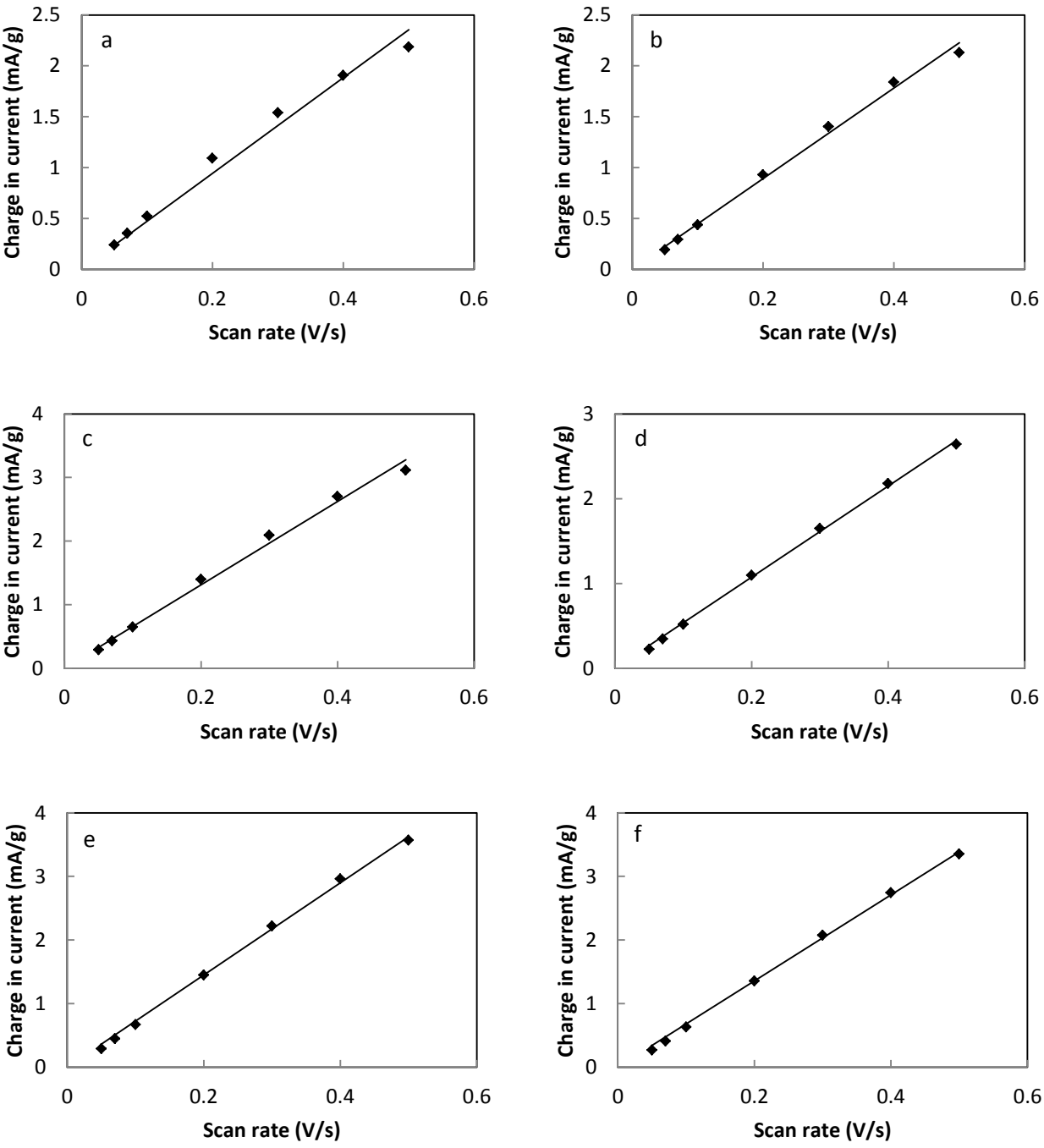

***Fig. 9.9**, Linear relations between the change in current and scan rate for the porous Cu samples with the pore size range of 250-425 µm and porosities of (a) 0.55, (b) 0.59, (c) 0.63, (d) 0.66, (e) 0.70 and (f) 0.73.*

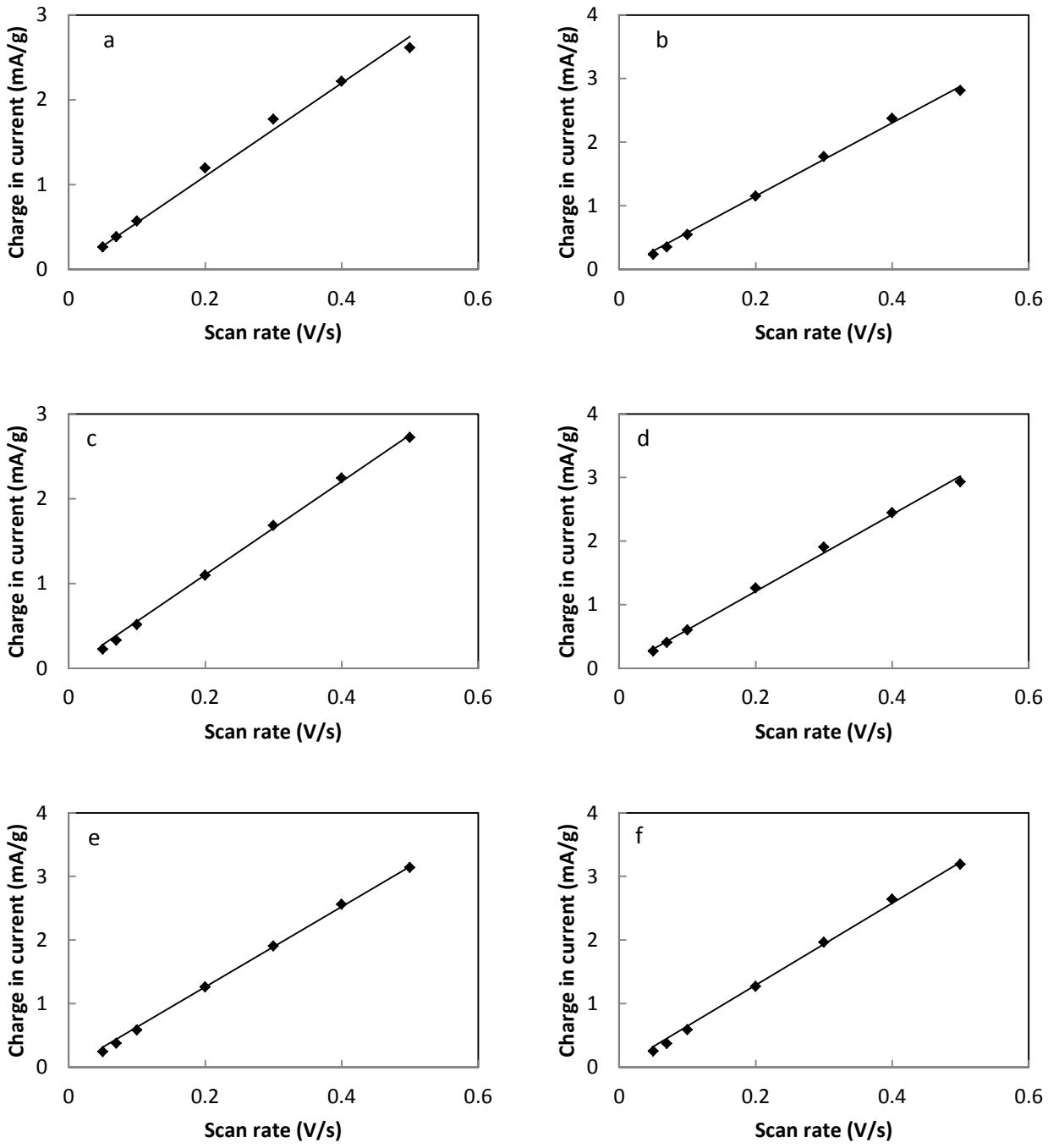

Fig. 9.10, *Linear relations between the change in current and scan rate for the porous Cu samples with the pore size range of 75-150 µm and porosities of (a) 0.53, (b) 0.56, (c) 0.61, (d) 0.63, (e) 0.67 and (f) 0.68.*

9.2 Effects of Porosity and Pore Size

The variations of volumetric and gravimetric specific real surface areas, measured by the CV – double layer capacitance method, as a function of porosity and pore size are shown in Fig. 9.11 (a) and (b), respectively. In the porosity range 0.5-0.8 and pore size range 75-1500 μm, the volumetric and gravimetric specific real surface areas are in the ranges of 700-1200 cm^{-1} and 200-360 cm^2/g, respectively. The specific real surface area is about one and two orders of magnitude higher than the electro active and geometric surface areas, respectively. In general, the volumetric specific real surface area decreases with porosity while the gravimetric specific real surface area increases with porosity. The values of gravimetric specific real surface areas are in the range of 400-700 cm^{-1} and slightly increase with porosity. The effect of pore size on the specific real surface areas is not pronounced. The trends of the effects of porosity and pore size on real surface area are again less clear than those on the geometric surface area.

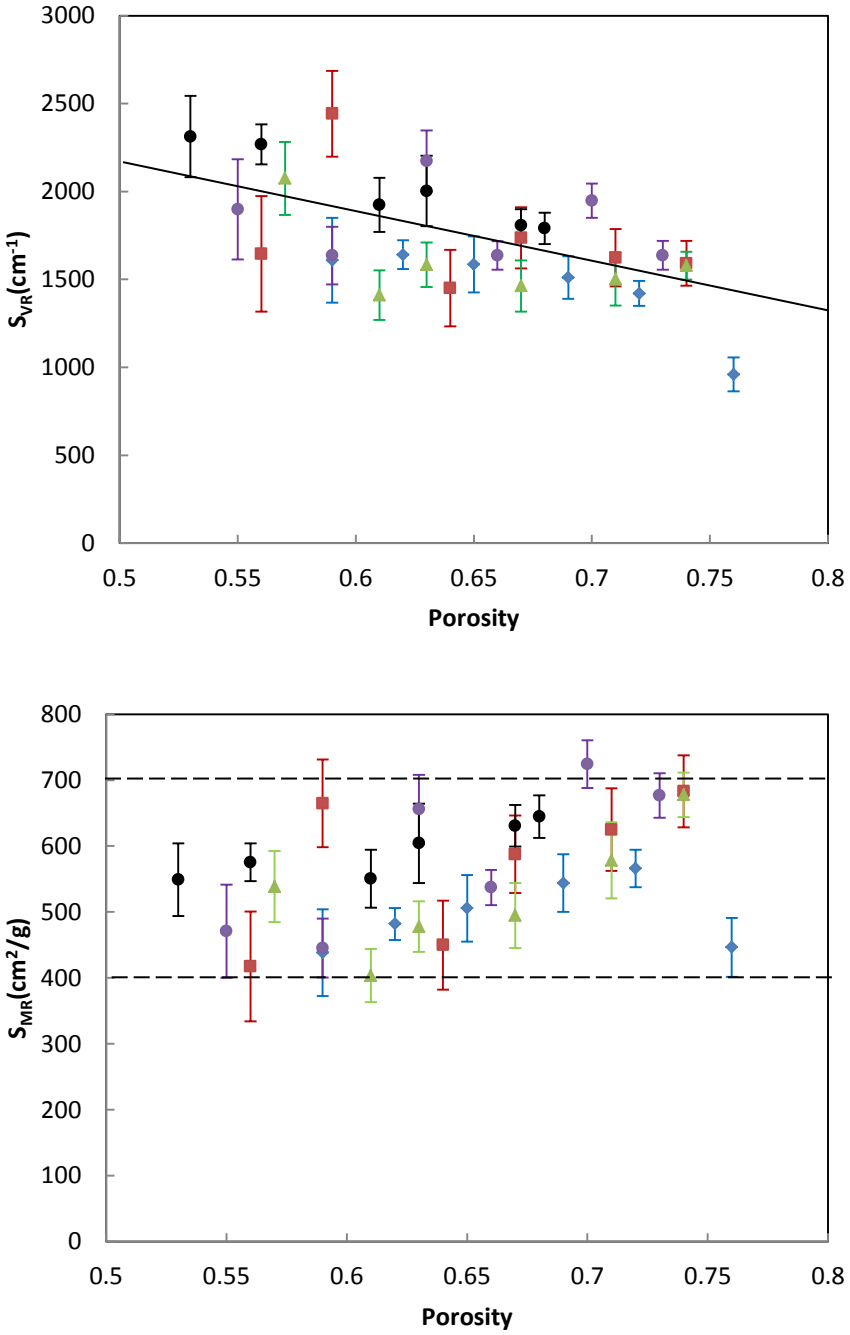

***Fig. 9.11**, Variations of (a) volumetric (S_{VR}) and (b) gravimetric (S_{MR}) specific real surface areas with porosity at different pore sizes: ● 75-150 µm, ● 250-425 µm, ▲ 425-710 µm, ■ 710-1000 µm, ◆ 1000-1500 µm.*

9.3 Discussion

The real surface area measured by the double layer capacitance method accounts for all surfaces in the porous Cu sample which can be reached by the electrolyte. Because of insufficient densification of Cu particles during sintering in LCS, the majority of the voids or interstices between the Cu particles are interconnected and therefore contribute to the real surface area. The real surface area is therefore the total surface area of all Cu particles, excluding the sintering necks between the Cu particles and the small number of isolated voids.

Fig. 9.12 plots the volumetric specific real surface area (S_{VR}) versus the theoretical volumetric specific surface area of the Cu particles (S_{VCu}), which is defined as the total surface area of all Cu particles per unit volume of the porous sample and is calculated by assuming that all Cu particles are perfect spheres of 72 µm diameter with a smooth surface. It shows that there is a good correlation between the real surface area of the porous Cu sample and the total surface area of the Cu particles in the sample. The former is about 5.8 times of the latter. This difference can be accounted for by the surface roughness of the Cu particles. As shown in Fig. 4.3 (section 4.2), the particles of the Cu powder used in this work are neither spherical nor smooth surfaced. The actual surface area of a Cu particle is much higher than predicted by assuming a perfect sphere.

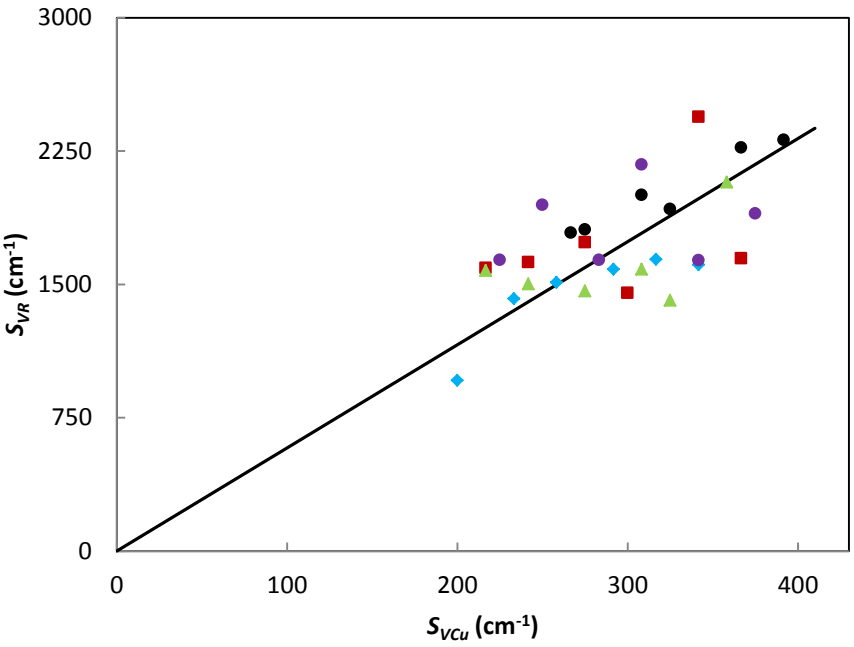

***Fig. 9.12**, Volumetric specific real surface area of porous Cu samples (S_{VR}) versus the theoretical volumetric specific surface area of the Cu particles (S_{VCu}) for different pore sizes: ● 75-150 µm, ● 250-425 µm, ▲ 425-710 µm, ■ 710-1000 µm, ◆ 1000-1500 µm.*

Chapter 10 Mass Transfer Coefficient

10.1 Effect of Flow Rate on Limiting Current

The mass transfer coefficient of porous Ni was measured by the LSV method in a flow electrolyte cell by controlling the flow rate in the experiment. Figs. 10.1-10.3 show the voltammograms of porous Ni samples with the porosity range of 0.62-0.77 and three pore size ranges of 1000-1500 μm, 710-1000 μm and 250-425 μm, respectively. In Figs. 10.1-10.3, the lines from top to bottom designate the flow rates of 0.24 ml/s, 0.48 ml/s, 0.8 ml/s, 2 ml/s and 2.8 ml/s, respectively. Table 10.1 shows the limiting current for the porous Ni samples. Figs. 10.4–10.6 show the variations of limiting current as a function of flow rate for the samples with three different pore size ranges.

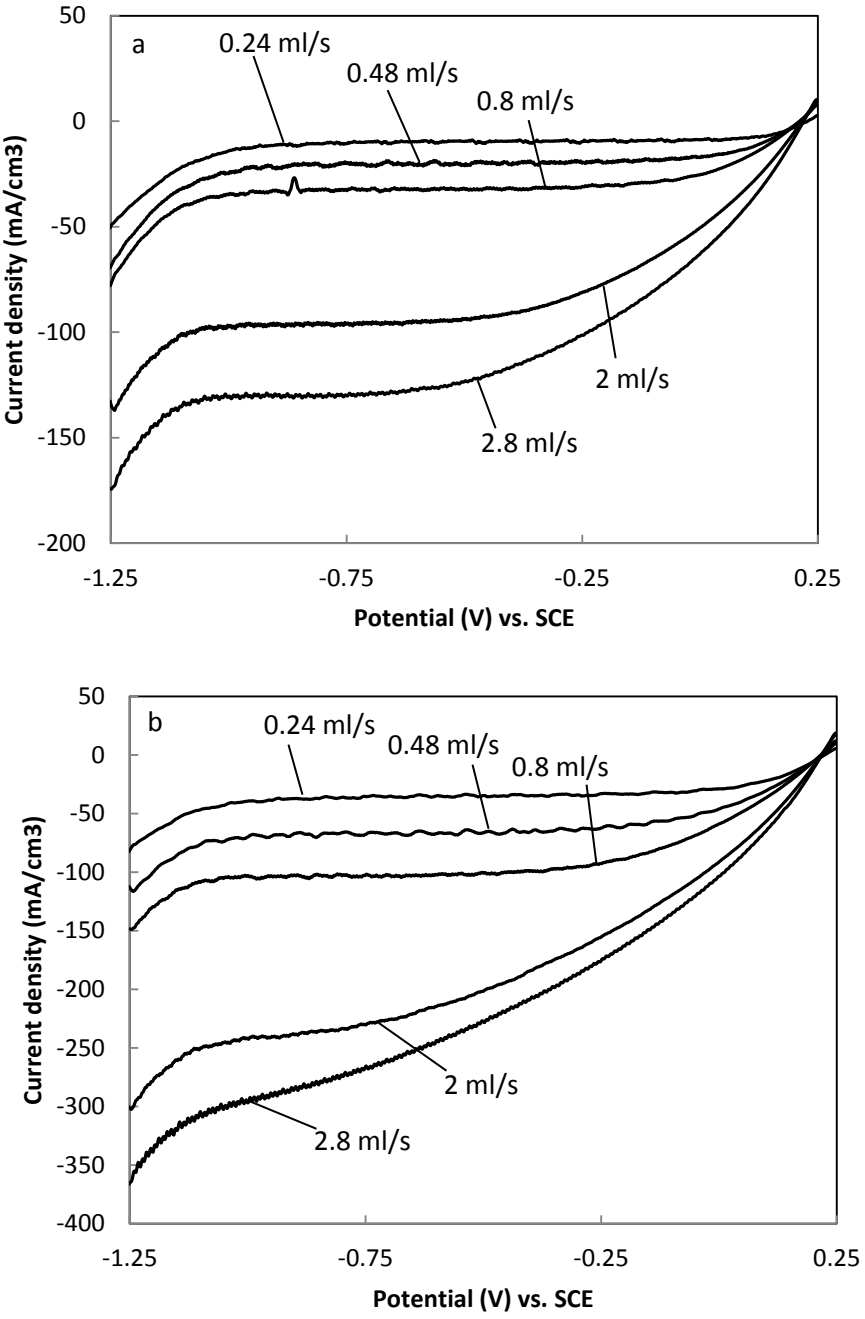

Fig. 10.1, *Voltammograms of porous Ni samples with the pore size range of 1000-1500 µm and porosity of (a) 0.65, (b) 0.67, (c) 0.70, (d) 0.73 and (e) 0.77 at different flow rates in the mass transfer measurement.*

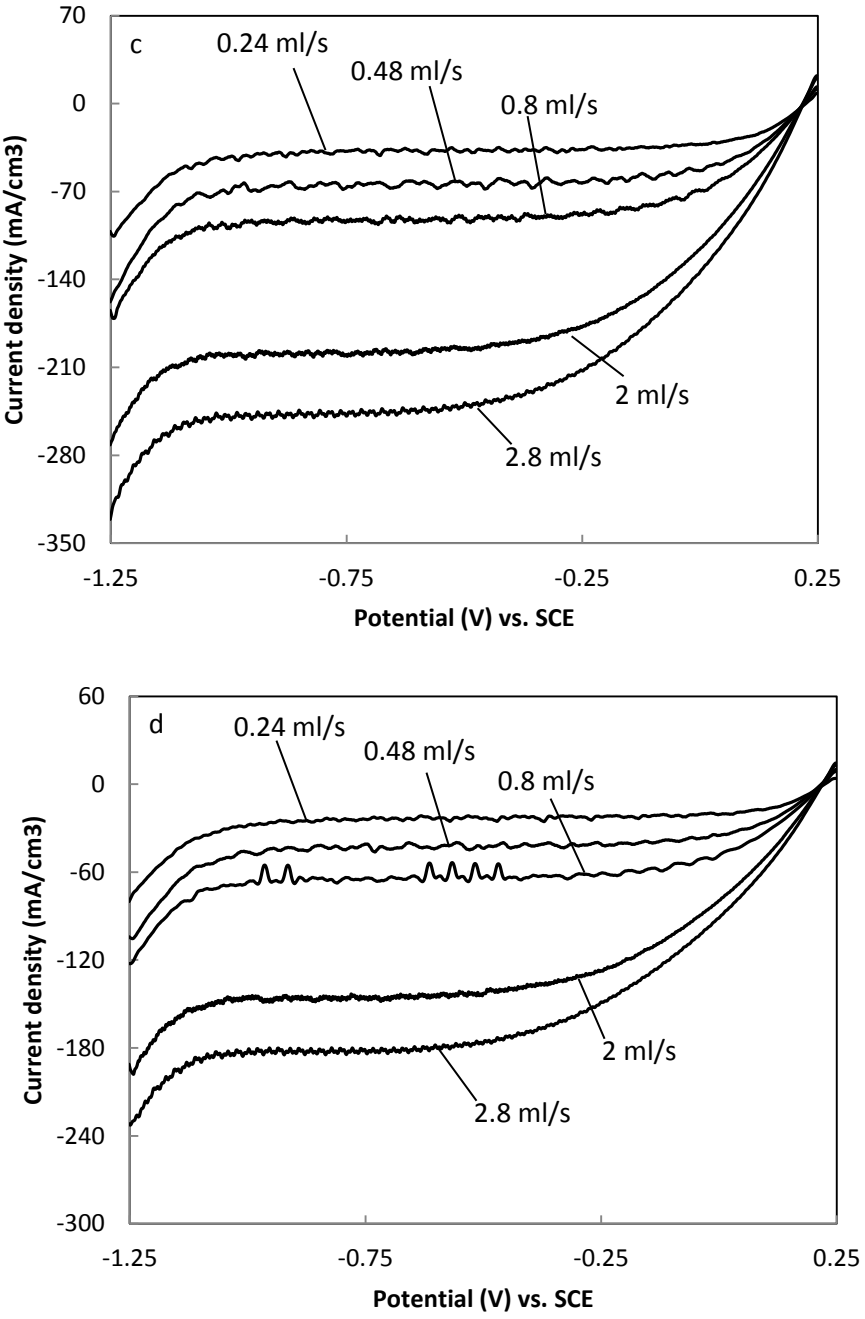

Fig. 10.1, *Voltammograms of porous Ni samples with the pore size range of 1000-1500 µm and porosity of (a) 0.65, (b) 0.67, (c) 0.70, (d) 0.73 and (e) 0.77 at different flow rates in the mass transfer measurement.*

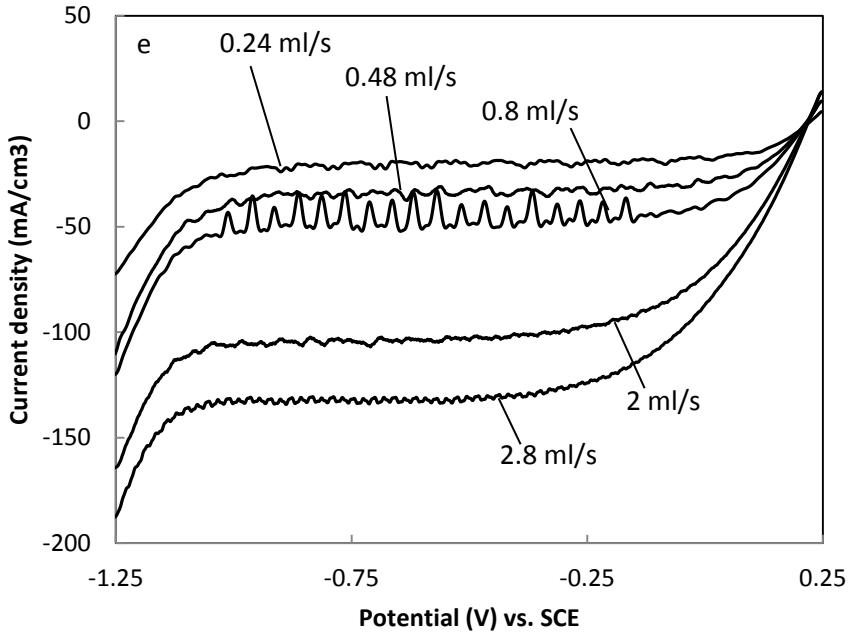

***Fig. 10.1**, Voltammograms of porous Ni samples with the pore size range of 1000-1500 µm and porosity of (a) 0.65, (b) 0.67, (c) 0.70, (d) 0.73 and (e) 0.77 at different flow rates in the mass transfer measurement.*

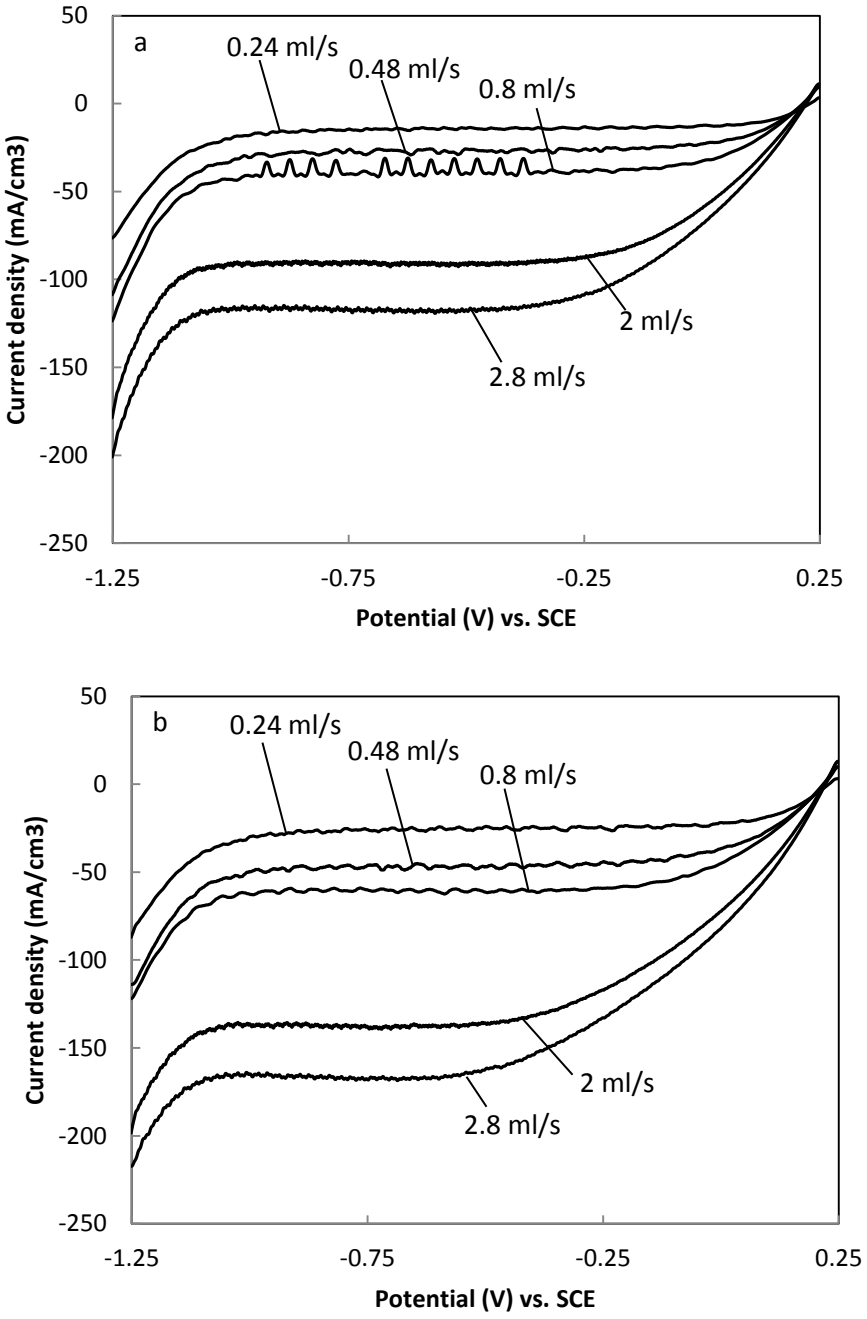

***Fig. 10.2**, Voltammograms of porous Ni samples with the pore size range of 710-1000 µm and porosity of (a) 0.63, (b) 0.66, (c) 0.68, (d) 0.72 and (e) 0.76 at different flow rates in the mass transfer measurement.*

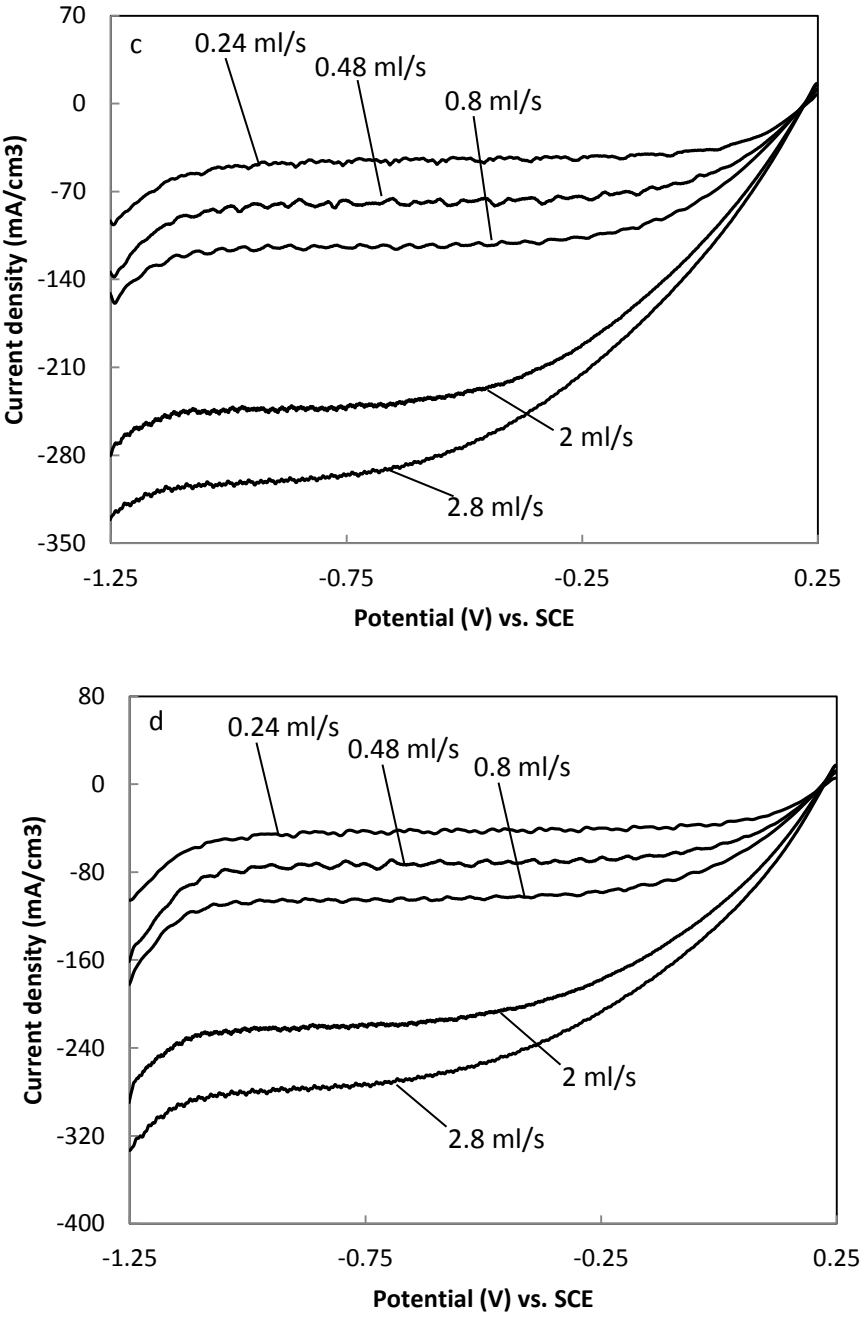

***Fig. 10.2**, Voltammograms of porous Ni samples with the pore size range of 710-1000 µm and porosity of (a) 0.63, (b) 0.66, (c) 0.68, (d) 0.72 and (e) 0.76 at different flow rates in the mass transfer measurement.*

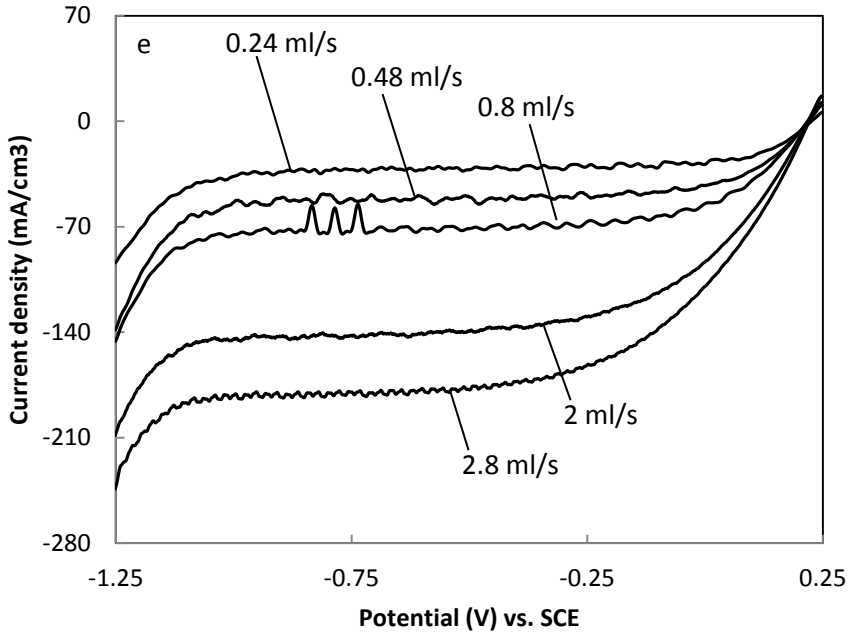

***Fig. 10.2**, Voltammograms of porous Ni samples with the pore size range of 710-1000 µm and porosity of (a) 0.63, (b) 0.66, (c) 0.68, (d) 0.72 and (e) 0.76 at different flow rates in the mass transfer measurement.*

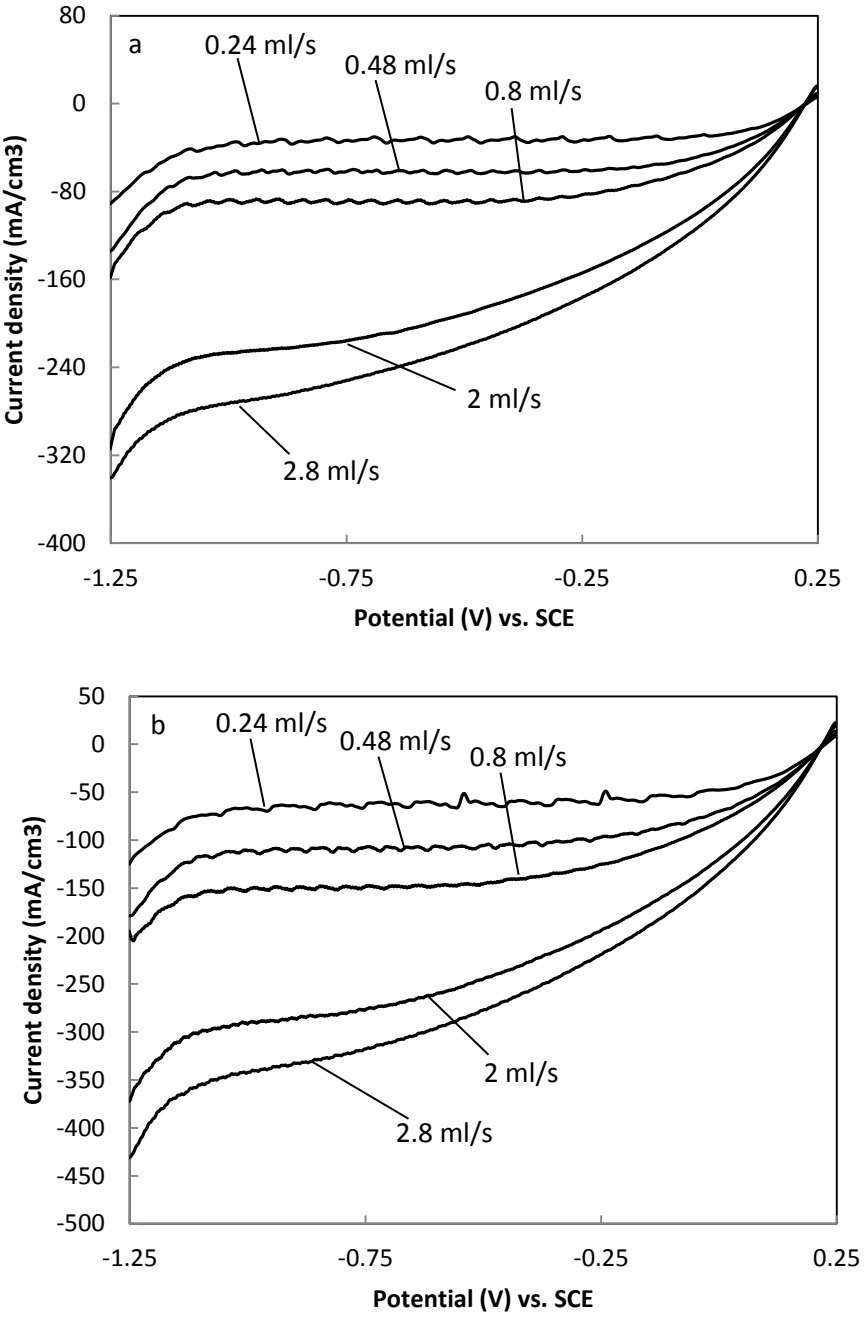

Fig. 10.3*, Voltammograms of porous Ni samples with the pore size range of 250-425 µm and porosity of (a) 0.62, (b) 0.65, (c) 0.68, (d) 0.71 and (e) 0.75 at different flow rates in the mass transfer measurement.*

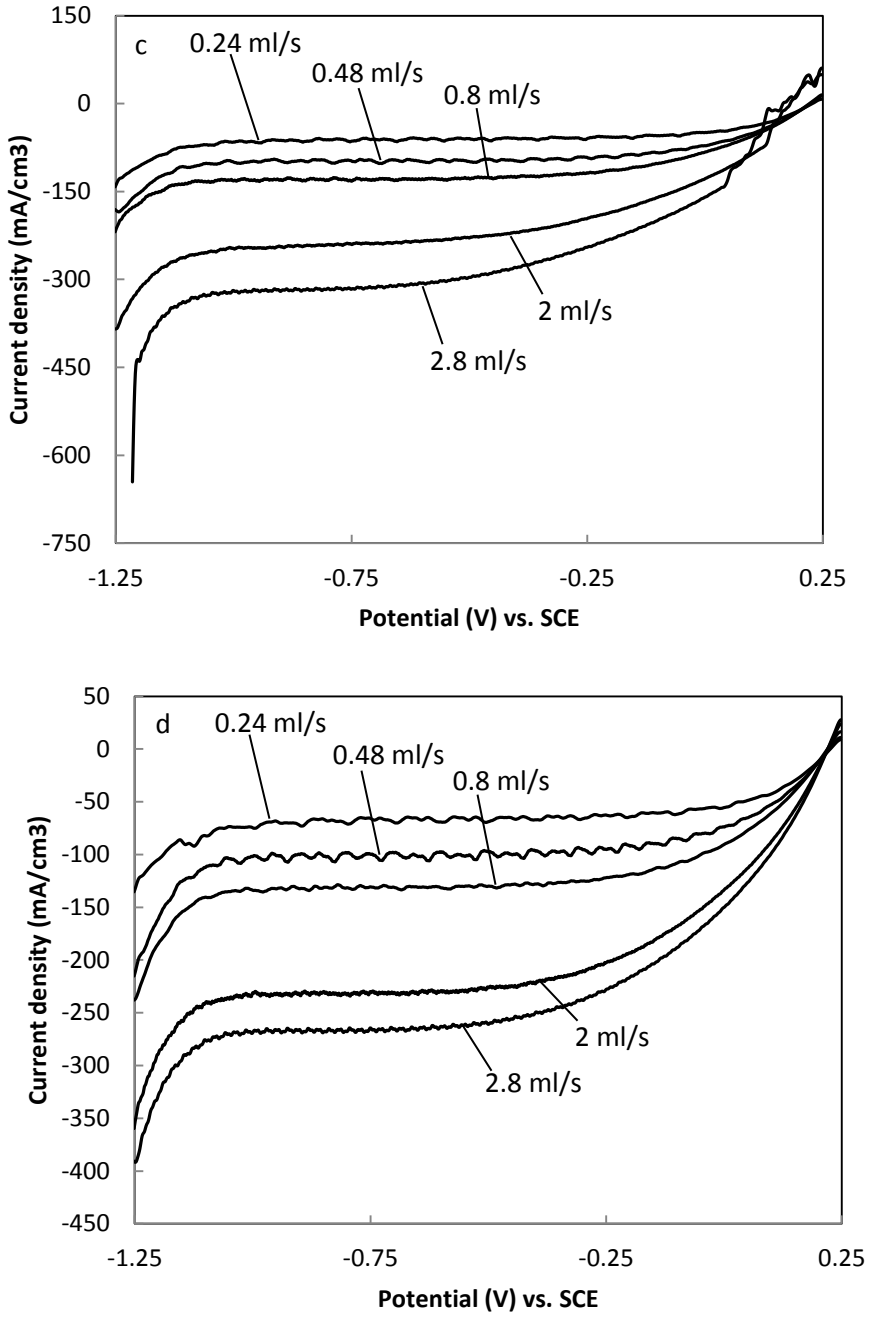

***Fig. 10.3**, Voltammograms of porous Ni samples with the pore size range of 250-425 µm and porosity of (a) 0.62, (b) 0.65, (c) 0.68, (d) 0.71 and (e) 0.75 at different flow rates in the mass transfer measurement.*

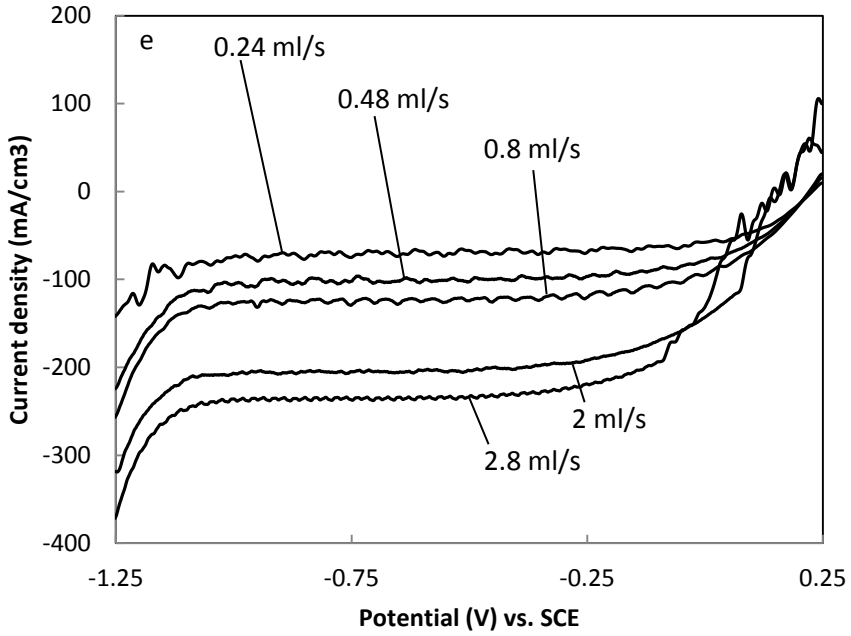

***Fig. 10.3**, Voltammograms of porous Ni samples with the pore size range of 250-425 µm and porosity of (a) 0.62, (b) 0.65, (c) 0.68, (d) 0.71 and (e) 0.75 at different flow rates in the mass transfer measurement.*

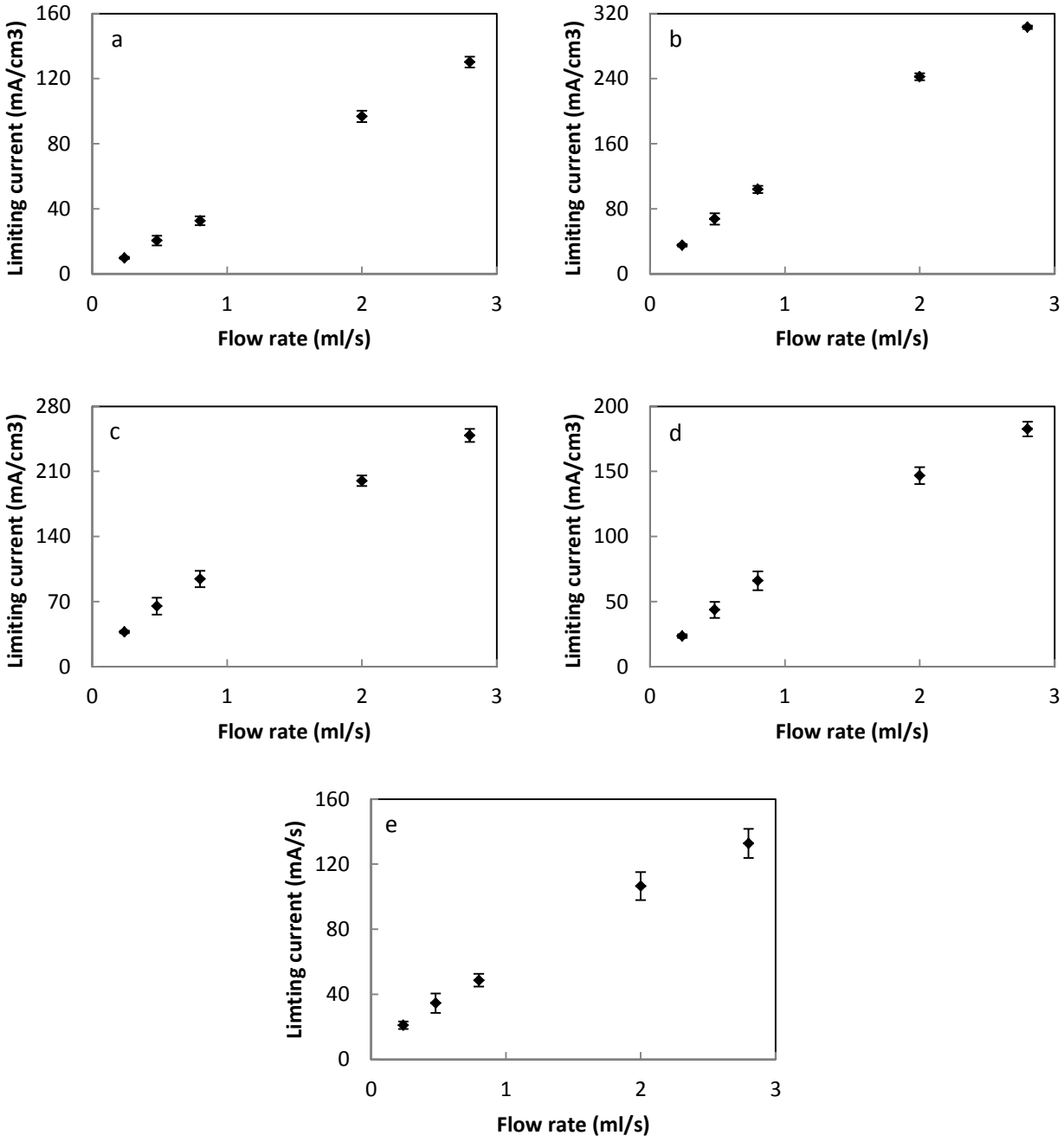

***Fig. 10.4**, Variations of limiting current with flow rate for porous Ni samples with the pore size range of 1000-1500 µm and porosity of (a) 0.65, (b) 0.67, (c) 0.70, (d) 0.73 and (e) 0.77.*

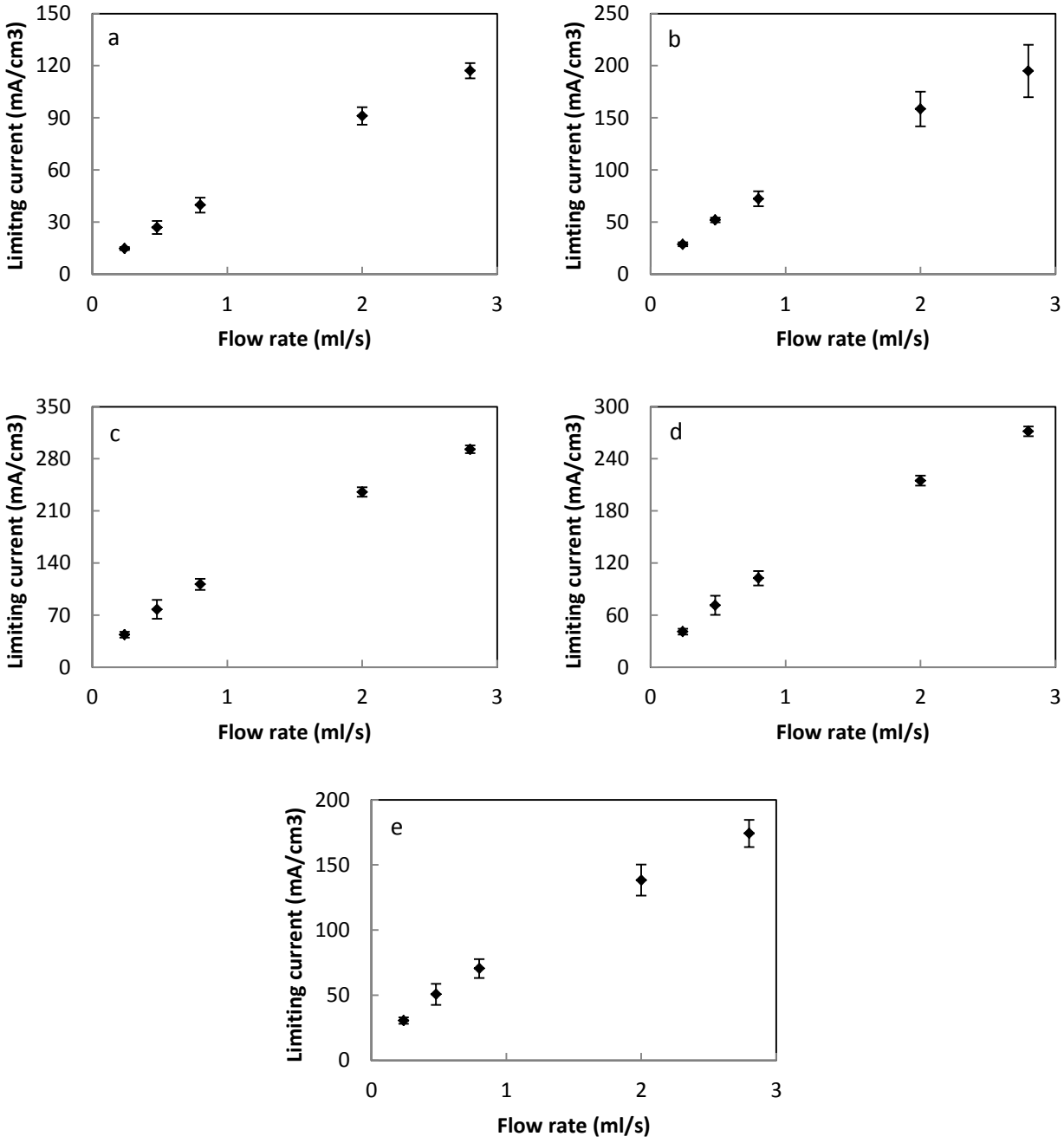

***Fig. 10.5**, Variations of limiting current with flow rate for porous Ni samples with the pore size range of 710-1000 µm and porosity of (a) 0.63, (b) 0.66, (c) 0.68, (d) 0.72 and (e) 0.76.*

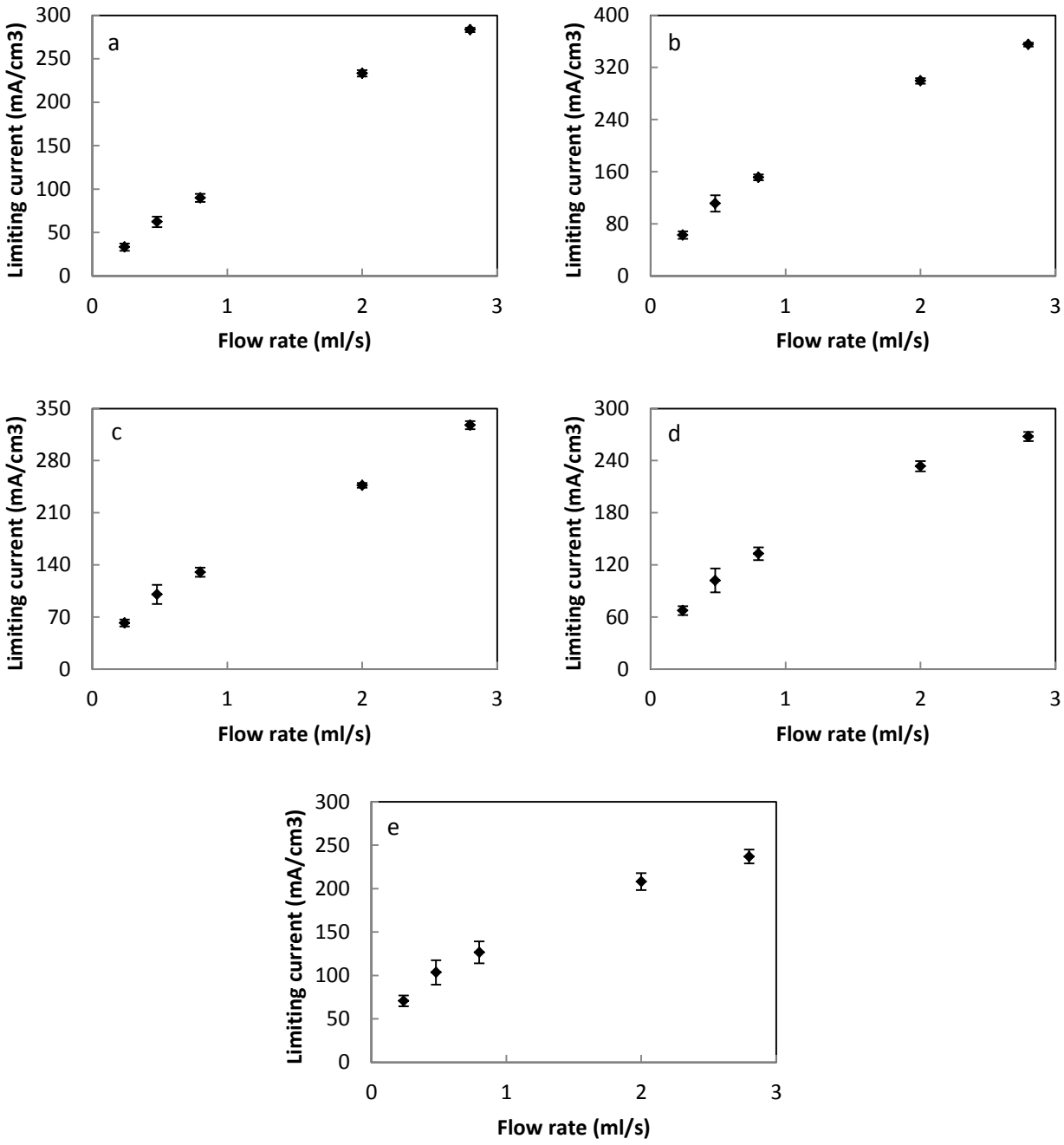

***Fig. 10.6**, Variations of limiting current with flow rate for porous Ni samples with the pore size range of 250-425 µm and porosity of (a) 0.62, (b) 0.65, (c) 0.68, (d) 0.71 and (e) 0.75.*

10.2 Effects of Porosity and Pore Size on Limiting Current

Fig. 10.7 shows the variations of limiting current with porosity at different flow rates and pore size ranges of (a) 1000-1500 μm, (b) 710-1000 μm and (c) 250-425. The porosity has a large effect on the limiting current. The limiting current first increases with porosity until reaching the maximum at a porosity around 0.65-0.70 and then generally decreases.

Fig. 10.8 shows the variations of limiting current with porosity with different pore sizes at different flow rates of (a) 0.24 ml/s, (b) 0.48 ml/s, (c) 0.8 ml/s, (d) 2 ml/s and (e) 2.8 ml/s. In general, the limiting current generated in the sample with a small pore size was higher than that with the large pore size. The peak values in Fig. 10.8 (a) to (e) are also increased with the decrease of pore size. This situation becomes more significant at low flow rates.

For samples with a high porosity, the reactant can easily pass through the sample so high porosity leads to a short resident time of the reactant in the sample (Zhou et al. 2015). The reactant cannot obtain enough time for adequate reaction in the experiment so the limiting current generated on the electrode surface was decreased. Samples with a low porosity result in much longer resident time. However, a too long resident time can accelerate the consumption of the reactant and lead to the decrease of the limiting current. At the same time, the contact area on the electrode which participated in the reaction was decreased because the flow channels (pores) in the porous Ni were easily blocked (Zhou et al. 2015). The limiting current in the mass transfer measurement also depends on the electro-active surface area of the electrode. In the samples with a low porosity, the low electro-active surface area can reduce the limiting current.

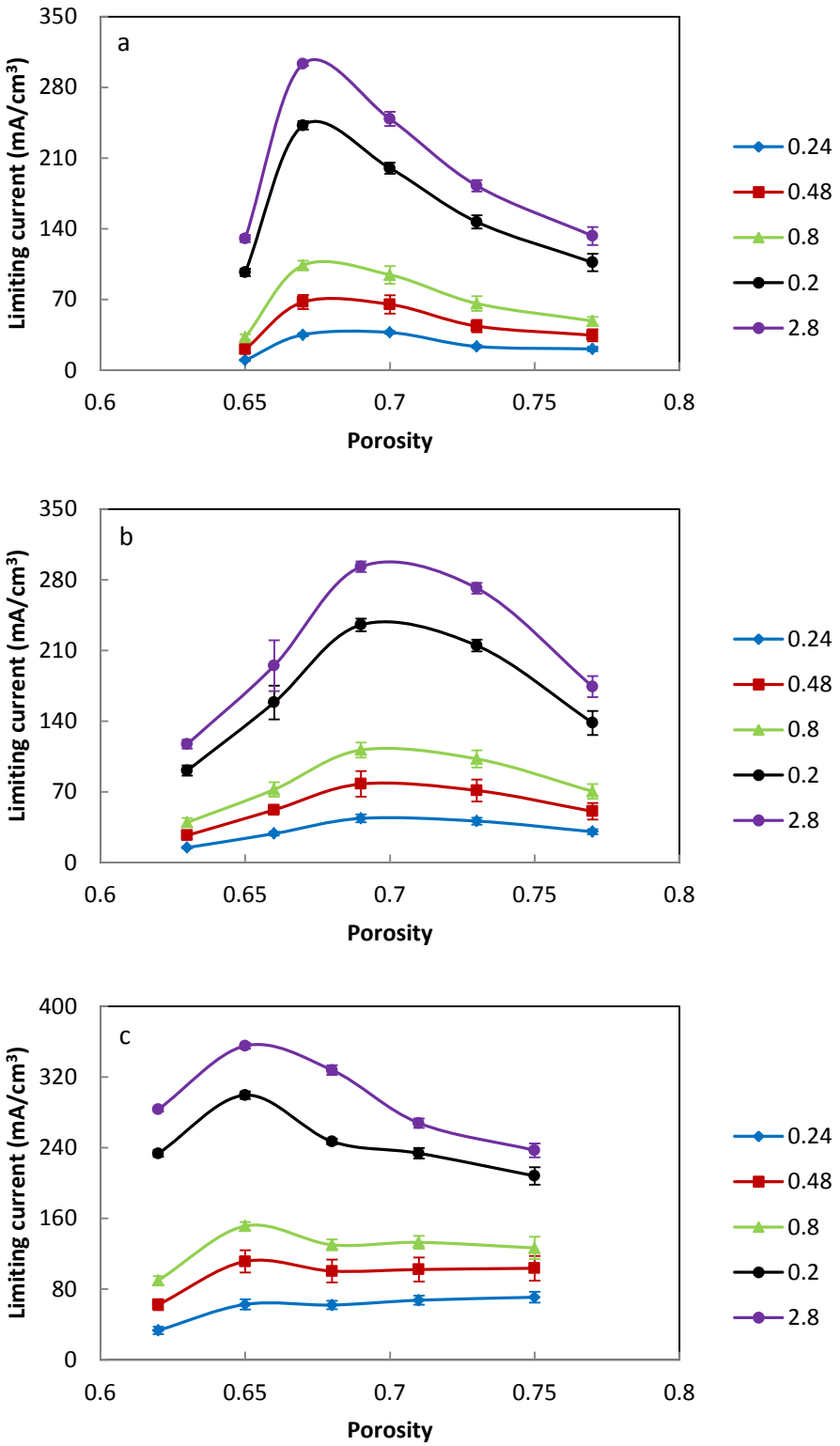

***Fig. 10.7**, Variations of limiting current with porosity at different flow rates and pore size ranges of: (a) 1000-1500 µm, (b) 710-1000 µm and (c) 250-425 µm.*

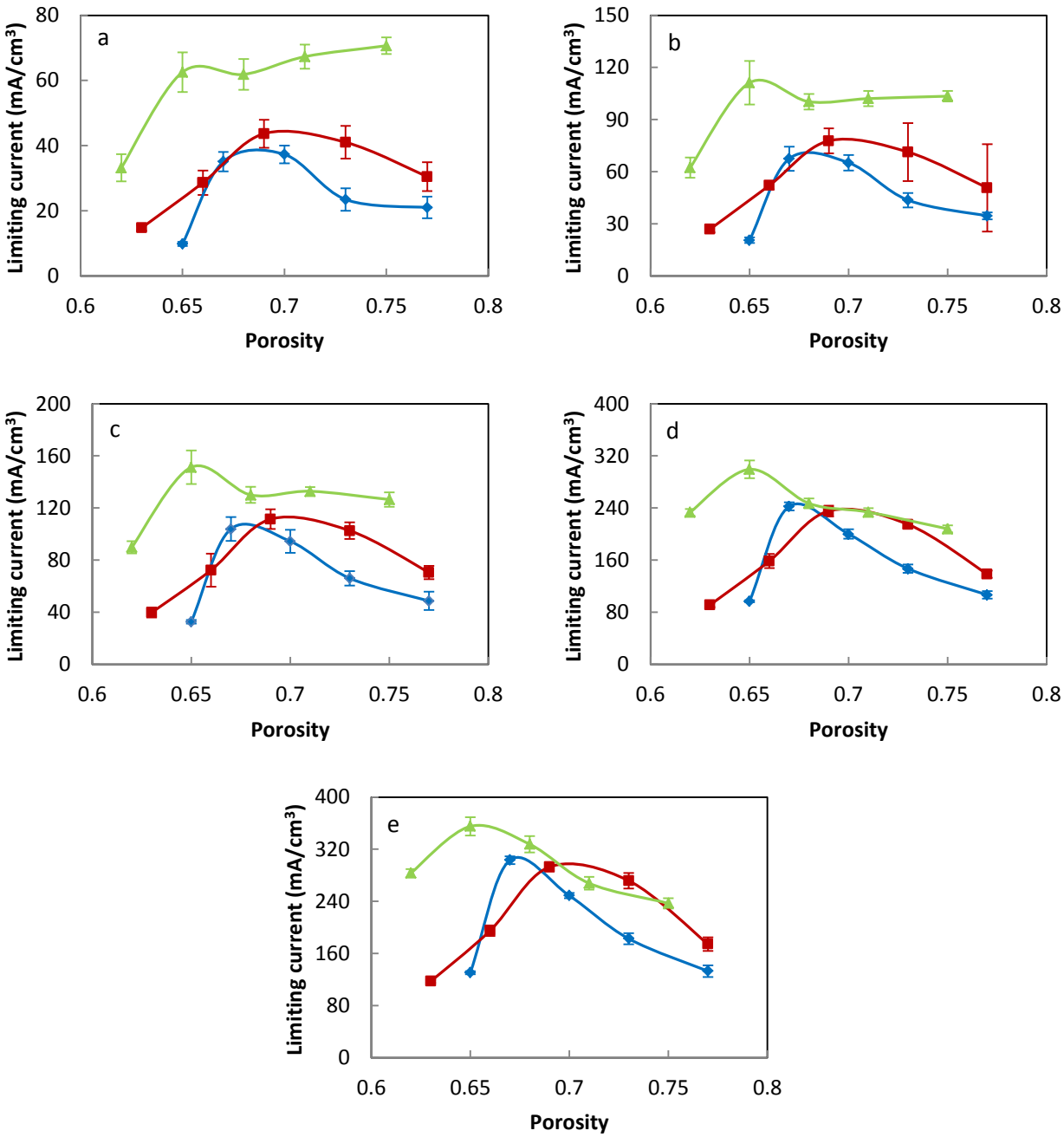

***Fig. 10.8**, Variations of limiting current with porosity at different pore sizes: ( ) 1000-1500 µm, ( ) 710-1000 µm and ( ) 250-425 µm and flow rates of: (a) 0.24 ml/s, (b) 0.48 ml/s, (c) 0.8 ml/s, (d) 2 ml/s and (e) 2.8 ml/s.*

10.3 Mass Transfer Coefficient

In the mass transfer controlled region, the limiting current (I_L) generated on the electrode surface depends upon the mass transfer coefficient (k) and the electrode area. The mass transfer coefficient can therefore be determined by (Recio et al. 2013):

$$k = \frac{I_L}{nAFc} \tag{10.1}$$

where A is volumetric specific geometric surface area, F is the Faraday constant of 9.64×10^4 C/mol and c is the bulk concentration of the reactant $K_3Fe(CN)_6$ (c = 1 mmol/L). Table A6.2 (see Appendixes) lists the geometric surface areas of the porous Ni samples measured by the QS method. Table A10.1 (see Appendixes) lists the limiting current, I_L, measured in the LSV experiment.

The mass transfer coefficients of the porous Ni samples with the pore size of 250-1500 μm and porosity of 0.62-0.77 at various flow rates (0.24-2.8 ml/s) were calculated by Eqn. 10.1 and are listed in Table A10.2 (see Appendixes). For all samples, the mass transfer coefficient increased with flow rate.

10.4 Effects of Porosity and Pore Size on Mass Transfer Coefficient

Fig. 10.9 shows the variations of mass transfer coefficient with porosity at different flow rates and pore size ranges of (a) 1000-1500 μm, (b) 710-1000 μm and (c) 250-425 μm. With increasing the porosity, the mass transfer coefficient first increases until reaching the highest values at the porosity around 0.65-0.70 and then generally decreases.

Fig. 10.10 shows the variations of mass transfer coefficient with porosity for different pore sizes at different flow rates of (a) 0.24 ml/s, (b) 0.48 ml/s, (c) 0.8 ml/s, (d) 2 ml/s and (e) 2.8 ml/s. In contrast to limiting current, the mass transfer coefficient of the samples with large pores was slightly higher than that of the samples with small pores. The peak values of mass transfer coefficient also increased with pore size as shown in Fig. 10.10.

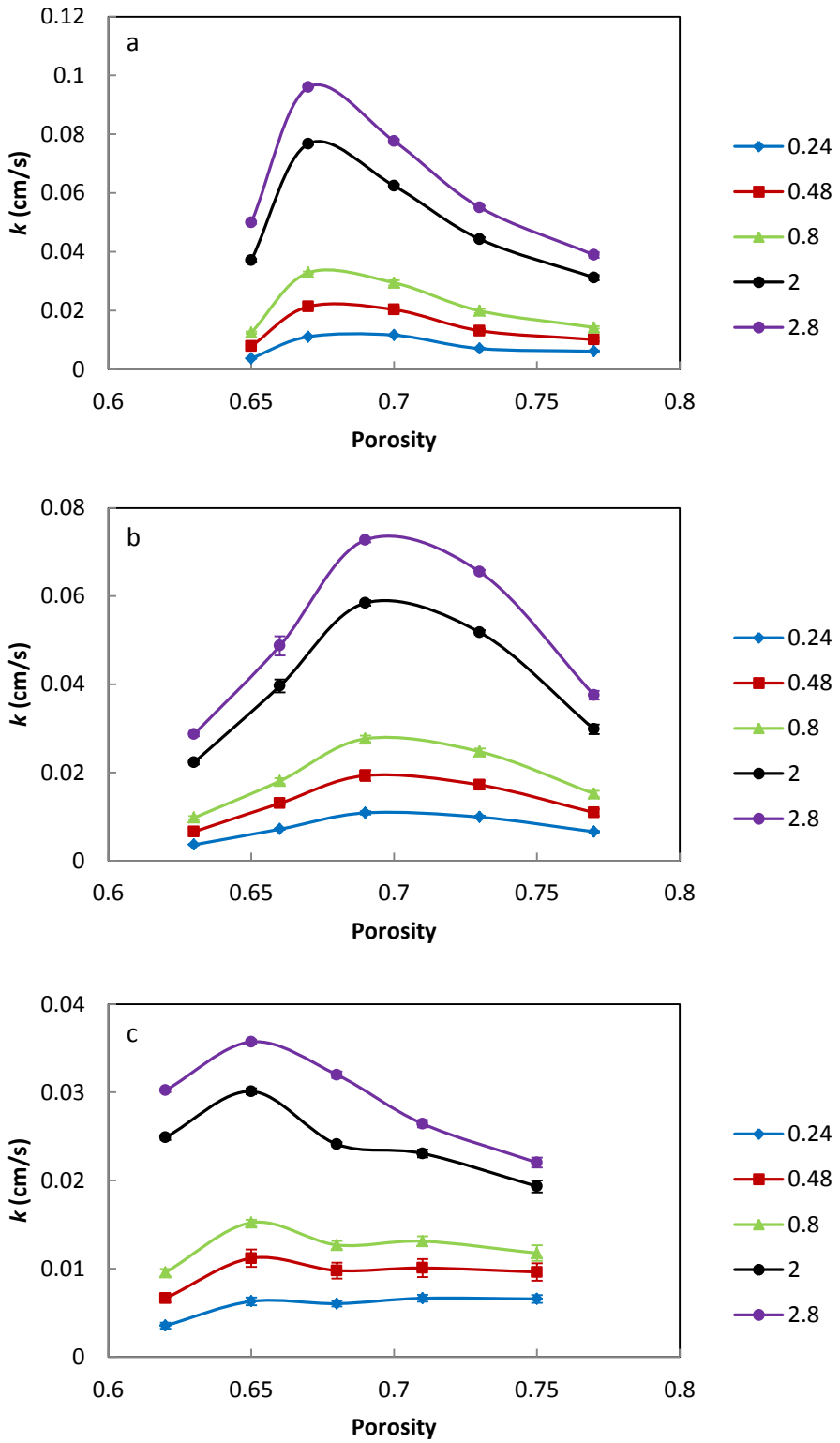

***Fig. 10.9**, Variations of mass transfer coefficient (k) with porosity at different flow rates and pore size range of (a) 1000-1500 µm, (b) 710-1000 µm and (c) 250-425 µm.*

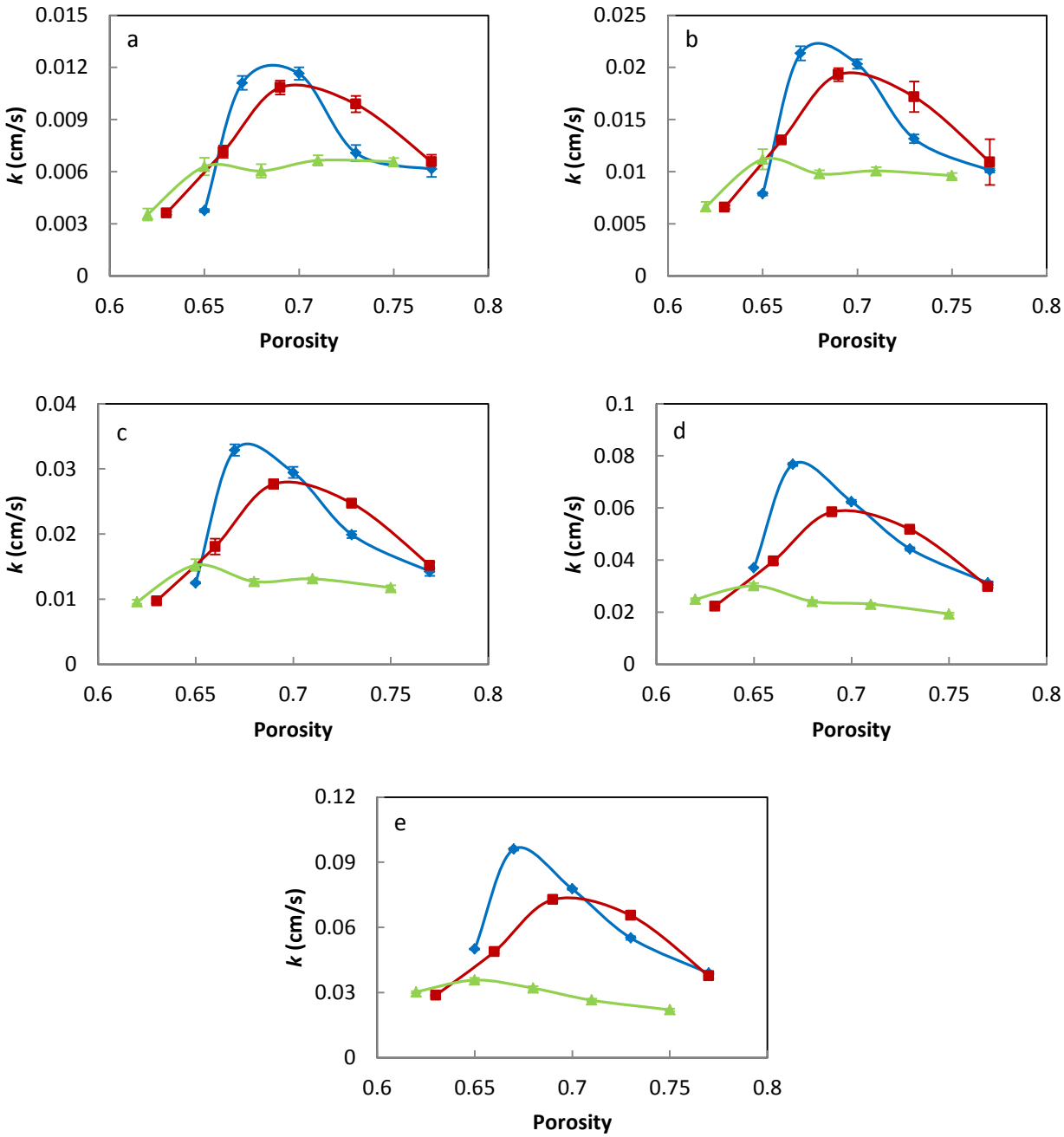

***Fig. 10.10**, Variations of mass transfer coefficient (k) with porosity at different pore sizes: ( ) 1000-1500 µm, ( ) 710-1000 µm and ( ) 250-425 µm and flow rates of: (a) 0.24 ml/s, (b) 0.48 ml/s, (c) 0.8 ml/s, (d) 2 ml/s and (e) 2.8 ml/s.*

10.5 Reynolds Number vs. Sherwood Number

Mass transfer to an electrode in the flow cell can be characterised by three dimensionless groups, namely the Sherwood (*Sh*), Reynolds (*Re*) and Schmidt (*Sc*) numbers. These dimensionless quantities are expressed in Eqns. 10.2, 10.3 and 10.4, respectively (Recio et al. 2013).

$$Re = \frac{Ud_p}{v} \tag{10.2}$$

$$Sh = \frac{kd_p}{D} \tag{10.3}$$

$$Sc = \frac{v}{D} \tag{10.4}$$

where ν is the kinematic viscosity of the electrolyte (9.56×10^{-3} cm^2s^{-1}), D is the diffusion coefficient of $Fe(CN)_6^{-3}$ (6.4×10^{-6} cm^2s^{-1}), d_p is the pore size and U is the flow velocity which can be expressed by:

$$U = \frac{Q}{\varepsilon \times A_C} \tag{10.5}$$

where Q is the flow rate, A_c is the cross-sectional area of the sample and ε is the sample porosity.

Table A10.3 (see Appendixes) shows the calculated values of Reynolds number (*Re*) and Sherwood number (*Sh*) at different flow rates for the porous Ni samples with different porosities and pore sizes. The volume weighted mean pore size *D[4,3]* (Table 4.2 in section 4.1) was used in calculating *Re* and *Sh*.

Figs. 10.11 (a) to (c) show the Sherwood number (*Sh*) as a function of Reynolds number (*Re*) at different porosities for the porous Ni samples with the pore sizes of 1000-1500 μm, 710-1000 μm and 250-425 μm, respectively. *Sh* increases with Re for all the samples and $log_{10}(Sh)$ is proportional to $log_{10}(Re)$.

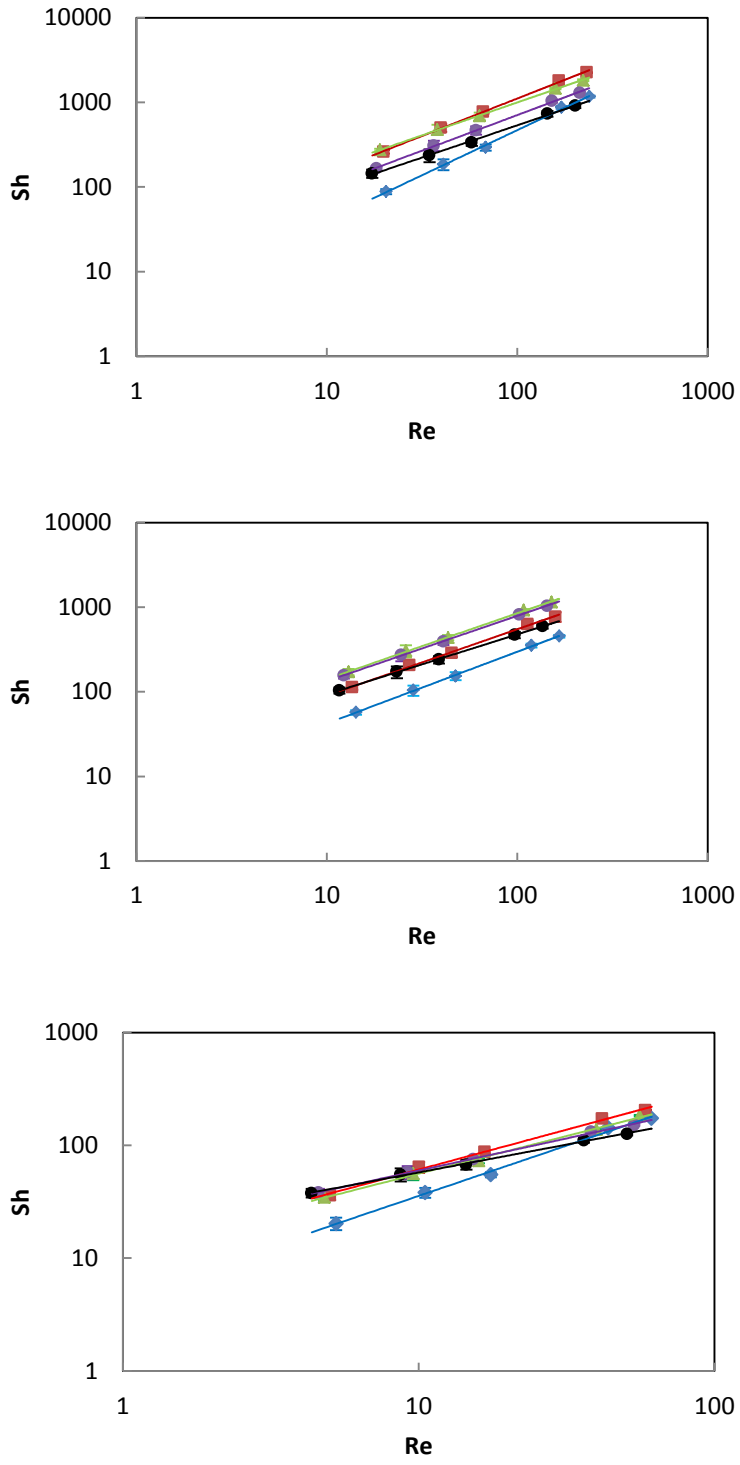

***Fig. 10.11**, Plots of Sherwood number (Sh) vs. Reynolds number (Re) at different pore sizes and porosities: (a) 1000-1500 µm (porosity: ◆ 0.65, ■ 0.67, ▲ 0.70, ● 0.73 and ● 0.77), (b) 710-1000 µm (porosity: ◆ 0.63, ■ 0.66, ▲ 0.69, ● 0.73 and ● 0.77), and (c) 250-425 µm (porosity: ◆ 0.62, ■ 0.65, ▲ 0.68, ● 0.71 and ● 0.75).*

10.6 Empirical Correlation

The three dimensionless groups, *Sh*, *Re* and *Sc*, can be correlated by (Walsh 1993):

$$Sh = aRe^{b}Sc^{\frac{1}{3}} \tag{10.6}$$

Constant *a* in Eq. 10.6 depends on both electrode geometry and flow conditions. The exponent *b* depends only on the flow condition. For example, *b* is greater in turbulent flow than in laminar flow. When the fluid flow is fully laminar, *b* is 0.33 (Walsh 1993). The log-log plots of Sherwood vs. Reynolds numbers shown in Fig. 10.11 indicate that the relationship between them fitted very well with Eqn. 10.6. The empirical correlation parameters *a* and *b* for porous Ni samples with different porosities and pore sizes are listed in Table. A10.4 (see Appendixes).

Fig. 10.12 shows the constants *a* and *b* as a function of porosity at different pore sizes. Fig. 10.12 (b) shows that *b* decreased with porosity, indicating that higher porosity resulted in a lower level of turbulence in the samples. Samples with small pore sizes had slightly low values of *b*. Because no solid matrix exists in the flow path to cause the turbulence, the fluid flow becomes fully laminar when porosity is 1 and value of *b* is 0.33 for the laminar fluid. Therefore, the values of trendlines should approach 0.33 when the porosity approaches 1.

Compared with *b*, *a* depends on both electrode geometry and flow conditions and is more complex (Walsh 1993). In general, the value of *a* was in the range of 1-2 as shown in Fig. 10.12 (a). The value of *a* first increases with porosity until reaching the maximum at a porosity of around 0.70 and then slightly decreases. For a sample with a low porosity, the contact area on the electrode, which participated in the reaction, was decreased because the flow channels in the porous Ni were easily blocked (Zhou et al. 2015). Therefore, *a* increases with porosity when porosity < 0.7. For a sample with high porosity, the reactant in

the electrolyte can easily pass through the electrode with low convection due to the low turbulence and has a short resident time for reaction (Zhou et al. 2015). In this situation, the reactant does not have enough time for adequate reaction in the experiment. Therefore, the value of *a* decreases with porosity when the samples have a high porosity (> 0.70).

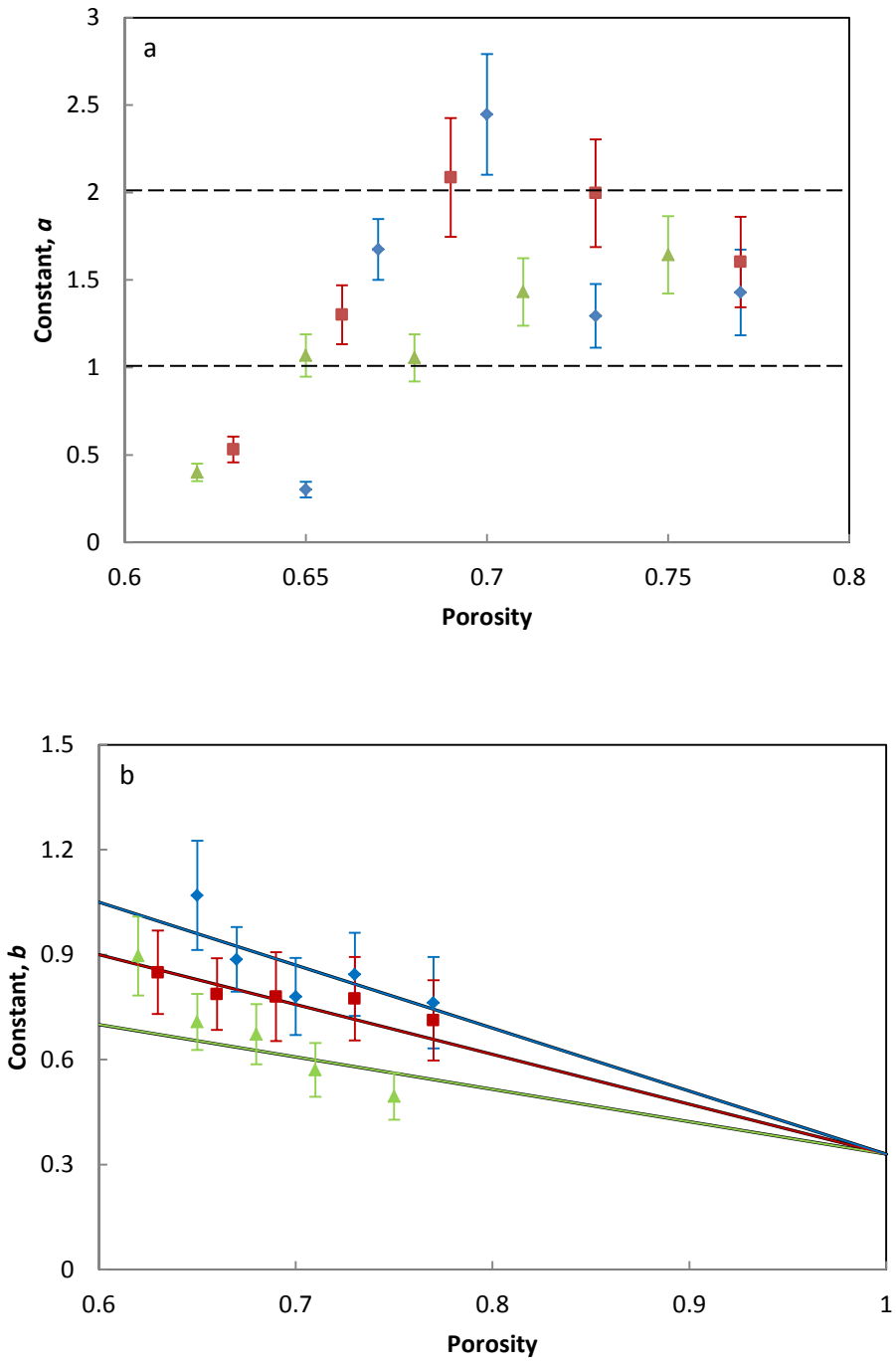

***Fig. 10.12**, Variations of the constants (a) a and (b) b with porosity at different pore sizes: ◆ 1000-1500 µm, ■ 710-1000 µm, and ▲ 250-425 µm.*

Chapter 11 Conclusions and Future Work

11.1 Conclusions

11.1.1 Pore Structure

The microstructures of porous Cu and Ni samples manufactured by the LCS process (decomposition route), such as pore shape, cell walls and sintering necks between metal particles, have been observed by SEM (JSM-6610). Both porous Cu and Ni samples are strongly bonded and have an interconnected open-cell structure.

The porous metal (Cu and Ni) samples have two kinds of pores, primary and secondary pores. The primary pores are the large open pores randomly distributed in the metal matrix and interconnected through small windows. They are effectively negative replicas of the particles of the potassium carbonate powder (75-1500 μm). The secondary pores are the small interstices or voids between the metal particles resulting from partial sintering.

The total porosity of the porous Cu and Ni samples has been determined by measuring their density. The primary porosity, i.e., the porosity contributed by the primary pores, has been measured by the quantitative stereology method. The secondary porosity, i.e., the porosity from the secondary pores, has been obtained by subtracting primary porosity from total porosity. The total porosity of the samples is in the range of 0.59-0.81. The primary porosities of porous Cu and Ni are in the ranges of 0.43-0.67 and 0.57-0.80, respectively. For porous Cu sample, secondary porosity increases with pore size and decreases with total porosity, because the big and uniform-sized particles of the Cu powder lead to more secondary pores in the samples with low porosity and big pore size. For porous Ni samples, the secondary porosity does not change significantly with porosity or pore size. The small and mixed-sized particles of the Ni powder reduce the volume of secondary pores and decrease the effect of secondary porosity on total porosity.

11.1.2 Tortuosity

A diaphragm cell method based on the diffusion of NaCl has been developed and used to measure the tortuosity of porous Cu samples. The tortuosity of porous Cu samples manufactured by the LCS process, with pore sizes 250-1500 μm and porosities 0.56-0.84, is in the range of 1.33-1.78. The tortuosity decreases with porosity and pore size. The relationship between tortuosity and porosity is consistent with an empirical correlation reported in the literature.

11.1.3 Geometric Surface Area

Geometric surface areas of porous Cu and Ni samples manufactured by the LCS process, with pore sizes 250-425 μm and porosities 0.59-0.81, have been measured successfully by the quantitative stereology method.

The volumetric and gravimetric specific geometric surface areas are in the ranges of 18-88 cm^{-1} and 5-40 cm^2/g, respectively, for porous Cu samples, and 26-110 cm^{-1} and 8-57 cm^2/g, respectively, for porous Ni samples. Both the volumetric and gravimetric specific geometric surface areas of porous Cu and Ni increase with porosity and decrease with pore size.

Geometric surface area is due to the contribution from primary porosity only. It is a function of porosity, pore size and metal (Cu and Ni) particle size, and can be described by the analytical stochastic model in 6.2. For the same porosity, the porous Ni samples have a greater geometric surface area than porous Cu, because the Ni powder has smaller particles than the Cu powder.

11.1.4 Electro-Active Surface Area

A cyclic voltammetry (peak current) procedure has been developed and used to measure the electro-active surface areas of porous Cu and Ni samples manufactured by the LCS process, with pore sizes 75-1500 μm and porosities 0.53-0.81.

The volumetric and gravimetric specific electro-active surface areas of porous Cu samples are in the ranges of 206-369 cm^{-1} and 53-128 cm^2/g, respectively, at a scan rate of 0.026 V/s. Both volumetric and gravimetric specific electro-active surface areas decrease with pore size. The latter increases with porosity, while the former is not affected by porosity.

The volumetric and gravimetric specific electro-active surface areas of porous Ni samples are in the ranges of 24-66 cm^{-1}, 32-85 cm^{-1}, 54-120 cm^{-1}, 63-130 cm^{-1}, 69-134 cm^{-1} and 70-135 cm^{-1}, and 8-35 cm^2/g, 10-45 cm^2/g, 17-63 cm^2/g, 20-65 cm^2/g, 22-67 cm^2/g and 23-69 cm^2/g, corresponding to scan rates of 0.005 V/s, 0.01 V/s, 0.05 V/s, 0.1 V/s, 0.2 V/s and 0.3 V/s, respectively. At the same scan rate, the volumetric and gravimetric specific electro-active surface areas increase with porosity and decrease with pore size. They are proportional to their geometric specific surface area. With increasing scan rate, more electro-active surface area is obtained, because the decreased diffusion layer thickness means that more surface area in the secondary pores can be accessed.

Electro-active surface area consists of contributions from primary and secondary porosities. The contribution from the secondary porosity increases with pore size and decreases with porosity in the porous Cu samples, but does not change significantly in porous Ni samples. This is because the small Ni particles can be filled into the interstices or voids between bigger Ni particles and decrease the size and volume of secondary pores.

Compared to other type of porous metals, e.g. Incofoam Ni, the electro-active surface area of LCS porous metal is considerably higher because of the existence of secondary pores. The secondary pores provide more surface area for the electrochemical reactions. Therefore, the LCS porous metal can provide higher surface area and lead to more current density in the applications of electrodes. In this case, LCS porous metal has the potential to be used in the electrochemical applications, such as fuel cells, flow batteries and wastewater treatment.

11.1.5 Real Surface Area

Real surface areas of porous Cu samples manufactured by the LCS process, with pore sizes 75-1500 μm and porosities 0.53-0.76, have been measured successfully by the cyclic voltammetry (double layer capacitance) method. Real surface area is the total surface area of all Cu particles less the sintering necks between Cu particles and isolated voids. It has a strong correlation with the total geometric surface area of all the Cu particles in the sample. The volumetric and gravimetric specific real surface areas are in the ranges of 700-1200 cm^{-1} and 200-360 cm^2/g, respectively.

11.1.7 Mass Transfer Coefficient

A linear sweep voltammetry procedure using a flow electrolyte cell has been developed and used to measure the mass transfer coefficient of porous Ni samples manufactured by the LCS process, with pore sizes 250-1500 μm and porosities 0.62-0.77.

The mass transfer coefficients of porous Ni samples are in the ranges of 9-70 mA/cm^3, 20-103 mA/cm^3, 32-126 mA/cm^3, 96-208 mA/cm^3 and 130-236 mA/cm^3, corresponding to the flow rate of 0.24 ml/s, 0.48 ml/s, 0.8 ml/s, 2 ml/s and 2.8 ml/s, respectively. The mass transfer coefficient of porous Ni samples increases with flow rate, and generally increases with pore size. It also changes with porosity, with the peak (maximum) value appearing at a porosity of 0.65-0.7.

The mass transfer coefficient of porous Ni is up to 9 times higher than a plain Ni plate. This is because the sintering of the Ni particles forms cell walls with rough surface and the tortuous pathway channel can provide a high level of turbulence for the fluid in the flow cell. Compared to traditional electrode, such as Cu and Al sheets in Li-ion flow batteries, the LCS porous metals can provide higher surface area and lead to higher level of turbulence. Therefore, LCS porous metals can improve the mass transport performance in the flow cell application, such as flow batteries and wastewater treatment.

11.2 Future Work

11.2.1 Measurement of Tortuosity

It would be valuable to study the effect of metal particle sizes used in manufacturing LCS porous metal samples through the measurement of tortuosity by the diffusion method.

The tortuosity of the porous metal samples can also be measured by CT scan and acoustic methods. The data from these methods can be compared with the experimental values from the diffusion method to shed some light on the accuracy and reliability of these methods.

11.2.2 Measurement of Electro-Active Surface Area

The measurement of electro-active surface area of porous Cu can be carried out with different electrolytes which do not react with Cu. Cu is an active metal. Any electrochemical reactions during the measurement of electro-active surface area can change the surface structure of the porous Cu samples. If the electrolyte does not react with Cu, the accuracy, repeatability and reliability of the measurement will be increased.

This research showed that metal particle size has a significant effect on the electro-active surface area. It would be interesting to manufacture the porous metal with different metal

particle sizes and study the effect of the secondary pore size on the electro-active surface area.

The Cyclic Voltammetry method can also be applied to the measurement of the electro-active surface area of other porous metals, such as porous Ti and porous steel.

11.2.3 Measurement of Mass Transfer Coefficient

The real flow velocity of fluid through the porous metal samples can be obtained from the relationship between flow rate and tortuosity. The dimensionless numbers for mass transport, such as Reynolds number and Sherwood number, need to revisited, taken into account the real flow velocity.

The effect of metal particle size on the mass transfer coefficient should also be studied. The Linear Sweep Voltammetry method can also be applied to the measurement of the mass transfer coefficient of the other porous metals.

11.2.4 Investigation of Electrochemical Applications

The LCS porous metals have shown a high electro-active surface area and can be used as electrodes in fuel cells. The next step of the research could be to design and set up a half cell to test the performance of porous metal samples in fuel cell applications.

LCS porous metals, with controlled pore structure (pore size, pore shape and porosity), have a great potential for electrochemical recovery of heavy metals. The LCS porous metal can form a porous flow-through configuration providing large surface area and high permeability, resulting in high deposition rate of heavy metal ions in the fluid flow. The next step of the research could be to design and set up an experimental flow circuit involving the porous metal electrochemical reactor to test its performance in heavy metal recovery.

References

Allard, J.F. & Atalla, N., 2009, *Propagation of sound in porous media : modelling sound absorbing materials.* Chichester : Wiley.

Amatore, C., Szunerits, S., Thouin, L. & Warkocz, J., 2001, "The real meaning of Nernst's steady diffusion layer concept under non-forced hydrodynamic conditions. A simple model based on Levich's seminal view of convection", *Journal of Electroanalytical Chemistry,* vol. 500, pp. 62-70.

Ambrose, J., Barradas, R.G. & Shoesmith, D.W., 1973, "Investigations of copper in aqueous alkaline solutions by cyclic voltammetry", *Journal of Electroanalytical Chemistry and Interfacial Electrochemistry,* vol. 47, no. 1, p. 47.

Arulepp, M., Permann, L., Leis, J., Perkson, A., Rumma, K., Janes, A. & Lust, E., 2004, "Influence of the solvent properties on the characteristics of a double layer capacitor", *Journal of Power Sources,* vol. 133, pp. 320-328.

Ashby, M.F., 2000, *Metal foams : a design guide,* Boston : Butterworth-Heinemann.

Babjak, J., Ettel, V.A. & Paserin, V., 1990, *Method of forming nickel foam.*

Banhart, J., 2001, "Manufacture, characterisation and application of cellular metals and metal foams", *Progress in Materials Science,* vol. 46, no. 6, p. 559.

Bard, A.J. & Faulkner, L.R., 2001, *Electrochemical methods : fundamentals and applications,* Hoboken : Wiley.

Bart-Smith, H., Bastawros, A., Mumm, D.R., Evans, A.G., Sypeck, D.J. & Wadley, H.N.G., 1998, "Compressive deformation and yielding mechanisms in cellular Al alloys determined using X-ray tomography and surface strain mapping", *Acta Materialia,* vol. 46, no. 10, pp. 3583-3592.

Bennion, D.N. & Newman, J., 1972, "Electrochemical removal of copper ions from very dilute solutions", *Journal of Applied Electrochemistry,* vol. 2, no. 2, pp. 113-122.

Bidault, F., Brett, D.J.L., Middleton, P.H., Abson, N. & Brandon, N.P., 2009, "A new application for nickel foam in alkaline fuel cells", *International Journal of Hydrogen Energy,* vol. 34, no. 16, p. 6799.

Brevnov, D.A. & Olson, T.S., 2006, "Double-layer capacitors composed of interconnected silver particles and with a high-frequency response", *Electrochimica Acta,* vol. 51, no. 7, p. 1172.

Brown, C.J., Pletcher, D., Walsh, F.C., Hammond, J.K. & Robinson, D., 1993, "Studies of space-averaged mass transport in the FM01-LC laboratory electrolyser", *Journal of Applied Electrochemistry,* vol. 23, no. 1, p. 38.

Brunauer, S., Emmett, P.H. and Teller, E., 1938, "Adsorption of gases in multimolecular layers", *Journal of the American Chemical Society,* vol. 60, no. 2, pp. 309-319.

Cao, L., Yan, P., Sun, K. & Kirk, D., 2009, "Gold 3D Brush Nanoelectrode Ensembles with Enlarged Active Area for the Direct Voltammetry of Daunorubicin", *Electroanalysis,* vol. 21, no. 10, p. 1183.

Chen, J., Liao, W., Hsu, C., Hsieh, W. & Chen, Y., 2015, "All-vanadium redox flow batteries with graphite felt electrodes treated by atmospheric pressure plasma jets", *Journal of Power Sources,* vol. 274, pp. 894-898.

Compton, R.G. & Sanders, G.H.W., 2006, *Electrode potentials.* Oxford : Oxford University Press.

Conizares, P., Garcia-Gomez, J., Fernandez, D.M., Rodrigo, M.A. & Lobato, J., 2006, "Measurement of mass-transfer coefficients by an electrochemical technique", *Journal of chemical education,* vol. 83, no. 8, pp. 1204-1207.

Corbin, S.F., Clemmer, R.M.C. & Yang, Q., 2009, "Development and characterization of porous composites for solid oxide fuel cell anode conduction layers using ceramic-filled highly porous ni foam", *Journal of the American Ceramic Society,* vol. **92**, no. 2, pp. 331-337.

Currie, J.A., 1960, "Gaseous diffusion in porous media. Part 2. - Dry granular materials", *British Journal of Applied Physics,* vol. 11, no. 8, pp. 318-324.

Cussler, E.L., 1984, *Diffusion: mass transfer in fluid systems,* Cambridge: Cambridge University Press.

Davies, T.J., Banks, C.E. & Compton, R.G., 2005, "Voltammetry at spatially heterogeneous electrodes", *Journal of Solid State Electrochemistry,* vol. 9, no. 12, p. 797.

Davies, T.J., Wilkins, S.J. & Compton, R.G., 2006, "The electrochemistry of redox systems within immobilised water droplets", *Journal of Electroanalytical Chemistry,* vol. 586, pp. 260-275.

De Radigues, Q., Sevar, P., Van Wonterghem, F., Santoro, R. & Proost, J., 2012, "Electrochemical characterization of mass transport in porous electrodes", *Industrial and Engineering Chemistry Research,* vol. 51, no. 43, pp. 14229-14235.

Degischer, H. & Kriszt, B., 2002, *Handbook of cellular metals : production, processing, applications.* Weinheim : Wiley-VCH.

Delahay, P., 1954, *New instrumental methods in electrochemistry: theory, instrumentation, and applications to analytical and physical chemistry.* New York: Interscience.

Dijkstra, E., 1959, "A note on two problems in connexion with graphs", *Numerische Mathematik,* vol. 1, no. 1, p. 269.

Doan, H.D., Wu, J. & Mitzakov, R., 2006, "Combined electrochemical and biological treatment of industrial wastewater using porous electrodes", *Journal of Chemical Technology and Biotechnology,* vol. 81, no. 8, pp. 1398-1408.

Droog, J.M.M., Alderliesten, C.A., Alderliesten, P.T. & Bootsma, G.A., 1980, "Initial stages of anodic oxidation of polycrystalline copper electrodes in alkaline solution", *Journal of Electroanalytical Chemistry,* vol. 111, no. 1, pp. 61-70.

Du, H., Jiao, L., Wang, Q., Huan, Q., Guo, L., Si, Y., Wang, Y. & Yuan, H., 2013, "Morphology control of CoCO3 crystals and their conversion to mesoporous Co3O4 for alkaline rechargeable batteries application", *CrystEngComm,* vol. 15, no. 31, pp. 6101-6109.

Dukic, A., Alar, V., Firak, M. & Jakovljevic, S., 2013, "A significant improvement in material of foam", *Journal of Alloys and Compounds,* vol. 573, no. 8, p. 128.

Eaborn, C., 1988, "Book review: Compendium of chemical Terminology: IUPAC Recommendations", *Journal of Organometallic Chemistry,* vol. 356, pp. C76-C77.

Eifert, H. & Banhart, J., 1998. *Metal foams : Fraunhofer USA Metal Foam Symposium,* Bremen : Verlag MIT Publishing.

El-Deab, M., Saleh, M.M., El-Anadouli, B. & Ateya, B.G., 1999, *Electrochemical removal of lead ions from flowing electrolytes using packed bed electrodes.*

Epstein, N., 1989. On tortuosity and the tortuosity factor in flow and diffusion through porous media. *Chemical Engineering Science,* **44**(3), pp. 777-779.

Fisher, A.C., 1996. *Electrode dynamics.* Oxford : Oxford University Press.

Focke, W.W., 1983, "On the mechanism of transfer enhancement by eddy promoters", *Electrochimica Acta,* vol. 28, no. 8, p. 1137.

Fragkou, V., Ge, Y., Turner, A.P.F., Freeman, D., Steiner, G. & Bartetzko, N., 2012, "Determination of the real surface area of a screen-printed electrode by chronocoulometry", *International Journal of Electrochemical Science,* vol. 7, no. 7, pp. 6214-6220.

Fujinaga, T. & Kihara, S., 1977, "Electrolytic Chromatography and Coulopotentiograhy. A Rapid Electrolysis at the Column Electrode Used for the Preparation, Separation, Concentration and Estimation of Trace and/or Unstable Substances", *Critical Reviews in Analytical Chemistry,* vol. 6, p. 223.

Gaunand, A., Hutin, D. & Coeuret, F., 1977, "Potential distribution in flow-through porous electrodes under limiting current conditions", *Electrochimica Acta,* vol. 22, no. 1, pp. 93-97.

Gergely, V., Degischer, H.P. & Clyne, T.W., 2000, *Recycling of MMCs and Production of Metallic Foams.*

Gibson, L.J. & Ashby, M.F., 1999, *Cellular solids : structure and properties,* Cambridge ; Cambridge University Press.

Gileadi, E., 2011, *Physical electrochemistry : fundamentals, techniques and applications.* Weinheim : Wiley-VCH.

Goodhew, P.J., Humphreys, F.J. & Beanland, R., 2001, *Electron microscopy and analysis.* London : Taylor & Francis.

Guo, Y., Zhang, H., Hu, J., Wan, L. & Bai, C., 2005, "Nanoarchitectured metal film electrodes with high electroactive surface areas", *Thin Solid Films,* vol. 484, no. 1, p. 341.

Han, F., Seiffert, G., Zhao, Y. & Gibbs, B., 2003, "Acoustic absorption behaviour of an open-celled aluminium foam", *Journal of Physics D: Applied Physics,* vol. 36, no. 3, p. 294.

Harris, D.C., 2006, *Quantitative chemical analysis.* New York ; W. H. Freeman & Company.

Harte, A., Fleck, N.A. & Ashby, M.F., 1999, "Fatigue failure of an open cell and a closed cell aluminium alloy foam", *Acta Materialia,* vol. 47, pp. 2511-2524.

Herman, G.T., 2009, *Fundamentals of computerized tomography. [electronic book] : image reconstruction from projections,* Dordrecht ; Springer.

Holman, J.P., 2012. *Experimental methods for engineers.* Boston : McGraw-Hill/Connect Learn Succeed.

Kawasaki, A., 2015, "Advances in powder and powder metallurgy", *Funtai Oyobi Fummatsu Yakin/Journal of the Japan Society of Powder and Powder Metallurgy,* vol. 62, no. 7, p. 356.

Kendall, J.M., Lee, M.C. & Wang, T.G., 1981, "Metal Shell Technology Based upon Hollow Jet Instability" *Journal of vacuum science & technology,* vol. 20, no. 4, pp. 1091-1093.

Kenny, L.D. & Thomas, M., 1994, *Process for shape casting of particle stabilized metal foam.*

Khayargoli, P., Loya, V., Lefebvre, L.P. & Medraj, M., 2005, *The impact of microstructure on the permeability of metal foams.* Canada: Proceedings of canadian society of mechanical engineers (CSME) 2004 Forum.

Kihlman, B A. 1958. "The effect of oxygen, nitric oxide, and respiratory inhibitors on the production of chromosome aberration by x-rays" *Experimental Cell Research,*vol. 14, no. 3, pp. 639-642.

Kino, N., 2015, "Further investigations of empirical improvements to the Johnson–Champoux–Allard model", *Applied Acoustics,* vol. 96, pp. 153-170.

Kline, S.J. & Mcclintock, F.A., 1953, "Describing Uncertainties in Single-Sample Experiments", *Mechanical Engineering,* p. 3.

Kobayashi, N., Ogata, H., Park, K.C., Takeuchi, K. & Endo, M., 2013, "Investigation on capacitive behaviors of porous Ni electrodes for electric double layer capacitors", *Electrochimica Acta,* vol. 90, pp. 408-415.

Koponen, A., Kataja, M. & Timonen, J., 1996, "Tortuous flow in porous media", *Physical Review E - Statistical Physics, Plasmas, Fluids, and Related Interdisciplinary Topics,* vol. 54, no. 1, pp. 406-410.

Lai, P., Moulton, K. & Krevor, S., 2015, "Pore scale heterogeneity in the mineral distribution and reactive surface area of porous rocks", *Chemical Geology,* vol. 411, pp. 260-273.

Laptev, A., Bram, M., Buchkremer, H.P. and Stover, D., 2004, "Study of production route for titanium parts combining very high porosity and complex shape" *Powder Metallurgy,* vol. 47, no. 1, pp. 85-92.

Leitz, F.B. & Marincic, L., 1977, "Enhanced mass transfer in electrochemical cells using turbulence promoters", *Journal of Applied Electrochemistry,* **7**(6), pp. 473.

Letord-Quemere, M.M., 1988, "Mass Transfer at the Wall of a Thin Channel Containing an Expanded Turbulence Promoting Structure", *Journal of the Electrochemical Society,* vol. 135, no. 12, p. 3063.

Lewandowski, A., Jakobczyk, P. & Galinski, M., 2012, "Capacitance of electrochemical double layer capacitors", *Electrochimica Acta,* vol. 86, no. 1, p. 225.

Lhuissier, P., Fallet, A., Salvo, L. & Brechet, Y., 2009, "Quasistatic mechanical behaviour of stainless steel hollow sphere foam: Macroscopic properties and damage mechanisms followed by X-ray tomography" *Materials Letters,* vol. 63, pp. 1113-1116.

Li, X., Zhang, H., Mai, Z., Zhang, H. & Vankelecom, I., 2011, "Ion exchange membranes for vanadium redox flow battery (VRB) applications", *Energy & Environmental Science,* vol. 4, no. 4, p. 1147.

Li, Y., Chang, S., Liu, X., Huang, J., Yin, J., Wang, G. & Cao, D., 2012, "Nanostructured CuO directly grown on copper foam and their supercapacitance performance", *Electrochimica Acta,* vol. 85, no. 11, p. 393.

Li, Y., Li, Y., Liu, Z., Wu, T. & Tian, Y., 2011, "A novel electrochemical ion exchange system and its application in water treatment", *Journal of Environmental Sciences,* vol. 23, pp. S14-S17.

Lukomska, A. & Sobkowski, J., 2004, "Potential of zero charge of monocrystalline copper electrodes in perchlorate solutions", *Journal of Electroanalytical Chemistry,* vol. 567, no. 1, pp. 95-102.

Ma, X., Peyton, A.J. & Zhao, Y.Y., 2005, "Measurement of the electrical conductivity of open-celled aluminium foam using non-contact eddy current techniques", *NDT & E International,* vol. 38, no. 5, p. 359.

Markaki, A.E. & Clyne, T.W., 2001, "The effect of cell wall microstructure on the deformation and fracture of aluminium-based foams" *Acta Materialia,* vol. 49, pp. 1677-1686.

Mattiusi, E.M., Kaminari, N.M.S., Ponte, M.J.J.S. & Ponte, H.A., 2015, "Behavior analysis of a porous bed electrochemical reactor the treatment of petrochemical industry wastewater contaminated by hydrogen sulfide (H2S)", *Chemical Engineering Journal,* vol. 275, pp. 305-314.

Merkus, HG 2009, *Particle Size Measurements. [Electronic Book] : Fundamentals, Practice, Quality*, n.p.: Dordrecht : Springer

Miyoshi, T., Itoh, M., Akiyama, S. & Kitahara, A., 2000, "ALPORAS aluminum foam: Production process, properties, and applications" *Advanced Engineering Materials,* vol. 2, no. 4, pp. 179-183.

Montillet, A., Comiti, J. & Legrand, J., 1994, "Application of metallic foams in electrochemical reactors of the filter-press type: Part II Mass transfer performance", *Journal of Applied Electrochemistry,* vol. 24, no. 5, pp. 384-389.

Montillet, A., Comiti, J. & Legrand, J., 1993, "Application of metallic foams in electrochemical reactors of filter-press type Part I: Flow characterization", *Journal of Applied Electrochemistry,* vol. 23, no. 10, pp. 1045-1050.

Montillet, A., Comiti, J. & Legrand, J., 1992, "Determination of structural parameters of metallic foams from permeametry measurements", *Journal of Materials Science,* vol. 27, no. 16, pp. 4460-4464.

Nava, J.L., Oropeza, M.T., Ponce, D.L., Gonzalez-Garcia, J. and Frias-Ferrer, A.J., 2008, "Determination of the effective thickness of a porous electrode in a flow-through reactor; effect of the specific surface area of stainless steel fibres, used as a porous cathode, during the deposition of Ag(I) ions", *Hydrometallurgy,* vol. 91, pp. 98-103.

Nersisyan, H.H., Won, H.I., Won, C.W., Kim, J.B., Park, S.M. & Kim, J.H., 2013, "Combustion synthesis of porous titanium microspheres", *Materials Chemistry and Physics,* vol. 141, pp. 283-288.

Nikiforidis, G. & Daoud, W.A., 2015, "Indium modified graphite electrodes on highly zinc containing methanesulfonate electrolyte for zinc-cerium redox flow battery", *Electrochimica Acta,* vol. 168, pp. 394-402.

Odler, I., 2003, "The BET-specific surface area of hydrated Portland cement and related materials", *Cement and Concrete Research,* vol. 33, pp. 2049-2056.

Panneton, R. & Olny, X., 2006, "Acoustical determination of the parameters governing viscous dissipation in porous media" *Journal of the Acoustical Society of America,* vol. 119, no. 4, pp. 2027-2040.

Park, S. & Seo, M., 2011, *Interface science and composites. [electronic book]*. Amsterdam : Academic Press.

Parsons, R., 1990, "Book reviews: Cyclic voltammetry and the frontiers of electrochemistry", *Journal of Electroanalytical Chemistry,* vol. 305, pp. 164-166.

Pletcher, D., 1991, *A first course in electrode processes,* Electrochemical Consultancy.

Podlaha, E.J. & Fenton, J.M., 1995, "Characterization of a flow-by RVC electrode reactor for the removal of heavy metals from dilute solutions", *Journal of Applied Electrochemistry,* vol. 25, no. 4, pp. 299-306.

Queheillalt, D.T., Hass, D.D., Sypeck, D.J. & Wadley, H., 2001, *Synthesis of open-cell metal foams by templated directed vapor deposition.*

Recio, F.J., Herrasti, P., Vazquez, L., Ponce De Leon, C. & Walsh, F.C., 2013, "Mass transfer to a nanostructured nickel electrodeposit of high surface area in a rectangular flow channel", *Electrochimica Acta,* vol. 90, p. 507.

Rehder, B., Banh, K. & Neithalath, N., 2014, "Fracture behavior of pervious concretes: The effects of pore structure and fibers" *Engineering Fracture Mechanics,* vol. 118, pp. 1-16.

Riquelme, R., Lira, I., Perez-Lopez, C., Rayas, J.A. & Rodriguez-Vera, R., 2007, "Interferometric measurement of a diffusion coefficient: Comparison of two methods and uncertainty analysis", *Journal of Physics D: Applied Physics,* vol. 40, no. 9, pp. 2769-2776.

Rogerio, P. & Carlos, S., 2012, "Implementation of acoustic materials to the VLS-1 Fairing - a sensitivity analysis using SEA", *Journal of the Brazilian Society of Mechanical Sciences and Engineering,* vol. 1, p. 82.

Roy, S., Wanner, A., Beck, T., Studnitzky, T. & Stephani, G., 2011, "Mechanical properties of cellular solids produced from hollow stainless steel spheres", *Journal of Materials Science,* vol. 46, no. 16, pp. 5519-5526.

Saltykov, S. A., 1967, "A Stereological Method for Measuring the Specific Surface Area of Metallic Powders", *Proceedings of the Second International Congress for Stereology,* p. 63.

Saltykov, S. A., 1958, *Stereometric Metallography.* 2nd edn. Moscow: Metallurgizdat.

Saleh, M.M., 2004, *On the effectiveness factor of flow-through porous electrodes.*

Sang, H., Kenny, L.D. & Jin, I., 1994, *Process for producing shaped slabs of particle stabilized foamed metal.*

Schindelin, J., Arganda-Carreras, I. & Frise, E. et al., 2012, "Fiji: an open-source platform for biological-image analysis", *Nature methods*, vol. 9, no. 7, pp. 676-682.

Scholz, F., 2002, *Electroanalytical methods : guide to experiments and applications,* Berlin : Springer, 2002.

Shanti, N.O., Chan, V.W.L., Stock, S.R., De Carlo, F., Thornton, K. & Faber, K.T., 2014, "X-ray micro-computed tomography and tortuosity calculations of percolating pore networks", *Acta Materialia,* vol. 71, pp. 126-135.

Shapovalov, V.I., 2007. *Prospective applications of gas-eutectic porous materials (gasars) in USA.*

Shapovalov, V.I. and Withers, J.C., 2009, "Hydrogen Technology for Porous Metals (Gasars) Production", *Carbon Nanomaterials in Clean Energy Hydrogen Systems,* p. 29.

Signorelli, R., Ku, D.C., Kassakian, J.G. & Schindall, J.E., 2009, "Electrochemical double-layer capacitors using carbon nanotube electrode structures" *Proceedings of the IEEE,* vol. 97, no. 11, pp. 1837-1847.

Smith, R.E.G., Nichols, R.J., Davies, T.J. & Baynes, N.D.B., 2015, "The electrochemical characterisation of graphite felts", *Journal of Electroanalytical Chemistry,* vol. 747, pp. 29-38.

Soltan, E.A., Nosier, S.A., Salem, A.Y., Mansour, I.A.S. & Sedahmed, G.H., 2003, "Mass transfer behaviour of a flow-by fixed bed electrochemical reactor under different hydrodynamic conditions", *Chemical Engineering Journal,* vol. 91, pp. 33-44.

Speed, S.E., 1976, *Foaming of metal by the catalyzed and controlled decomposition of zirconium hydride and titanium hydride.*

Srinivasan, S., 2006. *Fuel Cells. [electronic book] : From Fundamentals to Applications.* New York : Springer Science+Business Media.

Strohl, A.N. & Curran, D.J., 1979, "Flow injection analysis with reticulated vitreous carbon flow-through electrodes", *Analytical Chemistry,* vol. 51, no. 7, pp. 1045-1049.

Suarez, D.,J., Gonzalez, Z., Blanco, C., Granda, M., Menendez, R. & Santamaria, R., 2014, "Graphite felt modified with bismuth nanoparticles as negative electrode in a vanadium redox flow battery", *Chemsuschem,* vol. 7, no. 3, pp. 914-918.

Surace, R., De Filippis, L. A. C., Niini, E., Ludovico, A.D. & Orkas, J., 2009, "Morphological Investigation of Foamed Aluminum Parts Produced by Melt Gas Injection", *Advances in Materials Science & Engineering,* pp. 1-9.

Tan, Y.H., Davis, J.A., Fujikawa, K., Ganesh, N.V., Demchenko, A.V. & Stine, K.J., 2012, "Surface area and pore size characteristics of nanoporous gold subjected to thermal, mechanical, or surface modification studied using gas adsorption isotherms, cyclic voltammetry, thermogravimetric analysis, and scanning electron microscopy", *Journal of Materials Chemistry,* vol. 22, no. 14, p. 6733.

Thewsey, D.J. & Zhao, Y.Y., 2008, *Thermal conductivity of porous copper manufactured by the lost carbonate sintering process.*

Trainham, J.A. & Newman, J., 1977, "Flow-through Porous Electrode Model: Application to Metal-Ion Removal from Dilute Streams" *Journal of the Electrochemical Society,* vol. 124, no. 10, pp. 1528-1540.

Underwood, E.E., 1970, *Quantitative stereology.* Reading (Mass.): Addison-Wesley.

Vida-Simiti, I., Jumate, N., Bruj, E., Sechel, N., Thalmaier, G., Nemes, D. & Nicoara, M., 2011, *Metallic foams obtained from nickel based superalloy hollow spheres.*

Vielstich, W., Lamm, A. & Gasteiger, H.A., 2003, *Handbook of fuel cells : fundamentals, technology, and applications,* Chichester : Wiley.

Walsh, F.C., 1993, *A first course in electrochemical engineering.* Romsey : Electrochemical Consultancy.

Wan, H., Lv, L., Peng, L., Ruan, Y., Liu, J., Ji, X., Miao, L. & Jiang, J., 2015, "Hollow spiny shell of porous Ni–Mn oxides: A facile synthesis route and their application as electrode in supercapacitors", *Journal of Power Sources,* vol. 286, pp. 66-72.

Wang, Y., Li, L., Han, Y., Qiu, F., Liu, G., Yan, C., Jiao, L., Yuan, H., Wang, Y. & Song, D., 2011, "Mesoporous nano-Co 3O 4: A potential negative electrode material for alkaline secondary battery", *Journal of Power Sources,* vol. 196, no. 24, pp. 10758-10761.

Ward, K.R., Gara, M., Lawrence, N.S., Hartshorne, R.S. & Compton, R.G., 2013, "Nanoparticle modified electrodes can show an apparent increase in electrode kinetics due solely to altered surface geometry: The effective electrochemical rate constant for non-flat and non-uniform electrode surfaces", *Journal of Electroanalytical Chemistry,* vol. 695, no. 2, p. 1.

Ward, K.R., Xiong, L., Lawrence, N.S., Hartshorne, R.S. & Compton, R.G., 2013, "Thin-layer vs. semi-infinite diffusion in cylindrical pores: A basis for delineating Fickian transport to identify nano-confinement effects in voltammetry", *Journal of Electroanalytical Chemistry,* vol. 702, pp. 15-24.

Xiao, Z. & Zhao, Y., 2013, "Heat transfer coefficient of porous copper with homogeneous and hybrid structures in active cooling", *Journal of Materials Research,* vol. 28, no. 17, p. 2545.

Xu, Y.A., Wang, X.F., An, C.H., Wang, Y.J., Jiao, L.F. & Yuan, H., 2014, *Effect of the length and surface area on electrochemical performance of cobalt oxide nanowires for alkaline secondary battery application.*

Zhang, L.P., Mullen D., Lynn K. & Zhao Y.Y., 2009, "Heat Transfer Performance of Porous Copper Fabricated by the Lost Carbonate Sintering Process", *Materials Research Society,* vol. 1188, p. 07.

Zhao, Y.Y., Fung, T., Zhang, L.P. & Zhang, F.L., 2005, "Lost carbonate sintering process for manufacturing metal foams", *Scripta Materialia,* vol. 52, no. 4, p. 295.

Zhao, Y.Y. & Sun, D.X., 2001, "A novel sintering-dissolution process for manufacturing Al foams", *Scripta Materialia,* vol. 44, no. 1, p. 105.

Zhao, Y., 2013, "Porous Metallic Materials Produced by P/M Methods", *J Powder Metall Min,* vol. 2, no. 3, p. e113.

Zhao, Y.Y., 2003, "Stochastic Modelling of Removability of NaCl in Sintering and Dissolution Process to Produce Al Foams" *Journal of Porous Materials,* vol. 10, no. 2, pp. 105-111.

Zhou, W., Tang, Y., Pan, M., Wei, X., Chen, H. & Xiang, J., 2009, "A performance study of methanol steam reforming microreactor with porous copper fiber sintered felt as catalyst support for fuel cells", *International Journal of Hydrogen Energy*, vol. 34, pp. 9745-9753.

Zhou, W., Wang, Q., Qiu, Q., Tang, Y., Tu, J., Hui, K.S. & Hui, K.N., 2015, "Heat and mass transfer characterization of porous copper fiber sintered felt as catalyst support for methanol steam reforming", *Fuel*, vol. 145, pp. 136-142.

Appendixes

***Table A4.3**, Summary of the dimensions and porosities of the porous Cu samples used for CV measurements.*

Ref.	Pore size (µm)	Length (cm)	Width (cm)	Height (cm)	Mass (g)	Porosity
Cu01	1000-1500	2.80	2.11	0.59	12.70	0.59
Cu02	1000-1500	3.10	2.05	0.58	12.70	0.62
Cu03	1000-1500	3.07	2.06	0.58	11.40	0.65
Cu04	1000-1500	3.08	2.05	0.57	9.95	0.69
Cu05	1000-1500	3.06	2.06	0.58	9.10	0.72
Cu06	1000-1500	3.07	2.05	0.56	7.60	0.76
Cu07	710-1000	3.04	2.04	0.59	14.30	0.56
Cu08	710-1000	3.04	2.03	0.57	13.00	0.59
Cu09	710-1000	3.03	2.04	0.59	11.65	0.64
Cu10	710-1000	3.03	2.02	0.57	10.40	0.67
Cu11	710-1000	3.03	2.03	0.59	9.40	0.71
Cu12	710-1000	3.03	2.02	0.55	7.80	0.74
Cu13	425-710	3.08	2.07	0.58	14.30	0.57
Cu14	425-710	3.06	2.04	0.57	12.50	0.61
Cu15	425-710	3.06	2.05	0.57	11.95	0.63
Cu16	425-710	3.05	2.04	0.56	10.15	0.67
Cu17	425-710	3.06	2.05	0.58	9.35	0.71
Cu18	425-710	3.04	2.03	0.56	7.85	0.74
Cu19	250-425	3.04	2.04	0.59	14.7	0.55
Cu20	250-425	3.02	2.03	0.57	12.75	0.59
Cu21	250-425	3.02	2.02	0.58	11.85	0.63
Cu22	250-425	3.00	2.01	0.57	10.50	0.66
Cu23	250-425	3.00	2.01	0.57	9.25	0.70
Cu24	250-425	2.97	1.98	0.56	7.95	0.73
Cu25	75-150	3.01	2.02	0.57	14.45	0.53
Cu26	75-150	2.99	2.00	0.56	13.10	0.56
Cu27	75-150	3.00	2.02	0.57	11.90	0.61
Cu28	75-150	2.97	1.98	0.55	10.50	0.63
Cu29	75-150	2.94	1.96	0.55	9.20	0.67
Cu30	75-150	2.85	1.89	0.50	7.85	0.68

Table A4.4, *Summary of the dimensions and porosities of the porous Cu samples used for QS measurements.*

Ref.	Pore size (μm)	Length (cm)	Width (cm)	Height (cm)	Mass (g)	Porosity
S01	1000-1500	3.05	2.08	1.12	25.80	0.59
S02	1000-1500	3.05	2.09	1.13	23.75	0.63
S03	1000-1500	3.05	2.08	1.13	21.00	0.67
S04	1000-1500	3.05	2.09	1.12	18.60	0.71
S05	1000-1500	3.05	2.08	1.11	15.85	0.75
S06	710-1000	3.04	2.07	1.13	26.15	0.59
S07	710-1000	3.03	2.07	1.16	23.75	0.64
S08	710-1000	3.03	2.06	1.16	21.00	0.68
S09	710-1000	3.02	2.06	1.16	18.30	0.72
S10	710-1000	3.01	2.06	1.15	15.60	0.75
S11	425-710	3.03	2.07	1.14	26.25	0.59
S12	425-710	3.04	2.07	1.13	23.65	0.63
S13	425-710	3.03	2.07	1.12	20.80	0.67
S14	425-710	3.02	2.06	1.13	18.70	0.70
S15	425-710	3.02	2.06	1.11	15.55	0.75
S16	250-425	3.02	2.06	1.16	26.30	0.59
S17	250-425	3.01	2.06	1.16	23.85	0.64
S18	250-425	3.01	2.05	1.15	21.10	0.67
S19	250-425	3.00	2.05	1.15	18.60	0.70
S20	250-425	2.98	2.03	1.15	16.05	0.75

Table A4.5, *Summary of the dimensions and porosities of the porous Ni samples for CV and LSV measurements.*

Ref.	Pore size (µm)	Length (cm)	Width (cm)	Height (cm)	Mass (g)	Porosity
Ni01	1000-1500	3.06	2.10	0.61	12.25	0.65
Ni02	1000-1500	3.07	2.10	0.61	11.70	0.67
Ni03	1000-1500	3.06	2.09	0.61	10.40	0.70
Ni04	1000-1500	3.07	2.09	0.60	9.25	0.73
Ni05	1000-1500	3.07	2.10	0.60	7.80	0.77
Ni06	1000-1500	3.08	2.10	0.60	6.40	0.81
Ni07	710-1000	3.05	2.08	0.61	12.70	0.63
Ni08	710-1000	3.05	2.08	0.61	11.75	0.66
Ni09	710-1000	3.05	2.08	0.61	10.45	0.69
Ni10	710-1000	3.04	2.08	0.60	9.10	0.73
Ni11	710-1000	3.04	2.08	0.59	7.70	0.77
Ni12	710-1000	3.06	2.08	0.59	6.45	0.81
Ni13	425-710	3.05	2.08	0.61	13.20	0.62
Ni14	425-710	3.04	2.07	0.60	11.90	0.65
Ni15	425-710	3.04	2.07	0.60	10.70	0.68
Ni16	425-710	3.05	2.08	0.59	9.30	0.72
Ni17	425-710	3.04	2.07	0.58	7.90	0.76
Ni18	425-710	3.05	2.07	0.57	6.60	0.80
Ni19	250-425	3.03	2.06	0.62	13.25	0.62
Ni20	250-425	3.02	2.05	0.61	11.85	0.65
Ni21	250-425	3.01	2.05	0.60	10.55	0.68
Ni22	250-425	3.00	2.04	0.59	9.15	0.71
Ni23	250-425	3.00	2.04	0.59	7.85	0.75
Ni24	250-425	2.98	2.02	0.59	6.45	0.79

Table A4.6, *Summary of the porosities of the porous Cu samples (dimension: 2.4 cm^2 in diameter and 1 cm in thickness) for tortuosity measurements.*

Ref.	Pore size (μm)	Mass (g)	Porosity
T01	1000-1500	52.36	0.68
T02	1000-1500	46.45	0.71
T03	1000-1500	40.24	0.80
T04	1000-1500	25.77	0.84
T05	710-1000	57.79	0.64
T06	710-1000	50.51	0.69
T07	710-1000	43.40	0.73
T08	710-1000	36.10	0.78
T09	425-710	70.77	0.56
T10	425-710	64.41	0.60
T11	425-710	57.51	0.65
T12	425-710	51.02	0.69
T13	425-710	44.17	0.73
T14	250-425	72.11	0.56
T15	250-425	65.42	0.60
T16	250-425	58.83	0.64
T17	250-425	51.50	0.68
T18	250-425	44.95	0.72

***Table A4.7**, Primary porosity (ε_p) for porous Cu samples.*

Ref.	Pore size (µm)	Total porosity (ε)	P_{pore}	ε_P
S01	1000-1500	0.59	79	0.44
S02	1000-1500	0.63	84	0.47
S03	1000-1500	0.67	92	0.51
S04	1000-1500	0.71	99	0.55
S05	1000-1500	0.75	116	0.65
S06	710-1000	0.59	81	0.45
S07	710-1000	0.64	90	0.50
S08	710-1000	0.68	94	0.52
S09	710-1000	0.72	105	0.58
S10	710-1000	0.75	109	0.60
S11	425-710	0.59	84	0.47
S12	425-710	0.63	90	0.50
S13	425-710	0.67	99	0.55
S14	425-710	0.70	113	0.63
S15	425-710	0.75	120	0.67
S16	250-425	0.59	77	0.43
S17	250-425	0.64	109	0.60
S18	250-425	0.67	118	0.66
S19	250-425	0.70	126	0.70
S20	250-425	0.75	135	0.75

Table A4.8, *Primary porosity (ε_p) for porous Ni samples*.

Ref.	Pore size (µm)	Total porosity (ε)	P_{pore}	ε_P
Ni01	1000-1500	0.65	114	0.64
Ni02	1000-1500	0.67	120	0.67
Ni03	1000-1500	0.70	124	0.69
Ni04	1000-1500	0.73	131	0.73
Ni05	1000-1500	0.77	137	0.76
Ni06	1000-1500	0.81	144	0.80
Ni07	710-1000	0.63	112	0.61
Ni08	710-1000	0.66	114	0.64
Ni09	710-1000	0.69	124	0.69
Ni10	710-1000	0.73	128	0.71
Ni11	710-1000	0.77	137	0.76
Ni12	710-1000	0.81	143	0.79
Ni13	425-710	0.62	111	0.61
Ni14	425-710	0.65	116	0.65
Ni15	425-710	0.68	122	0.68
Ni16	425-710	0.72	128	0.71
Ni17	425-710	0.76	137	0.76
Ni18	425-710	0.80	143	0.79
Ni19	250-425	0.62	103	0.57
Ni20	250-425	0.65	116	0.65
Ni21	250-425	0.68	120	0.67
Ni22	250-425	0.71	128	0.71
Ni23	250-425	0.75	135	0.75
Ni24	250-425	0.79	141	0.78

Table A4.9, *Secondary porosity (ε_S) of porous Cu samples.*

Ref.	Pore size (μm)	Total porosity (ε)	Secondary porosity (ε_S)
S01	1000-1500	0.59	0.15
S02	1000-1500	0.63	0.16
S03	1000-1500	0.67	0.16
S04	1000-1500	0.71	0.16
S05	1000-1500	0.75	0.10
S06	710-1000	0.59	0.14
S07	710-1000	0.64	0.14
S08	710-1000	0.68	0.16
S09	710-1000	0.72	0.14
S10	710-1000	0.75	0.15
S11	425-710	0.59	0.12
S12	425-710	0.63	0.13
S13	425-710	0.67	0.12
S14	425-710	0.70	0.07
S15	425-710	0.75	0.08
S16	250-425	0.59	0.16
S17	250-425	0.64	0.04
S18	250-425	0.67	0.01
S19	250-425	0.70	0.00
S20	250-425	0.75	0.00

Table A4.10, *Secondary porosity (ε_S) of porous Ni samples.*

Ref.	Pore size (μm)	Total porosity (ε)	Secondary porosity (ε_S)
Ni01	1000-1500	0.65	0.01
Ni02	1000-1500	0.67	0.00
Ni03	1000-1500	0.70	0.01
Ni04	1000-1500	0.73	0.00
Ni05	1000-1500	0.77	0.01
Ni06	1000-1500	0.81	0.01
Ni07	710-1000	0.63	0.02
Ni08	710-1000	0.66	0.02
Ni09	710-1000	0.69	0.00
Ni10	710-1000	0.73	0.02
Ni11	710-1000	0.77	0.01
Ni12	710-1000	0.81	0.02
Ni13	425-710	0.62	0.01
Ni14	425-710	0.65	0.00
Ni15	425-710	0.68	0.00
Ni16	425-710	0.72	0.01
Ni17	425-710	0.76	0.00
Ni18	425-710	0.80	0.01
Ni19	250-425	0.62	0.05
Ni20	250-425	0.65	0.00
Ni21	250-425	0.68	0.01
Ni22	250-425	0.71	0.00
Ni23	250-425	0.75	0.00
Ni24	250-425	0.79	0.01

Table A5.2, *Tortuosity of porous Cu samples.*

Ref.	Pore size (μm)	Porosity	V_t (cm^3)	V_b (cm^3)	$c_{t,t}$ (mol/L)	$c_{b,t}$ (mol/L)	Tortuosity
T01	1000-1500	0.68	106.52	109.31	0.13	1.46	1.78
T02	1000-1500	0.71	106.59	107.05	0.24	1.44	1.57
T03	1000-1500	0.80	110.58	107.70	0.36	1.30	1.41
T04	1000-1500	0.84	110.17	110.43	0.35	1.32	1.35
T05	710-1000	0.64	106.59	107.05	0.19	1.50	1.70
T06	710-1000	0.69	108.46	106.08	0.24	1.49	1.62
T07	710-1000	0.73	110.58	107.70	0.24	1.40	1.50
T08	710-1000	0.78	110.17	110.43	0.32	1.32	1.33
T09	425-710	0.56	114.08	111.20	0.18	1.57	1.75
T10	425-710	0.60	106.52	109.31	0.18	1.52	1.70
T11	425-710	0.65	106.59	107.05	0.21	1.46	1.59
T12	425-710	0.69	108.46	106.08	0.25	1.40	1.45
T13	425-710	0.73	110.58	107.70	0.26	1.35	1.40
T14	250-425	0.56	114.08	111.20	0.18	1.54	1.63
T15	250-425	0.60	106.52	109.31	0.23	1.53	1.61
T16	250-425	0.64	106.59	107.05	0.23	1.48	1.57
T17	250-425	0.68	108.46	106.08	0.27	1.43	1.47
T18	250-425	0.72	110.58	107.70	0.29	1.40	1.42

Table A5.3, *Uncertainties of concentration difference and tortuosity for porous Cu samples with different porosities and pore sizes.*

Ref.	Pore size (μm)	Porosity, ε	$c_{b,t}$-$c_{t,t}$	$ln[(c_{b,i}-c_{t,i})/(c_{b,t}-c_{t,t})]$	Tortuosity, τ	Error %
T01	1000-1500	0.68	1.33±0.03	0.28±0.02	1.78±0.08	4.3%
T02	1000-1500	0.71	1.20±0.03	0.38±0.03	1.57±0.05	3.4%
T03	1000-1500	0.80	0.95±0.03	0.61±0.03	1.41±0.03	2.4%
T04	1000-1500	0.84	0.98±0.03	0.58±0.03	1.35±0.03	2.5%
T05	710-1000	0.64	1.31±0.03	0.29±0.02	1.70±0.07	4.2%
T06	710-1000	0.69	1.25±0.03	0.34±0.03	1.62±0.06	3.8%
T07	710-1000	0.73	1.15±0.03	0.42±0.03	1.50±0.05	3.1%
T08	710-1000	0.78	1.00±0.03	0.56±0.03	1.33±0.03	2.6%
T09	425-710	0.56	1.40±0.03	0.23±0.02	1.75±0.09	5.3%
T10	425-710	0.60	1.34±0.03	0.27±0.02	1.70±0.08	4.5%
T11	425-710	0.65	1.25±0.03	0.33±0.02	1.59±0.06	3.7%
T12	425-710	0.69	1.15±0.03	0.42±0.03	1.45±0.05	3.1%
T13	425-710	0.73	1.09±0.03	0.47±0.03	1.40±0.04	2.8%
T14	250-425	0.56	1.35±0.03	0.26±0.02	1.63±0.08	4.7%
T15	250-425	0.60	1.30±0.03	0.30±0.03	1.61±0.07	4.2%
T16	250-425	0.64	1.25±0.03	0.33±0.03	1.57±0.06	3.8%
T17	250-425	0.68	1.16±0.03	0.41±0.03	1.47±0.05	3.2%
T18	250-425	0.72	1.11±0.03	0.46±0.03	1.42±0.04	3.0%

Table A6.1, *Volumetric and gravimetric specific geometric surface areas (S_{VG} and S_{MG}) of porous Cu samples.*

Sample Ref.	Pore size (μm)	Total porosity (ε)	P	S_{VG} (cm^{-1})	S_{MG} (cm^2/g)
S01	1000-1500	0.59	66	18.31	4.98
S02	1000-1500	0.63	71	19.85	5.99
S03	1000-1500	0.67	75	20.77	7.02
S04	1000-1500	0.71	80	22.15	8.52
S05	1000-1500	0.75	85	23.54	10.51
S06	710-1000	0.59	100	27.85	7.58
S07	710-1000	0.64	109	30.15	9.35
S08	710-1000	0.68	115	32.00	11.16
S09	710-1000	0.72	118	32.77	13.06
S10	710-1000	0.75	126	35.08	15.66
S11	425-710	0.59	144	40.00	10.89
S12	425-710	0.63	165	45.85	13.83
S13	425-710	0.67	172	47.85	16.18
S14	425-710	0.70	182	50.62	18.83
S15	425-710	0.75	208	57.69	25.75
S16	250-425	0.59	236	65.69	17.88
S17	250-425	0.64	254	70.62	21.89
S18	250-425	0.67	265	73.54	24.87
S19	250-425	0.70	295	82.00	30.51
S20	250-425	0.75	317	88.15	39.35

Table A6.2, *Volumetric and gravimetric specific geometric surface areas (S_{VG} and S_{MG}) of porous Ni samples.*

Sample Ref.	Pore size (μm)	Total porosity (ε)	P	S_{VG} (cm^{-1})	S_{MG} (cm^2/g)
Ni01	1000-1500	0.65	97	26.89	8.62
Ni02	1000-1500	0.67	117	32.54	11.07
Ni03	1000-1500	0.70	119	32.99	12.35
Ni04	1000-1500	0.73	123	34.15	14.20
Ni05	1000-1500	0.77	127	35.17	17.17
Ni06	1000-1500	0.81	123	34.03	20.10
Ni07	710-1000	0.63	151	42.08	12.77
Ni08	710-1000	0.66	148	41.22	13.61
Ni09	710-1000	0.69	149	41.47	15.02
Ni10	710-1000	0.73	154	42.74	17.77
Ni11	710-1000	0.77	172	47.80	23.33
Ni12	710-1000	0.81	167	46.27	27.34
Ni13	425-710	0.62	162	44.88	13.26
Ni14	425-710	0.65	205	57.02	18.29
Ni15	425-710	0.68	192	53.33	18.71
Ni16	425-710	0.72	236	65.60	26.30
Ni17	425-710	0.76	245	67.94	31.78
Ni18	425-710	0.80	240	66.60	37.38
Ni19	250-425	0.62	348	96.62	28.54
Ni20	250-425	0.65	369	102.45	32.86
Ni21	250-425	0.68	380	105.57	37.03
Ni22	250-425	0.71	376	104.36	40.40
Ni23	250-425	0.75	399	110.79	49.75
Ni24	250-425	0.79	390	108.23	57.85

Table A7.2, *Volumetric specific electro-active (S_{VE}) and geometric (S_{VG}) surface areas and their ratio (θ) for porous Cu samples with different porosities and pore sizes.*

Ref.	Pore size (μm)	Porosity, ε	S_{VE} (cm^{-1})	S_{VG} (cm^{-1})	θ
Cu01	1000-1500	0.59	234.98	18.31	12.97
Cu02	1000-1500	0.62	275.56	19.47	13.31
Cu03	1000-1500	0.65	293.03	20.31	14.09
Cu04	1000-1500	0.69	255.69	21.46	9.53
Cu05	1000-1500	0.72	251.98	22.50	8.88
Cu08	710-1000	0.59	244.11	27.85	7.16
Cu09	710-1000	0.64	281.19	30.15	7.86
Cu10	710-1000	0.67	209.39	31.54	5.27
Cu11	710-1000	0.71	304.37	32.58	7.08
Cu12	710-1000	0.74	287.88	34.31	5.55
Cu14	425-710	0.61	299.33	40.00	7.26
Cu15	425-710	0.63	244.61	45.85	5.28
Cu16	425-710	0.67	274.34	47.85	5.30
Cu17	425-710	0.71	284.45	52.03	4.39
Cu18	425-710	0.74	238.02	56.28	3.25
Cu20	250-425	0.59	235.91	65.69	2.98
Cu21	250-425	0.63	259.08	65.70	3.32
Cu22	250-425	0.66	265.38	70.62	3.10
Cu23	250-425	0.70	280.43	82.00	3.22
Cu24	250-425	0.73	261.56	85.69	2.44
Cu25	75-150	0.53	316.31	156.50	1.80
Cu26	75-150	0.56	345.92	157.28	1.97
Cu27	75-150	0.61	327.85	156.00	1.90
Cu28	75-150	0.63	340.47	154.54	2.00
Cu29	75-150	0.67	369.17	149.90	2.27
Cu30	75-150	0.68	366.83	148.36	2.26

Table A7.1, *Volumetric and gravimetric specific electro-active surface areas (S_{VE} and S_{ME}) of porous Cu samples.*

Sample Ref.	Pore size (μm)	Total Porosity (ε)	I_P (mA/g)	S_{VE} (cm^{-1})	S_{ME} (cm^2/g)
Cu01	1000-1500	0.59	24.60	234.98	63.96
Cu02	1000-1500	0.62	31.13	275.56	80.93
Cu03	1000-1500	0.65	35.94	293.03	93.44
Cu04	1000-1500	0.69	35.40	255.69	92.05
Cu05	1000-1500	0.72	38.63	251.98	100.44
Cu06	1000-1500	0.76	43.52	243.32	113.15
Cu07	710-1000	0.56	30.98	317.52	80.54
Cu08	710-1000	0.59	25.56	244.11	66.45
Cu09	710-1000	0.64	33.53	281.19	87.17
Cu10	710-1000	0.67	27.24	209.39	70.82
Cu11	710-1000	0.71	45.05	304.37	117.14
Cu12	710-1000	0.74	47.53	287.88	123.57
Cu13	425-710	0.57	20.60	206.38	53.57
Cu14	425-710	0.61	32.95	299.33	85.66
Cu15	425-710	0.63	28.38	244.61	73.78
Cu16	425-710	0.67	35.68	274.34	92.78
Cu17	425-710	0.71	42.10	284.45	109.47
Cu18	425-710	0.74	39.30	238.02	102.17
Cu19	250-425	0.55	25.34	265.66	65.89
Cu20	250-425	0.59	24.70	235.91	64.22
Cu21	250-425	0.63	30.06	259.08	78.15
Cu22	250-425	0.66	33.50	265.38	87.11
Cu23	250-425	0.70	40.13	280.43	104.33
Cu24	250-425	0.73	41.58	261.56	108.12
Cu25	75-150	0.53	28.89	316.31	75.11
Cu26	75-150	0.56	33.75	345.92	87.74
Cu27	75-150	0.61	36.08	327.85	93.82
Cu28	75-150	0.63	39.50	340.47	102.70
Cu29	75-150	0.67	48.02	369.17	124.85
Cu30	75-150	0.68	49.21	366.83	127.94

Table A8.1, *Peak current (I_P) for porous Ni samples with the pore size of 250-1500 µm and porosity of 0.62-0.81.*

Ref.	Pore size (µm)	Total porosity	Peak current, *Ip*, (mA/g)					
			0.005 V/s	**0.01 V/s**	**0.05 V/s**	**0.1 V/s**	**0.2 V/s**	**0.3 V/s**
Ni01	1000-1500	0.65	0.68	1.27	4.74	7.79	12.19	15.26
Ni02	1000-1500	0.67	1.07	1.91	6.70	10.83	16.67	21.93
Ni03	1000-1500	0.70	1.17	2.10	7.62	12.45	19.47	24.87
Ni04	1000-1500	0.73	1.21	2.16	7.53	12.23	18.65	26.27
Ni05	1000-1500	0.77	1.58	2.70	9.38	14.88	23.43	30.46
Ni06	1000-1500	0.81	2.04	3.36	11.28	18.03	28.23	36.20
Ni07	710-1000	0.63	0.98	1.79	6.27	10.14	16.22	20.76
Ni08	710-1000	0.66	1.00	1.85	6.83	11.16	17.65	24.02
Ni09	710-1000	0.69	1.22	2.14	7.33	11.65	18.36	23.74
Ni10	710-1000	0.73	1.43	2.55	8.89	14.44	23.01	29.16
Ni11	710-1000	0.77	1.80	3.05	10.25	16.99	26.40	33.41
Ni17	425-710	0.77	2.42	4.11	13.06	20.45	30.78	39.10
Ni18	425-710	0.81	2.59	4.38	13.81	21.51	34.08	43.50
Ni19	250-425	0.62	0.93	1.81	6.94	11.15	17.18	22.84
Ni20	250-425	0.65	1.26	2.42	8.82	13.90	21.16	26.10
Ni21	250-425	0.68	1.62	3.09	10.64	16.37	24.40	32.05
Ni22	250-425	0.71	2.02	3.73	11.95	18.18	27.00	32.91
Ni23	250-425	0.75	2.31	4.32	14.70	22.56	32.92	40.73
Ni24	250-425	0.79	3.06	5.56	17.15	25.41	36.97	46.38

Table A8.2, *Gravimetric specific surface areas (S_{ME}) for the porous Ni samples with the pore size of 250-1500 µm and porosity of 0.62-0.81.*

Ref.	Pore size (µm)	ε	Gravimetric specific surface area (cm^2/g)					
			0.005 V/s	0.01 V/s	0.05 V/s	0.1 V/s	0.2 V/s	0.3 V/s
Ni01	1000-1500	0.65	7.80	10.42	17.30	20.09	22.23	22.71
Ni02	1000-1500	0.67	12.36	15.60	24.42	27.93	30.39	32.63
Ni03	1000-1500	0.70	13.47	17.13	27.78	32.09	35.49	37.02
Ni04	1000-1500	0.73	13.94	17.62	27.46	31.53	33.99	39.10
Ni05	1000-1500	0.77	18.21	21.98	34.20	38.37	42.70	45.33
Ni06	1000-1500	0.81	23.47	27.37	41.11	46.48	51.46	53.87
Ni07	710-1000	0.63	11.25	14.59	22.86	26.14	29.57	30.89
Ni08	710-1000	0.66	11.50	15.06	24.91	28.76	32.16	35.75
Ni09	710-1000	0.69	14.02	17.45	26.73	30.04	33.46	35.33
Ni10	710-1000	0.73	16.45	20.77	32.42	37.21	41.93	43.39
Ni11	710-1000	0.77	20.72	24.89	37.36	43.80	48.12	49.73
Ni17	425-710	0.77	27.95	33.46	47.61	52.70	56.10	58.19
Ni18	425-710	0.81	29.82	35.73	50.33	55.44	62.12	64.73
Ni19	250-425	0.62	10.68	14.73	25.29	28.74	32.30	34.00
Ni20	250-425	0.65	14.52	19.74	32.13	35.84	38.57	38.84
Ni21	250-425	0.68	18.71	25.20	38.77	42.20	44.47	47.69
Ni22	250-425	0.71	23.31	30.37	43.55	46.85	49.20	48.99
Ni23	250-425	0.75	26.67	35.25	53.59	58.14	60.00	60.61
Ni24	250-425	0.79	35.28	45.32	62.52	65.50	67.38	69.02

Table A8.3, *Volumetric specific surface areas (S_{VE}) for the porous Ni samples with the pore size of 250-1500 µm and porosity of 0.62-0.81.*

Ref.	**Pore size (µm)**	***ε***	**Volumetric specific surface area (cm^{-1})**					
			0.005 V/s	**0.01 V/s**	**0.05 V/s**	**0.1 V/s**	**0.2 V/s**	**0.3 V/s**
Ni01	1000-1500	0.65	24.33	32.49	53.93	62.64	69.30	70.80
Ni02	1000-1500	0.67	36.34	45.84	71.77	82.10	89.34	95.92
Ni03	1000-1500	0.70	35.99	45.77	74.25	85.75	94.84	98.92
Ni04	1000-1500	0.73	33.54	42.38	66.05	75.84	81.75	94.04
Ni05	1000-1500	0.77	37.31	45.04	70.07	78.61	87.48	92.87
Ni06	1000-1500	0.81	39.73	46.32	69.58	78.67	87.09	91.18
Ni07	710-1000	0.63	37.08	48.08	75.33	86.16	97.47	101.81
Ni08	710-1000	0.66	34.82	45.60	75.44	87.11	97.41	108.26
Ni09	710-1000	0.69	38.72	48.20	73.80	82.95	92.39	97.57
Ni10	710-1000	0.73	39.57	49.95	77.97	89.50	100.85	104.37
Ni11	710-1000	0.77	42.45	50.99	76.54	89.74	98.60	101.88
Ni17	425-710	0.77	57.26	68.56	97.54	107.97	114.94	119.22
Ni18	425-710	0.81	50.46	60.48	85.18	93.83	105.13	109.56
Ni19	250-425	0.62	36.16	49.88	85.60	97.29	105.97	115.08
Ni20	250-425	0.65	45.27	61.56	100.19	111.73	120.25	121.09
Ni21	250-425	0.68	53.34	71.83	110.53	120.30	126.77	135.95
Ni22	250-425	0.71	60.22	78.47	112.50	121.04	127.11	126.55
Ni23	250-425	0.75	59.39	78.50	119.35	129.48	133.62	134.98
Ni24	250-425	0.79	66.00	84.78	116.95	122.54	126.04	129.12

Table A8.4, *Ratio between electro-active and geometric surface area (θ) at different predicted diffusion layer thicknesses for porous Ni samples with different porosities and pore sizes.*

Ref.	Pore size (μm)	ε	Ratio between electro-active and geometric surface area, θ					
			δ=102 (μm)	δ=72 (μm)	δ=32 (μm)	δ=23 (μm)	δ=16 (μm)	δ=13 (μm)
Ni01	1000-1500	0.65	0.90	1.21	2.01	2.33	2.58	2.63
Ni02	1000-1500	0.67	1.12	1.41	2.21	2.52	2.75	2.95
Ni03	1000-1500	0.70	1.22	1.55	2.51	2.90	3.20	3.34
Ni04	1000-1500	0.73	0.98	1.24	1.93	2.22	2.39	2.75
Ni05	1000-1500	0.77	1.06	1.28	1.99	2.24	2.49	2.64
Ni06	1000-1500	0.81	1.17	1.36	2.04	2.31	2.56	2.68
Ni07	710-1000	0.63	0.88	1.14	1.79	2.05	2.32	2.42
Ni08	710-1000	0.66	0.84	1.11	1.83	2.11	2.36	2.63
Ni09	710-1000	0.69	0.93	1.16	1.78	2.00	2.23	2.35
Ni10	710-1000	0.73	0.93	1.17	1.82	20.9	2.36	2.44
Ni11	710-1000	0.77	0.89	1.07	1.60	1.88	2.06	2.13
Ni17	425-710	0.77	0.88	1.05	1.50	1.66	1.77	1.83
Ni18	425-710	0.81	0.80	0.96	1.35	1.48	1.66	1.73
Ni19	250-425	0.62	0.45	0.62	1.07	1.22	1.32	1.44
Ni20	250-425	0.65	0.50	0.68	1.10	1.23	1.32	1.33
Ni21	250-425	0.68	0.60	0.80	1.23	1.34	1.42	1.52
Ni22	250-425	0.71	0.58	0.75	1.08	1.16	1.22	1.21
Ni23	250-425	0.75	0.54	0.71	1.08	1.17	1.21	1.22
Ni24	250-425	0.79	0.61	0.78	1.08	1.13	1.16	1.19

Table A9.1, *Double layer capacitance and specific real surface areas (S_{MR} and S_{VR}) for porous Cu samples.*

Ref.	Pore size (μm)	Porosity	C (mF)	R^2	S_{MR} (cm^2/g)	S_{VR} (cm^{-1})
Cu01	1000-1500	0.59	4.38	0.98	219.10	804.87
Cu02	1000-1500	0.62	4.82	1	240.90	820.21
Cu03	1000-1500	0.65	5.06	0.99	252.79	792.73
Cu04	1000-1500	0.69	5.44	1	271.94	755.35
Cu05	1000-1500	0.72	5.66	1	283.00	709.99
Cu06	1000-1500	0.76	4.47	0.99	223.18	479.82
Cu07	710-1000	0.56	4.13	0.94	208.72	822.85
Cu08	710-1000	0.59	6.65	0.99	332.38	1221.03
Cu09	710-1000	0.64	4.50	0.97	224.88	725.37
Cu10	710-1000	0.67	5.88	1	293.70	868.41
Cu11	710-1000	0.71	6.25	0.99	312.50	811.99
Cu12	710-1000	0.74	6.83	1	341.61	795.8
Cu13	425-710	0.57	5.39	0.99	269.29	1037.50
Cu14	425-710	0.61	4.04	0.99	201.79	705.12
Cu15	425-710	0.63	4.78	0.99	238.90	792.00
Cu16	425-710	0.67	4.95	0.98	247.34	731.34
Cu17	425-710	0.71	5.79	0.99	289.13	751.26
Cu18	425-710	0.74	6.89	1	338.79	789.24
Cu19	250-425	0.55	4.71	0.98	235.42	949.20
Cu20	250-425	0.59	4.46	0.99	222.64	817.88
Cu21	250-425	0.63	6.56	0.99	327.85	1086.88
Cu22	250-425	0.66	5.37	1	268.58	818.20
Cu23	250-425	0.70	7.25	1	362.16	973.48
Cu24	250-425	0.73	6.77	1	338.33	818.49
Cu25	75-150	0.53	5.49	0.99	274.50	1155.98
Cu26	75-150	0.56	5.76	1	287.69	1134.17
Cu27	75-150	0.61	5.51	1	275.30	962.01
Cu28	75-150	0.63	6.04	1	302.07	1001.43
Cu29	75-150	0.67	6.31	1	322.37	895.42
Cu30	75-150	0.68	6.45	1	315.37	904.24

Table A10.1, *Limiting current I_L for porous Ni samples with the pore size of 250-1500 µm and porosity of 0.62-0.77.*

Ref.	Pore size (µm)	Porosity	Limiting current (mA/cm^3)				
			0.24 ml/s	0.48 ml/s	0.8 ml/s	2 ml/s	2.8 ml/s
Ni01	1000-1500	0.65	9.80	20.53	32.62	96.76	130.26
Ni02	1000-1500	0.67	35.08	67.43	103.81	242.34	303.19
Ni03	1000-1500	0.70	37.29	65.10	94.35	199.93	248.69
Ni04	1000-1500	0.73	23.45	43.58	65.98	146.73	182.58
Ni05	1000-1500	0.77	20.98	34.54	48.65	106.57	132.82
Ni07	710-1000	0.63	14.76	26.87	39.73	91.04	117.15
Ni08	710-1000	0.66	28.60	52.06	72.25	158.46	194.94
Ni09	710-1000	0.69	43.65	77.72	111.35	235.28	292.78
Ni10	710-1000	0.73	41.01	71.28	102.54	214.73	271.57
Ni11	710-1000	0.77	30.46	50.64	70.43	138.27	174.15
Ni19	250-425	0.62	33.15	62.26	89.80	233.36	283.30
Ni20	250-425	0.65	62.56	111.21	151.27	299.27	355.11
Ni21	250-425	0.68	61.86	100.28	129.97	246.94	327.62
Ni22	250-425	0.71	67.31	102.06	132.79	233.56	267.75
Ni23	250-425	0.75	70.67	103.45	126.46	207.92	236.87

Table A10.2, *Mass transfer coefficient (k) for porous Ni samples with the pore size of 250-1500 µm and porosities of 0.62-0.77.*

Ref.	Pore size (µm)	Porosity	Mass transfer coefficient (cm/s)				
			0.24 ml/s	0.48 ml/s	0.8 ml/s	2 ml/s	2.8 ml/s
Ni01	1000-1500	0.65	0.0038	0.0079	0.0125	0.0371	0.0499
Ni02	1000-1500	0.67	0.0111	0.0214	0.0329	0.0767	0.0960
Ni03	1000-1500	0.70	0.0116	0.0203	0.0295	0.0624	0.0776
Ni04	1000-1500	0.73	0.0071	0.0132	0.0199	0.0443	0.0551
Ni05	1000-1500	0.77	0.0061	0.0101	0.0143	0.0312	0.0389
Ni07	710-1000	0.63	0.0036	0.0066	0.0097	0.0223	0.0287
Ni08	710-1000	0.66	0.0071	0.0130	0.0181	0.0396	0.0487
Ni09	710-1000	0.69	0.0108	0.0193	0.0277	0.0584	0.0727
Ni10	710-1000	0.73	0.0099	0.0172	0.0247	0.0518	0.0655
Ni11	710-1000	0.77	0.0066	0.0109	0.0152	0.0298	0.0375
Ni19	250-425	0.62	0.0035	0.0066	0.0096	0.0249	0.0302
Ni20	250-425	0.65	0.0063	0.0112	0.0152	0.0301	0.0357
Ni21	250-425	0.68	0.0060	0.0098	0.0127	0.0241	0.0320
Ni22	250-425	0.71	0.0066	0.0101	0.0131	0.0231	0.0264
Ni23	250-425	0.75	0.0066	0.0096	0.0118	0.0193	0.0220

Table A10.3, *Reynolds number (Re) and Sherwood number (Sh) at different flow rates for porous Ni samples with different porosities and pore sizes.*

Ref.	Pore size (μm)	ε	0.24 ml/s		0.48 ml/s		0.8 ml/s		2 ml/s		2.8 ml/s	
			Re	***Sh***	***Re***	***Sh***	***Re***	***Sh***	***Re***	***Sh***	***Re***	***Sh***
Ni01	1000-1500	0.65	20.05	88.05	41.00	184.47	68.33	293.09	170.84	869.53	239.17	1170.56
Ni02	1000-1500	0.67	19.89	260.32	39.78	500.43	66.29	770.44	165.74	1798.51	232.03	2250.10
Ni03	1000-1500	0.70	19.04	272.84	38.07	476.39	63.45	690.39	158.63	1462.97	222.09	1819.76
Ni04	1000-1500	0.73	18.25	165.85	36.51	308.19	60.85	466.55	152.11	1037.59	212.96	1291.02
Ni05	1000-1500	0.77	17.31	144.03	34.61	237.15	57.68	334.02	144.21	731.63	201.90	911.83
Ni07	710-1000	0.63	14.24	57.03	28.48	103.80	47.47	153.50	118.68	351.75	166.15	452.60
Ni08	710-1000	0.66	13.59	112.82	27.19	205.39	45.31	285.03	113.29	625.11	158.60	769.01
Ni09	710-1000	0.69	13.00	171.15	26.01	304.70	43.34	436.56	108.36	922.40	151.71	1147.84
Ni10	710-1000	0.73	12.29	156.03	24.58	271.20	40.97	390.15	102.42	816.98	143.39	1033.25
Ni11	710-1000	0.77	11.65	103.61	23.30/	172.29	38.84	239.61	97.10	470.38	135.94	592.44
Ni19	250-425	0.62	5.26	20.28	10.52	38.08	17.53	54.92	43.82	142.73	61.35	173.27
Ni20	250-425	0.65	5.02	36.08	10.03	64.14	16.72	87.24	41.80	172.60	58.52	204.81
Ni21	250-425	0.68	4.79	34.63	9.59	56.13	15.98	72.76	39.95	138.23	55.94	183.40
Ni22	250-425	0.71	4.59	38.11	9.18	57.78	15.31	75.18	38.27	132.23	53.57	151.59
Ni23	250-425	0.75	4.35	37.69	8.69	55.17	14.49	67.44	36.22	110.88	50.71	126.33

Table A10.4, *Empirical correlation parameters a and b for porous Ni samples with different porosities and pore sizes.*

Sample Ref.	**Pore size (μm)**	**Porosity, ε**	***a***	***b***
Ni01	1000-1500	0.65	0.30	1.07
Ni02	1000-1500	0.67	1.67	0.89
Ni03	1000-1500	0.70	2.45	0.78
Ni04	1000-1500	0.73	1.30	0.84
Ni05	1000-1500	0.77	1.43	0.76
Ni07	710-1000	0.63	0.53	0.85
Ni08	710-1000	0.66	1.30	0.79
Ni09	710-1000	0.69	2.09	0.79
Ni10	710-1000	0.73	2.00	0.77
Ni11	710-1000	0.77	1.60	0.71
Ni19	250-425	0.62	0.40	0.90
Ni20	250-425	0.65	1.07	0.71
Ni21	250-425	0.68	1.05	0.67
Ni22	250-425	0.71	1.43	0.57
Ni23	250-425	0.75	1.64	0.50